InSAR-based analysis and monitoring of hazardous glacial lakes in the Himalaya

Ylana van Hout

TU Delft

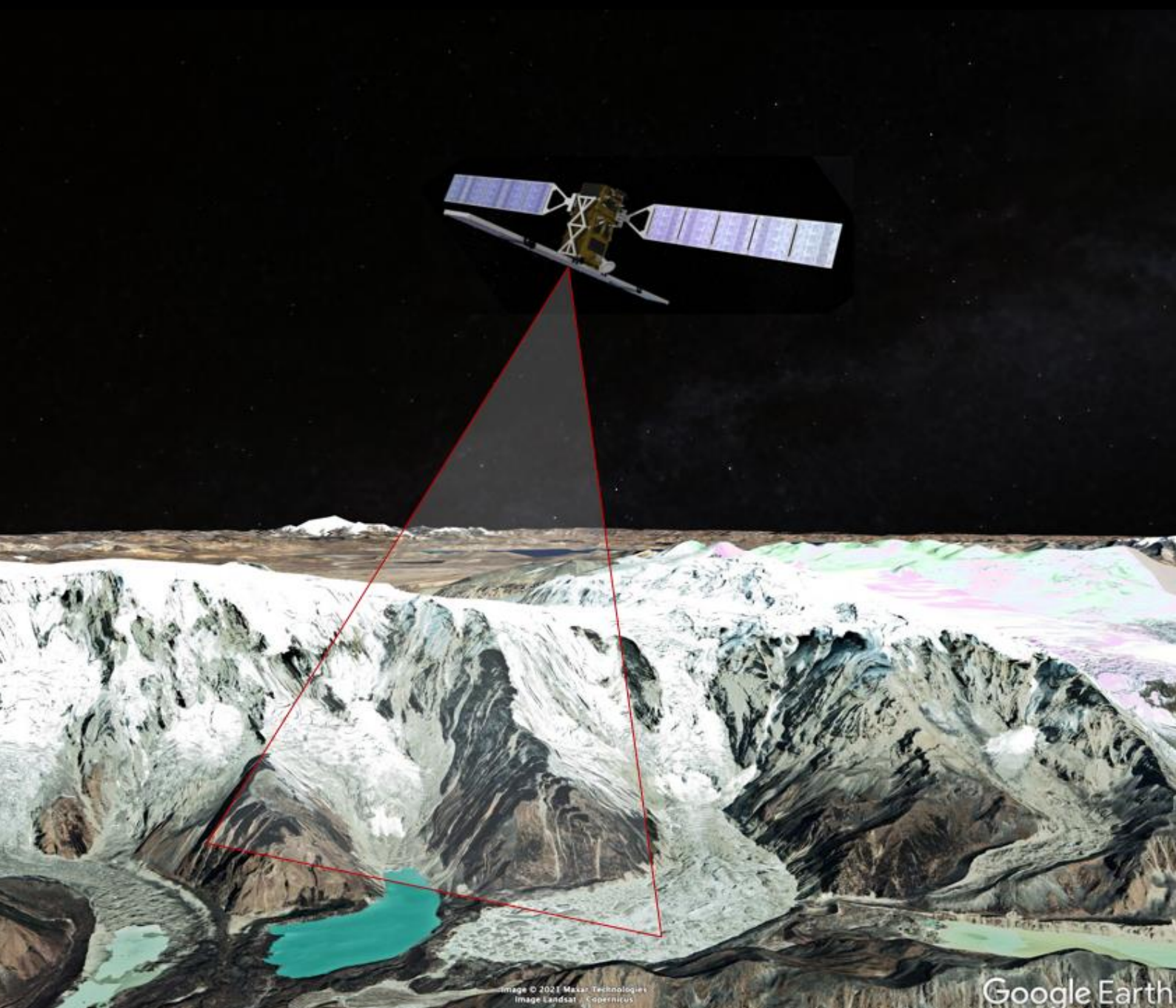

InSAR-based analysis and monitoring of hazardous glacial lakes in the Himalaya

Ylana van Hout
Master of Science Thesis
Delft University of Technology, MSc Applied Earth Sciences (Track Geo-Engineering)
Student No.: 4340647, mailto: ylanavanhout@gmail.com

Thesis committee:
Dr. G. Giardina (TU Delft)
Dr. M. Whitworth (AECOM)
D. Malinowska (University of Bath)
Dr. P. Milillo (University of Houston)
Dr. A. Askarinejad (Swiss Federal Office of Energy)
Dr. S. Lhermitte (TU Delft)

Abstract

Glacial lake outburst floods (GLOFs) are outbursts caused by the failure of glacial lake moraine dams. Longer ongoing processes, such as moraine dam degradation, or instantaneous events, such as landslides, can trigger dam failure. GLOFs have a catastrophic downstream impact leading to significant economic damages and more than 12000 casualties worldwide until 2015, with Bhutan and Nepal being impacted the most. Climate change leads to increasing temperature and precipitation, leading to the expansion of glacial lakes and the destabilisation of glaciers, slopes and moraine dams. Consequently, GLOFs are likely to become more frequent, and glacial lakes require continuous monitoring and analysis to understand and predict GLOF-related hazards. Since glacial lakes often lie in inaccessible mountainous regions, on-site monitoring is challenging and remote sensing proposes a safe and cost-effective solution. Satellite radar is unaffected by nighttime and clouds enabling continuous displacement measurements. Interferometric synthetic aperture radar (InSAR) using Sentinel-1 data from 2014 to 2021 was applied at six Himalayan glacial lake areas (Imja, Lunana, Barun, Rolpa, Thulagi and Lumding) to identify potential GLOF hazards and to investigate InSAR's capability as a monitoring tool. Optical, meteorological and topographical data were used to aid in interpreting the InSAR observations; linking displacements to potential hazards and evaluating the limitations of an InSAR-based analysis.

Significant deformation was detected at the terminal moraines of Imja, Thulagi, Rolpa, Lunana and Barun Lakes; on lateral moraines at Rolpa and Lunana Lakes; and on rock glaciers at Imja, Rolpa, Barun and Lunana Lakes. In addition, significant seasonal variation could be distinguished, showing the impact of temperature and precipitation on geomorphological processes and potential hazard developments at glacial lakes. InSAR-related limitations arose in regions with significant topographic variations, extant snow or vegetation covers, and rapid displacements.

This study demonstrates the capability of satellite InSAR as a glacial lake monitoring tool. An InSAR-based analysis is instrumental in highlighting areas from where GLOFs could originate, requiring mitigation measures or further investigation to map the impact of failure. By extending the research frame over multiple years, continuous and long-term monitoring could demonstrate the climatic influence on displacements and GLOF trigger developments.

Contents

Abbreviations

ALOS Advanced Land Observation Satellite

AOI area of interest

APS atmospheric phase screen

asc ascending

ASI amplitude stability index

AW3D30 ALOS World 3D-30m

CDInSAR conventional differential interferometric synthetic-aperture radar

DEM digital elevation model

desc descending

DInSAR differential interferometric synthetic-aperture radar

DLR German Aerospace Center

DSM digital surface map

DTM digital terrain map

ESA European Space Agency

GCP ground control point

GE Google Earth

GIS geographic information system

GLOF glacial lake outburst flood

GPS Global Positioning System

HMA High Mountain Asia

InSAR interferometric synthetic-aperture radar

JAXA Japan Aerospace Exploration Agency

LiDAR light detection and ranging

LOS line of sight

NASA National Aeronautics and Space Administration

NDVI Normalised Difference Vegetation Index

NGA National Geospatial-Intelligence Agency

PS persistent scatterers

PSC persistent scatterer candidate

PSI persistent scatterer interferometry

QGIS Quantum Geographic Information System

ref. point reference point

RI range index

RGB	red green blue
SAR	synthetic-aperture radar
SLC	Single Look Complex
SRTM	Shuttle Radar Topography Mission
SWIR	short-wavelength infrared
VIS	visible
VNIR	visible-and-near-infrared
w.r.t.	with respect to

List of Figures

List of Tables

1 Introduction

Glacial lake outburst floods (GLOFs) are outbursts caused by the failure of glacial lake dams and can have a catastrophic downstream impact. GLOFs are a severe consequence of climate change induced glacier retreat and concurrent glacial lake growth (GAPHAZ et al., 2017). The dams of moraine-dammed glacial lakes are susceptible to failure because they are often steep and narrow, sparsely vegetated, consist of loose and poorly sorted material, and usually consist of an ice-core or interstitial ice (Bajracharya et al., 2020; Clague and O'Conner, 2021). As a result, dynamic and self-destructive events can trigger GLOFs. Dynamic events comprise initiating events, such as glacier calving, landslides and earthquakes. These events can produce high waves that flood, erode and destroy the moraine dam. Self-destructive events consist of slow-developing moraine dam destabilisation due to ice core melting, seepage, or the increasing hydrostatic pressure caused by expanding lakes (Emmer and Cochachin, 2013). Glacial lakes can contain large water volumes, and outburst floods tend to consist of low viscosity debris flows, resulting in devastating damage, including life loss and the destruction of agriculture and infrastructure (Westoby et al., 2014a). Figure 1 displays news article images that have been captured during or after GLOFs, showing the destructive power of such floods. Because of the increase in human settlements, anthropogenic activities and infrastructure development, the GLOF risk has also increased. Especially in mountain countries, much of the population is settled along the fertile grounds near the rivers downstream of hazardous glacial lakes (Bajracharya et al., 2007b). Until 2015, 1348 GLOFs have directly caused at least 12000 deaths worldwide, with the highest numbers in central Asia (6300) and South America (5745) (Carrivick and Tweed, 2016).

Glaciers started to retreat at the end of the Little Ice Age (about 1850), and ever since, the number and size of glacial lakes have been increasing due to climate change. Concurrently, the number of GLOF events has risen significantly (Ahmed et al., 2021; Carrivick and Tweed, 2016; Fischer et al., 2006; Harrison et al., 2018). Figure 2 displays the worldwide frequency of historical GLOFs. The graphs reveal the increment in GLOFs once glacial lakes started to grow in the 19th century. Larger lakes are more susceptible to bursting since there is more chance of

Figure 1: Destructive downstream impact of GLOFs. (a) India 2021 (retrieved from https://theshillongtimes.com) , (b) India 2012 (retrieved from https://climatechangenews.com), (c) Nepal 2011 (Photo from Astrid Hovden), (d) Pakistan 2019 (retrieved from https://dawn.com)

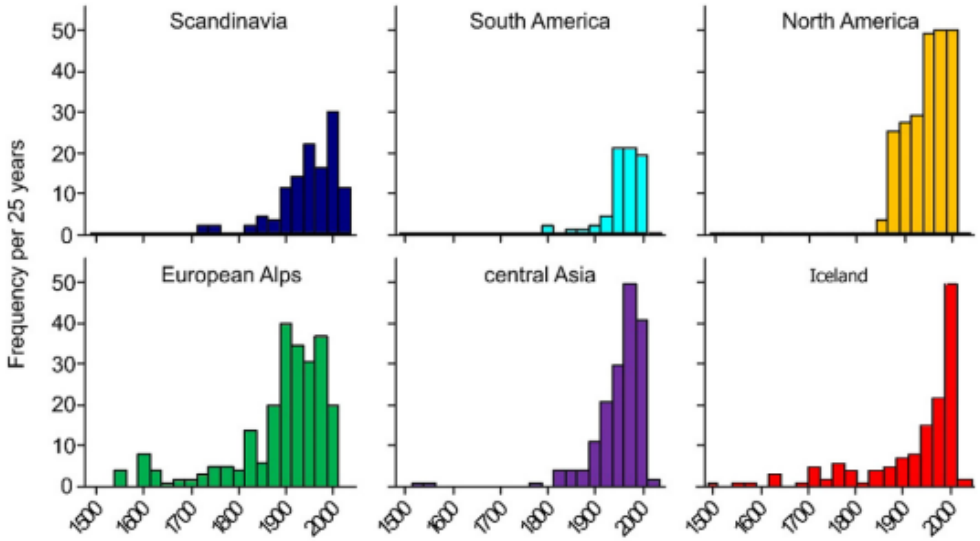

Figure 2: Worldwide GLOF frequency over the last centuries (Carrivick and Tweed, 2016)

mass falling into the lake, and the hydrostatic pressure on the end moraine containing the dam increases (Fischer et al., 2020). Shugar et al. (2020) found a global glacier lake volume increase of 48% between 1990 and 2018, with lake number increasing by 53% and lake area by 51%. This trend is likely to continue with the ongoing climate change, leading directly to increasing GLOF risk. In addition, the GLOF triggers mentioned in the first paragraph will become more frequent due to climate change, as the stability of slopes and moraine dams is directly influenced by temperature and precipitation (Emmer et al., 2020; GAPHAZ et al., 2017).

Consequently, phenomena associated with GLOF triggers require great attention. Outburst triggers consist of complex and varying mechanisms and only a few extensively documented historical GLOFs exist. These factors prevent a complete understanding of GLOF triggers and make hazard identification and GLOF prediction extremely challenging. Therefore, glacial lakes require continuous monitoring and extensive analyses to map and mitigate hazards (Emmer et al., 2020; GAPHAZ et al., 2017; Nie et al., 2018; Peppa et al., 2020; Petrakov et al., 2012). Alpine glacial lakes often contain dam stabilisations, controlled outflows and monitoring systems. However, other mountain ranges, such as the Himalaya, have large inaccessible areas and have fewer economic resources. As a result, on-site surveys to investigate lake expansion, slope instabilities and moraine dam degradation are costly and mitigation is difficult (Strozzi et al., 2012). These issues are reflected in the number of casualties and economic consequences of glacier flood impacts, which are highest in Nepal and Bhutan (Carrivick and Tweed, 2016).

Remote sensing is a safe and cost-effective solution for monitoring and analysing glacial lakes in hazardous and inaccessible areas. Glacial lakes have been successfully researched using optical remote sensing, focusing on lake expansion and hazard identification (Bajracharya et al., 2020; Begam and Sen, 2019; Khadka et al., 2019; Maharjan et al., 2018; Peppa et al., 2020; Quincey et al., 2007; Veh et al., 2018; Xie et al., 2013). However, frequent cloud and snow cover and the constriction to daytime operations prevent continuous monitoring. Synthetic aperture radar (SAR) overcomes these issues using radar waves that penetrate clouds and snow and enable operation 24 hours a day. SAR is an active microwave technology that measures the amplitude and phase of reflected radar waves to generate high-resolution surface images. The amplitude depends on the surface reflective properties; it can therefore provide information about the surface type. Phase differences of radar waves between SAR images can produce millimetre displacements, referred to as interferometric SAR (InSAR) (Ferretti et al., 2007). Consequently, InSAR can identify and quantify surface features, slope movements and subsidence areas. InSAR has

proved capable of delineating glacial lakes (Strozzi et al., 2012; Wangchuk et al., 2019) and analysing mountainous slope processes (Carlá et al., 2019; Dini et al., 2019; Kos et al., 2016; Scapozza et al., 2019). Various studies highlight the necessity of integrating geomorphological and meteorological data with InSAR to improve the understanding of glacial lake phenomena and GLOF triggers, aiming for identifying hazards and potentially predicting GLOFs (Khadka et al., 2018; Klimeš et al., 2016; Scapozza et al., 2019; Strozzi et al., 2012). Still, studies that apply InSAR for analysing potential hazards at glacial lakes are scarce.

The challenge of quantifying and identifying potential outburst triggers, the increasing GLOF risk due to continuous lake expansion, the inaccessibility of glacial lakes, the lack of monitoring methods and mitigation measures and the large number of downstream casualties and destruction underline the essence of researching glacial lake monitoring and analysing techniques, especially in regions such as the Himalaya. Research questions have been formed beforehand as a guide to performing this study. This thesis investigates the capability of an InSAR-based analysis to investigate the susceptibility and stability of six Himalayan glacial lakes, focusing on the identification and likelihood of GLOF hazard development. This leads to the main research question:

- **How does satellite InSAR contribute to monitoring and analysing potentially dangerous glacial lakes?**

The main research question will be answered by breaking this question into five subquestions. First, the observations should be integrated with other information, such as geomorphological, meteorological and optical data, to interpret the InSAR results and understand potential hazards and limitations. This leads to the first subquestion:

- How should the InSAR observations at glacial lakes be interpreted?

Then, an integrated analysis is applied to the six Himalayan glacial lakes selected for this research. This analysis will focus on identifying geomorphological processes that might link to GLOF hazards at the lakes, leading to the second subquestion:

- What does the InSAR-based analysis conclude about GLOF hazards and stability at the six glacial lakes?

Various InSAR methods exist, so it is helpful to analyse how the specific InSAR methods in this thesis perform; which one is more applicable and why:

- What is the applicability of the specific InSAR methods used in this study to glacial lakes?

While applying the InSAR-based approach, limitations of the method will arise. Limitations might relate to InSAR in general, a particular glacial lake, or glacial lakes in general. Finding and explaining limitations is essential in assessing the applicability of an InSAR-based analysis to glacial lakes, leading to the fourth subquestion:

- What are the limitations and inaccuracies of applying InSAR to glacial lakes?

Finally, to analyse the contribution of the InSAR-based method proposed in this thesis, the approach should be compared to existing studies that address analysing and monitoring glacial lakes, leading to the last subquestion:

- What does this study add, and how does it compare to existing methods and studies?

In this thesis, conventional differential InSAR and persistent scatterer interferometry (PSI) have been applied to obtain displacements with InSAR at the six glacial lakes. SARPROZ, a software based on MATLAB codes, has been used to process Sentinel-1 SAR data from 2014 to 2021. The InSAR results are integrated with topographical data, optical imagery, weather data, and site surveys. Subsequently, the displacements will be linked to geomorphological processes

and GLOF hazard developments. These additional data sources will also aid in explaining the applicability and limitations of InSAR.

Chapter 2 gives an overview of glacial lakes, outbursts, associated triggers and monitoring strategies and the chapter introduces the six glacial lakes investigated in this research. Chapter 3 explains the theory and application of InSAR, together with the InSAR results, and Chapter 4 demonstrates the integration of InSAR with other data sources for analysing glacial lakes and contains the integrated analysis results. Finally, Chapter 5 provides a discussion of the research and Chapter 6 presents the conclusion.

2 Glacial lake outburst floods

This chapter starts with a review of the formation of glacial lakes and accompanying outbursts in sections 2.1 and 2.2. Section 2.3 introduces the six Himalayan glacial lakes investigated in this research and section 2.4 describes existing GLOF monitoring and analysing techniques.

2.1 Glacial lakes

This section describes the formation and geomorphology of glacial lakes and the surrounding slopes. Glacial lakes are water bodies formed by glaciation; the origin of a lake lies in glacier melting. When a glacier starts to melt, the glacier retreats and meltwater will accumulate in the depression created by the glacier, forming a glacial lake. The exact climate change effect on glacial lakes is complex, but glacier melt and retreat increased since the last decades' temperature rise, indicating glaciers' sensitivity to climate change (Bajracharya et al., 2007a; Khadka et al., 2018; Zemp et al., 2008). Many studies reported a significant temperature rise in the Himalaya (Baidya et al., 2008; Harrison et al., 2018; Shrestha et al., 1999), and climate models also predict a future temperature rise (Agrawala et al., 2003). Consequently, the number and size of glacial lakes are likely to increase. The Himalaya contains approximately 9000 glacial lakes, and around 200 lakes are considered potentially hazardous (Prakash and Nagarajan, 2018). The lake expansion depends on the outflow, glacier ice velocity and lake geometry. The lake volume can stabilise if a continuous outflow counters meltwater inflow. Higher glacier velocities tend to have higher melt rates, and the lake geometry is determinative of the rate and possibility of expansion. For example, wider calving fronts experience enhanced melting since a larger proportion of glacier ice is in contact with the relatively warmer lake water. In addition, the basin geometry also determines whether an expansion of the lake is possible (Costa and Schuster, 1988; Khadka et al., 2018; Röhl, 2008).

Various classification systems for glacial lakes exist based on aspects such as dam type and its location to the glacier. One of the classification methods is listed in Table 1. Bedrock-dammed lakes lie in the depression created by the glacier, and the water is dammed by bedrock. These lakes are usually less dangerous than the other classes since a bedrock dam is more stable than an ice or moraine dam. Ice-dammed lakes are dammed by glacier ice. Either a different glacier than the feeding glacier is blocking a glacial lake, or a branched glacier retreated and separated from the main glacier forming a lake in between. Supraglacial lakes are lakes formed by melting on the glacier surface. Such lakes can be stable or have annual or inter-annual variability depending on subglacial water pathways. Subglacial or englacial lakes are water bodies within a glacier; these lakes are often impossible to see from optical imagery and require ground-penetrating instruments for detection.

Moraine-dammed lakes are water bodies lying between a moraine ridge and glacier. As glaciers advance, material in front and beneath the glacier is eroded. This eroded material accumulates in front of the glacier, forming a ridge of material, and debris on top of glaciers is also transported to the front as the top layer moves faster than the bottom because of less friction. Then glacial meltwater accumulates between the moraine ridge and glacier terminus when a glacier retreats, forming a moraine-dammed lake. Lateral moraines are ridges of deposited material adjacent to the glacier. After glacier retreat, these ridges are left behind. Water can accumulate besides a lateral moraine instead of being dammed by an end moraine. Moraine thaw lakes are thermokarst lakes formed by melting dead ice inside a moraine dam. The melting causes depressions, which are filled by the meltwater. Lastly, lakes can also form behind landslides, avalanches and debris flows that obstruct the passage of water. Most severe GLOFs have occurred at end moraine-dammed glacial lakes, as large lakes can develop behind these dams and because these lakes are dammed by loose and unstable material and can easily breach due to hydrostatic pressure or flood waves (Bajracharya et al., 2020; Clague and O'Conner, 2021; Evans et al., 2021; Yao et al., 2018). Therefore, this thesis focuses on moraine-dammed glacial lakes. Figure 3 shows an example of a conceptual cross-section of a moraine-dammed glacial lake. The image shows the significant depth relative to the lake area, indicating the amount of

Class	Subclass	Description
Bedrock-dammed	Cirque lake	In a cirque
	Glacial valley Lake	In a U-shaped valley by glaciation
	Other glacial erosion lake	Formed by glacier erosion but does not belong to the classes above
Ice-dammed	Advancing glacier-blocked lake	blocked by an advancing glacier
	Other glacier-blocked lake	A lake with the dam being glacier ice
Supraglacial		On the glacier surface
Subglacial		Within the glacier
Moraine-dammed	**End moraine-dammed lake**	**Between the end moraine ridge and the glacier terminus**
	Lateral moraine-dammed lake	Dammed by a lateral moraine ridge
	Moraine thaw lake	On a moraine ridge
Other		Blocked by a landslide, avalanche, debris flow, etc.

Table 1: A classification system of glacial lakes, adjusted from Yao et al. (2018)

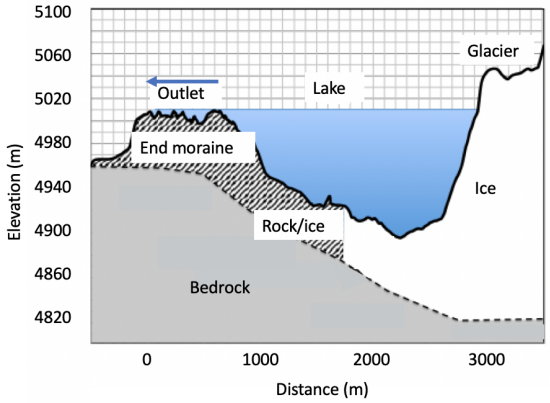

Figure 3: Conceptual longitudinal cross-section of a moraine-dammed glacial lake (based on Imja Lake), adjusted from Somos-Valenzuela et al. (2014)

water that could be released at dam failure.

Depending on the glacier properties, different end moraines can be created. The moraine dam type depends on the longitudinal elevation profile of the glacier and the presence of debris for glacial transport. Short and steep glaciers are characterised by mass balances advancing and retreating at higher rates over larger distances, creating small or narrow terminal ridges. Conversely, long valley glaciers with shallow longitudinal profiles are more subjected to thickening and thinning where the glacier front remains relatively stable, constructing vast moraines (Westoby et al., 2014a). Three types are distinguished; ice-thrust, push and dump moraines. Ice-thrust moraines are formed by eroded material from the glacier base, which is then thrust along the shear planes to the ice front shelve. These moraine dams can be higher than 100 m if the glacier has been actively eroding and flowing fast enough. The dam material is finer and more compact than other dams, as the ice overlaid it. Usually, the moraine slopes are steep, often more than 40^o. Push moraines only consist of a few metre high ridges. They form when glaciers advance and shove material at the front, constructing small dams. Usually, no large lake will develop behind these dams. Dump moraines originate from material deposition at the glacier front. The moraine shape depends on glacier velocity, ablation rate, sediment amount, and meltwater effect. Large dump moraines will form if the glacier velocity balances the melting rate. Usually, these dams are unstable, consisting of heterogeneous non-cohesive material, with steep upstream and flatter downstream slopes. Finally, sediment and water moving upward from the base to the glacier surface can form ice cores in moraines by compression and thrusting

processes (Costa and Schuster, 1988). Figure 4 displays two moraine-dammed glacial lakes with different moraine dams. Figure 4a shows a wide and flat terminal moraine with thermokarst lakes, and Figure 4b shows a steep and narrow moraine dam.

Two types of surrounding slopes can be distinguished. First, there are the mountain slopes surrounding the lakes. Their steepness and proximity to the water are different for each glacial lake and depend on the valley geometry. For example, Figure 4a is surrounded by less steep slopes that do not directly bound the lake, whereas the lake in Figure 4b lies directly adjacent to significantly steeper slopes. These slopes are often dominated by rock glaciers and prone to avalanches. Rock glaciers are bodies containing ice-rock mixtures. They originate from rock debris frozen in ice or former glaciers overlain by talus layers, and internal ice deformation causes their downslope creep movement. The rock glacier velocity depends on multiple aspects, including headwall erosion rates, debris origin, liquid water pressure and temperature (Cicoira et al., 2019; Lugon and Stoffel, 2010; Ritter et al., 1995). Lateral moraines often lie directly adjacent to the lake. These ridges consist of loose material transported by the glacier and deposited at the sides. After the glacier retreats, these ridges are left behind and laterally dam a glacial lake. Their height and steepness depend on the glacier properties and lake level, but they can be relatively steep because their inner slope was (partially) overlain by the glacier. Figure 4a shows lateral moraine ridges that form a ridge between the mountain slopes and the lake, whereas at the lake in Figure 4b, the lateral moraines lie directly on the surrounding mountain slopes.

2.2 Failure mechanisms

This section explains the failure mechanisms that can trigger GLOFs and describes the cause and impact of documented historical GLOFs. Figure 5 displays various GLOF triggers. These triggers consist of two types: dynamic and self-destructive processes. Initiating events cause dynamic processes, such as landslides and glacier calving, resulting in waves that can flood and breach the dam. Longer ongoing processes cause self-destructive outbreaks, such as moraine failure due to seepage or ice core melting. Dynamic failures have been more common than self-destructive failures (Emmer and Cochachin, 2013; Falátková, 2016; Liu et al., 2019; Richardson and Reynolds, 2000). Section 2.2.1 explains dynamic failures, and section 2.2.2 describes self-destructive failures.

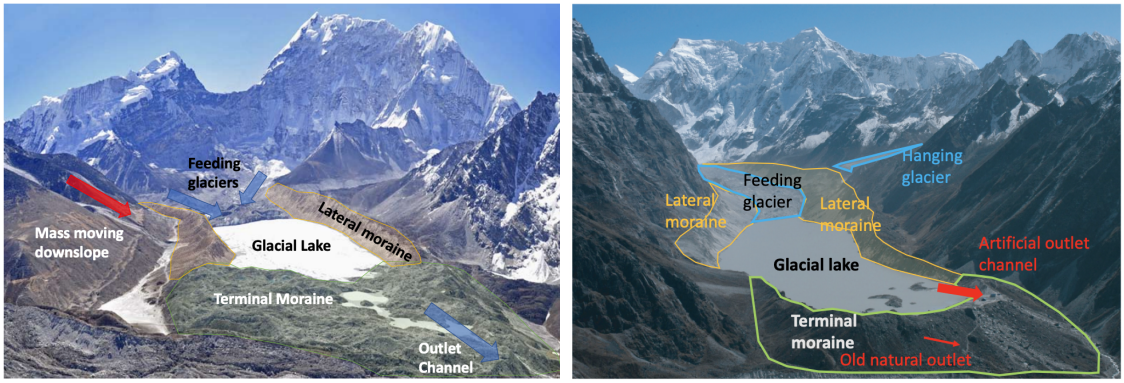

(a) **(b)**

Figure 4: Moraine-dammed glacial lakes. (a) A wide and flatter end moraine (Imja Lake, same lake as the conceptual cross-section in Figure 3), retrieved from ICIMOD (2011). (b) A steep end moraine (Rolpa Lake). Photograph from November 2007 by Mr Osafumi Sato, retrieved from Sakai (2012).

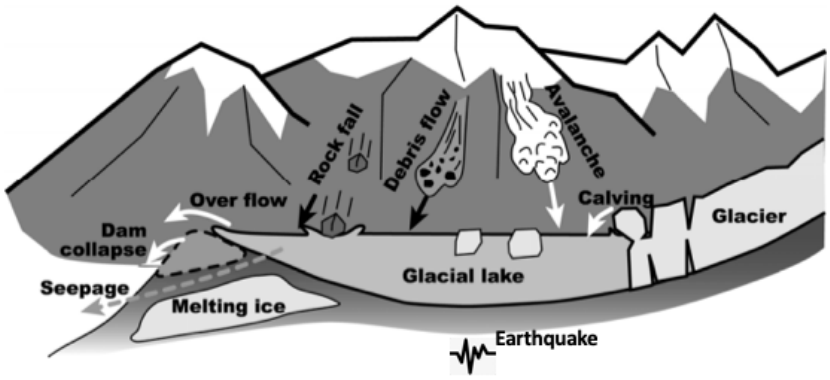

Figure 5: GLOF triggers for moraine-dammed glacial lakes. Image adjusted from Fujita et al. (2012)

2.2.1 Dynamic failures

Dynamic failures involve initiating events; mass entering lakes from adjacent slopes, glacier calving and earthquakes. These events can cause large waves that could overflow and destroy terminal moraines. Rock and ice avalanches can originate from unstable slopes and (rock) glaciers. Larger ice chunks breaking from the feeding glacier - glacier calving - can additionally lead to high waves. Melting and longitudinal stretching forming crevasses are the primary causes for calving (Benn et al., 2007). For example, Langmale Lake in Nepal flooded due to a rock avalanche in 2017 (Byers et al., 2019) and ice avalanches presumably triggered GLOFs at Chongbaxia Lake in Tibet in 2001, Queen Bess Lake in Canada in 1997, Dig Lake in Nepal in 1985 and 2015, and Sangwang Lake in Tibet in 1954 (Byers et al., 2017; Kershaw et al., 2005; Liu et al., 2019; Nie et al., 2020; Vuichard and Zimmermann, 1985). As the Himalaya lies at the active Indian and Eurasian plate boundary, tension build-ups and releases often result in earthquakes (Bilham, 2019). Earthquakes can destablise slopes, moraines and cause vibration-induced flood waves leading to moraine breaching. An earthquake in 1988 led to the dam failure of Tam Pokhari Lake in Nepal (Westoby et al., 2014a). Earthquakes and glacier calving are hardly predictable, just like the effect on the slope and dam they will have. That is why the direct impact of earthquakes and glacier calving is out of this research's scope. The focus regarding dynamic events will be on the lake's surrounding mountain slopes and lateral moraines.

Mass can fall, topple, slide, spread or flow downslope and can consist of snow, ice, rock, debris, or a combination such as rock glaciers. Rock glaciers are a significant source of rockfall, ice avalanches or debris flows (Lugon and Stoffel, 2010; Ritter et al., 1995). Theoretically, slope displacement occurs when the downward force exceeds the soil or rock strength. Gravity is the main force behind slope failure, and mountains consist of many high and steep slopes, often becoming even more vertical after failures. The main factors influencing mountainous slope instabilities are bedrock lithology, slope angle, seismic activity, stream erosion, precipitation, glacier retreat and permafrost melting (Evans et al., 2021; Fischer et al., 2006; Highland and Bobrowsky, 2008; Kahlon et al., 2014; Khatiwada and Dahal, 2020; Klimeš et al., 2016; Kovács et al., 2019; Shroder, 1998). The paragraphs below will elucidate these factors, divided into slope features, glacier retreat and weather events.

Slope features, such as gradient, aspect and lithology, significantly influence slope stability. Steep inclines pose higher rockfall and avalanche threats as gravity exerts a downward force on rocks and snow (Kovács et al., 2019). According to Larsen and Montgomery (2012), landslide erosion significantly increases once the slope angle exceeds 30 degrees. Regarding rock glaciers, loose slope material transports downhill as rock glacier toes encounter steep slope parts. This process prevents rock glaciers from stabilising as no debris layer can form in front to prevent the glacier and associated debris from moving further downslope (Cicoira et al., 2019). Moreover, sun-facing slopes experience enhanced ice and snow melting. The melting of interstitial ice that

holds rocks and soils together can cause rocks and soil to fall downslope. Finally, bedrock geology determines the rock strength and influences the limiting slope angle. Tectonically active mountains can consist of bedrock so extensively fractured that it could exhibit similar stability as a sand pile (Larsen and Montgomery, 2012). The bedrock geology's significant influence is present at layer boundaries, and the mountains consist of many rock and sediment types. For instance, slip surfaces can activate at layer boundaries, initiating slope failure (Shroder, 1998).

Glacial retreat is the leading cause of slope instability on lateral moraines, as glacier slope support falls away. Lateral moraines are generally steep and unconsolidated, and slope deglaciation changes slope stress and strength, possibly leading to slope failure. Deglaciation can cause direct and indirect slope displacement. Direct movements include snow and ice avalanches, while indirect are associated with rock falls and landslides, which can even happen decades after glacial retreat (Emmer et al., 2014; Evans et al., 2021; Kos et al., 2016; Shroder, 1998).For example, a lateral moraine landslide caused a GLOF in 2003 in Peru (Klimeš et al., 2016; Vilímek et al., 2005).

Weather-related events like heavy monsoon rains, snowfall, frost weathering and ice melting significantly influence slope behaviour. Generally, the Himalaya experiences two precipitation periods per year. First, moderate amounts fall in the winter due to low-pressure storms coming from the west, mainly condensing in snowfall. Second, southwest monsoon winds cause heavy summer precipitation, resulting in rain or snow. The temperatures are usually below zero in the winter and above zero during the day in the summer (Burbank et al., 2012). Kahlon et al. (2014) found that between 1971 and 2009, 77% of landslide events in the Indian Himalaya occurred during the monsoon season, 12% during the pre-monsoon showers and 7% during winter snowfall. Figure 6 shows the monthly distribution of GLOFs based on 128 cases. The figure shows a distinctive pattern of increasing GLOFs during the summer months (Falátková, 2016).

Snowfall causes extra weight adding to the gravitational force, and freeze-thaw cycles cause rock fractures and displacements (Shroder, 1998). Temperature changes, permafrost melt and water percolation, alter the stresses inside rocks resulting in rockfalls (Deline et al., 2021). Interstitial ice between rocks and soils can melt at high precipitation or temperatures, decreasing slope stability and inducing slope movements (Klimeš et al., 2016). Furthermore, stream erosion causes soil and rock particle dislodgement. Along drainage paths, rain and meltwater run off can induce landslides. In addition, the relatively warmer run-off water compared to the ice on the slope enhances the melting (Dahal, 2015). Rock glacier studies in the Swiss Alps found that water and external temperature variation are essential processes controlling the rock glacier dynamics at seasonal and inter-annual scales (Cicoira et al., 2019). Rock glaciers destabilise due to thermal changes increasing the velocity of the top layer, causing collapses, debris flows, and rockfalls (Deline et al., 2021). In addition, rock glaciers can fail due to the saturation of the top layer caused by precipitation and snow (Kofler et al., 2021; Lugon and Stoffel, 2010).

2.2.2 Self-destructive events

Self-destructive events involve outbursts that are not caused by initiating episodes. Instead, they develop from longer ongoing processes that weaken terminal moraines and can finally result in outburst floods. Self-destruction causes are hydrostatic pressure exerted by the lake, ice core melting and a weak moraine structure. These features induce moraine seepage and subsidence, destabilising the dam (Emmer and Cochachin, 2013). Self-destructive events caused GLOFs at Lugge Lake in Bhutan in 1994, Jialonge Lake in Tibet in 2002 and Ventisquero Negro Lake in Argentina in 2009 (Liu et al., 2019; Watanabe and Rothacher, 1996; Worni et al., 2012).

Glacial lakes exert hydrostatic pressure on their dams, which increases for expanding lakes with no outflow. Glacial lakes expand due to glacial retreat, lake bottom ice melting, permafrost melting or increasing precipitation. The pressure exerted on the end moraine depends on the

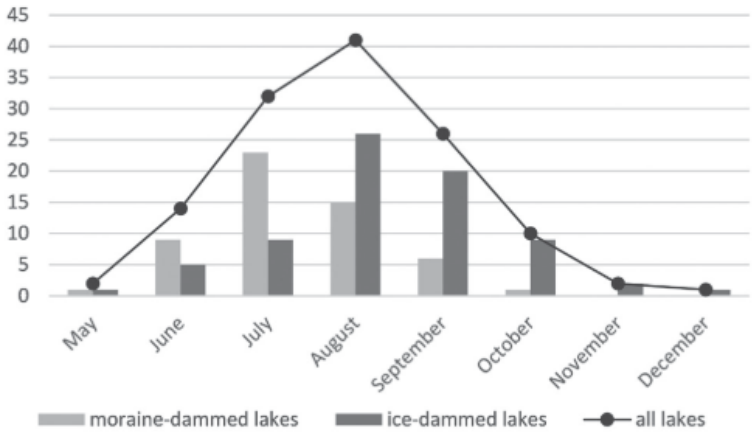

Figure 6: Monthly distribution of GLOFs regarding moraine-dammed and ice-dammed glacial lakes, based on 128 cases in Asia (Falátková, 2016)

bathymetric profile, the lake width and lake volume. For example, a steep and deep lake profile towards the end moraine will exert more significant pressure on the dam. As explained in section 2.1, the resulting moraine geometry depends on the basin and the glacier properties. High and narrow moraine dams will be less able to withstand the pressure than wide and lower dams. The hydrostatic pressure can induce seepage and subsequent piping, leading to internal displacements and subsequent failure (Clague and Evans, 2000).

Moreover, the dam lithology significantly influences the dam's stability. Often moraine dams consist of unsorted and unconsolidated material. As a result, water can readily form pathways and the dam can experience subsidence. These dams are often ice-cored with heterogeneously distributed ice, causing local subsidence areas and variable displacements over the moraine (Dahal et al., 2018). Due to higher temperatures and seepage, ice in moraine dams will degrade, causing subsidence and dam instability. As ice cores form impermeable barriers in dams, water will concentrate and route along the ice, thermally eroding the ice and removing overlying sediment. Therefore, higher temperatures and precipitation will directly affect dams, causing subsidence and moraine weakening (Watanabe et al., 1995; Zhang and Liu, 2015). Furthermore, anthropogenic activities can influence moraine stability. For example, artificial lake lowering might increase the outflow and decrease the hydrostatic pressure, but it could also induce melting and erosion, increasing the subsidence (Dahal et al., 2018).

2.2.3 Historical outbursts

This section lists some of the lakes, failure mechanisms and impact of historical GLOFs. The moraine dam of Sangwang Lake (Tibet) was breached in 1954 due to overtopping waves caused by an ice avalanche and released $250 * 10^6 m^3$ water. Approximately 400 people died, and more than 20,000 people were affected by this debris flood with a 10,000 m^3/s discharge (Liu et al., 2019).

Dig Lake (Nepal), a glacial lake fed by the Langmoche glacier, with an area of 0.5 km^2, experienced a GLOF in 1985. A 150000 m^3 ice avalanche caused waves and breached the relatively narrow end moraine. Figure 7 displays the breach and outburst flow path. This outburst of 5-10 million m^3 lasted four hours and caused five fatalities, destroyed a hydroelectric power station, 14 bridges, 30 houses and arable land. Because of the destroyed terminal moraine, the lake cannot obtain its previous volume, slightly decreasing its risk (ICIMOD, 2011; Vuichard and Zimmermann, 1985). Unfortunately, this burst still did not diminish the risk; ice avalanches and rockfall plunged in the lake during the earthquake in April 2015. The resulting flood damaged three bridges (Byers et al., 2017).

Figure 7: Dig Lake in Nepal (April 2009) with the outburst path and visible farmland at the bottom of the image. Image retrieved from ICIMOD (2011)

In 1988 the moraine dam of Guangxieco Lake (Tibet) failed due to piping, which was likely triggered by extreme precipitation and persistent high temperatures before the event. In 1994, hydrostatic pressure caused the moraine dam of Lugge Lake in Bhutan to fail, resulting in a GLOF. As a result, the water level of Lugge dropped 23 m. Due to this outburst, a lake downstream (Tshopdak lake) also flooded. The GLOF caused 23 fatalities and significant damage to infrastructure and buildings (Nayar, 2009; Westoby et al., 2014a).

A GLOF occurred at Sabai Lake (Nepal) in 1998. Presumably, an earthquake destabilised the moraine dam, leading to dam failure with a 10000 $m^3 s^{-1}$ peak discharge (Westoby et al., 2014a).

A GLOF occurred in 2001 at Chongbaxia Lake (Tibet). The lake decreased from 0.80 km^2 to 0.34 km^2 after the GLOF with a 37 m lake level drop. The trigger is likely an ice avalanche caused by extreme precipitation (Nie et al., 2020). In 2002, the moraine dam of Jialonge Lake in Tibet experienced a 15 m breach, releasing a volume of $23.6 * 10^6 m^3$ with a 1242 m^3/s peak discharge. The dam likely failed due to increased hydrostatic pressure caused by enhanced glacier melting and precipitation. The resulting GLOF consisted of viscous debris flows, destructing a reinforced concrete bridge, farmland, four houses, and 3.05 million yuan financial loss (Liu et al., 2019).

A catastrophic outburst occurred at Chorabari Lake (India) in 2013. The extreme meteorological conditions, unfavourable topographical lake disposition and unstable dam structure formed the causes for moraine breaching. High temperatures and precipitation led to significant inflow of water and debris. Presumably, the water started to overflow the moraine dam, initiating erosion and forming a breach. Thousands of people were killed, countless roads and bridges damaged and many hydropower plants destroyed (Allen et al., 2016).

Gya Lake (India) burst on August 6, 2014. The lake area had expanded from $0.06 km^2$ to 0.12 km^2 in 15 years and in 2014 the lake rapidly increased by 0.02 km^2 in one month. Piping caused by degrading ice cores likely triggered the GLOF that released an estimated amount of 360,650 m^3. In situ investigation showed no erosion on the moraine dam, indicating a subsurface drainage process (Majeed et al., 2021; Schmidt et al., 2020).

On April 20 in 2017, Langmale Lake (Nepal) flooded due to a rock avalanche. The moraine dam was relatively steep and had no vegetation cover or ice core. A 30 m wave breached the

terminal moraine up to 25 m. The dam was close to the glacier and vertical slope walls, making it a high-risk lake. Satellite images from February 19 and May 8 were compared and showed a lake area decrease from 0.083 km^2 to 0.036 km^2 and empirical formulas estimated a volume reduction from 1.1 million m^3 to 0.3 million m^3 (Byers et al., 2019).

Also mountain ranges in other parts of the world have sustained GLOFs. Lake Palcacocha (Peru) burst in 1941, destroying a third of the city Huaraz and killing 5000 people (Carey, 2005). The cause is unknown, it could have been both a dynamic or self-destructive failure (Klimeš et al., 2016).

The moraine dam in Queen Bess Lake (Canada) was breached in August 1997 due to waves overtopping the moraine caused by a $2.3 * 10^6 m$ ice avalanche from the glacier snout. The lake was 1.4 km long, 700 m wide and released 6.5 million m^3 water with a peak discharge over 1000 $m^3 s^{-1}$. The GLOF occurred during a hot summer which probably initiated the ice avalanche. Besides this, the glacier was retreating from the lake up a steep rock face for two years, resulting in an unsupported glacier front (Kershaw et al., 2005).

The ice-cored terminal moraine of Ventisquero Negro Lake (Argentina) failed in May 2009. The lake likely flooded due to self-destructive failure from increasing lake levels caused by unusually high precipitation and temperatures. A study suggests that the high lake level initiated dam erosion with subsequent breaching and lake outflow. Presumably, the moraine dam had already destabilised before the extreme weather because of lake expansion and ice core degradation. A breach of 350 m was created, releasing ten million m^3 of debris and water in 3 hours (Worni et al., 2012).

2.3 Study areas

This section describes the six glacial lakes this research focuses on and highlights why they require monitoring. The selection consists of Imja Lake (Nepal), Lunana Lakes (Bhutan), Thulagi Lake (Nepal), Rolpa Lake (Nepal), Lumding Lake (Nepal) and Barun Lakes (Nepal). Figure 8 displays the locations of the six lakes, and Table 2 lists their coordinates, altitude and size. These lakes are moraine-dammed, are considered hazardous in other research, have considerable downstream impacts, and belong to the relatively larger Himalayan glacial lakes. Furthermore, expansion rates differ per lake, some have had mitigation measures, and their danger level varies per research study.

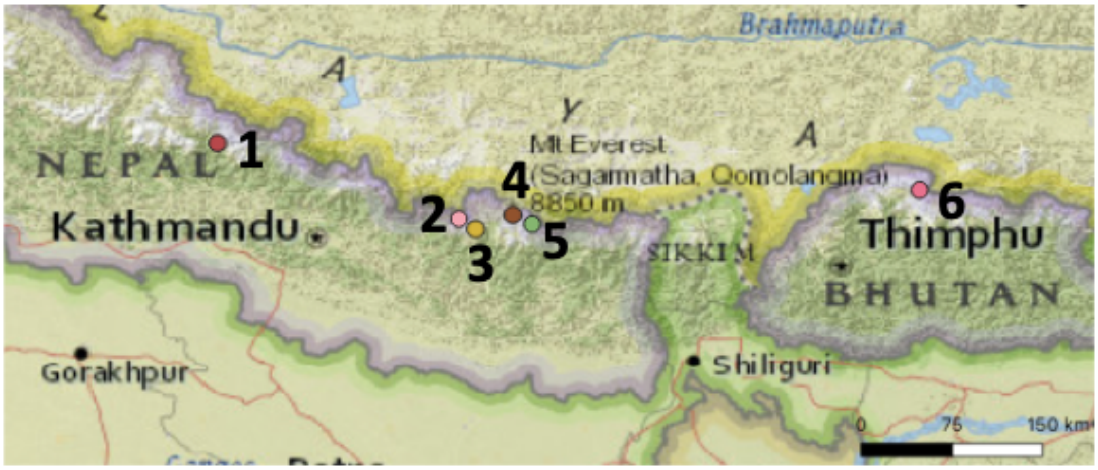

Figure 8: The locations of the six Himalayan glacial lakes: 1. Thulagi Lake, 2. Rolpa Lake, 3. Lumding Lake, 4. Imja Lake, 5. Barun Lakes, 6. Lunana Lakes. Map retrieved from Esri National Geographic.

Lake	Location [lon,lat]	Altitude [m]	Area [km^2]	Volume [$x10^6 m^3$]
Thulagi	84.48, 28.49	4050	0.94 (1)	36.1 (2)
Rolpa	86.48, 27.86	4550	1.60 (5)	85.9 (5)
Lumding	86.61, 27.78	4850	1.18 (7)	57.7 (7)
Imja	86.92, 27.90	5000	1.34 (3)	78.4 (2)
Lower Barun	87.09, 27.82	4550	2 (8)	112.3 (2)
Lugge (Lunana)	90.28, 28.10	4450	1.53 (6)	58.3 (4)

Table 2: Lake coordinates, altitude, area and volume. Retrieved from (1) Maskey et al. (2020), (2) Haritashya et al. (2018), (3) Khadka et al. (2018), (4) Yamada et al. (2004), (5) ICIMOD (2011), (6) Wangchuk et al. (2019), (7) Rounce et al. (2016), (8) Byers et al. (2017)

Imja Lake

As one of the largest glacial lakes in the Himalayas, in a relatively densely populated region and tourist destination, an outbreak of Imja Lake could cause severe damage. The flood could destroy downstream villages, tourist areas, trails and bridges. These aspects make it a critical lake to analyse. Figure 9 displays an image of Imja Lake. The lake lies at the Imja and Lhotse Shar glaciers terminus and is bounded by a glacier to the east, lateral moraines to the north and south, and an ice-cored moraine dam to the west. Imja Lake expanded rapidly from 0.64 km^2 in 1987 to 1.34 km^2 in 2016 with a volume expansion of 140% between 1992 and 2002. The maximum depth is approximately 150 m (Khadka et al., 2018), and volume 78.4 million m^3 (Haritashya et al., 2018). The hummocky ice-cored end moraine is relatively large and flat, about 700 m by 600 m, which according to Fujita et al. (2013) and Hambrey et al. (2008) significantly decreases the risk of bursting. The lake was artificially drained 4 million m^3 through the outlet channel in the moraine in October 2016. However, the lake is still expanding due to the glacier and bottom ice melting, and according to Khadka et al. (2018), this drainage is not enough to prevent a GLOF in the future. In addition, the artificial and continued lake lowering might increase buried ice melting as it comes into contact with relatively warmer water passing by (Dahal et al., 2018). New thermokarst lakes formed on the moraine surface, and the moraine experiences seepage and piping, making it susceptible to self-destructive failure (Cuellar and McKinney, 2017; Kroczek and Vilimek, 2020; Rounce et al., 2016; Sattar et al., 2021). Sattar et al. (2021) argue that either the melting of ice within the moraine will gradually lower the lake, or the moraine will evolve into a narrow, unstable structure, of which the latter decreases the moraine's stability. Furthermore, the slopes outside the lateral moraine primarily consist of rock glaciers and scree, but high lateral moraines protect the lake from slope material sliding into the lake (Kroczek and Vilimek, 2020; Khatiwada and Dahal, 2020). Still, the lateral moraines themselves are unstable and steep and prone to landslides into the lake (Byers et al., 2017; Hambrey et al., 2008).

Lunana Lakes

The analysed lakes in the Lunana region consist of Lugge Lake, Thorthormi Lake, Raphstreng Lake and Bechung Lake. The area has an early warning system using wireless radio sets and satellite. Regular water level reporting takes place using gauges installed along the river, monitored at different time intervals depending on the distance from the base camp (Singh, 2009). Figure 10 shows that the lakes lie in each other's direct vicinity and are bounded by narrow moraines. All three lakes contain large volumes of water, and if an upstream lake fails, the downstream might break too, causing a collective GLOF. This highlights the importance of analysing all lakes.

A GLOF at Lugge Lake in October 1994 was caused by moraine failure due to the significant hydrostatic pressure on the dam. This GLOF also flooded a lake downstream (Tshopdak Tsho). The GLOF caused 23 fatalities and considerable damage to infrastructure and buildings

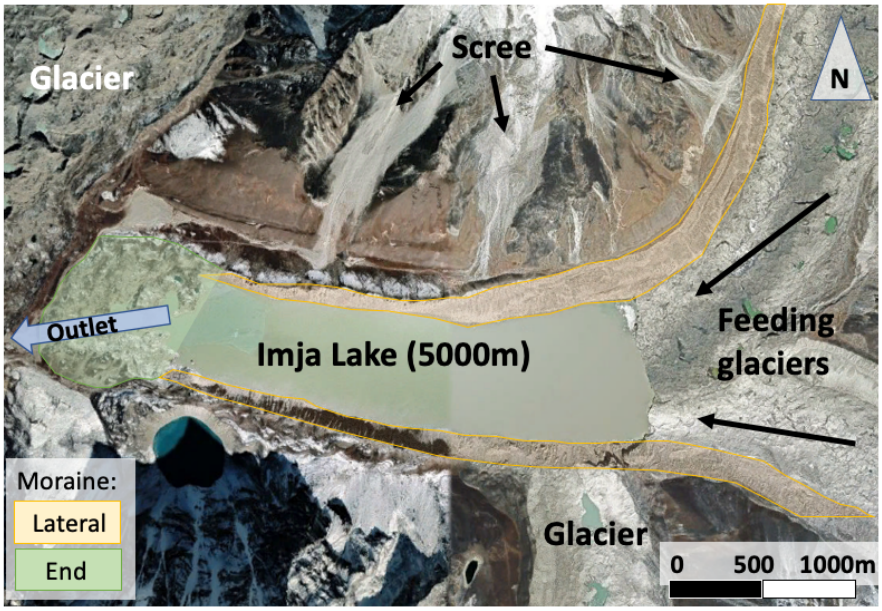

Figure 9: Imja Lake. Background image from GE (October 2019)

(Westoby et al., 2014a). As a result, the lake area decreased from 1.12 km^2 to 0.92 km^2. Since then, the lake has expanded to 1.39 km^2 in 2021, about 0.3 km^2 larger than before the GLOF event (Rinzin et al., 2021). Lugge Lake's outbreak is still visible on satellite images. Figure 10 shows the outlet channel in the southwest corner of the lake, which was flood path during the GLOF.

Thorthormi lake is a collection of supraglacial ponds on the glacier, visible from Figure 10. Over time these supraglacial lakes are growing and merging, on their way to becoming a more substantial lake and increasing the hydrostatic pressure on the moraine. In October 2009, Thorthormi Lake was artificially drained almost a metre (Singh, 2009). Still, on June 20 2019, a partial breach occurred at Thorthormi lake, draining 2.73 million m^3 water. The leading cause was probably the exceptionally high temperatures three months before. Satellite images revealed that excessive glacier melting took place during May and June. Furthermore, the glacier had been moving a lot, and icebergs had been floating around in the lake. Probably the increased hydrostatic pressure breached a weaker moraine part. The outlet channel showed significant erosion evidence (NCHM, 2019).

Raphstreng Lake lies approximately 80 metres lower than Thorthormi lake. In 1996 the Bhutan government artificially drained the lake a few metres. However, the lake still poses a risk since a narrow (30 m) unstable ice-cored moraine separates Thorthormi and Raphstreng lake. Because of this narrow dam and significant height difference, the strength of the moraine is limited. Primarily since Thorthormi lake is growing, the increasing pressure will increase the chance of collapse. Thorthormi lake will flow into Raphstreng lake if the moraine breaks, probably causing a breach at Raphstreng Lake's end, inducing a collective flood (Nayar, 2009). The ice-cored moraine has subsided for years, and the lateral moraine slopes reveal landslide scars (Singh, 2009).

Barun Lakes

The Barun Lakes consist of Lower Barun, Upper Barun and a third unnamed lake, which this research calls Barun-3 Lake for simplicity (see Figure 11). Lower Barun Lake is currently the largest moraine-dammed lake in Nepal. Figure 15 in the following section shows the expansion rate, which is the highest of all lakes, primarily due to the great width at the calving front (770 m). Lower Barun poses a high risk, mainly due to the presence of two upstream lakes, the possibility of mass movements entering the lakes and the fact that the lake is bearing a large

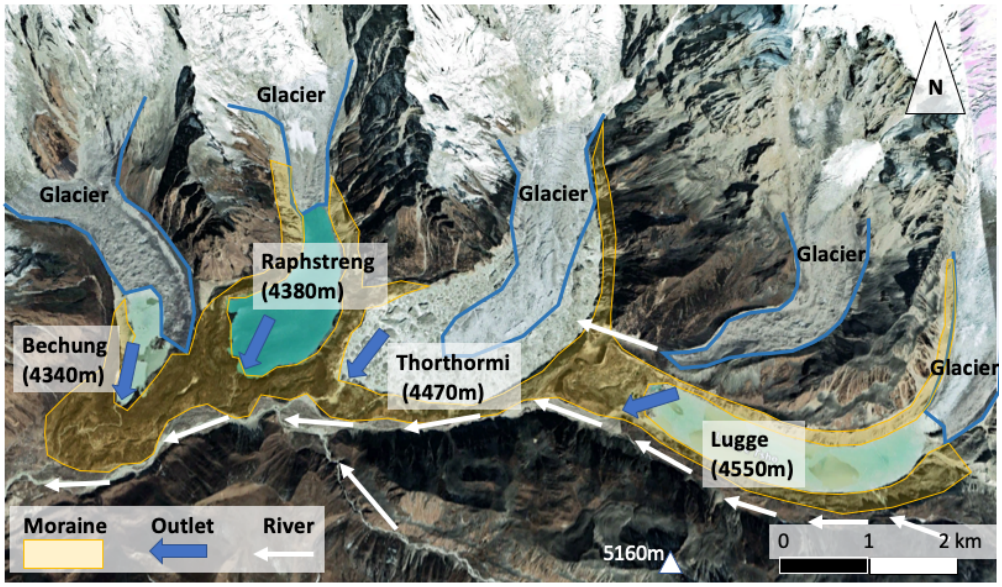

Figure 10: The lakes of the Lunana area. Background image from GE (January 2021)

amount of water with its maximum depth of 205 m and an estimated volume of 112.3 million m^3 (Haritashya et al., 2018). An ice-cored moraine bounds Lower Barun Lake on the east. The lake lies at an altitude of 4530 m and measured an area of $2km^2$ in 2018. The moraine dam is 930 m long and 15 m wide with a maximum height of 128 m (Maskey et al., 2020). Upper Barun and Barun-3 lakes are considerably smaller; however, they lie upstream of Lower Barun Lake, making an outburst of one of these lakes dangerous since it may trigger a GLOF at Lower Barun Lake. Upper Barun is 1.4 km long and 350 m wide halfway, and Barun-3 is 550 m long and 250 m wide halfway.

Rolpa Lake

Rolpa Lake in Figure 12 is often considered the most dangerous due to its immense potential flood volume, steep surrounding slopes with hanging glaciers and unstable ice-cored moraine. The 150 m high moraine is narrow and steep and reveals seepage, cracks and subsidence signs (Bajracharya et al., 2020; Byers et al., 2017; Fujita et al., 2013; Khadka et al., 2018; Rana et al., 2000; Rounce et al., 2017b; Shrestha et al., 2012). Moreover, the lake presents a high risk due to downstream villages, bridges, agricultural land and hydro-power stations. The lake was lowered 2.8 m in 2000 through an outlet channel to 1.53 km^2, stabilising the expansion (Khadka et al., 2018). However, due to the melting of the lake bottom ice, the lake is deepening with an annual rate of 1.2 m in 2000 and 0.43 m in 2009, so the lake volume is still increasing (Khadka et al., 2019; Sakai et al., 2000). Rolpa Lake is 3.45 km long, 0.5 km wide, and the volume was estimated 86 million m^3 in 2011 (Peppa et al., 2020). The lake has an average depth of 56.4 m and a maximum of 133.5 m (Byers et al., 2017). The government installed an early warning system in 2015 that measures the water level at the lake and downstream. However, according to Byers et al. (2017), villagers have little understanding of the system's working and what to do after an alarm. In addition, cell phone signals are often weak or absent in the area.

Thulagi Lake

Thulagi Lake in Figure 13 measured an area of 0.94 km^2 in 2018, with a volume of 39 million m^3 and a maximum depth of 82 m. The terminal moraine is 20 m wide, 305 m long and 67 m high (Maskey et al., 2020). The lake has not been experiencing a high expansion rate over the last few years, but the ice-cored end moraine is experiencing subsidence, increasing the risk of

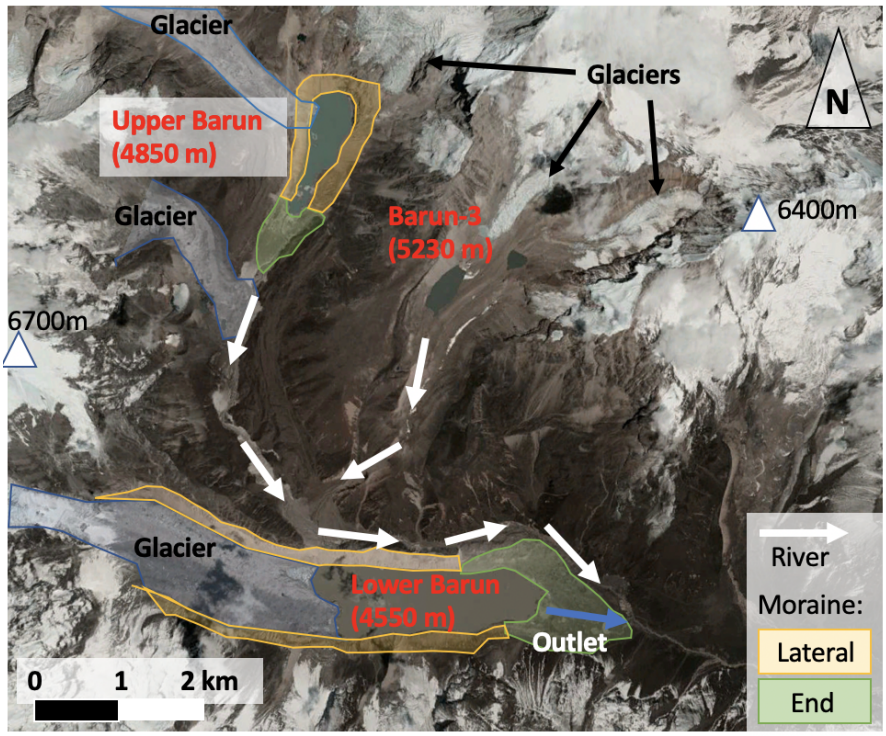

Figure 11: The Barun Lakes. Background Image from GE (April 2016)

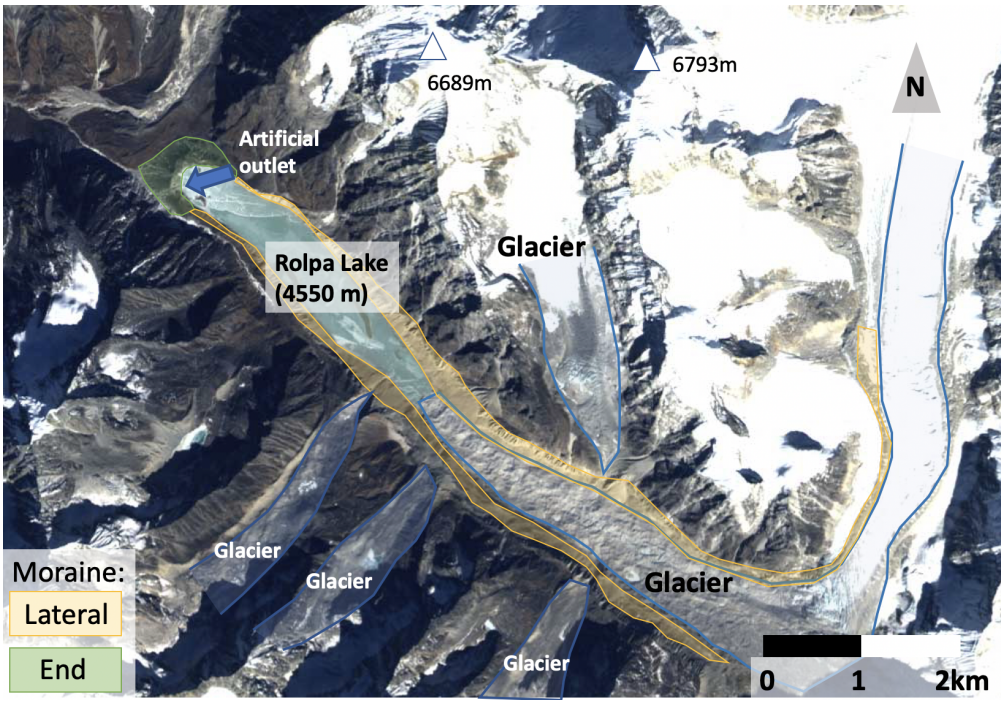

Figure 12: Rolpa Lake (Background image from JAXA)

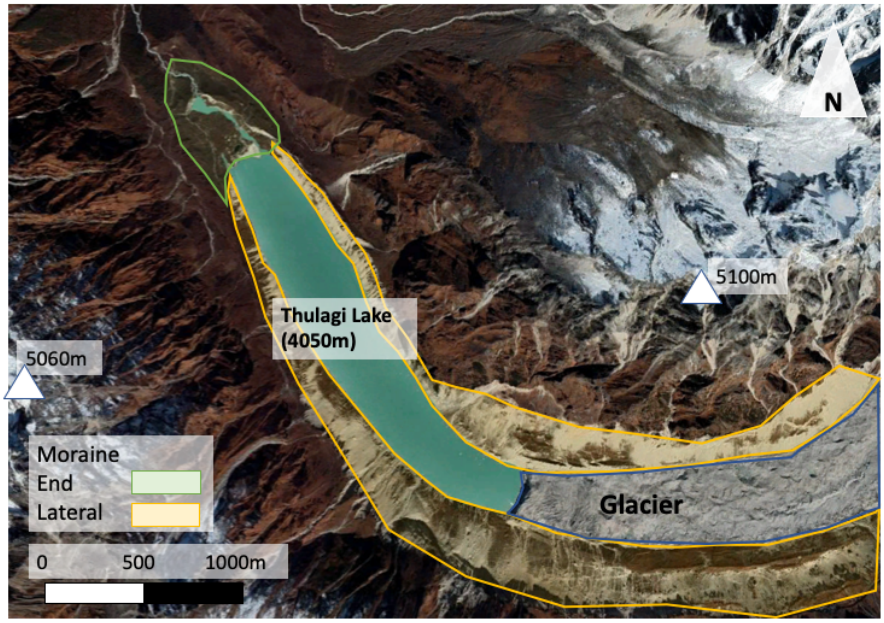

Figure 13: Thulagi Lake (Background image from GE (October 2019))

dam failure. The possibility of mass movements entering the lake and the fact that there is a village downstream, including trekking routes and electric power infrastructure, makes this lake a severe threat (Byers et al., 2019; Haritashya et al., 2018; Rounce et al., 2016). Vegetation covers the end moraine, in contrast to the other lakes in this research. Thulagi Lake lies at an altitude of 4003 m, which is significantly lower than the other lakes in this research, so the region experiences a different climate and vegetation regime (ICIMOD, 2011).

Lumding Lake

Figure 14 displays Lumding Lake. As one of the less investigated lakes, information is scarcer than for the other lakes. The primary reason is a lower downstream impact than other lakes (Khadka et al., 2018). Nevertheless, studies do address the potential dynamic and self-destructive dangers. For example, mass can fall into the lake, hanging glaciers are present, a smaller lake lies upstream on the north, the lake is expanding, and the moraine is theoretically susceptible to failure because of its slope angle of 10.5 degrees. Still, studies argue that the moraine is not ice-cored and contains a stable outlet channel compared to most other analysed glacial lakes. In addition, no seepage or water puddles are visible at the moraine, and the moraine is relatively wide, slightly decreasing the risk. The lake lies at an altitude of 4831 m, has an area of 1.18 km^2, and the maximum depth is 114 m with a total estimated volume of 57.7 million m^3 (Rounce et al., 2016).

2.4 Monitoring and analysing techniques

A GLOF hazard assessment generally consists of the susceptibility and impact assessment. The susceptibility assessment comprises identifying the location and likelihood of the initiation of the GLOF triggers described in section 2.2. The impact assessment consists of identifying the potential threat to downstream areas. Since this thesis focuses on the GLOF susceptibility, this section will only describe current monitoring and analysing techniques related to the susceptibility and stability assessment. This assessment provides a basis for identifying and prioritising the focus of subsequent impact studies (GAPHAZ et al., 2017). Investigating GLOF susceptibility is primarily addressed by deriving GLOF hazard-related parameters from historical GLOFs or monitoring techniques focusing on lake expansion, glacier dynamics, moraine stability and slope

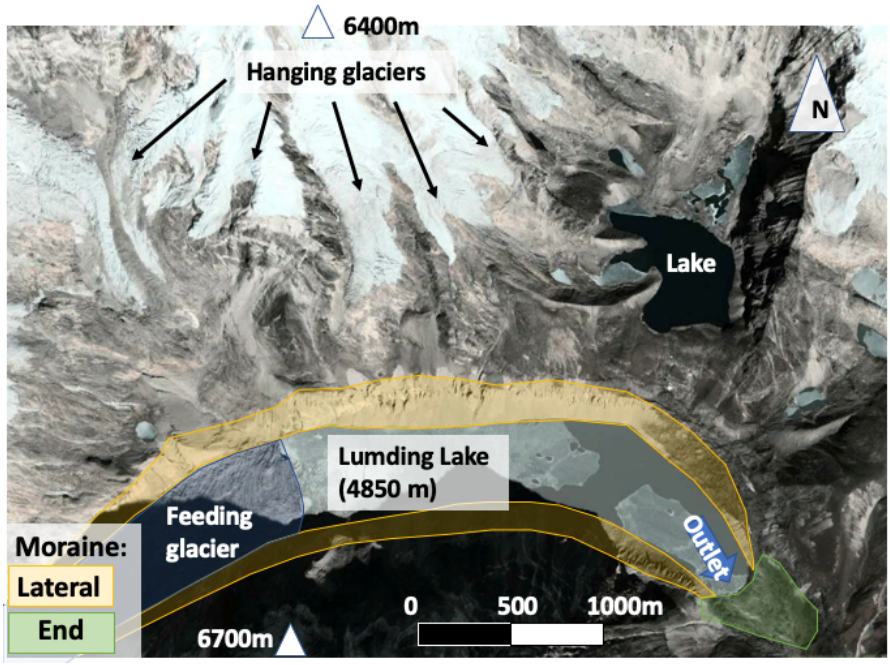

Figure 14: Lumding Lake. Background image from GE (December 2017)

conditions using in-situ observations and remote sensing. The paragraphs below will elaborate on these methods.

Various studies researched outburst predictions and glacial lake hazard identifications using parametric approaches with variables such as glacier velocity, lake size, the floating ice on the lake, the distance between the lake and glacier and moraine's slope angle (Fischer et al., 2020; Peppa et al., 2020; Petrakov et al., 2012; Rounce et al., 2017b; Wang et al., 2011, 2012; Westoby et al., 2014a; Xie et al., 2013). However, their research found no overall method for identifying dangerous lakes and predicting outbursts. One reason is that the data is limited because not enough historical GLOFs have been well documented. A second reason is that glacial lakes differ too much to find a universal approach.

Many researchers have addressed mapping glacial lakes and their expansion with optical remote sensing, as expanding lakes exert increasing hydrostatic pressure and pose higher downstream risks (Haritashya et al., 2018; Khadka et al., 2018; Peppa et al., 2020). Optical data can suffice for mapping lakes as a relatively straightforward tool without many processing steps. Figure 15 shows an example of lake expansion tracked from optical imagery. However, more frequent monitoring might be necessary for rapidly expanding or dangerous lakes. Then SAR could be more convenient since it enables data acquisition during nighttime and cloudy conditions. Strozzi et al. (2012) and Wangchuk and Bolch (2020) have proved that SAR is capable of mapping glacial lakes. Furthermore, glacier velocity and thinning can be monitored to predict lake expansion (Ahmed et al., 2021). Monitoring lake expansion significantly contributes to initial susceptibility assessments, such as indicating increased hydrostatic pressure. However, assessing the lakes' susceptibility to GLOFs requires more integrated approaches concerning the stability of the lake's surroundings (Strozzi et al., 2012).

Moraine monitoring generally involves performing site investigations and using digital elevation models (DEMs) to analyse the lithology and subsidence. Cracks can indicate moraine instability due to hydrostatic pressure or an earthquake and subsurface information about ice, debris, cracks and water infiltration can be obtained by conducting geophysical surveys. Figure 16 shows an example of a geophysical survey revealing the subsurface along a cross-section. In ad-

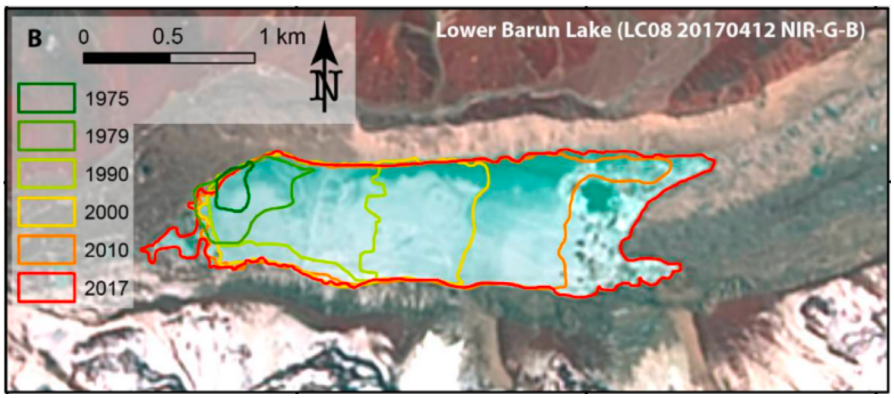

Figure 15: Lower Barun Lake's expansion (Haritashya et al., 2018)

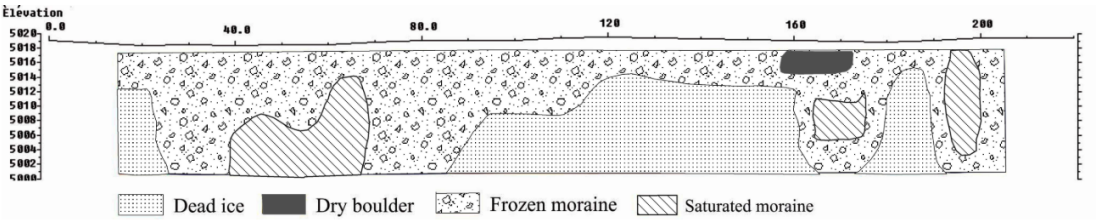

Figure 16: Geological cross-section interpreted from a geophysical resistivity survey at a glacial lake's terminal moraine (Dahal et al., 2018)

dition, identifying thermokarst features or lakes can provide evidence of buried ice. Thermokarst features are topographic depressions created in a variety of shapes and sizes as a result of thawing ground ice; Figure 17 shows an end moraine consisting of thermokarst lakes and depressions. Moraine ice cores indicate the dam's susceptibility to subsidence with rising temperatures and seepage (Janský et al., 2009; Sawagaki et al., 2012; Watanabe et al., 1995). Furthermore, comparing DEMs from different years can quantify moraine subsidence (Bennett and Evans, 2012; Haritashya et al., 2018). However, DEM comparisons only show the elevation difference between multiple years and do not comprise a continuous monitoring strategy. When the subsidence started, whether the movements are seasonal and if moraines deform homogeneously or heterogeneously cannot be derived. A thorough and continuous investigation of the moraine condition is required to identify appropriate mitigation measures (ICIMOD, 2011).

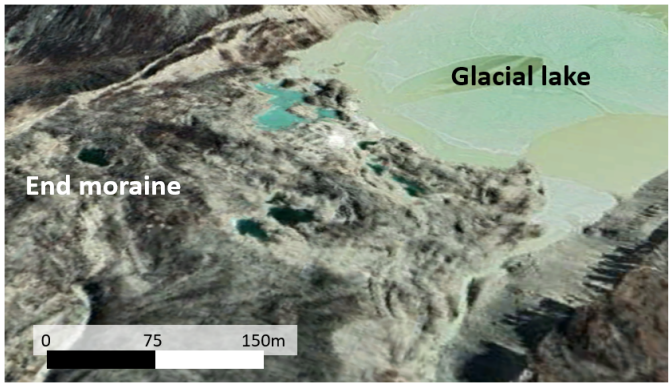

Figure 17: Visible thermokarst lakes and depressions on a terminal moraine. Optical image at Lugge Lake, Bhutan, Google Earth (January 2021).

Generally, slope analyses focus on surface changes, assuming deformations precede slope failures (Carlá et al., 2019; Raspini et al., 2018; Sousa et al., 2021). The slope analyses at glacial lakes have often been based on combining optical imagery and DEM-derived topographical data. Debris areas and previous landslides can be visible on optical imagery and slope instability can be identified by comparing slope features before and after an extreme precipitation event or earthquake. Using slope angles derived from DEMs, a downstream flattening of the slope can indicate a previous landslide or rock glacier lobes. Hanging glaciers or rock glaciers can also be visible from optical imagery. Flow lobes might be visible on high-resolution images at the front of rock glaciers. However, it might be more challenging if they are covered by debris. Mass movement trajectories have been constructed to link slope movements to GLOF hazards, assessing the likelihood of flood waves after slope failure (Khatiwada and Dahal, 2020; Rounce et al., 2016). However, these methods do not reveal whether the identified slopes are still active, how fast they are heading downslope, and their seasonal response. In addition, unstable slopes are not always visible from optical imagery. For that purpose, InSAR techniques have been implemented to quantify and identify unstable slopes at lakes in Peru and Bhutan (Klimeš et al., 2016; Scapozza et al., 2019; Wangchuk et al., 2022). InSAR uses radio waves to generate maps of surface deformation or digital elevation. A detailed explanation of InSAR can be found in Chapter 3. The studies of Klimeš et al. (2016) and Scapozza et al. (2019) conclude that continuous remote sensing and monitoring combined with geomorphological mapping to detect the mechanism that triggers the slope displacements are essential in managing GLOF hazards. Still, InSAR-based slope analyses at glacial lakes are scarce.

Lastly, glacier calving is challenging to predict, but crevasses might be observed beforehand. Such areas can be mapped using optical imagery. In addition, monitoring glacier velocity might point out crevasses by observing spatial velocity variations. Observations of accelerations or increased thinning rates might also indicate a higher chance of glacier calving (Benn et al., 2007). Glacier velocity can be monitored using optical imagery and InSAR. Optical imagery focuses on glacier outlines, whereas InSAR can measure glacier displacements. Since a different InSAR technique is required to measure glacier velocity than the methods used in this research, glacier monitoring is out of this research's scope.

In conclusion, a GLOF susceptibility assessment requires analysing and monitoring failure development signs and identifying unstable moraines and slopes. Ongoing displacements on dams can indicate self-destructive failure developments, such as ice core degradation or hydrostatic pressure leading to moraine dam collapse. The analysis of slope movement can identify unstable landforms, such as landslides, active rock glaciers and creep, providing a warning for possible dynamic failures. Glacial lake stability assessments primarily focus on analysing lake expansion, slope instabilities and moraine subsidence using site visits, optical imagery and DEMs. However, these approaches lack a continuous monitoring strategy, cannot quantify displacements, might skip unstable landforms or are time-consuming. InSAR can improve monitoring continuity since it does not require daytime or cloudless conditions. In addition, InSAR is a fast and cost-effective method for obtaining detailed quantification of displacements, their course over time, the deformation's reaction to specific events and it could discover previously unknown displacement areas. Continuous remote monitoring and integrated approaches involving optical and radar satellite data, meteorology and geomorphology are essential for identifying glacial lake hazards and applying mitigation measures. The following chapter will explain the application of InSAR, and chapter 4 describes integrating InSAR with additional data sources.

3 InSAR-based displacement monitoring

This chapter focuses on obtaining displacements with InSAR. First, section 3.1 describes the theoretical background of InSAR. Subsequently, section 3.2 will explain the methods used in this research to obtain displacements with InSAR. Finally, the application of InSAR to one of the glacial lakes accompanied by the results is described in section 3.3.

3.1 Theoretical background

This section describes the theoretical background of InSAR. The description will cover the SAR signal and geometry, the interferometric phase and introduce obtaining displacements with Differential InSAR.

3.1.1 Synthetic aperture radar (SAR)

Synthetic aperture radar (SAR) is a coherent radar system that transmits radio waves to a target scene and records the received pulse. Synthetic refers to a moving antenna, creating higher resolution images with smaller antennas. SAR systems use different wavelengths to measure specific features. Larger wavelengths can penetrate more deeply into surface covers, whereas smaller wavelengths reach higher accuracy of millimetres. X-band wavelengths range from 2.5 to 4 cm, C-band from 3.75 to 7.5 cm, S-band from 7.5 to 15 cm, L-band from 15 to 30 cm and P-band from 30 to 100 cm (NASA, 2022). Radar waves can penetrate clouds and are not affected by nighttime, allowing the continuous operation of SAR. SAR systems can be mounted on satellites or aeroplanes, capturing wave reflections of an area from different antenna locations or at different times. Multiple antenna positions are used for mapping topography and multiple acquisition times are used to measure displacement. Usually, sun-synchronous polar-orbiting satellites are used for the latter application. Figure 18 displays this orbit, circling from the South to the North Pole (ascending) and from the North to the South (descending). Since the earth turns around the poles' axis, every region is covered by the ascending and descending path. The near-polar orbit of 98.18 degrees arranges the satellite's angle to be similar at every revisit for the ascending or descending path (King, 2007). The revisit time varies per satellite. Figure 19 displays SAR satellites that have operated or are currently operating, with their revisit time and wavelength. This research uses SAR data from the Sentinel-1 satellite constellation with a 12 day revisit time per path and a C-band wavelength of 5.6 cm. The antenna is right-looking, which means the region is observed from a different compass direction for the ascending and descending path. The antenna looks eastward for the ascending path, and the antenna looks westward for the descending path (ESA, 2022).

Figure 20 shows the geometry of a SAR system. SAR satellites send out radar signals along the line of sight (LOS) in the range direction towards the earth's surface while flying in the azimuth direction. The angle between the vertical and the LOS is the incidence angle (θ). Every reflection is stored in a pixel. Pixels form matrices, where rows correspond to azimuth direction (x), called lines, and columns correspond to range direction (y), referred to as samples. All lines consist of satellite positions, and all columns are pulse samples. Scanning frequencies in the range direction are significantly higher than the azimuth direction. The resolution depends on the cell sizes on the ground, defined by the satellite and swath mode (Ferretti et al., 2007). The Sentinel-1 has a 5-metre resolution perpendicular to the flight path or the looking direction (range) and a 20-metre resolution along the flight path (azimuth) (ESA, 2022).

The two fundamental properties of SAR signals are the amplitude and phase. Each pixel's value is the sum of all scatterers within the resolution cell on the ground, and all pixels aligned form a SAR image. Every pixel contains a phasor (P), consisting of the wave's amplitude (A in dB) and the phase (ϕ in radians):

$$P = Ae^{i\phi} \tag{1}$$

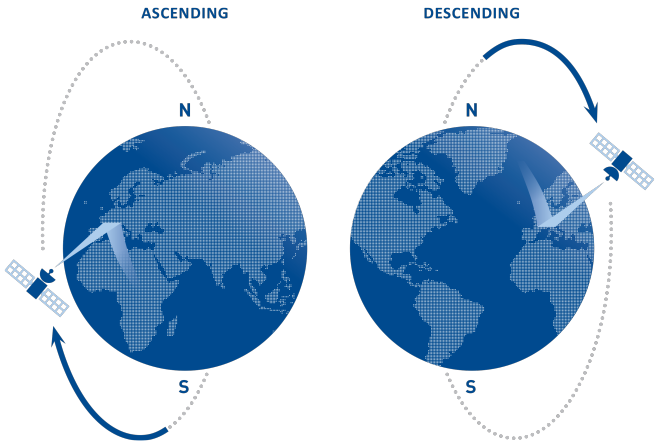

Figure 18: Ascending and descending path of a (near) polar-orbiting satellite (ESA, 2022)

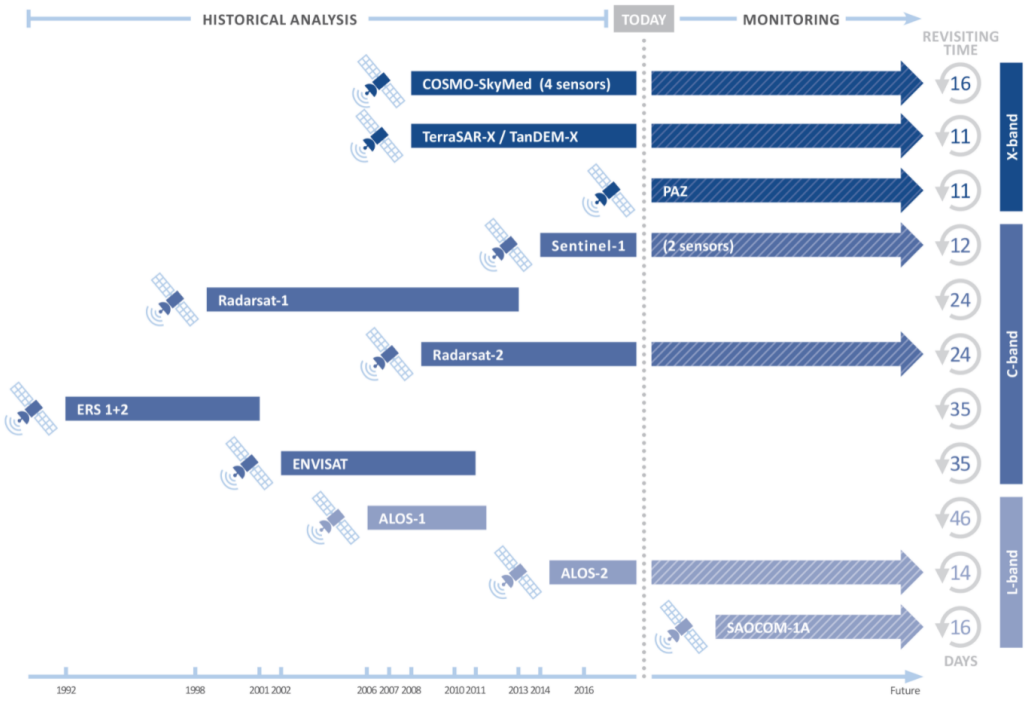

Figure 19: SAR satellites (ESA, 2022)

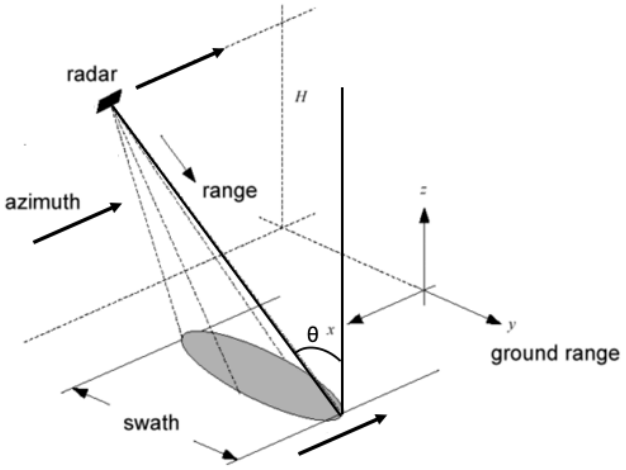

Figure 20: The geometry of a SAR system. Image adjusted from Bamler (1999)

The measured reflected fractional phase is determined by the range travel time. Consequently, the phase provides information on the distance between the satellite and the surface. Figure 21 displays the phase and amplitude of a SAR image. The amplitude is the backscattering intensity, which depends on the amount of radiation reflected to the satellite. Sensor properties such as wavelength, bandwidth, incidence angle, and surface characteristics such as slope gradient, roughness, soil moisture and dielectric constant influence the amplitude. Flat and high reflective surfaces, such as water bodies, will reflect the radio waves away from the satellite, resulting in low backscattering values. Surface roughness causes proportions of waves to reflect back to the satellite, which is why rippled water surfaces do show some backscattering intensity. A larger wavelength is less sensitive to surface roughness and therefore a smaller proportion is reflected back to the satellite than for a smaller wavelength. For smaller incidence angles also a larger proportion will be reflected back to the satellite. The reflection can contain dominant reflecting objects in resolution cells (dominant scatterers) and various smaller scattering objects (distributed scatterers) (Leijen, 2014). Objects that provide consistent scattering over time all called stable reflections or scatterers, having a high amplitude stability. Generally, solid structures have stable reflections, whereas vegetation and snow layers cause varying backscattering over time and consequently return unstable amplitude signals (Ferretti et al., 2007; Perissin, 2016). Figure 22a displays a reflectivity map; this map displays averaged backscattering intensities of 180 SAR images covering five years. Consistent and robust reflection targets, such as bare rock, show enhanced reflectivity. Areas without backscattering appear black, like water bodies or regions in the satellite's shadow, and areas without stable amplitude show no scattering objects, such as snow layers. C-band SAR can penetrate through several metres of dry snow since the wavelength (5.6 cm) is significantly larger than snow molecules of 0.1-0.3 mm, preventing the backscattering of snow. However, the dielectric constant increases significantly for wet snow, and the penetration depth decreases to around 3 cm (Tsai et al., 2019). Regions experiencing melting snow or consisting of thick snow layers will result in decreased amplitude stability. Therefore, the bottom right of Figure 22a, which consists of thick snow layers, does not reveal apparent scattering objects.

The ratio between SAR's incidence angle (θ) and the surface slope angle (α) can cause geometric radar distortions and limitations visualised in Figure 22b. First, foreshortening causes spatial distortions at slopes facing the radar. This issue arises at slopes facing the satellite (A-B), appearing as compressed slopes in the radar image (a-b). Consequently, the signal contributions of the slope will be compressed into a smaller radar pixel, enhancing the reflectivity. These areas are still analysable, but the resolution will be worse than at flat terrain. Second, layover

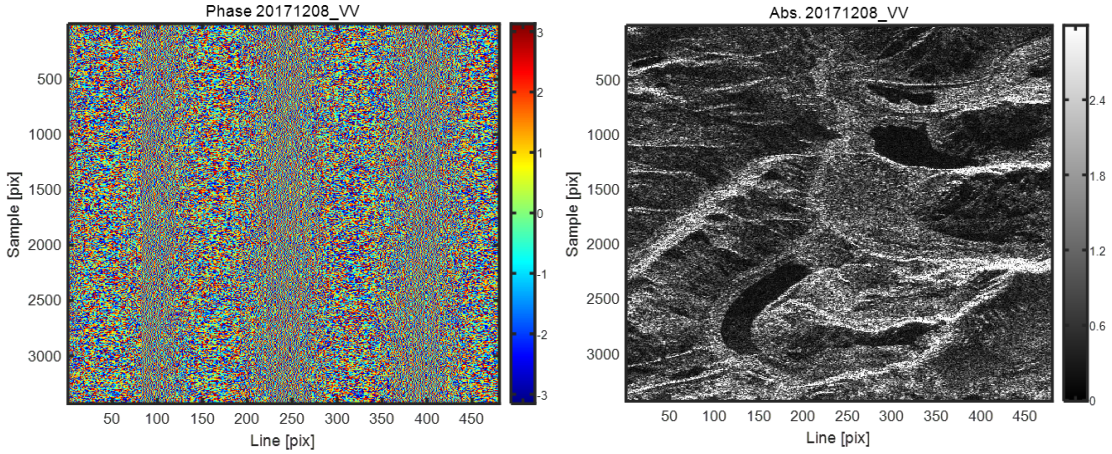

(a) **(b)**

Figure 21: Phase in radians (a) and amplitude in decibel (b) of a SAR Image from the ascending dataset of the Lunana Lakes.

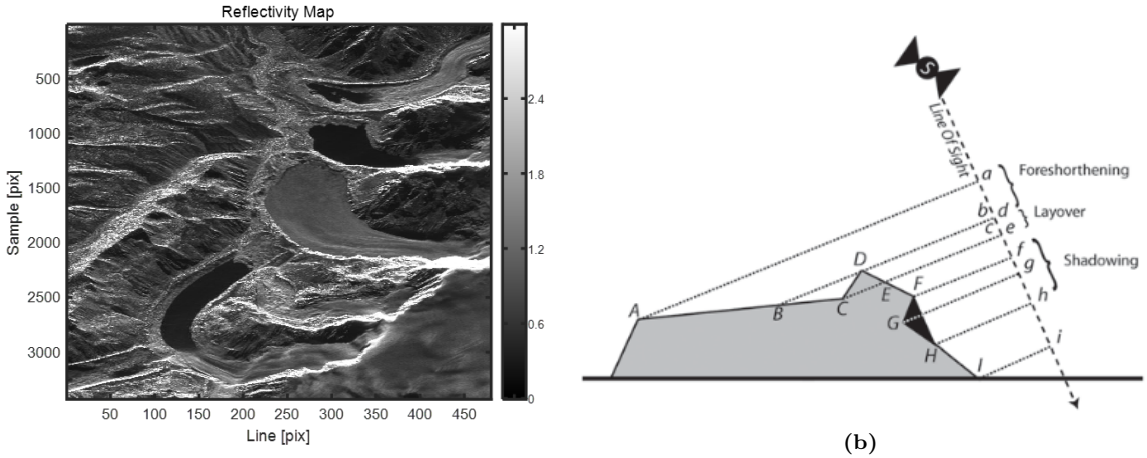

(a) **(b)**

Figure 22: (a) Reflectivity map of the Lunana Lakes (ascending). (b) Geometric limitations (Barboux et al., 2014).

occurs when slope gradients facing the satellite are larger than the incidence angle ($\alpha > \theta$ at C-D). As a result, reflecting waves from hilltop points (D) return earlier than valley points (C). Consequently, radar images will overlay mountain top results (d) above valley results (c), and intensities will be superimposed, returning as high reflecting compressed areas. Figure 22a shows the layover areas as the white high-intensity bands on mountain ridges. Layover is a widespread problem for space satellites acquiring images over mountains as these areas are not analysable. Finally, shadowing happens when slopes not facing the satellite (F-G and G-H) are larger than 90-θ; this slope will lie in the shadow of the LOS and will not reflect radar waves and consequently be dark in reflectivity images. These areas will also not be analysable. Apart from the lake bodies, Figure 22a shows darker areas on specific slopes, corresponding with shadow. Lastly, north or south-facing slopes are more challenging to analyse since the LOS is in the east-west direction for a polar-orbiting satellite (Barboux et al., 2014; Colesanti and Wasowski, 2006; Ferretti et al., 2007).

3.1.2 Interferometric SAR (InSAR)

Interferometric SAR (InSAR) refers to interfering SAR images (Figure 21) acquired at different times or viewing positions to generate surface deformation or digital elevation maps. The principle is to obtain the phase difference between two SAR images. First, the pixels of two images are aligned, referred to as coregistration. Then, the phasor multiplication between the images forms this complex interferogram,

$$I_{MS} = I_M - I_S^* = A_M A_S e^{i(\phi_M - \phi_S)} \tag{2}$$

where * is the complex conjugate, M is the main image, S is the secondary image, A is the amplitude, and ϕ is the interferometric phase. The amplitude varies per image if surface characteristics change during the acquisition period. Phase changes can imply surface displacements but can also consist of other contributions. Equation 3 denotes the interferometric phase,

$$\phi_{MS} = W(\phi_M - \phi_S) = W(\phi_F + \phi_T + \phi_D + \phi_A + \phi_N) \tag{3}$$

where W is the wrapping operator, and the interferometric phase consists of the flat terrain term, the topographic phase, the deformation phase, atmospheric delay and noise due to the measurement equipment, processing errors and differences in surface backscattering properties. Figure 23 displays the interferometric phase of two images twelve days apart. The goal is to separate coherent signals from noisy, incoherent signals. Depending on the application, coherent components could include topography, atmosphere properties, surface displacement, and noisy features can include random attributions from snow, water and vegetation or measurement errors (Perissin, 2016).

The **flat terrain phase** is dependent on the target's slant range coordinate. Therefore, phase differences will still occur without topographic variations between measured points due to the range difference between two images, causing phase ramps in range direction in interferograms. Longer geometric baselines will result in higher fringe frequencies in interferograms. Orbital information can estimate this phase term,

$$\phi_F = \frac{4\pi}{\lambda} \frac{B_n}{R_k} \frac{\Delta r}{tan\theta} \tag{4}$$

where λ is the wavelength, B_n (normal baseline) divided by R_K (the main range of a reference point) is the relative incidence angle ($\Delta\theta$) between two satellite antenna positions, and Δr

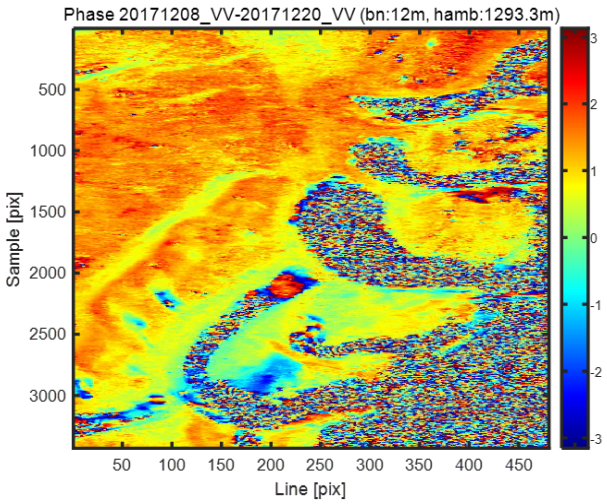

Figure 23: Interferogram of two SAR images 12 days apart. The colour legend corresponds to the interferometric phase in radians. Image is taken from the ascending dataset of the Lunana Lakes.

divided by $tan\theta$ is the slant range component (Perissin, 2016).

The **topography phase** term,

$$\phi_T = \frac{4\pi}{\lambda}\frac{B_n}{R_k}\frac{\Delta h}{sin\theta} \tag{5}$$

where λ is the wavelength, B_n (normal baseline) divided by R_K (the main range of a reference point) is the relative incidence angle ($\Delta\theta$) between two satellite antenna positions and Δh is the difference in height between the target and reference point. Dividing this term by $sin\theta$ makes up for the height component. As the surface height also accounts for the phase, InSAR is suitable for developing digital elevation maps. For this application, two SAR images of different incidence angles taken on the same date are used to avoid surface displacements. If the topography is not the target, digital elevation models (DEMs) and satellite orbit information allow for the removal of this term and two SAR images of the same incidence angle on different dates are used.

The **deformation phase** can be translated into surface displacement between two SAR images taken on different dates. The term is calculated with

$$\phi_D = \frac{-4\pi}{\lambda}D_{LOS} \tag{6}$$

where D_{LOS} is the mm deformation in the LOS direction (Hanssen, 2001; Perissin, 2016).

Finally, the **atmospheric phase** may significantly affect the accuracy of results, even when the results seem coherent and correctly unwrapped into height or displacements. The atmospheric delay comes in different forms. First, surface pressure differences between two acquired images cause hydrostatic delay variations. Second, atmospheric turbulence causes wet delay, which its spatial heterogeneity makes it challenging to account for. Third, atmospheric water vapour delays radar signals, depending on the cloud's water content. Lastly, vertical stratification occurs in areas with significant height differences, such as mountainous areas, meaning that waves travel longer distances through the atmosphere to lower-lying points, increasing the path delays (Hanssen, 2001). Multiple approaches can slightly overcome these distortions, such as spectrometers, numerical weather models and GPS networks to construct vapour maps. Still, this does not entirely remove the atmosphere's effect, preventing millimetre accuracy for deformations (Perissin, 2016). However, as atmospheric contributions are highly variable over time and low in space, selecting multiple images — preferably more than 25 — and using high-pass filtering in time and low-pass filtering in space will filter out most atmospheric disturbances. Using an image stack is often referred to as Multi-Temporal InSAR (MT-InSAR). Based on low atmospheric variation over space, the atmosphere can be neglected for small areas — up to a few kilometres — considering the atmosphere impact being equal over the entire image and because displacements are calculated in a differential manner, that is with respect to a reference point (Budillon et al., 2019). The following sections will explain this in more detail.

3.1.3 Differential InSAR (DInSAR)

Differential InSAR (DInSAR) is the approach of removing all components except for the deformation from Equation 3. Differences in phases between two acquisition images can translate to accurate displacements between two acquisitions, as ground displacements cause modified reflected wavelengths. Various methods exist for obtaining displacements; methods can be amplitude-based or phase-based, rely on distributed or dominant scattering objects and have different geometric or temporal baseline configurations. Examples of DInSAR techniques are persistent scatterer interferometry (PSI), SBAS, conventional DInSAR and SqueeSAR; many methods have been described by Virk et al. (2018). DInSAR has successfully been applied to analyse slope displacements (Bayer et al., 2017; Carlá et al., 2019; Ciampalini et al., 2016; Eriksen et al., 2017; Fárová et al., 2019; Kos et al., 2016; Liu et al., 2012; Rosi et al., 2018; Scapozza

et al., 2019; Schlögel et al., 2015; Tessari et al., 2017; Wasowski and Bovenga, 2014), subsidence areas (Aslan et al., 2019; Furst et al., 2021; Kumar et al., 2020; Pasquali et al., 2014) and glacier movement (Haritashya et al., 2018; Strozzi et al., 2002).

An issue that arises with DInSAR is decorrelation or decoherence. This implies an abrupt change in terrain characteristics between two satellite observations that prevents obtaining correct phase information. A variety of factors can cause signal decorrelation. A high geometric baseline can cause spatial decorrelation, and changes in scattering properties or excessive displacements can cause temporal decorrelation (Sica et al., 2021). First, vegetation and snow cover cause temporal surface changes. The scattering of vegetated or snow-covered surfaces can vary significantly between two acquisitions. Vegetation disturbs the backscattering and returns a more random volume scattering instead, changing over seasons, after precipitation or due to wind (Barboux et al., 2014; Ferretti et al., 2007). Dry snow should be penetrable until several metres. However, wet snow induces changes in dielectric properties and decorrelates the signal (Barboux et al., 2014; Malinverni et al., 2014; Tsai et al., 2019). Second, the signal can decorrelate when displacements are too excessive or random over time. Examples are brittle rock instabilities that happen over a short time (Carlá et al., 2019). The type and severity of decorrelation depend on the specific DInSAR method used, elaborated on in section 3.2.

3.2 Method

This section explains the applied DInSAR methodology for this research. Sentinel-1 C-band (5.6 cm wavelength) data is acquired through the Alaska Satellite Facility website. The data consists of georeferenced single look complex (SLC) images containing information on the signal's wave and amplitude. Every lake has an ascending and descending data set, up to 160 images covering 2015 to 2021, with usually 12 day revisits. Table 3 displays the Sentinel-1 acquisition data for each lake. This research uses the Sarproz software tool in Matlab for InSAR processing (Perissin et al., 2011). DInSAR is applied with conventional DInSAR (CDInSAR) and persistent scatterer interferometry (PSI). CDInSAR and PSI use different temporal baselines and unwrapping techniques. Therefore, applying both methods could extend the spatial and temporal coverage and validate the results. Figure 24 displays the simplified workflow of obtaining displacement results using Sarproz.

First, the area of interest (AOI) is selected, and then the image stack is coregistered. Coregistration assures that all images precisely overlap, despite the variations in viewing geometry. Patches throughout the SAR image are matched between the main and secondary images aided by a DEM. Selecting a large enough AOI and image stack is essential to account for noise and weather influences. Then the reflectivity map and amplitude stability are generated, followed by selecting a ground control point (GCP). The GCP is necessary for correctly geocoding the results. The GCP has been selected manually by matching a pixel of the reflectivity map to geographical coordinates using Google Earth. As explained in section 3.1.1, the radar image contains geometric distortions because it is in LOS view. Especially for areas with steep and high slopes, areas can be foreshortened or stretched. As a result, the distances on the radar image using SAR coordinates are not similar to those for a geographical coordinate system. Consequently, areas lying too far from the GCP can be geocoded incorrectly. In that case, the AOI has been split to use multiple GCPs. For example, this has been applied for the Barun Lakes, which consists of three lakes and produced incorrect geocoded results when using one GCP for the whole area. The following paragraphs will describe the CDInSAR and PSI methods.

Lake(s)	**Barun**		**Imja**		**Lumding**	
Coordinates	87.09, 27.82		86.92, 27.90		86.61, 27.78	
Orbit	Asc	Desc	Asc	Desc	Asc	Desc
Path	12	121	12	121	12	121
Subswath	1&2	2	1	2	1	2
Incidence angle (deg)	36.82	36.62	35.85	37.75	33.81	38.31
Nr. of images	150	146	150	151	150	153
Time frame	Dec 2015 to Jul 2021	Sep 2016 to August 2021	Dec 2015 to Jul 2021	Sep 2016 to Apr 2021	Dec 2015 to Jul 2021	Sep 2016 to Apr 2021
Main image	2018-11-02	2018-11-10	2018-11-02	2018-10-29	2018-10-21	2018-10-11

Lake(s)	**Lunana**		**Rolpa**		**Thulagi**	
Coordinates	90.28, 28.10		86.48, 27.86		28.49, 84.49	
Orbit	Asc	Desc	Asc	Desc	Asc	Desc
Path	114	150	85	121	158	19
Subswath	3	3	3	2	3	2
Incidence angle (deg)	43.54	42.25	44.90	40.25	44.28	40.64
Nr. of images	190	167	160	179	99	185
Time frame	Oct 2014 to May 2021	Oct 2014 to Apr 2021	Nov 2015 to Jul 2021	Sep 2016 to Apr 2021	June 2016 to Dec 2019	Oct 2014 to May 2021
Main image	2017-08-22	2018-06-08	2018-11-19	2018-10-29	2017-11-05	2017-12-02

Table 3: Sentinel-1 acquisition data

3.2.1 Conventional DInSAR (CDInSAR)

CDInSAR refers to the original method of measuring deformations with DInSAR. With CDInSAR, displacements are obtained by spatially unwrapping consecutive interferograms, thus using a small temporal baseline. Figure 25a shows this interferogram relationship. The small temporal baseline configuration often suits homogeneous terrains with large displacements or small data sets (Hooper, 2008). Consecutive interferograms unwrap to absolute phase values, which can be translated into deformations between the two images.

Several methods apply to unwrapping interferograms, such as the residue-cut, minimal cost flow or the least-squares algorithm. The applicability of the approaches depends on the application. Generally, a residue or branch cut algorithm performs poorly in noisy regions, but the least-squares algorithm performs poorly in images containing many phase discontinuities. Details of the unwrapping algorithms can be found in the studies of Hanssen (2001), Werner et al. (2002) and Zebker and Lu (1998). This research uses the least-squares method, as this algorithm returned the best results for the study areas in this research. However, phase continuities can cause unwrapping errors to propagate throughout the image with the least-squares method, causing useless image pairs (Bi and Wei, 2016; Zebker and Lu, 1998).

Since the phases unwrap in the spatial dimension, spatial phase discontinuities or large spatial phase gradients can cause decorrelation. First, CDInSAR requires smoothness of deformation signals in space; the phase difference between neighbouring pixels should be in the interval $-\pi, \pi$. Therefore CDInSAR works best in homogeneous deforming terrains. Phase noise, such as temporal decorrelation, phase under-sampling, or phase discontinuities, such as layover or discontinuous surface deformation, cause significant phase differences. When possible, increasing the spatial resolution can overcome this limitation (Cuenca et al., 2011; Werner et al., 2002). Second, a small perpendicular baseline (the satellite distance between acquisitions) of less than 200m is necessary to avoid geometric decorrelation (Ferretti et al., 2000). Generally, the temporal baseline is smaller than this value for the data sets in this research. However, since the relationship is only focused on a small temporal baseline and not the geometric baseline, relatively large geometric baselines can arise and account for decorrelation.

Consequently, the method requires minimal geometric distortions, atmospheric disturbances, poor weather conditions and temporally varying backscattering caused by vegetation and wet snow. Unfortunately, since many areas contain such features, the applicability of CDInSAR is often limited (Fárová et al., 2019; Ferretti et al., 2000; Leijen, 2014). Often spatial filtering and multi-looking are applied to reduce noise and avoid phase discontinuities. However, multi-looking smooths out outliers, possibly losing critical information. For example, isolated autonomously moving areas might be undetectable if uncorrelated pixels surround them (Leijen, 2014). Filtering reduces noisy areas and makes fringes more clear. For this research, a spatial filter and a spatial coherence threshold have been applied to minimise the influence of incoherent regions such as glaciers, snowy mountain tops and lakes. However, the threshold must be low enough to retain challenging areas like rock glaciers and moraines. Therefore, a spatial coherence filter of 0.3 was applied before the unwrapping. As a result, noisy regions did cause some incorrectly unwrapped regions, but smaller displacements at moraines could still be obtained. The images have not been multi-looked to limit the averaging of small and rapidly moving areas.

The main advantages of CDInSAR are high spatial coverage, the applicability to small data sets and the ability to measure fast deformation. The main disadvantages are the low performance in spatially discontinuous and temporally heterogeneous areas, sensitivity to atmospheric contributions and the dependence on a small perpendicular baseline.

3.2.2 Persistent scatterer interferometry (PSI)

A larger image stack and a focus on stable scattering objects reduce errors due to temporal, geometrical and atmospheric decorrelations, which are significant limitations of unwrapping interferograms with CDInSAR. PSI is an example of such a multi-temporal approach; the technique

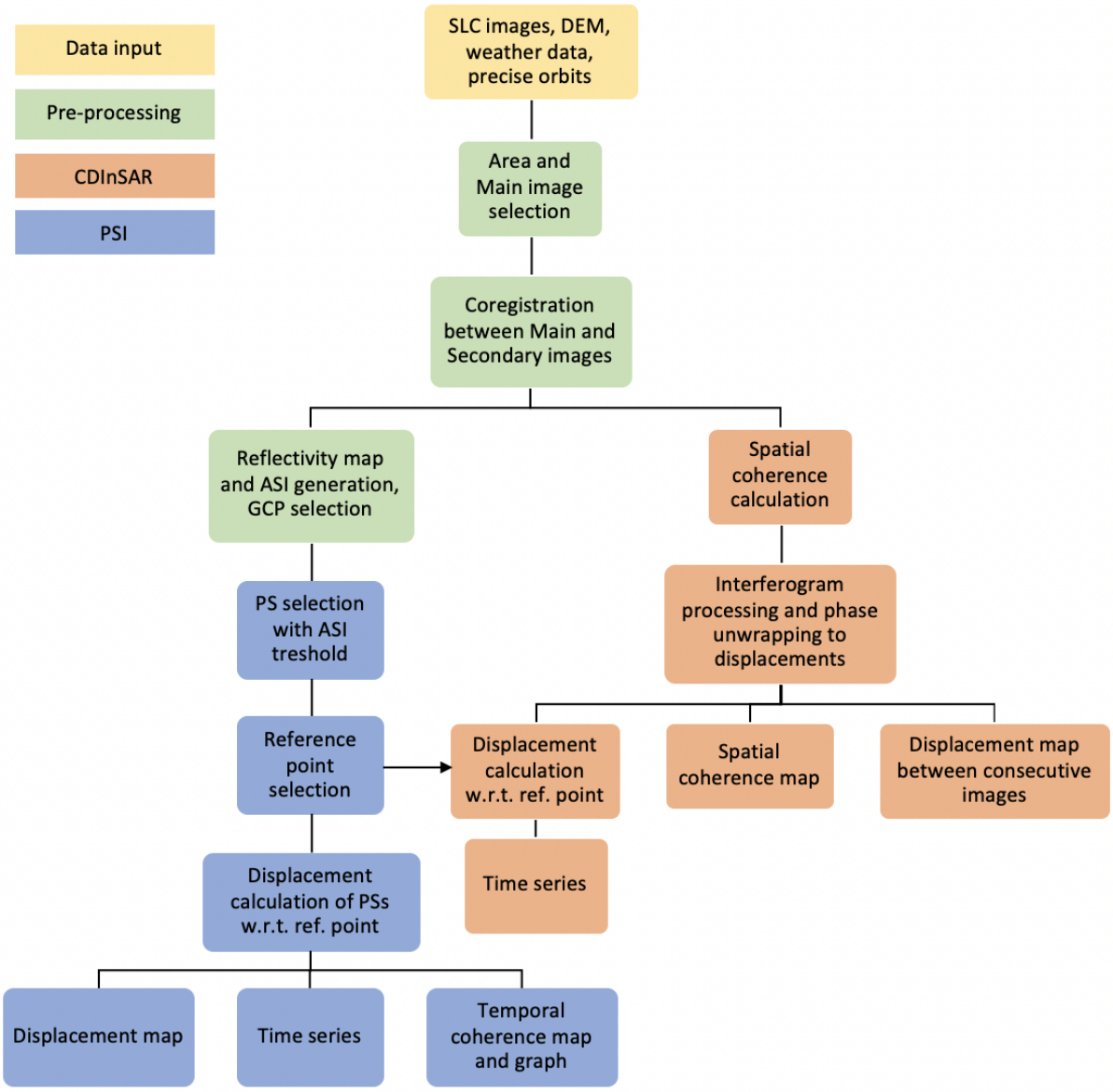

Figure 24: Simplified CDInSAR and PSI workflow that has been applied for obtaining displacements with Sarproz

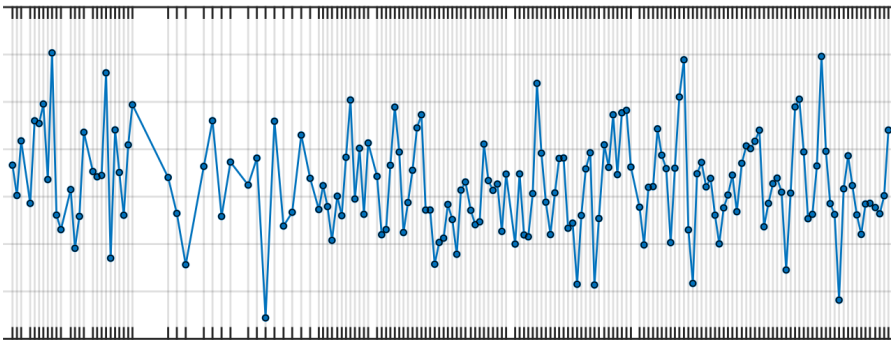

(a) Small Temporal Baseline graph (CDInSAR)

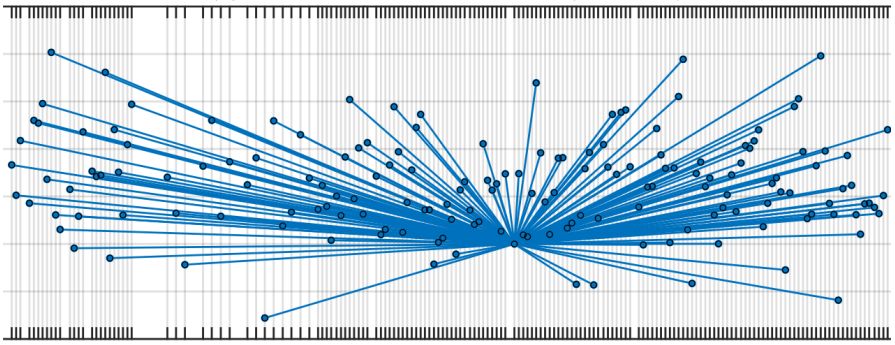

(b) Star graph (PSI)

Figure 25: Baseline configurations for DInSAR with acquisition date on the x-axis and normal baseline on the y-axis

was invented in 2000 (Ferretti et al., 2001). Persistent scatterers (PS) are dominant and consistent reflecting objects in resolution cells, and the pixels are processed separately without being affected by nearby incoherent areas. Moreover, using large image stacks reduces the impact of the atmosphere and errors or decorrelation related to single acquisitions. Together, these features make it possible to analyse extensive deformation time series (Ferretti et al., 2000). The star graph (or single main image configuration) in Figure 25b is used as the baseline configuration for PSI. All images interferometrically connect to the main image. Therefore, the main image should ideally minimise spatial and temporal baselines and contain little atmospheric noise. Various researchers developed PSI techniques over the years for specific applications, many of which have been discussed by Crosetto et al. (2016). Figure 24 displays the simplified workflow for obtaining displacements with Sarproz.

PS candidates (PSC) are selected by the amplitude stability index (ASI). Equation 7 denotes this index' calculation, where σ_a is the standard deviation and a_{mean} is the mean amplitude value over time per point:

$$ASI = 1 - \frac{\sigma_a}{a_{mean}} \tag{7}$$

A high value indicates a stable backscattering intensity over time; a smaller standard deviation decreases the fraction. The amplitude stability exhibits a statistical relation to phase stability. High amplitude stability values have little phase contributions by the atmosphere, topography, deformation and noise. So it can be assumed that points with a high ASI are stable points. An ASI > 0.75 is desired to construct an accurate atmospheric phase screen (APS) (Ferretti et al., 2001). A smaller value is usually applied to densify the PS network for calculating displacements. A higher ASI returns more reliable results but will also return fewer points. Therefore, PSI works well in areas with steady scattering objects, such as urban or rocky areas, with many continuously high reflecting points over time. Conversely, significant temporally

varying surfaces such as vegetated areas or fast-moving surfaces will reduce persistent scatterers and could require a different technique (Crosetto et al., 2016; Ferretti et al., 2007). In addition, PSI needs many images (typically over 30) to average out random amplitude variability. This is visualised in a reflectivity map by uniform amplitude levels and reduced speckle like features. This research applies a relatively low ASI threshold of 0.5-0.55. The amplitudes contain reduced stability over the image stack because the glacial lake regions are subjected to seasonal snow, frost, precipitation and melting. For example, a higher ASI returned nearly no points on end moraines and rock glaciers.

All displacement points are calculated by referring to a single reference point that is stable over time. If all points lie near the reference point, the atmospheric contribution can be neglected since the atmosphere tends to be spatially homogeneous over multiple kilometres. In other cases, it is necessary to estimate the atmospheric contribution and subtract it from the interferometric phase (Budillon et al., 2019). The study areas in this research have been analysed using subsets, with the maximum distance between the reference point and other PS being approximately 1-5 km. PSI has been processed with and without calculating the APS for a few data sets containing slightly larger areas to verify the atmosphere neglection, resulting in no difference in results. Therefore, the atmosphere has been neglected for the final results of each data set, which is particularly convenient for analysing challenging areas that do not contain many PS with high ASI, disabling the construction of an accurate APS.

PSI assumes that the deformations follow a model to correctly assign points as PS and avoid noise contributions and random displacement jumps. The displacement model can be linear or non-linear. The substantial seasonal variation in temperature and precipitation and non-gradual movements of loose mass in high mountain areas expect to cause non-linear displacements (Tofani et al., 2013). Linear and non-linear models have been applied at two lakes to verify this assumption. A measure of how well the displacements follow the displacement model over time is the temporal coherence. Figure 26 demonstrates that the PS temporal coherence is higher for the non-linear model. Many PS and high temporal coherence indicate that the displacements fit the proposed model well. When using the linear model and if PSC do not follow linear movements, the scatterers are either not identified as PS or the non-linear component is incorrectly attributed to atmospheric contribution (Ferretti et al., 2000). Figure 27 displays an example of a cumulative displacement time series of a PS. The scatters represent the actual measured values, and the line shows the modelled displacement following a non-linear deformation model. Directly at the second acquisition date, the displacement shifts 12.2 mm upwards. As this behaviour does not fit the non-linear displacement model, the model treats this value as incorrect. Consequently, this jump is ignored, which also happens for other random outliers. This figure shows a point with high temporal coherence (0.89), so the behaviour of the PS fits the model well. Temporal coherence thresholds of 0.65-0.8 are used for final displacement mapping, depending on the visual arrangement of displacement points and additional geomorphological analysis to conclude whether the results are realistic.

In the case of large and fast displacements, aliasing can arise. The phase shift could reflect both upward and downward displacement if the phase equals half of the signal phase. This amount corresponds to a displacement of one-fourth of the radar signal's wavelength between consecutive images. Theoretically, this is 14 mm for Sentinel-1 C-band data, but this value can lie slightly lower in practice. Aliasing can underestimate the final displacement as the displacement throughout the time series can be modelled in the opposite (incorrect) direction between acquisitions. In addition, if displacements continuously reach this value, the displacement might be continuously reflected in the wrong direction, resulting in a final displacement flipped in the wrong direction. Decreasing the temporal baseline can overcome this limitation when possible. Therefore, short temporal baseline interferograms, such as for CDInSAR, might be better applicable for fast-moving areas (Ajourlou et al., 2019; Ferretti et al., 2005).

In conclusion, some advantages of PSI are the reductions of temporal and spatial decorre-

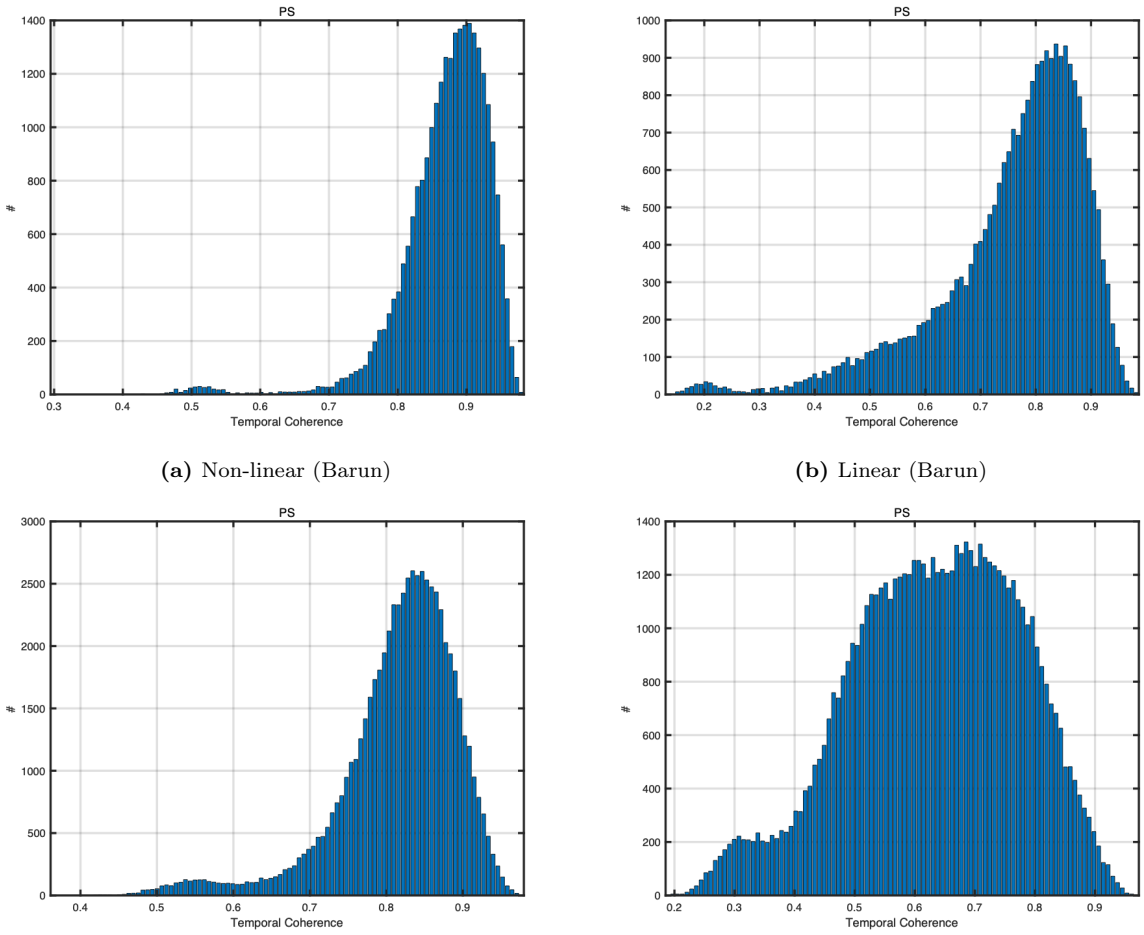

(a) Non-linear (Barun)

(b) Linear (Barun)

(c) Non-linear (Rolpa)

(d) Linear (Rolpa)

Figure 26: The difference in temporal coherence of PS points (ascending) regarding a linear or non-linear displacement model with ASI>0.6

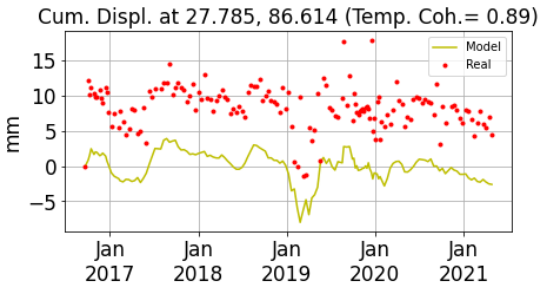

Figure 27: Cumulative displacement time series of the 'real' measured and modelled values at a stable area

.

lation and atmospheric distortions, resulting in more usable and accurate data and thus the construction of time series. Another advantage is the possibility of detecting autonomous moving pixels. On the other hand, the main limitations of PSI are aliasing or decorrelation for fast-moving areas, low spatial coverage for areas containing few persistent scatterers, and the need for a larger image stack.

3.2.3 Displacement decomposition

As mentioned in section 3.1.1, SAR can only measure deformations along the LOS. Consequently, the final displacements obtained only reveal whether the surface moves towards or away from the satellite along the LOS. The Sentinel-1 is near polar-orbiting, and the antenna is right-looking, with a 5-metre resolution perpendicular to the flight path or the looking direction (range) and a 20-metre resolution along the flight path (azimuth). Therefore the satellite is less sensitive in the north-south direction. In addition, for satellite incidence angles below 45 degrees, InSAR sensitivity in the vertical direction is higher than in the horizontal direction (Alatza et al., 2020; Leijen, 2014).

Combining ascending and descending measurements enables finding displacement directions in primarily vertical and east-west orientations. The ascending satellite goes towards the north-north-west direction, looking to the right, so positive values indicating displacements towards the satellite correspond to up or westward direction. Conversely, negative ascending values indicate subsidence or eastward displacement. The descending satellite moves south-south-east, so positive values indicate upward or westward movement, and negative values indicate subsidence or eastward displacement. The amount of displacement for both ascending and descending paths can indicate the primary displacement direction. For example, if both orbits show similar negative values, the principal deformation is subsidence. However, suppose an area measured from an ascending view contains a more significant negative value than a descending orbit. In that case, the area is experiencing vertical subsidence but slightly eastward. In addition, if the values for both orbits were exactly opposite, the site is experiencing mainly horizontal displacement in either west or east direction. Furthermore, adding geomorphological features, such as slope angle and orientation, will aid in estimating the displacement direction, as mass tends to move downslope.

The magnitude of decomposition of vertical and east-west deformations can be calculated with:

$$d_{East} = \frac{1}{2}\left(\frac{d_{Dsc}}{sin(\theta_{Dsc})} - \frac{d_{Asc}}{sin(\theta_{Asc})}\right) \tag{8}$$

$$d_{Up} = \frac{1}{2}\left(\frac{d_{Dsc}}{cos(\theta_{Dsc})} + \frac{d_{Asc}}{cos(\theta_{Asc})}\right) \tag{9}$$

where d_{Dsc} and d_{Asc} are displacements measured in descending and ascending direction, and θ_{Dsc} and θ_{Asc} are the incidence angles (Milillo et al., 2016). These equations have been used to automatically decompose displacements in the east-west and vertical direction for areas covered by both orbits. A spatial threshold of 20 m has been applied to pair ascending and descending points.

Mountainous areas often experience geometric limitations — either for one or both orbits (Figure 22b on page 24). Consequently, InSAR's coverage and coherence at specific regions are not typically similar for both data sets. In addition, the temporal coverage not only differs per location but also per orbit, which can result in different time frames used for ascending and descending data sets. For example, data sets ranging from 2014 to 2021 often have gaps up to several months, especially at the start, decreasing temporal and spatial coherence. That is why the data sets listed in Table 3 have varying time frames. Especially in critical and challenging areas, such as moraines and steep slopes, the area might be subjected to geometric limitations or decoherence for one of the orbits. So, employing both ascending and descending

data sets often extends spatial coverage rather than decomposing the displacements. Therefore, decomposed displacements are combined with LOS displacements for interpreting movement directions. Adding geomorphological and topographical features will aid in the interpretation, which will be explained in Chapter 4.

3.3 Application to Imja Lake

This section describes the CDInSAR and PSI processing and displacement results of Imja Lake obtained using the workflow of Figure 24. The CDInSAR results of the other lakes can be found in Appendix A, the PSI displacements in Appendix B and the processing results in Appendix C. Figure 28 displays the footprint of the ascending path heading north-north-west and the descending path heading south-south-west, with Imja Lake located in the yellow rectangle. Figure 29 shows an aerial Google Earth image of Imja Lake, displaying the AOI. Figure 30 displays the reflectivity maps, consisting of the mean amplitude values. The reflectivity maps show the black areas consisting of zero amplitude values corresponding with water bodies and regions in the shadow of the satellite LOS. Furthermore, some mountain ridges show up white, indicating very high amplitude values. These areas are causing slight layover, overlaying signals and thus increasing the amplitude. The reflectivity map is convenient in seeing which regions do not return coherent signals or are subjected to geometric limitations.

3.3.1 CDInSAR

Figure 32 displays the spatial coherence maps revealing spatially homogeneous and less homogeneous areas. Figures 33a and 33b show the timeline of coherent interferograms for the ascending and descending stack, respectively. The first two years do not show coherent results for the ascending stack. For a part, this can be explained by the larger temporal baseline visible in Figure 31. However, the figure shows that the baseline is not continuously large during those two years. Therefore other influences such as geometric baseline, atmosphere and snow could have caused decoherence. Two coherent interferograms and unwrapped displacements are plotted in the Figures 34 and 35. The unwrapped displacement images are plotted with a spatial coherence threshold of 0.3, masking out the dark red area. Fringes and rapid colour differences in the interferogram should translate into displacements in the unwrapped image. The speckle in the interferograms relates to noise, mainly consisting of water bodies, glaciers and snowy mountain tops.

Some large deformations are found in glacier areas. However, these values should not be

Figure 28: Footprint of the ascending (red) and descending (blue) path for the AOI Imja Lake (yellow)

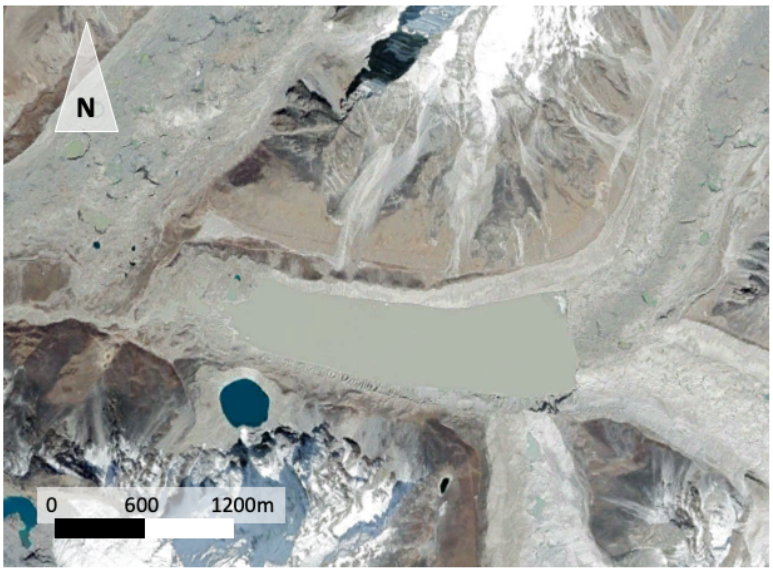

Figure 29: Google Earth Image (October 2019) of the AOI Imja Lake

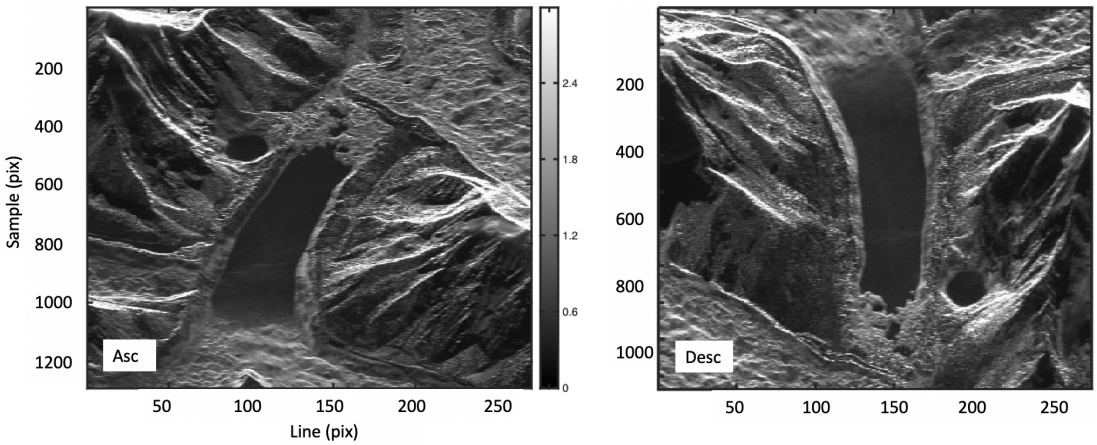

Figure 30: Ascending and descending reflectivity map of Imja Lake

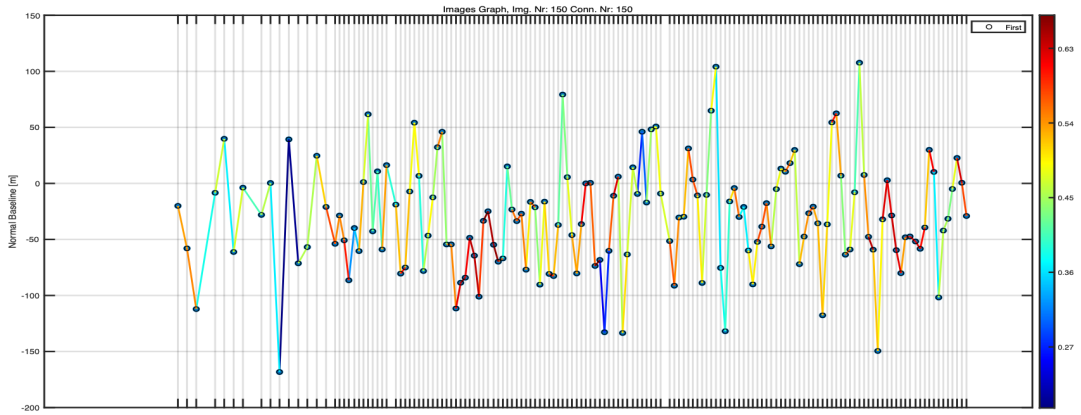

Figure 31: Small temporal baseline graph (ascending)

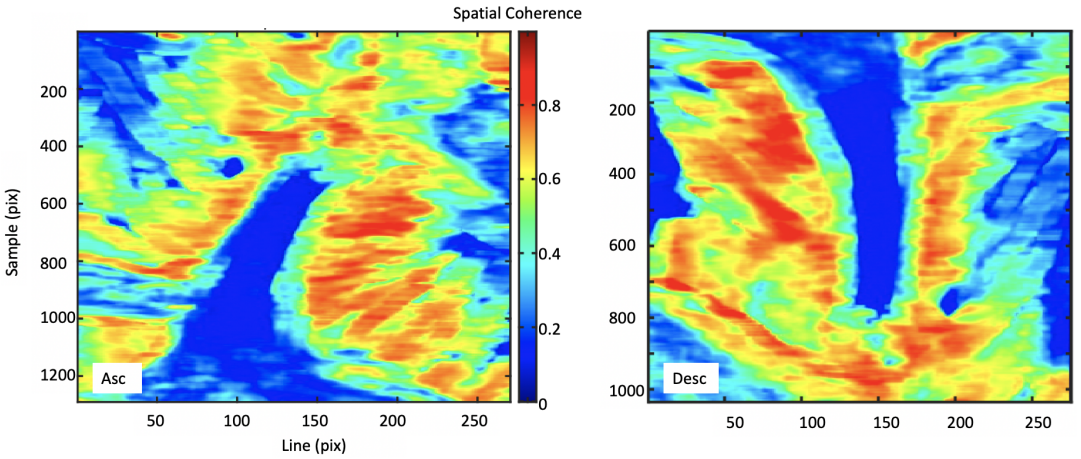

Figure 32: Ascending and descending spatial coherence map at Imja Lake

considered accurate. As section 3.2.1 explained, CDInSAR behaves poorly in regions with sharp phase boundaries or low coherency. Such regions consist of glacier boundaries, where a significant difference in deformation rate arises between a glacier and an adjacent stable slope. In addition, the temporal coherence significantly decreases at mountain slopes covered in snow. The glaciers and mountain tops in Figures 34 and 35 show that the regions are either incoherent or unwrapped incorrectly. Increasing the spatial coherence threshold could eliminate such areas. However, it will also lose relevant displacement information in challenging areas such as at the end moraine; therefore, the threshold is kept at a low value.

3.3.2 PSI

The ASI threshold (Equation 7) for finding PSC has been set to 0.5. This value is relatively low, but since the area is subjected to seasonal precipitation and melting a low value is necessary to obtain many points. Figure 37 displays the amount of PS with their temporal coherence, which is mapped in Figure 38. These figures reveal whether the area is suitable for PSI and which areas are more challenging. The temporal coherence maps show no scatterers in the water bodies, corresponding with the reflectivity maps. The end moraine, glaciers and mountain tops show significantly lower coherence values than the surrounding areas. A reference point is chosen based on its stability and temporal coherence. In this case, the reference point for the ascending set is Sample 647, Line 163, and for the descending Sample 629, Line 118. Still, it is

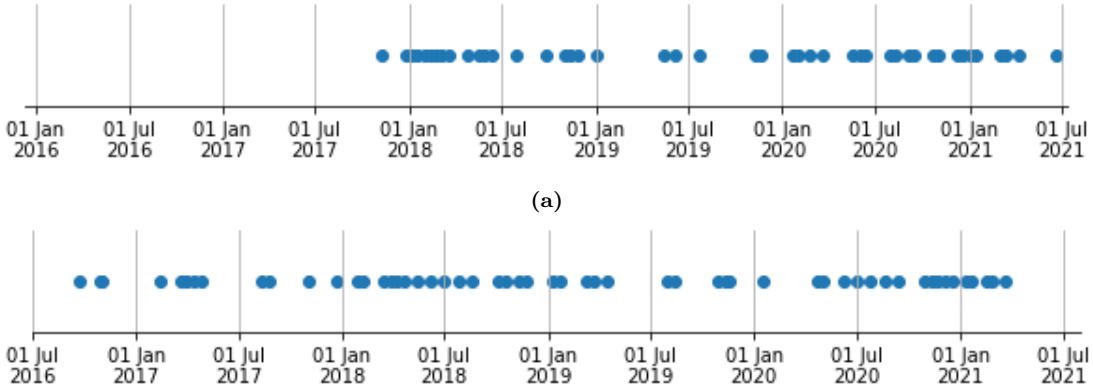

(a)

(b)

Figure 33: Time-line of coherent interferograms. (a) ascending. (b) descending.

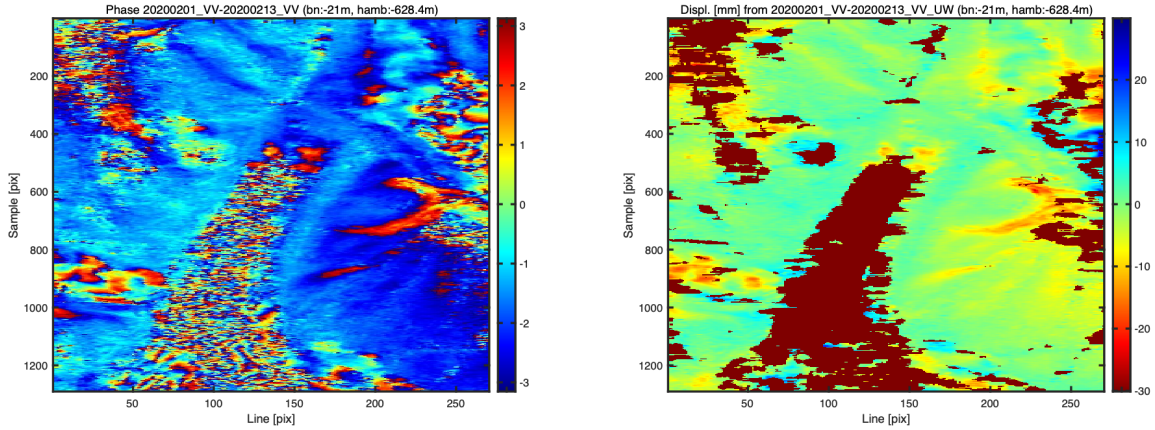

(a) **(b)**

Figure 34: Ascending interferogram between 01-02-2022 and 13-02-22. (a) wrapped phase. (b) unwrapped into displacements in mm (spatial coherence > 0.3).

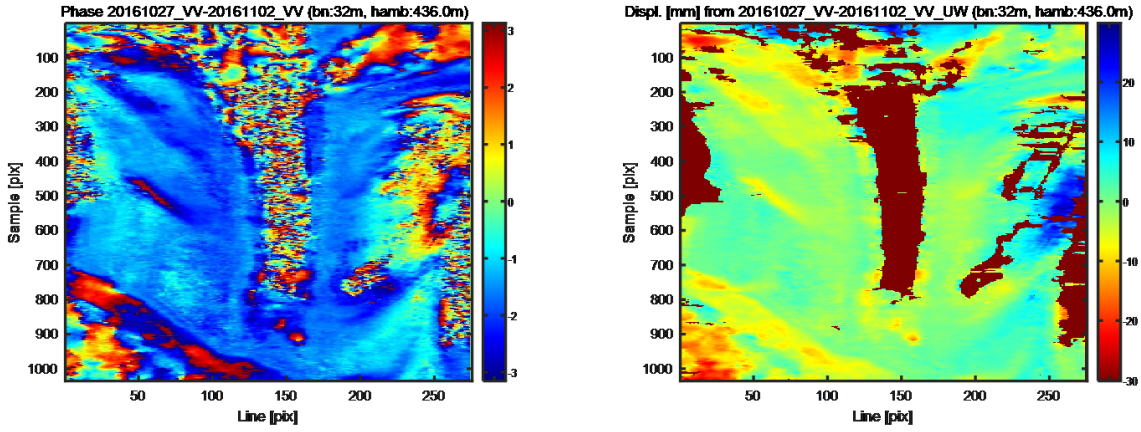

(a) **(b)**

Figure 35: Ascending interferogram between 27-10-2016 and 02-11-2016. (a) wrapped phase. (b) unwrapped into displacements in mm (spatial coherence > 0.3).

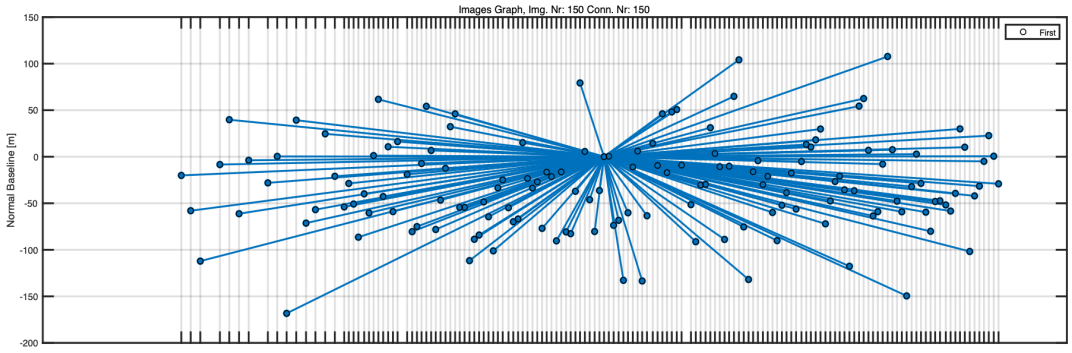

Figure 36: Star graph for Imja Lake (ascending)

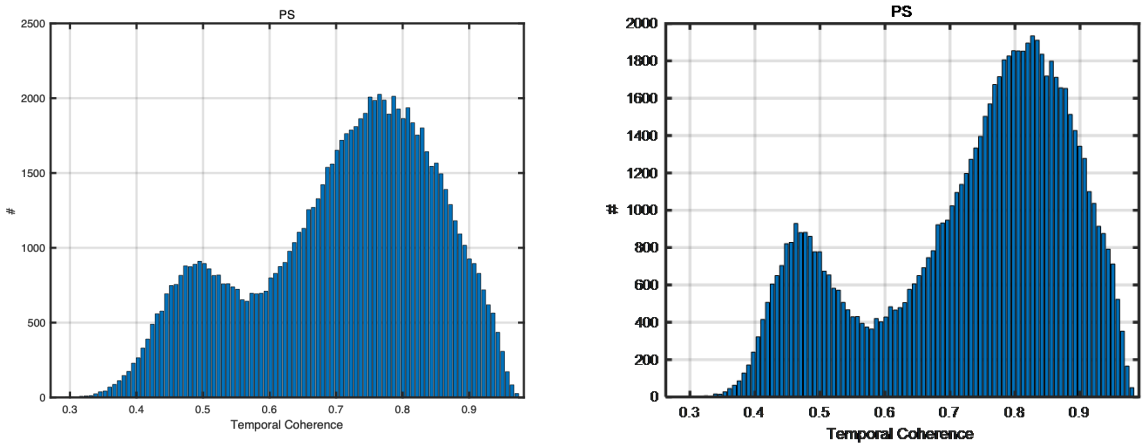

(a) **(b)**

Figure 37: Temporal Coherence graph of PS at Imja Lake. (a) ascending. (b) descending.

essential to check the final displacement results whether indeed a stable point has been taken as the reference point. If a moving point were chosen, whole areas would be moving incorrectly. Checking different reference points and adding geomorphological analysis to assess the logic and possibility of obtained displacements can prevent choosing an unstable point. The spatial and temporal coherence graphs and maps are additionally used for applying thresholds when plotting values. For example, a higher coherence threshold can be applied if the AOI shows high overall coherence, which will increase the accuracy of the final results.

Figure 39 displays the cumulative displacements obtained with PSI. In this case, the results are plotted with a temporal coherence threshold of 0.65. Areas without PS consist of the lake body, glaciers and all-year-round snow. As mentioned in section 3.2.2, high deformation rates can cause aliasing or decorrelation. Therefore, most glacier regions do not show PS, just as fast-moving parts of the moraine. The points on the glacier should not be considered accurate due to aliasing, but the results do prove that the region is deforming fast. Moreover, areas covered in thick snow also do not show PS, as they lost coherence. Figure 40 displays the decomposed displacements in east-west and up-down directions, plotted in a geographical coordinate system. Positive values correspond to eastward and upward movement.

3.3.3 Comparison and time series

The unwrapped interferograms in Figure 34 and 35 show slightly higher spatial coverage than the PSI cumulative displacement maps in Figure 39. However, the unwrapped interferograms

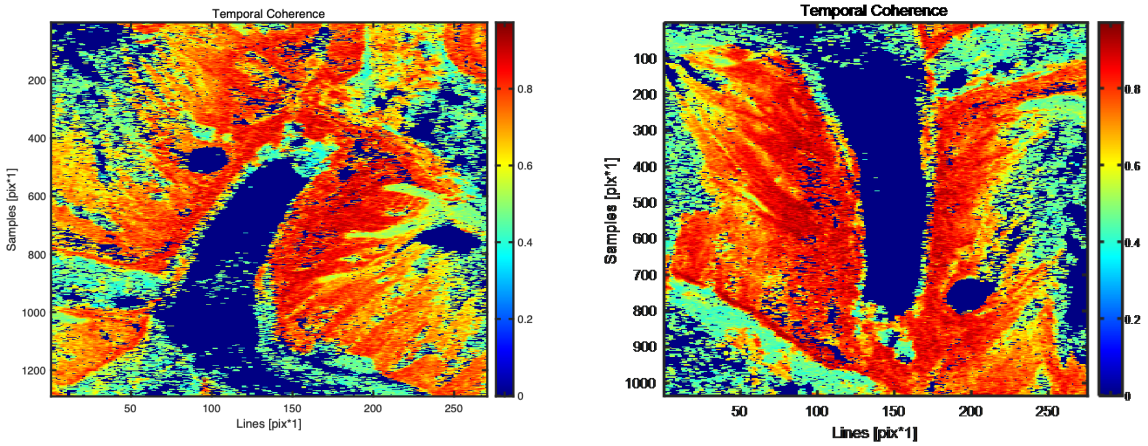

(a) (b)

Figure 38: Temporal coherence map of PS at Imja Lake. (a) ascending. (b) descending.

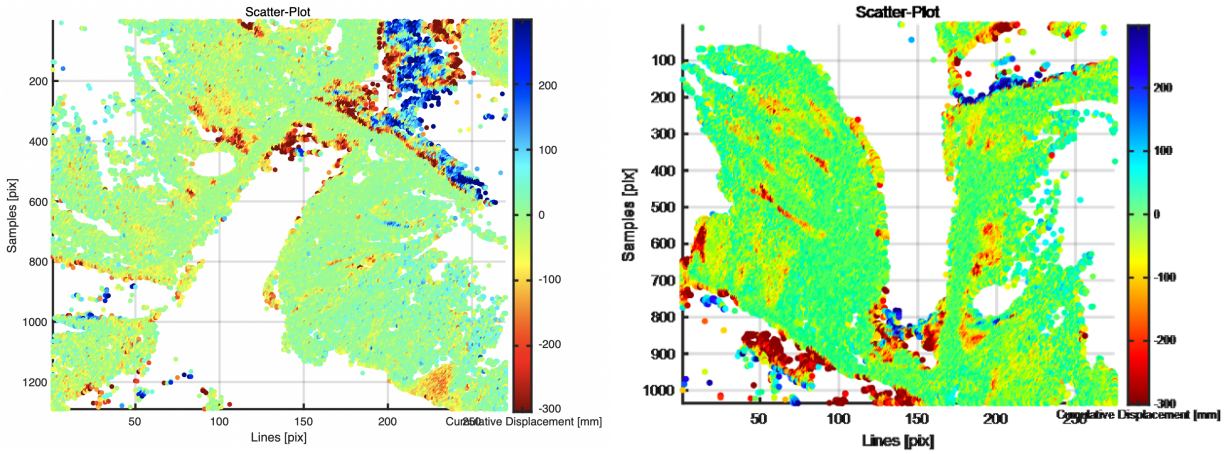

(a) (b)

Figure 39: PSI cumulative displacement scatter plots (temporal coherence > 0.65). (a) ascending. (b) descending.

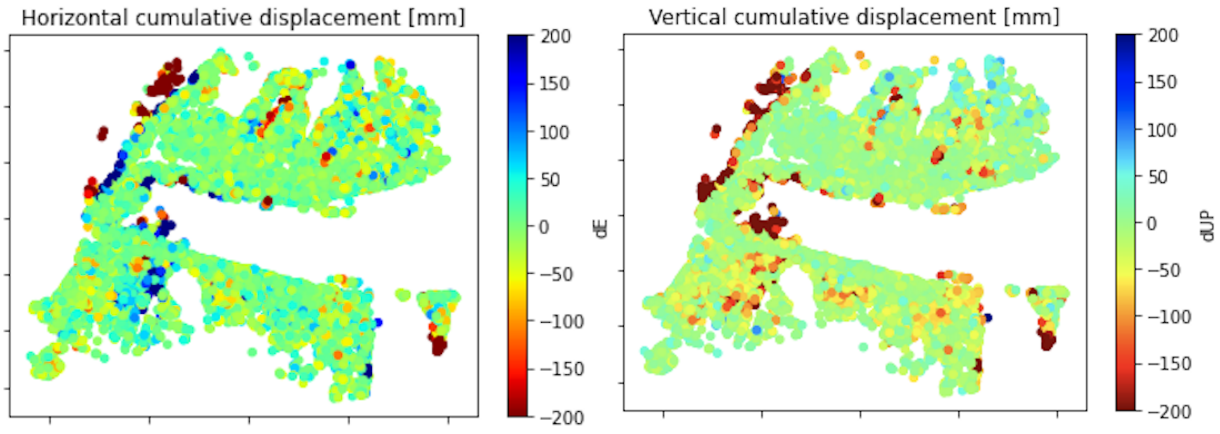

(a) (b)

Figure 40: Decomposed displacements (temporal coherence > 0.65). (a) horizontal (east-ward). (b) vertical (upward).

also show incorrect unwrapping at glacier and snow areas. In addition, the timelines show that the coherent CDInSAR results are not continuous over time, decreasing the temporal coverage. Nevertheless, both methods reveal similar displacements on the slopes and end moraine.

To validate and compare the DInSAR methods in detail, single PS have been compared using the CDInSAR and PSI approach. Both methods have generated time series using the same reference points for moving and stable PS. PSI generates a continuous time series, but as CDInSAR is often incoherent, this method does not return a continuous series, so instead of cumulative displacement time series, velocity time series have been constructed. Since the temporal baseline differs throughout the timeline, the displacement time series has been translated from millimetre per 6, 12 or 24 days to metre/year. Figure 41 displays the locations of the nine points used for the analysis. Ascending points 1 to 3 lie near the reference point and are in a stable area that is not experiencing large deformation. Ascending points 4 to 6 lie on the end moraine, in an area experiencing large negative displacement in both ascending and descending LOS. Descending points 7 to 9 lie on a rock glacier exhibiting seasonal deformation and negative displacement for both ascending and descending orbit. Figures 42 to 50 display the cumulative displacement time series in (a) and velocity time series in (b) at each point. The cumulative displacement time series were obtained with PSI; the scatters correspond to measured displacements and the line to the displacement model. The Temporal coherence value in the title indicates how well the scatters match with the line following the displacement model. The velocity time series display scatters corresponding to the displacement rate using the CDInSAR and PSI method. STB in the images refers to the short temporal baseline graph used for the CDInSAR approach.

The velocity series coincide roughly in displacement direction and magnitude, but they do not precisely overlap. Various reasons could cause this difference. First, the CDInSAR and PSI points can lie some 20 metres apart, since roughly this threshold has been used to match points. Second, whereas PSI calculates separate points, CDInSAR unwraps spatially, considering the area nearby, and errors might propagate throughout the region caused by atmospheric contributions or nearby incoherent areas. In addition, the atmospheric influence differs for both approaches. Finally, constructing the velocity time series provides an additional check to remove incorrectly unwrapped interferograms skipped in the first removal round using visual output. For example, a CDInSAR velocity value on a specific date lying far from the corresponding PSI value at every location might indicate an incorrectly unwrapped interferogram. Subsequently, these images have also been removed from the stack. Now all remaining images contain seemingly correctly unwrapped displacements, at least in the investigated areas of interest.

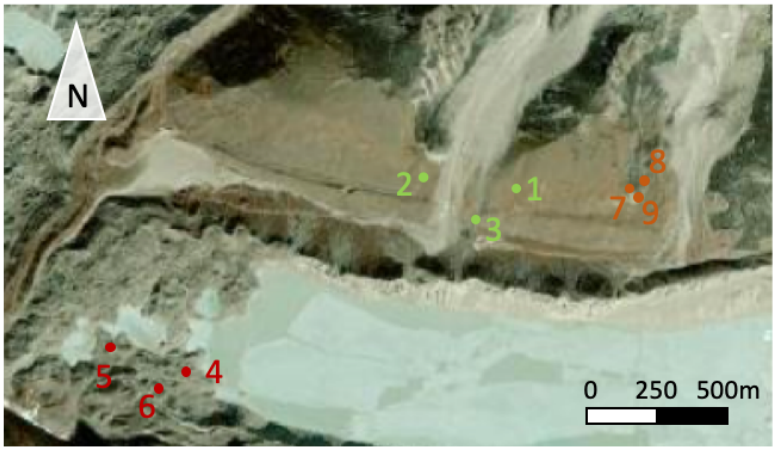

Figure 41: Locations of the points used for the time series comparison

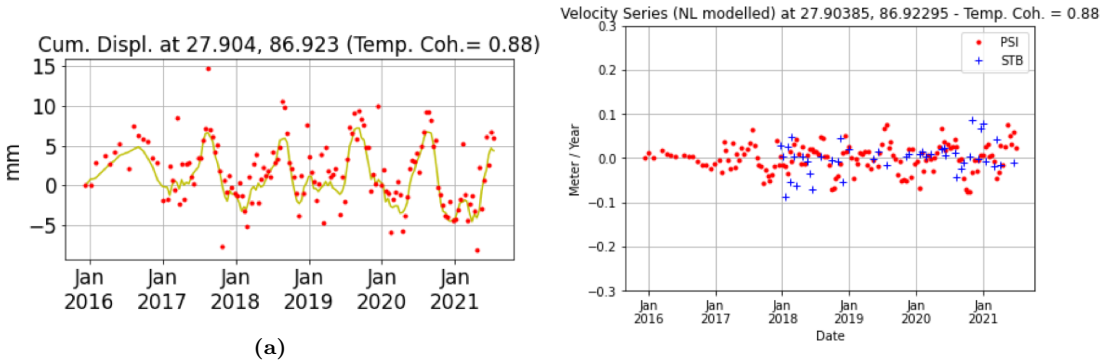

(a) (b)

Figure 42: Deformation at a stable area (Ascending point 1). (a) Cumulative displacement time series (PSI). (b) Velocity series.

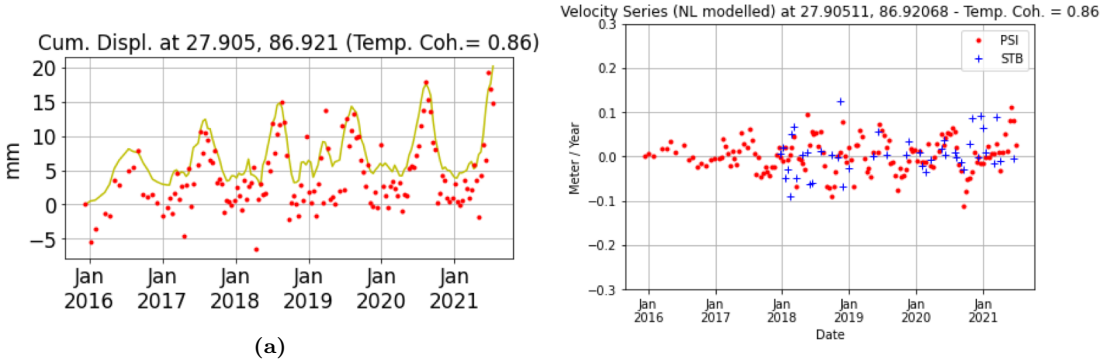

(a) (b)

Figure 43: Deformation at a stable area (Ascending point 2). (a) Cumulative displacement time series (PSI). (b) Velocity series.

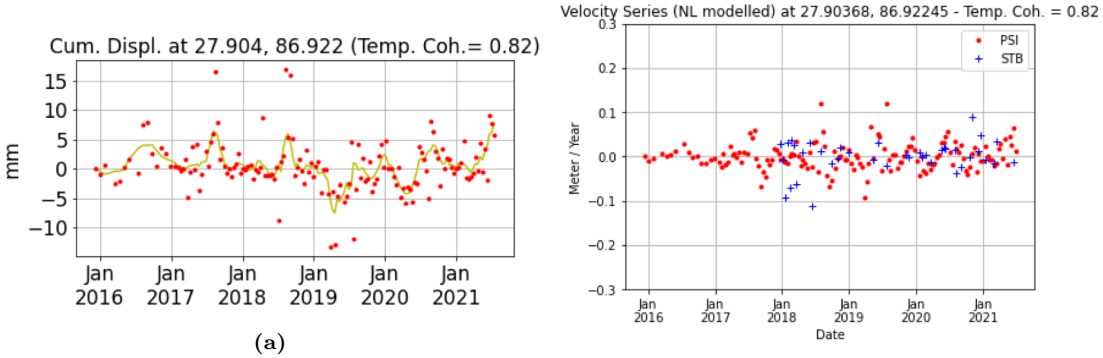

(a) (b)

Figure 44: Deformation at a stable area (Ascending point 3). (a) Cumulative displacement time series (PSI). (b) Velocity series.

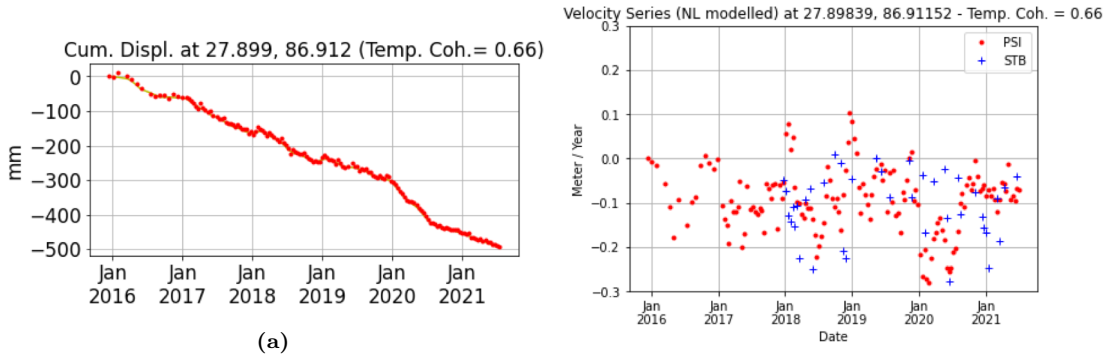

(a) (b)

Figure 45: Deformation at the end moraine (Ascending point 4). (a) Cumulative displacement time series (PSI). (b) Velocity series.

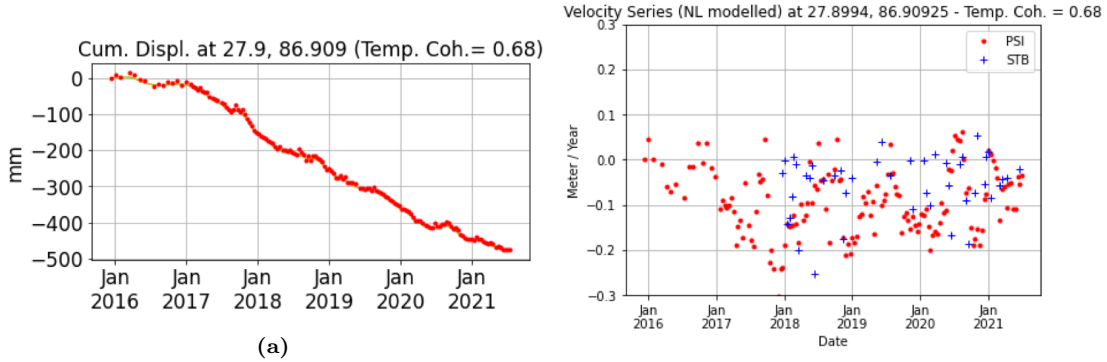

(a) (b)

Figure 46: Deformation at the end moraine (Ascending point 5). (a) Cumulative displacement time series (PSI). (b) Velocity series.

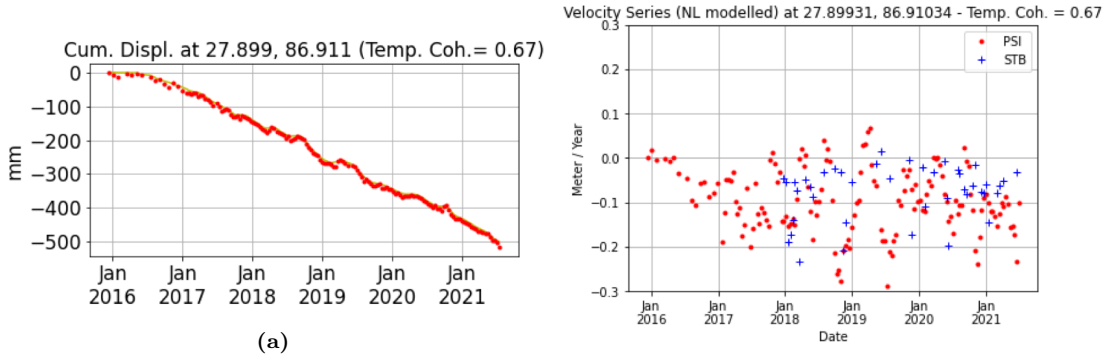

(a) (b)

Figure 47: Deformation at the end moraine (Ascending point 6). (a) Cumulative displacement time series (PSI). (b) Velocity series.

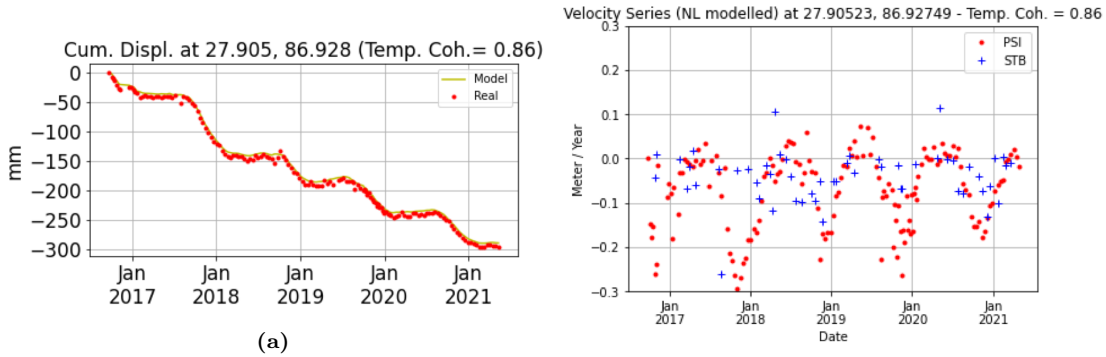

(a) **(b)**

Figure 48: Deformation at the end moraine (Descending point 7). (a) Cumulative displacement time series (PSI). (b) Velocity series.

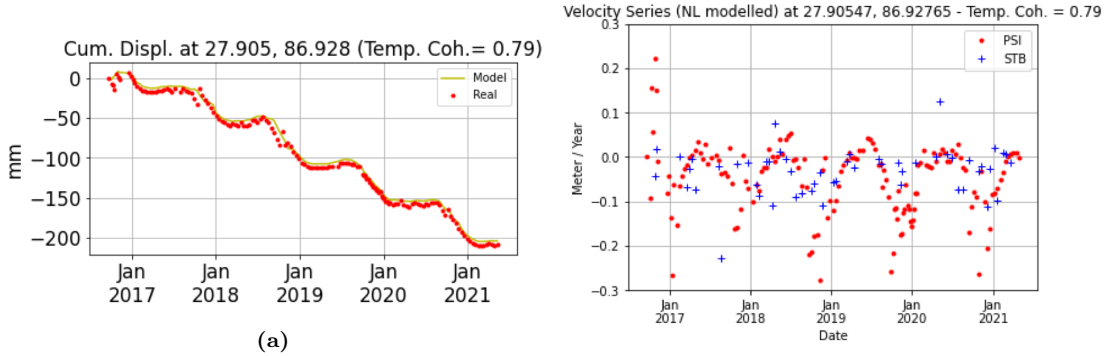

(a) **(b)**

Figure 49: Deformation at the end moraine (Descending point 8). (a) Cumulative displacement time series (PSI). (b) Velocity series.

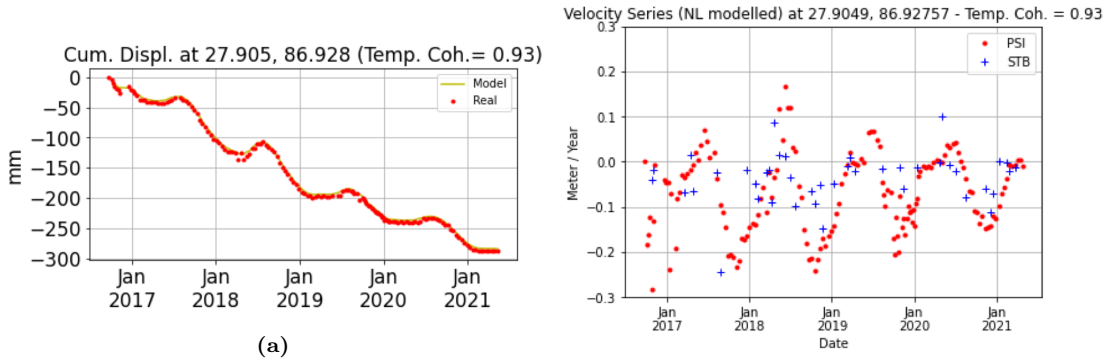

(a) **(b)**

Figure 50: Deformation at the end moraine (Descending point 9). (a) Cumulative displacement time series (PSI). (b) Velocity series.

4 Integrated analysis

This research aims to investigate the potential of InSAR as a glacial lake monitoring tool by analysing physical phenomena and associated hazards at the six glacial lakes. InSAR-based displacements must be interpreted by integrating geomorphological, topographical, optical and meteorological data sources to determine how InSAR observations contribute to analysing and monitoring potentially dangerous glacial lakes. Combining these data sources can provide a better insight into deformation causes and relate them to features such as permafrost degradation, lithology, glacial retreat and water infiltration. Consequently, the trigger mechanisms of displacements can be determined; these are necessary to link deformations to (future) GLOF risks (Klimeš et al., 2016; Scapozza et al., 2019). Furthermore, combining different data sources can support the validation of the InSAR results, explain InSAR-related limitations and demonstrate InSAR's capability of analysing GLOF-related phenomena at glacial lakes. This chapter describes which data sources are integrated with InSAR displacements, the methodology adopted to interpret the displacements, and the final results after integrating InSAR with these additional data sources.

4.1 Methodology

Geological maps, geophysical surveys, meteorological data, optical imagery and topographical analyses have been used to interpret the InSAR observations. These information sources support the interpretation of geomorphological phenomena and InSAR-based displacements and help define the limits of applying InSAR. Geological maps are often constructed during site visits and display features such as lithology, fault structures and scree debris. Figure 51 shows an example of a detailed geological map. Site visit studies, including thermokarst investigations and geophysical surveys, can indicate subsurface features. Thermokarst features are topographic depressions created in various shapes and sizes due to thawing ground ice. With geophysical surveys, cross-sections can be generated to analyse moraine ice presence and lithology, which can support the interpretation of InSAR displacements at the moraine. The data sources used to interpret the InSAR observations are listed in Table 4.

As explained in section 2.2, events such as extreme weather, earthquakes or anthropogenic activities can influence the geomorphology and induce displacements. Therefore, event timings might aid in identifying correlations between displacements and such episodes. Precipitation and temperature significantly influence slope response and moraine degradation, and most GLOFs have occurred during the summer after heavy rains and high temperatures (Falátková, 2016; Kahlon et al., 2014). That is why precipitation and temperature data are used to find connections between displacement time-series and weather events. In addition, the variation in temperature and precipitation between the six study areas might explain the differences observed between the lakes. For example, seasonal displacements might be more apparent at specific lakes, and

Data	Source
Digital elevation models (DEMs)	National Snow & Ice Data Center (NSIDC): High Mountain Asia (HMA) 8m DEM
	OpenTopography: AW3D30 30m DEM
Temperature and precipitation data	Meteomatics
Optical imagery	Sentinel Hub: Sentinel-2 images
	Google Earth
	Esri
	Earth Observing System (EOS)
Geological maps, geophyscial and other in situ surveys	Literature
	Government reports

Table 4: Data sources used for integrating the InSAR observations

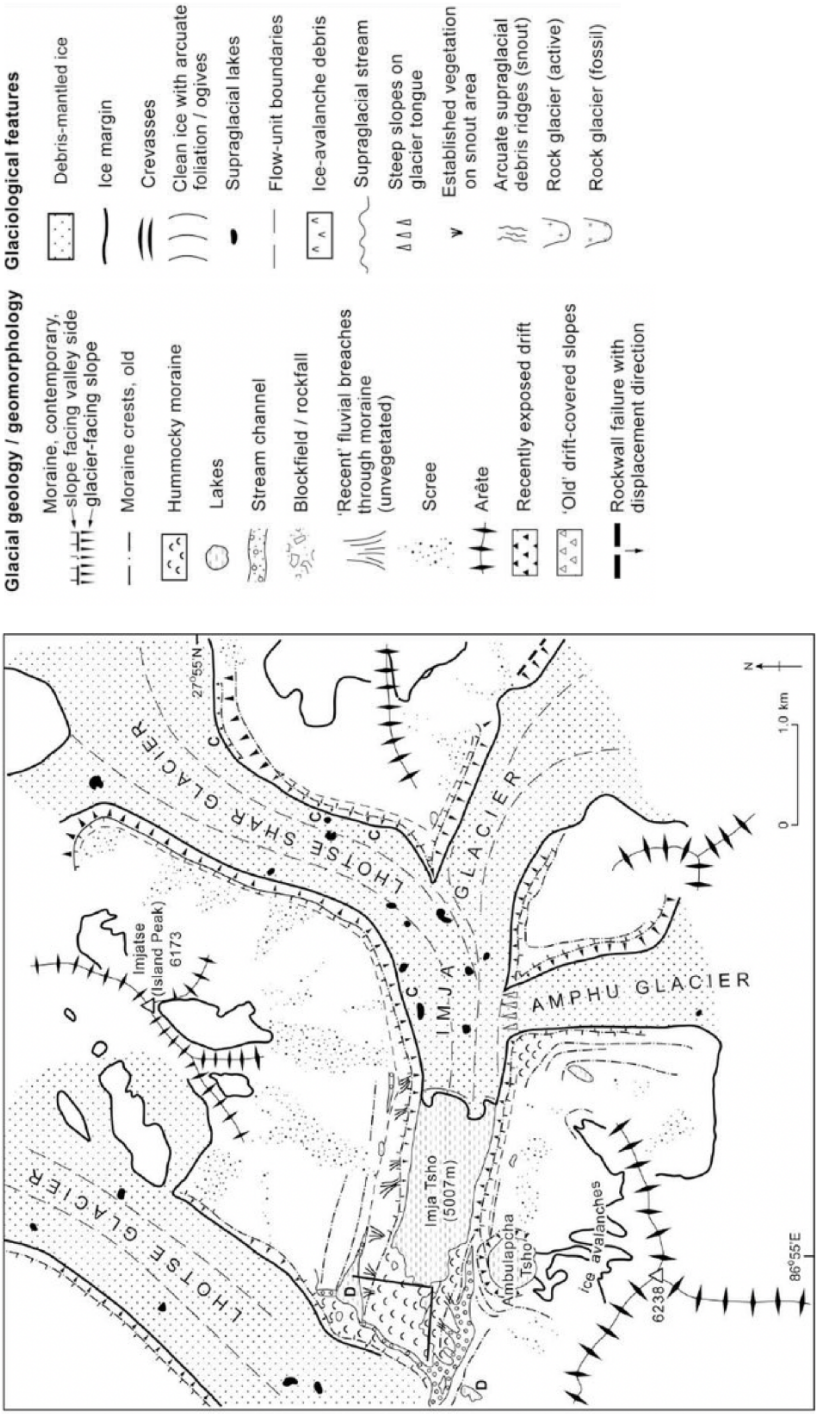

Figure 51: A geological map at Imja Lake (Hambrey et al., 2008)

InSAR's applicability might be limited for those lakes receiving more precipitation. Hourly temperature and precipitation data from Meteomatics, a private weather data company, was used for this study. The weather data is based on various data sources, combining interpolation models, satellite data and in situ measurements (Meteomatics, 2021). Figure 52 displays the temperature and precipitation at Imja Lake, modelled to weekly and monthly values. The weather data for the other lakes can be found in Appendix D. Moreover, earthquakes can induce displacements by destabilising slopes, relocating boulders and producing waves. Research at glacial lakes after the large Gorka earthquake in 2015 revealed the effects of that event (Byers et al., 2017), enabling using that information. However, the influences of more minor earthquakes are complex and are out of this research's scope. Third, human activities and artificial measures, such as moraine reinforcement or lake drainage, could explain increased or decreased deformation in the moraine dam.

As mentioned in the introduction, glacial lakes are often inaccessible and dangerous to visit, especially in the Himalaya. As a result, geological maps and site surveys are scarce. Therefore, just as why using satellite radar is convenient to analyse physical phenomena, remote sensing tools are also necessary to obtain information other than displacements at these lakes. The following sections will explain how remotely sensed optical imagery and topographical data are applied to obtain geomorphological features and interpret the InSAR results.

4.1.1 Optical imagery

With optical imagery InSAR observations can be linked to visible surface features explaining certain geomorphological phenomena or InSAR's limitations related to surface features. This paragraph will explain what optical imagery is, how it is acquired, and how it is integrated into this research. In this case, optical imagery is images of the earth's surface formed using the visible light spectrum. The visible light spectrum is the segment of wavelengths visible to the human eye. These wavelengths range from 100 nm to 1 mm and include ultraviolet, visible and

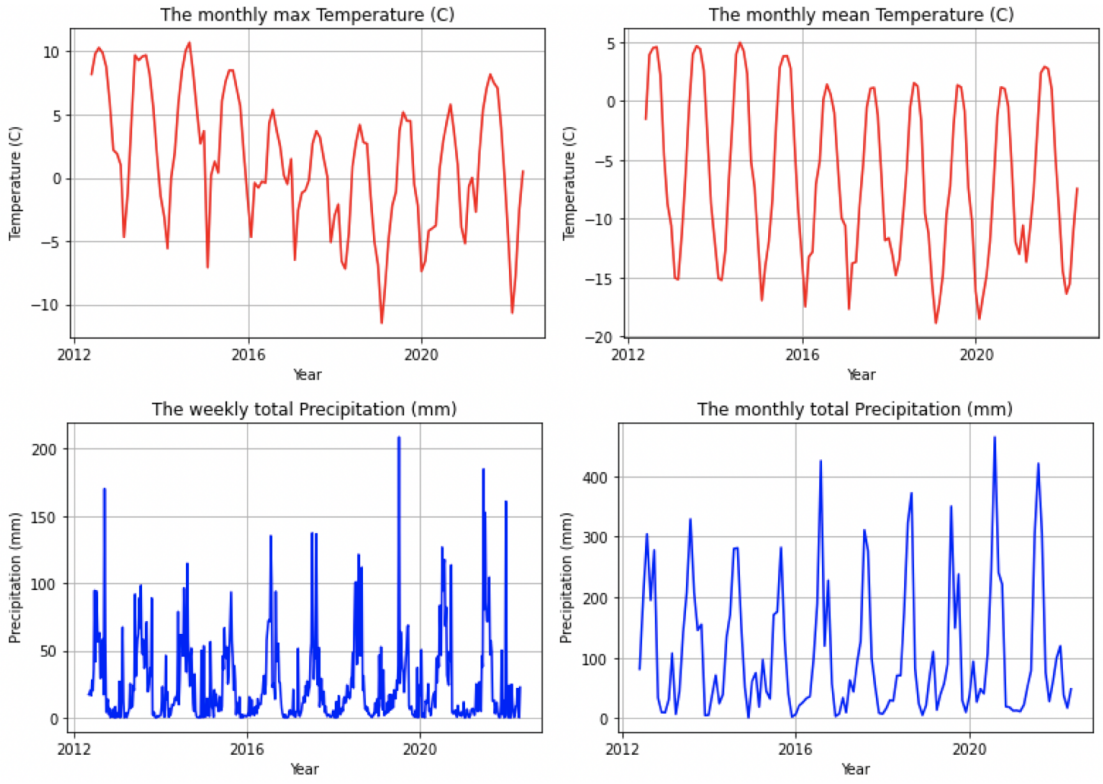

Figure 52: Temperature and precipitation data at Imja Lake

infrared light. Optical images can be used for various applications, such as vegetation monitoring, land cover mapping, urban planning, disaster mapping and water pollution. Regarding glacial lakes, optical imagery can reveal surface covers and their seasonal variations and distinguish scree debris, landslide scars, (rock) glaciers, thermokarst lakes and outlet channels. Such observations could explain the InSAR results and link them to GLOF hazards. For example, InSAR might be not or less applicable to regions covered by snow and vegetation, and InSAR deformations could be linked to visible rock glaciers and landslide scars. CORONA, SPOT, Landsat and Sentinel-2 are examples of optical imagery satellites. Landsat and Sentinel-2 images are publicly available, with a resolution of 10-60 m. Google Earth often acquires images from private satellite companies, such as Maxar and Airbus Intelligence, providing very high resolution up to 30 cm. This study uses Esri maps, Sentinel-2 images, Google Earth and photographs as optical imagery. Esri is a geographic information system (GIS) company that supplies various pre-made maps covering the world's surface, and the use of Sentinel-2 images and Google Earth will be explained below.

The Sentinel-2 satellite carries a 10-60 m resolution multispectral imager with 13 spectral bands, listed in Table 5. The bands consist of ultra-blue, blue, green, red, visible-and-near-infrared (VNIR) and short-wavelength infrared (SWIR) bands. The red, green and blue channels form true-colour images. Figure 53 displays the sensitivity of surface types towards specific wavelengths in the visible (VIS), VNIR and SWIR range. A high reflectance value (towards 1) means that the surface greatly reflects that wavelength, whereas a low value means the surface absorbs that wavelength. For example, the figure reveals that water absorbs all wavelengths and ice and snow reflect VIS, VNIR and less significantly SWIR bands. Vegetation poorly reflects the VIS spectrum but highly reflects VNIR bands. The various bands can be assigned to colours so that a high reflectance of a specific surface type to a particular wavelength will display that colour. Features reflecting all bands will appear white. Conversely, surface types absorbing all wavelengths, such as water bodies, will turn out black. By combining different bands, 'false-colour' images are generated, highlighting specific features. Table 6 shows commonly applied band combinations, where the name refers to the application. In this report, the geology, moisture index, NDVI, SWIR, true colour and vegetation combinations have been used as they proved to highlight relevant features at glacial lakes well. The surface conditions change significantly throughout the year and are lake dependent, influencing the choice of the most convenient band combination. The agriculture, bathymetric and urban band do not add useful information in the case of glacial lake areas. Figure 54 displays the used band combinations at Imja Lake. The paragraph below will explain the colours' meaning and the band combinations' applicability using tables 5 and 6 and Figure 53.

Figure 54a displays a natural colour image; the VIS red band (B4) is shown in red, the VIS green band (B3) is shown in green, and the VIS blue band (B2) is shown in blue. This band combination reflects the natural colours visible to the human eye. The challenges with this combination are distinguishing snow and clouds and observing vegetation. Snow and clouds both reflect the VIS bands, and vegetation does not sufficiently reflect the VIS bands (even the green band).

Figure 54b uses the false-colour geology combination; the B12 SWIR band appears red, the B11 SWIR band in green and the B2 blue band in blue. Snow and ice absorb the SWIR bands but reflect the blue bands, so they appear bright blue (cyan), whereas clouds reflect all bands, appearing white. Each rock type reflects SWIR bands differently, enabling to map out geology by using multiple SWIR bands. Since the glacial lake does not consist of clear water but suspended sediment, the lake will still reflect wavelengths instead of absorbing each band and appearing black. This combination clearly distinguishes snow and ice from scree debris, bedrock outcrops from debris and clean glacier ice from debris-covered ice.

Figure 54c displays the moisture index, which is the ratio between the VNIR B8a and SWIR B11 bands. This ratio is often used to map water stress and water content in vegetation. Water should absorb both bands, so a small value relates to very high moisture content, and a high value means very low moisture content. High moisture is set to dark blue, and low moisture

Band	Resolution	Central Wavelength	Description
B1	60 m	443 nm	Ultra blue (Coastal and Aerosol)
B2	10 m	490 nm	Blue (VIS)
B3	10 m	560 nm	Green (VIS)
B4	10 m	665 nm	Red (VIS)
B5	20 m	705 nm	Visible and near-infrared (VNIR))
B6	20 m	740 nm	Visible and near-infrared (VNIR))
B7	20 m	783 nm	Visible and near-infrared (VNIR)
B8	10 m	842 nm	Visible and near-infrared (VNIR)
B8a	20 m	865 nm	Visible and near-infrared (VNIR)
B9	60 m	940 nm	Short-wave infrared (SWIR)
B10	60 m	1375 nm	Short-wave infrared (SWIR)
B11	20 m	1610 nm	Short-wave infrared (SWIR)
B12	20 m	2190 nm	Short-wave infrared (SWIR)

Table 5: Sentinel-2 bands (GISGeography, 2021)

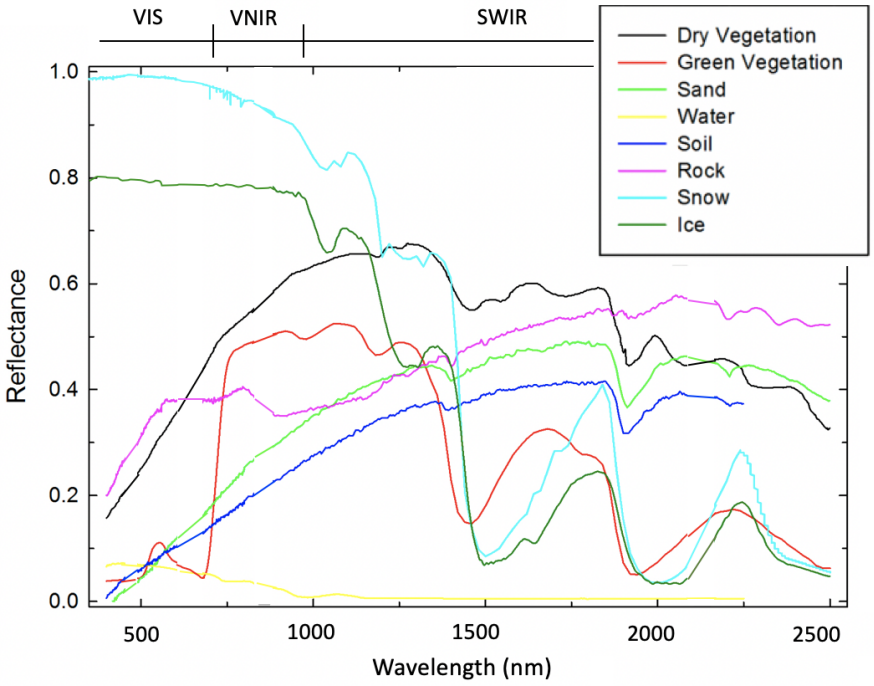

Figure 53: Typical spectral reflectance curves for vegetation, sand, water, soil, rock, snow and ice in the visible (VIS) blue, green, red, visible and near-infrared (VNIR) and short-wave infrared (SWIR) range. Image adjusted from Tian and Sun (2016)

Name	Combination of red, green, blue (RGB)
Agriculture	B11, B8, B2
Bathymetric	B4, B3, B1
Geology	B12, B11, B2
SWIR	B12, B8a, B4
True colour	B4, B3, B2
Urban	B12, B11, B4
Vegetation	B8, B4, B3
	Index calculation
Moisture index	(B8a-B11)/(B8a+B11)
NDVI	(B8-B4)/(B8+B4)

Table 6: Common Sentinel-2 band combinations and indexes (GISGeography, 2021)

content is set to red. Consequently, this index shows the water, clean ice and snow bodies as dark blue, clouds as lighter blue, and the debris-covered glacier only blue in areas that do not contain debris. In addition, wet vegetation would also appear blue in the case of denser vegetation (which is not the case for Imja Lake). Snow, water bodies and wet vegetation significantly change the dielectric constant, affecting the applicability of InSAR, as explained in sections 3.1.1 and 3.1.3, so using this index is relevant for this research. Rocks and dry soils will appear red. However, areas consisting of glaciers and possible water runoff paths appear yellow, indicating a higher moisture content than the rest of the area. Consequently, besides mapping stream networks with a DEM, the moisture index can also reveal drainage paths.

Figure 54d shows the SWIR combination, which maps the B12 SWIR band as red, the B8a VNIR band as green and the B4 VIS red band as blue. VNIR bands reflect vegetation very well, corresponding with green on the image, and reflects significantly better than the VIS green band (as observed in the true colour image in (a)). Mapping vegetation is relevant since it can prevent the application of InSAR, causing temporal correlation, as explained in section 3.1.3. Snow and ice primarily reflect the VIS bands well, consequently appearing cyan. The clouds are reflecting all bands, turning out white. Clean water bodies appear black, and because of the SWIR band only reflecting certain rocks, some rock outcrops appear red, whereas debris and moraine appear more beige/grey.

Figure 54e presents the Normalised Difference Vegetation Index (NDVI) index, which denotes the ratio between the VNIR B8 and the red VIS B4 bands. This index is applied chiefly to map vegetation density. VNIR reflects the chlorophyll in vegetation, resulting in a high reflectance value, whereas vegetation does not reflect the red band, resulting in a very low value. As water does not reflect both bands, both values will be small, so the ratio will also be small, and as both bands reflect snow and ice well, both values will be high, so the ratio will still be small. Negative values correspond to water (black), and values around zero (red) indicate bare rock, sand, ice or snow. Then yellow and brown represent very light shrubs, and light blue indicates slightly denser shrubs or low vegetation, with green (not present in this image) corresponding to dense vegetation. The NDVI clearly shows the vegetated areas and is, therefore, a helpful method for distinguishing even very light vegetation.

Finally, Figure 54f displays the false-colour vegetation combination where the VNIR B8 band is mapped as red, the red VIS band as green and the green VIS band as blue. This combination is commonly used to assess vegetation density and health and their variations over time. Healthy vegetation contains more chlorophyll, which highly reflects the VNIR B8 band and turns out bright red using this combination. Scree and debris turn out beige or light-brown to brown, clean water bodies appear black, less clean water bodies (such as the glacial lake) appear lighter blue and snow and clouds appear white. For the application to glacial lakes, this combination was more challenging to distinguish vegetation from no vegetation than the SWIR combination

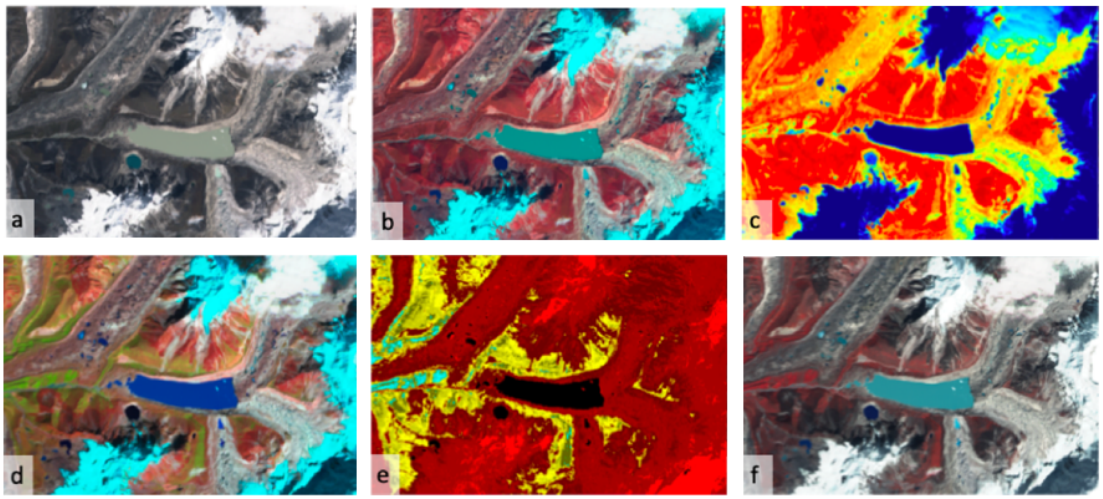

Figure 54: Sentinel-2 images of Imja Lake (September 2020) using the different band combinations listed in Table 6. (a) True/natural colour. (b) Geology. (c) Moisture index. (d) SWIR. (e) NDVI. (f) Vegetation.

in Figure 54d, or the NDVI in Figure 54e, as the contrast between red and brown is not always apparent. However, this combination clearly distinguishes rock, debris and moraine, making it a suitable combination focussing on geological features. Furthermore, clouds are not distinguished from snow, reflecting the VNIR and VIS bands.

The SWIR and NDVI band combinations were most convenient for mapping the scarce vegetation in the glacial lake areas. The false-colour vegetation combination might be more useful in areas with abundant vegetation, focusing on vegetation health and density. The geology and SWIR combinations are the most suitable for distinguishing snow and ice from clouds. For distinguishing vast rock from scree debris, the false colour vegetation and geology index turned out to be the most suitable combinations. Furthermore, since the moisture index will highlight snow, ice, water, wet vegetation or rock and (rain) clouds, this index can indicate SAR's applicability in specific regions or during certain periods. More optical imagery can be found in Appendix E.

The primary advantages of Sentinel-2 imagery are the ability to use different wavelengths to highlight certain surface features, the high temporal global coverage and that it can be freely downloaded so the images can be plotted with DEMs and stream networks in GIS software. A disadvantage involves the resolution of 10-60 m; small objects cannot be seen, and zooming in will blur the image. Adding Google Earth imagery and on-site photographs form a solution for this problem as they can have resolutions up to centimetres. A disadvantage is that the relief is slightly flattened when using the Google Earth application in 3D; slopes appear less steep, and moraines appear less hummocky and high. On-site photographs are of great value since they can have a high resolution and do not flatten the area. However, GIS software cannot use on-site photographs, and they are not available for every glacial lake. In conclusion, using different optical imagery sources is desirable to obtain as many details as possible.

4.1.2 Topographical analysis

Topographical data refers to the elevation and relief of surfaces. Especially in the mountains where significant topographic variations occur, the topography will significantly influence geomorphological features and InSAR's application. This section will first describe elevation data and how it can provide relevant information such as slope angle, slope aspect and drainage paths. Second, this section explains how slope angle and slope aspect are integrated with InSAR data to map geometric limitations and project displacements along slopes.

DEM applications

While the topography was usually depicted by contour lines on maps in the past, the topography is now often digitalised, generating DEMs. A DEM is a continuous topographic representation of the earth. The term DEM is often used as a generic term for digital surface map (DSM) and digital terrain map (DTM), where DSM is the topography including buildings and other objects, and DTM is the surface without objects. DEMs can be derived through photogrammetry, light detection and ranging (LiDAR), InSAR or land surveying. Photogrammetry uses aerial photograph pairs, and LiDAR and InSAR use the time it takes for a laser or radar signal to return to the antenna. The elevation over the area can be retrieved using photographs, laser beams and radar waves from different angles (Li et al., 2004). A grid with rows and columns is filled with pixels containing elevation values. Figure 55 displays an example of a DEM grid with equally spaced values. A continuous elevation map can be generated by performing interpolation between the cells.

The DEM accuracy depends on various factors such as surface conditions during measuring like terrain roughness and vegetation, and instrumental aspects such as sampling density, grid resolution, interpolation algorithms and vertical resolution (Szypula, 2019). Several DEMs exist, containing different resolutions and coverage. This thesis uses the ALOS World 3D-30m (AW3D30) and High Mountain Asia (HMA) DEMs. The global coverage AW3D30 DEM was generated with photogrammetry in 2017 by Japan Aerospace Exploration Agency (JAXA) and is 30 m accurate. The 8 m accurate HMA DEMs cover several parts of the Himalayas and were generated between 2002 and 2016 using high-resolution imagery from DigitalGlobe satellites. Often, especially in rural locations, DEMs contain no-data patches (Figure 56a). These patches can be filled by interpolating surrounding data points. However, the depth of glacial lakes is challenging to measure. Therefore, DEM techniques are not applicable for measuring below the surface of these lakes, and the lakes usually appear as no-data patches or contain incorrectly interpolated elevation data. Relief has been applied to distinguish surface features in Figure 56b, contouring the mountains, glaciers and lake by applying 'hillshade'. With hillshade, a light source from a certain angle is applied to create shading contours. The tool obtains the hypothetical illumination of a surface by determining illumination values for each cell in the DEM raster. In addition to creating relief, this tool is helpful for mapping geometric LOS limitations, which will be explained later in this section.

DEMs are useful for many applications, such as flight routes, urban planning, infrastructure designs, ski and hiking paths, environmental and climatic issues, river mapping, slope analysis, modelling mass movement trajectories, mountain engineering, mining and resource engineering, modelling sun illumination, remote sensing and surveying (Li et al., 2004). Topographic mapping is essential for analysing physical phenomena at glacial lakes, involving topographical

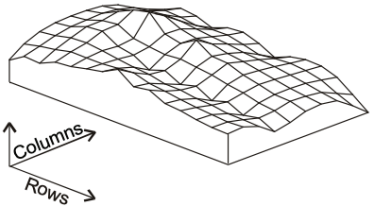

Rows \ Columns	0	1	2	3	4	5	6	7	8	9
0	50.0	62.5	70.7	74.3	75.0	75.1	73.3	67.7	55.7	45.0
1	62.7	67.4	73.5	77.0	77.7	78.6	76.6	71.0	62.0	55.0
2	60.9	70.9	77.5	84.3	84.5	88.2	82.0	74.7	67.9	63.4
3	70.0	75.3	78.9	86.1	86.9	97.5	86.6	76.7	67.5	61.5
4	71.6	75.4	76.8	75.4	77.3	99.9	89.8	76.6	64.7	55.0
5	76.3	75.0	73.7	71.8	74.5	83.2	81.8	74.9	67.2	61.6
6	79.8	76.8	71.2	61.0	72.5	79.0	77.5	72.9	67.6	63.8
7	90.3	79.1	70.1	67.3	74.4	90.0	78.0	70.9	63.5	57.3
8	76.5	73.4	65.8	58.2	71.7	77.5	74.3	68.6	58.8	48.0
9	80.0	71.5	65.6	63.2	69.7	76.2	71.1	67.1	61.2	56.0
10	70.6	68.2	62.8	53.0	65.0	69.6	67.7	65.4	62.6	60.4
11	69.3	66.6	61.9	58.6	62.2	65.6	64.5	62.9	60.9	59.1
12	65.7	64.8	59.3	50.0	57.9	60.4	60.8	59.7	56.5	53.3
13	63.3	63.1	58.9	53.8	55.5	59.7	58.5	56.2	48.0	39.3
14	62.7	64.7	58.2	44.3	48.7	55.0	56.5	53.7	40.2	25.0

Figure 55: DEM representation using a regular grid (Prodanović et al., 2009)

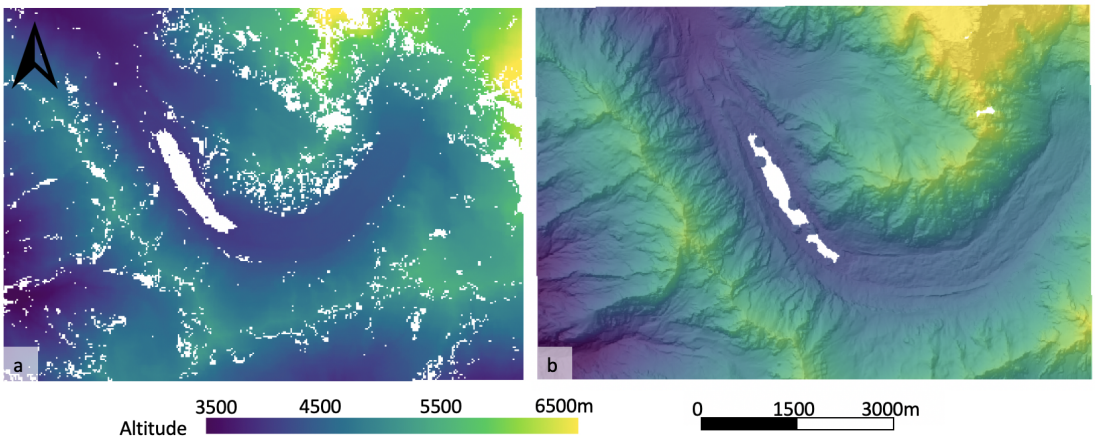

Figure 56: (a) HMA DEM of Thulagi Lake. (b) DEM with hillshade and interpolation of no-data patches

$$\text{Slope} = \arctan\sqrt{(\frac{dz}{dx})^2 + (\frac{dz}{dy})^2} \quad (10)$$

$$\frac{dz}{dx} = \frac{(c + 2f + i) - (a + 2d + g)}{8 * cellsize} \quad (11)$$

$$\frac{dz}{dy} = \frac{(g + 2h + i) - (a + 2b + c)}{8 * cellsize} \quad (12)$$

a	b	c
d	e	f
g	h	i

Figure 57: 9-cell DEM window representation for using equations 10 to 12

features that influence displacements such as slope angles, slope aspect and stream networks. The following paragraphs will explain how topographical features are obtained from DEMs.

First, slope angles can be generated with DEMs. The slope represents the rate of elevation change over the DEM cells, so it is the first derivative of a DEM. The slope in degrees ranges from 0 to 90 and can be computed using equations 10 to 12. A moving 3x3 window passes each cell of the input DEM, using all neighbouring cells for the slope algorithm. The letters of the DEM window representation in Figure 57 represent the input values in the slope equations. So this slope algorithm uses the rate of change in the x and y direction for the centre cell 'e' (Burrough and McDonell, 1998).

Figure 58a shows an example of a slope angle map. The slope gradient significantly influences slope displacements because steep slopes exhibit higher gravitational force, so a slope map can be derived to distinguish steep areas. Additionally, the moraine steepness significantly influences the moraine stability. A narrow and steep moraine will be less able to withstand hydrostatic pressure and waves resulting from dynamic events than a wide and less steep dam. Moreover, observing breaking slopes on slope maps can reveal talus cones, indicating previous landslides. The slope angle is also used to map areas subjected to geometric limitations such as foreshortening, layover and shadowing, this will be explained later in this section. These factors distort the radar image for InSAR and prevent too steep areas from being analysed; this issue has been explained in section 3.1.1.

Second, with a DEM, the slope aspect can be derived. The aspect is the compass direction that a terrain faces. The slope aspect can influence slope displacements since slopes facing the sun might experience induced permafrost degradation. In addition, just as for the slope angle in the previous paragraph, the aspect can be used to indicate regions subjected to geometric

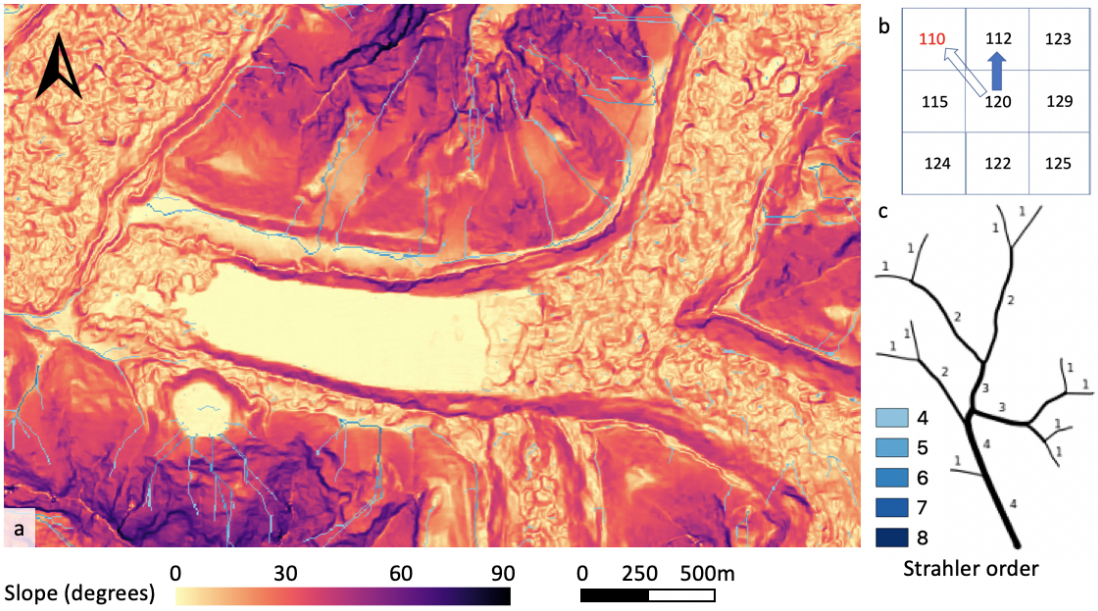

Figure 58: (a) Slope angle map and stream network (Imja Lake). (b) D8 flow direction method applied to a DEM. (c) Strahler stream network and legend.

limitations regarding InSAR, which will be elucidated later in this section. Figure 59 displays an example of a slope aspect map. The definition of the colours is such that 0° indicates the slope is facing north, 90° faces east, 180° faces south, and 270° is facing the west.

Third, a stream network visualised in Figure 58a can be generated from a DEM using an algorithm to find the flow direction and accumulation. This formula is indicated as the D8 flow direction algorithm, where D8 refers to each pixel's eight possible flow directions. The D8 algorithm is a steepest descent algorithm that approximates the primary flow direction using the maximal gradient of neighbouring pixels. Figure 58b shows how the flow direction is calculated from a DEM with the D8 method. For this case, the numbers depict the pixel's elevation and the blue arrow points towards the flow direction (north). Even though the elevation difference is larger between the centre pixel and the north-west pixel, the slope will be steeper towards the north pixel since the horizontal distance is shorter, resulting in the flow towards the north (Garbrecht and Martz, 1997; Jenson and Domingue, 1988). The drainage lines can be redefined to the Strahler stream order, which is based on the hierarchy of tributaries in Figure 58c. A higher stream order indicates higher water runoff. The order can range from 1, a stream without tributaries, to 12, the globally mightiest river at its mouth (Strahler, 1957). Water runoff can induce displacements due to stream erosion, so constructing drainage lines might indicate paths experiencing increased displacement or instability. These lines reveal where precipitation and melting will have their most significant influence on displacements. The accuracy of constructed drainage lines is limited by the resolution of the available DEM - varying from 30m (AW3D30 DEM) to 8m (HMA DEM) - and if surface changes have taken place after the DEM was constructed. Therefore, the drainage lines will not always be precise, and distinguishing flow paths will also require other data sources such as optical imagery and geological maps in the previous sections. Still, constructing such a stream network could also find water runoff paths invisible from optical imagery.

The DEMs, slope angle, slope aspect and stream networks in this report have been constructed and visualised in Quantum Geographic Information System (QGIS), an open-source software that supports viewing, editing and analysing geospatial raster, vector and point data. InSAR displacement points have been plotted in the software while overlaying DEMs, slope an-

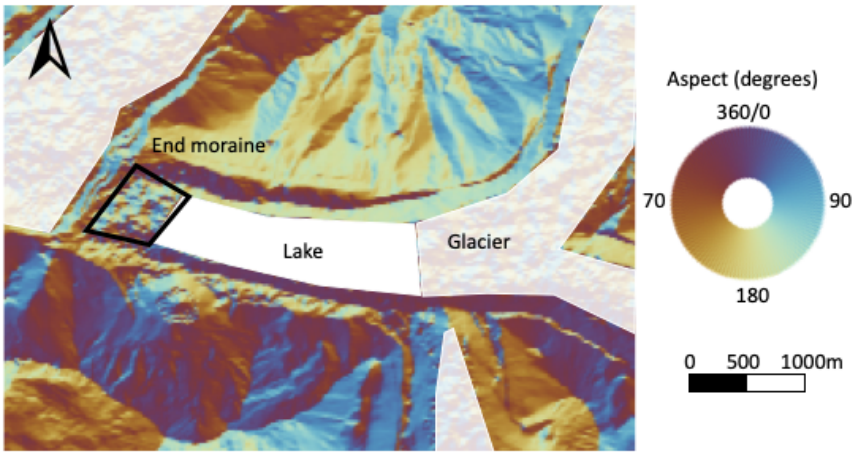

Figure 59: Slope aspect map of Imja Lake

gle, aspect and drainage lines to visually integrate the displacements with topographical data. In addition, the constructed slope angle and aspect have been integrated with the InSAR parameters and displacement results to map geometric limitations and calculate displacements along the slope direction. The following two paragraphs will explain these applications.

Mapping geometric limitations

As explained in section 3.1.1, the relation between the satellite orientation, incidence angle and slopes can cause geometric limitations such as layover, foreshortening and shadowing. These areas are impossible or more challenging to analyse with InSAR. Identifying these regions in mountainous regions is essential to assess the applicability of InSAR or a specific satellite sensors. That way, a quick assessment can be made whether, for example, an InSAR-based analysis with Sentinel-1 data at a particular slope of interest is possible. The range index (RI) provides a method to map such areas using the local slope aspect and angle and the satellite's incidence and azimuth angle. The RI indicates the distortion between the pixel size in SAR slant and ground range and can be calculated with

$$\mathrm{RI} = -sin(S * sin(A - \alpha + 180^\circ) - \theta) \tag{13}$$

where S is the local terrain slope angle, A the local slope aspect, α the azimuth satellite heading angle and θ the incidence angle. The azimuth heading and incidence angle are depicted in Figure 60a and b. The incidence angles in this study range from 33.8 to 44.9 degrees, and the azimuth heading angles are approximately 350 and 190 degrees for Sentinel-1 ascending and descending orbit, respectively. The resulting RI values range between -1 and 1. Generally, layover occurs for a RI between -1 and 0, foreshortening occurs for positive values near 0, and a RI of 1 indicates a LOS precisely perpendicular to the slope (Notti et al., 2014; Vecchiotti et al., 2017). High RI values can also indicate shadow depending on the slope angle and orientation of the slope. For mapping purposes, the RI is divided into five categories:

- Class 1: $-1 < \mathrm{RI} \leq 0$
- Class 2: $0 < \mathrm{RI} < 0.33$
- Class 3: $0.33 < \mathrm{RI} < 0.66$
- Class 4: $0.66 < \mathrm{RI} \leq 1$
- Class 5: S $>(90^\circ\text{-}\theta)$ & A $\approx \alpha{+}90^\circ$

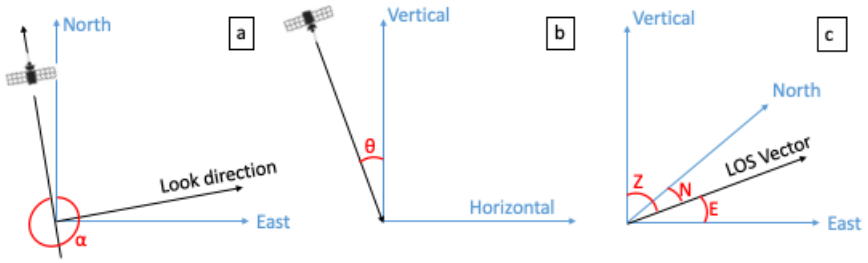

Figure 60: a) Azimuth satellite heading angle (350° for ascending orbit and 190° for descending orbit). b) Incidence angle. c) Direction cosines N, E and Z.

with the pixels in Class 1 indicating layover, Class 2 significant distortion due to foreshortening, Class 3 less distortion, Class 4 the best conditions, and Class 5 indicating areas subjected to shadowing (Bianchini et al., 2013; Cigna et al., 2014). Equation 13 will map active layover and shadowing, referring to the pixels directly producing layover or shadow in the SAR image. Passive layover and shadow regions consist of the pixels affected by these active regions. So these areas are overlaid by or lie in the shadow of the active regions. Consequently, the resulting RI map might not show all the regions subjected to geometric limitations, providing a too optimistic result. As a solution, hill-shading can be added to the analysis to indicate passive shadow and layover areas (Kropatsch and Strobl, 1990; Notti et al., 2014). Two factors have been added to equation 13:

$$\text{RI} = -sin(S * sin(A - \alpha + 180°) - \theta) * Lo + Sh \tag{14}$$

where Lo is the layover factor and Sh the shadow factor. This equation has been slightly adjusted from Notti et al. (2014) to ensure that passive shadow pixels will not fall in the same class as layover. Hillshade has been calculated with QGIS using the incidence and azimuth angles of the satellite and the terrain's slope and aspect. The illumination value indicates whether the cell is affected by shadow or layover. The hillshade value for shadowing is calculated with:

$$\text{Hillshade (shadow)} = 255*[(cos(90°-\theta)*cos(S))+(sin(90°-\theta)*sin(S)*cos((450°-\alpha)\%360°-A))] \tag{15}$$

where % is the modulo operator so the value goes back to 0° after 360°. The hillshade value ranges from 0 to 255, with 0 indicating complete shadow. To calculate layover, equation 15 is adjusted to equation 16, using the supplementary LOS azimuth angle and the LOS incidence angle:

$$\text{Hillshade (layover)} = 255*[(cos(\theta)*cos(S))+(sin(\theta)*sin(S)*cos((450°-\alpha)\%360°+180°-A))] \tag{16}$$

where the hillshade value also ranges from 0 to 255, with 0 indicating complete layover. Instead of an actual hillshade map, a binary output raster has been created, such as in Figure 61, to distinguish values of 0 from values between 1 and 255. For the RI equation, Sh is set to 2 for hillshade values of 0 and to 0 for hillshade values between 1 and 255. If Sh is 2, the RI of equation 14 will be larger than 1, so an extra condition will then be added to class 5: RI $>$ 1. So if there is shadow, RI will be larger than 1 and fall in class 5. Lo is set to 0 for hillshade values of 0 and to 1 for hillshade values from 1 to 255. Consequently, the RI in equation 14 will be 0 when there is layover (since Sh will also be 0 in layover areas), and the pixel will fall in class 1 (esri, 2022; Mallet et al., 2018; Notti et al., 2014).

Figure 62 shows the RI maps at Imja Lake for the ascending and descending orbit. This region's slope and aspect map have been displayed in Figures 58a and 59 respectively. For example, the RI map in Figure 62b indicates significant layover and foreshortening in the northeast

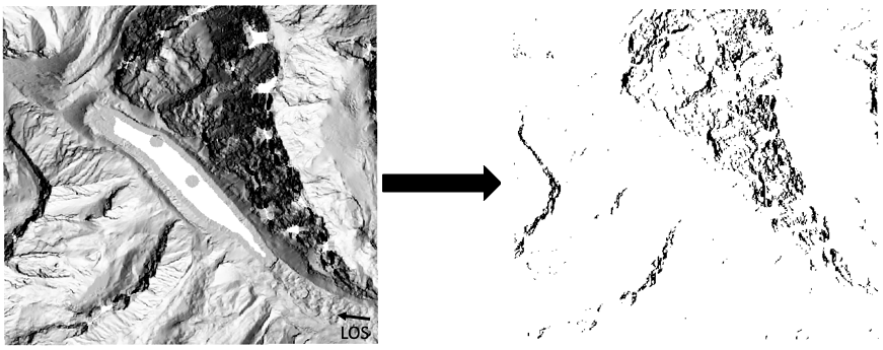

Figure 61: Hillshade map with values ranging from 1 to 255 converted to a binary map with either shadow (0 or black) or no shadow (1 or white).

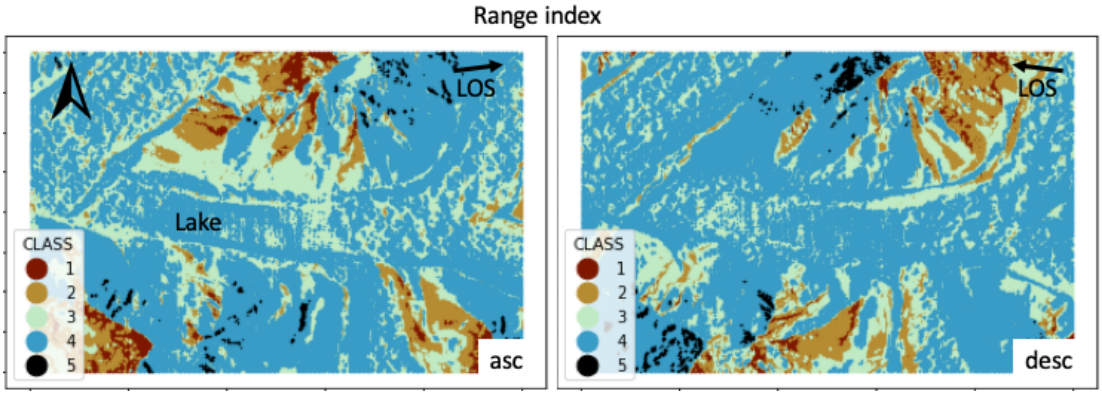

Figure 62: Example of RI maps at Imja Lake for the ascending ($\alpha = 350°$ and $\theta = 35.85°$) and descending ($\alpha = 190°$ and $\theta = 37.75°$) orbit. Class 1 is layover, 2 is severe foreshortening, 3 is less foreshortening, 4 is ideal area and 5 is shadowing

region, while the area surrounding the lake in the middle seems less subjected to distortions. So from this image, it can be expected that the slopes in Class 1, 2 or 5 will show no or less persistent scatterers. The RI maps for other lakes are in Appendix F.

Displacement along slope direction

As mentioned in section 3.1.1, the sensitivity of InSAR-derived LOS displacements depends on the slope angle and aspect. If a slope is inconveniently oriented (in this case north or south), it might seem that the area is not experiencing significant displacement compared to areas facing more east or west. Displacements from a single orbit (ascending or descending) can be projected along the steepest slope by integrating LOS displacements with slope and aspect data to accommodate this issue. This projection might be more convenient than decomposing displacements in east-west and vertical directions for mountainous areas where the ascending and descending displacements do not cover the same areas and where displacements mainly move along slope direction instead of solely vertical or horizontal. This projection assumes that displacement occurs parallel along the steepest slope and can be calculated with:

$$D_{slope} = \frac{D_{LOS}}{C} \tag{17}$$

where coefficient C provides the percentage of actual displacement and represents the sensitivity of the LOS vector to the steepest slope projection. This conversion factor is a function of the directional cosines of the LOS and slope vectors:

$$C = N_{dir} * N_{slope} + E_{dir} * E_{slope} + Z_{dir} * Z_{slope} \tag{18}$$

where the directional cosines of the LOS vector in the north (N), east (E) and vertical (Z) direction are multiplied with the directional cosines of the slope in N, E and Z direction (Notti et al., 2014). The direction cosines are the cosines of the angles between the vector and the three positive coordinate axes, which are depicted in Figure 60c. The LOS vector direction cosines are a function of the satellite incidence and azimuth heading angle:

$$N_{dir} = cos(90^\circ - \alpha) * cos(180^\circ - \theta) \tag{19}$$

$$E_{dir} = cos(90^\circ - \alpha) * cos(270^\circ - \theta) \tag{20}$$

$$Z_{dir} = cos(\alpha) \tag{21}$$

where α is the satellite azimuth heading angle (350° for ascending and 190° for descending orbit) and θ the incidence angle. The slope direction cosines are calculated with the slope angle and aspect:

$$N_{slope} = cos(S) * sin(A - 90^\circ) \tag{22}$$

$$E_{slope} = -cos(S) * cos(A - 90^\circ) \tag{23}$$

$$Z_{slope} = sin(S) \tag{24}$$

where S is the local terrain slope angle and A the local aspect. The conversion factor is close to zero for areas with very low sensitivity to LOS deformations. In this case, C is set to -0.3 for $-0.3 < C < 0$ and to 0.3 for $0 < C < 0.3$ to avoid an incorrectly large D_{slope} in equation 17. This means that the projected displacement along the steepest slope cannot be larger than 3.33 times the LOS displacement. This value has been validated in previous studies by comparing the results with GPS measurements and empirical relations (Aslan et al., 2020; Herrera et al., 2013; Kalia, 2018). Figure 63 shows the conversion factor at Imja Lake with the corresponding multiplication to project the displacements along the slope. D_{slope} is only calculated for slope angles larger than 5° to make sure the projected displacement is indeed along the slope. Flatter areas might experience displacements contributed to mechanisms such as subsidence or frost heave, with the displacement not being in the steepest slope direction. Figure 63 shows that the hummocky moraine and glaciers contain high multiplication values, while the movements do not necessarily behave along the steepest slope, so the projection should only be used for the surrounding slopes. For positive D_{slope} values along a slope, it is either assumed that the D_{LOS} value is correct or that the movement is attributed to noise since it is unlikely to encounter displacements moving upslope. The point might experience frost heave, which is not along the slope, or the conversion factor is incorrect. This could, for example, be caused by inaccuracies between the location of the pixel and the DEM. In addition, several limitations arise for this projection. First, the projection is only valid for displacements parallel to the slope. Second, the projection could amplify minor errors on slopes, which would especially become apparent for data with less stable amplitudes or affected by noise (Notti et al., 2014). All PSI displacements projected along the steepest slope can be found in Appendix B.

Section 3.3 showed the InSAR results, and the sections above explained how to interpret them. This paragraph shortly describes what could be expected from the InSAR results regarding glacial lakes and associated hazards. Figure 64 provides a hypothetical example of the InSAR results relating to surface features and GLOF triggers. The failure mechanisms on this image have been explained in section 2.2. For simplicity, this image displays negative values (red and yellow) as downslope displacements or subsidence, around zero values (green) indicating no significant displacement and positive values (blue) as uplift. First, unstable slopes consisting of

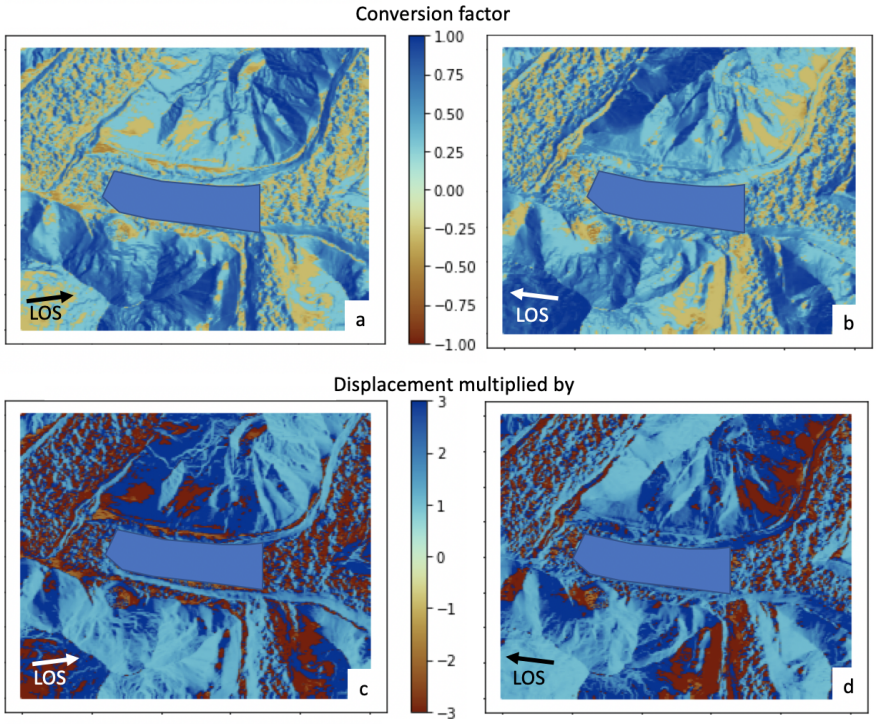

Figure 63: The conversion factor for ascending (a) and descending (b) and multiplication factor for ascending (c) and descending (d) orbit to project displacements along the steepest slope at Imja Lake.

scree debris or rock glaciers would be expected to show downslope movements. Especially rock glaciers might show significant continuous downslope displacement. Scree debris is expected to move less consistently with smaller movements since it might behave more brittlely; it might not even move before failure. Since lateral moraines experience glacial debuttressing and are relatively steep, also here, downslope displacements are expected. Second, terminal moraines experiencing subsidence due to ice melting will be expected to show negative vertical displacements. Some positive movements could also be possible since the lake level might be rising, just as the amount of water beneath the soil or dead ice in the moraine. It is also expected that InSAR will reveal which areas are stable (green points) and do not experience any downslope displacements or subsidence. Finally, it is assumed that no (coherent) results will be obtained on snowy mountain tops, densely vegetated areas and on the glacier that might be moving too fast and cause decorrelation, as explained in section 3.1.3. The following section will show and explain the integrated InSAR observations at the six glacial lakes.

4.2 Results

This chapter presents the results of InSAR integrated with the data sources and methods described in the previous sections. The integrated results at each lake are limited to areas that might directly influence the lake and pose a GLOF risk. Such areas consist of the terminal and lateral moraines and slope trajectories towards the lake. In addition to the figures in this chapter, each lake's CDInSAR and PSI results can be found in Appendix A and B respectively.

4.2.1 Imja Lake

Figure 65 displays the ascending and descending PSI displacement rates along the LOS at Imja Lake. The feeding glaciers are on the east, and the terminal moraine is on the west. Another glacier lies in the northwest corner; however, this glacier does not (yet) feed into the lake. The figure shows some distinctive slope areas and the terminal moraine that experience significant

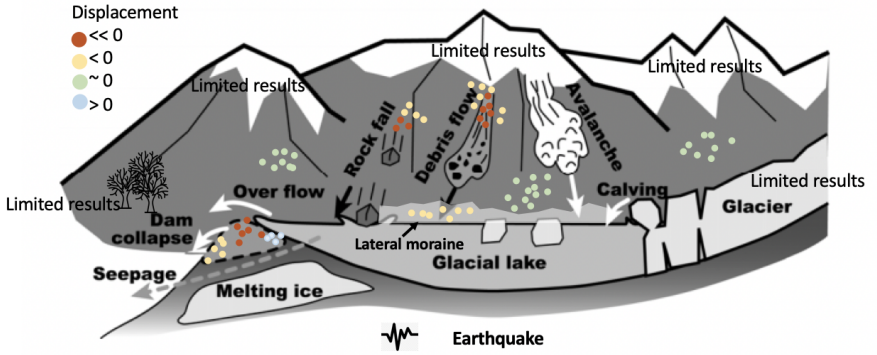

Figure 64: Expected InSAR observations linked to geomorphological phenomena and potential GLOF hazards

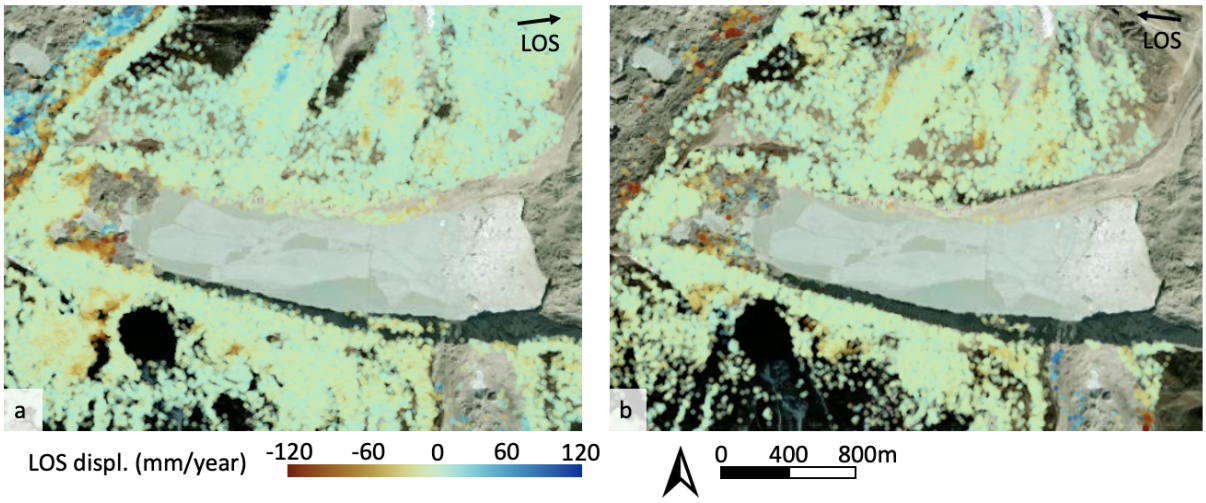

Figure 65: PSI displacement rates along the LOS at Imja Lake (temporal coherence > 0.7) (a) ascending. (b) descending.

displacements over 120 mm/year.

The west bank of the circular lake south of Imja Lake shows many PS experiencing displacement rates up to -70 mm/year for both ascending and descending orbits, showing subsidence and movement down the slope towards the circular lake. The surface has a hummocky pattern; presumably, melting subsurface ice is causing the subsidence. The 400 m diameter lake lies 15 m lower than Imja Lake, and the edge between the lakes is almost 40 m high. Therefore it seems unlikely that this lake poses a hazard, but if mass from the steep surrounding slopes falls into the lake, water might still flow out into Imja Lake, destroy the ridge between the two lakes, and create a larger flood.

Besides the two feeding glaciers, a glacier lies south of Imja Lake. This glacier does not yet reach the lake; the lateral moraine is still continuous. Also, no significant displacements have been found at this ridge yet. However, the displacements at the lateral moraines indicate that this glacier might have been melting fast, causing glacial debuttressing, resulting in instability and deformation. In addition, Figure 65 reveals supraglacial lakes on this glacier. Meltwater could directly flow into Imja Lake, or a glacial lake could start to form behind this lateral moraine. Especially in the latter scenario, this poses additional hazards for Imja Lake, increasing the possibility of dynamic failure. If a larger lake forms and the ridge collapses, a significant amount of water would be discharged into Imja Lake.

Figure 66a displays downslope displacement rates exceeding 40 mm/year at Imja Lake's north slope. Scree deposits have been found in the lighter areas (Khatiwada and Dahal, 2020; Westoby et al., 2014b). The slope map in Figure 66b shows that these scree debris areas also correspond with slightly breaking slopes. These slopes could be loose and unstable, and as they lie at drainage lines, water runoff from melting and rainfall can trigger movement by dislodging mass and melting interstitial ice. The scree areas show various displacement points, but most are concentrated at the darker lobes adjacent to the scree debris areas. These movements are highlighted by circles and show seasonal signals, as shown by the time series in Figure 66c. Their displacement rate is near zero in the winter and reaches downslope rates of 200 mm/year between July and January. The lobe shape and seasonal pattern are typical for rock glaciers (Dini et al., 2019; Strozzi et al., 2020). Rock glaciers gradually move downslope, and the active top part of a rock glacier is susceptible to high precipitation and temperature, explaining the increase in summer movement (Deline et al., 2021). Conversely, the scree deposit displacements do not exhibit a specific pattern. Rock glaciers and scree slopes pose hazards for debris flows and rockfalls (Kofler et al., 2021), but as long as the lateral moraine lies in-between, the mass will be trapped and not reach the lake (Khatiwada and Dahal, 2020; Kroczek and Vilimek, 2020; Rounce et al., 2016). The lateral moraine also exhibits downslope displacement rates up to -160 mm/year. These movements are likely attributed to the slope steepness and glacial relief after glacier melting.

Figure 67 highlights the PSI displacements at Imja Lake's end moraine. Figure 67a shows the descending displacement rates along the LOS, and Figures 67d and 67e display the displacement rates decomposed into eastward and vertical components. The outer moraine experiences almost no displacement with most velocities lower than 10 mm/year. In contrast, the inner moraine experiences significant movement up to 100 mm/year along the LOS. This difference in deforming regions coincides with the geophysical survey of Hambrey et al. (2008), revealing that the outer part is a stable ice-free structure of sand, debris and boulders, and the inner part consists of several metres of dead ice covered in debris. The magnitude of displacements varies over the moraine, corresponding with the heterogeneous subsurface consisting of ice, boulders and saturated or unsaturated debris or sand (Dahal et al., 2018; Hambrey et al., 2008).

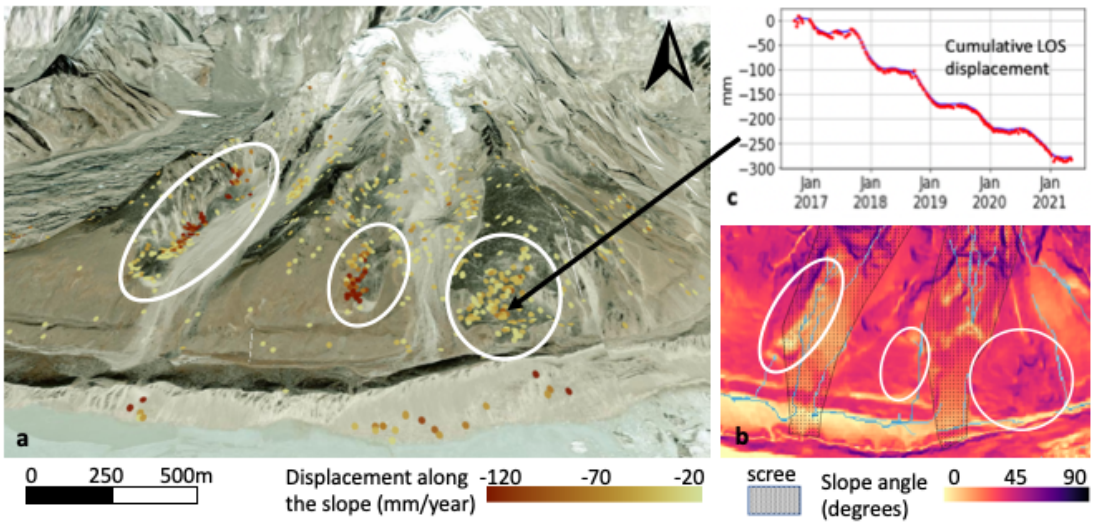

Figure 66: Imja Lake's north slope with rock glaciers and scree debris. **(a)** Descending PSI displacement rates along the steepest slope exceeding 40 mm/year (temporal coherence > 0.65). The white circles indicate areas with significant downslope displacements that show a seasonal pattern. **(b)** the slope angle and drainage lines at the scree deposits and rock glaciers. **(c)** Cumulative displacement time series along the descending LOS of a red point in figure (a)

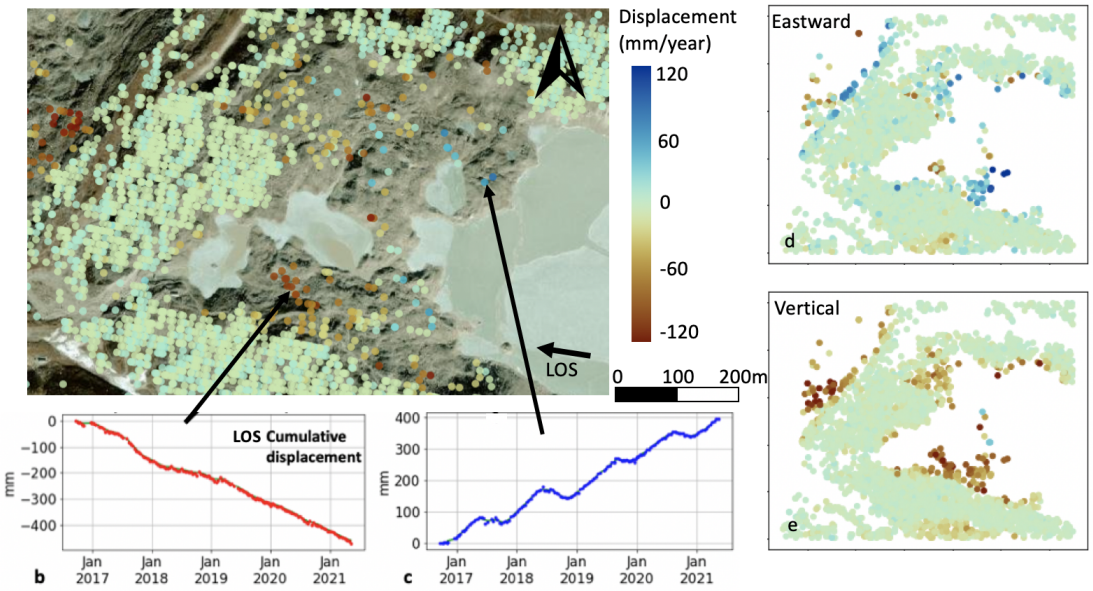

Figure 67: **(a)** Descending PSI displacement rates along the LOS (temporal coherence > 0.6) at the terminal moraine of Imja Lake, the outlet channel is located at the southwest corner of the moraine. **(b)** Cumulative displacement time series of a red point (temporal coherence = 0.80). **(c)** Cumulative displacement time series of a blue point (temporal coherence = 0.82). **(d)** Decomposed displacement rates in the east-west direction, where positive displacement corresponds to eastward movement. **(e)** Decomposed displacement rates in the vertical direction, where negative displacement indicates downward movement.

The inner moraine shows fewer points for the ascending orbit (Figure 65a), so Figure 67a shows more points than Figures 67d and 67e. This is presumably because of the wet moraine surface and excessive displacements causing temporal decorrelation. The points covered by both orbits show a dominant subsiding and eastward direction, which is lake inwards. The points move up to -150 mm/year in the vertical direction and 100 mm/year eastward. The area not covered by the ascending PSI data set shows positive displacements for the descending data set up to 120 mm/year along the LOS. The descending CDInSAR results in Figure 68 show positive LOS movement up to 20 mm over 12 days and correspond with the PSI displacements. The ascending CDInSAR results show a significant negative LOS displacement of -20 mm over 12 days. From these observations, it can be concluded that the area is subsiding while moving lake inwards.

The time series in Figure 67c shows the seasonal pattern of the area moving towards the satellite for the descending PSI. The points are stagnant or move slightly away from the satellite in the summer and towards the satellite from early winter to the summer. This temporal behaviour suggests that temperature governs the intra-annual displacement, with ice melt explaining the decreasing thickness of dead ice in the summer. Since the artificial drainage channel was constructed in October 2016, water should be moving towards the outlet channel, which is westwards, so displacement eastward seems illogical at first. An explanation could be that because of the lake lowering, the hydrostatic pressure of the lake on the moraine dam has decreased, enabling the loose soil and dead ice to move lake inwards while also moving downwards, of which the latter is increased by ice melting. The artificial drainage could have increased the melting since relatively warmer water passes the interstitial ice (Dahal et al., 2018). Unfortunately, the Sentinel-1 data was too sparse between 2014 and 2016, causing a too large temporal baseline for the InSAR analysis to accurately determine the moraine's behaviour before the artificial drainage in October 2016, which might explain specific displacements. A more detailed investigation of the moraine might help to pinpoint the mechanisms and behaviour causing these deformations.

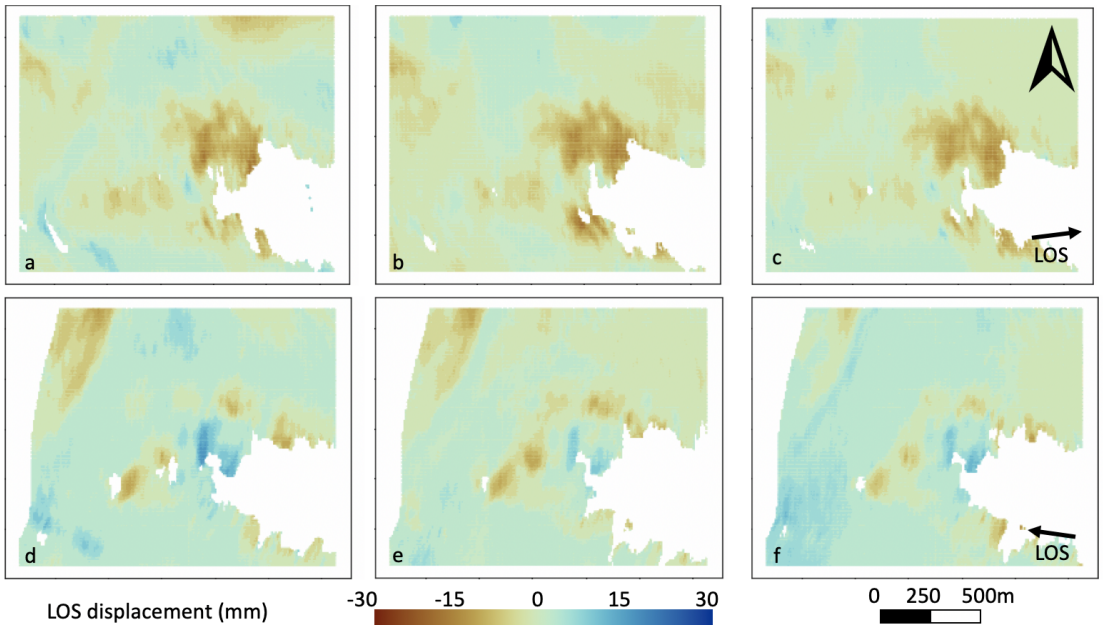

Figure 68: CDInSAR displacement at Imja Lake's terminal moraine from December 2017 to February 2018. Ascending: (a) 2017-12-25 to 2018-01-06. (b) 2018-01-18 to 2018-01-30. (c) 2018-02-11 to 2018-02-23. Descending: (d) 2017-21-21 to 2018-01-02. (e) 2018-01-26 to 2018-02-07. (f) 2018-02-07 to 2018-02-19.

Haritashya et al. (2018) found that the end moraine had subsided between 2000 and 2016 with a maximum velocity of -1.9 m/year and an average velocity of below -0.5 m/year by differencing DEMs. As explained in section 3.2.2, PSI can only measure up to approximately 400 mm/year due to aliasing, provided that the displacement is linear over the whole time frame. Quite some areas do not return PS points, especially surrounding the puddles, which is where Haritashya et al. (2018) found the most significant subsidence. Presumably, the wet surface and the excessive displacements cause temporal decorrelation, and the subsidence rates might be higher than Figure 67 implies. As a result of ice melting, the inner moraine will eventually disappear, and the lake will reach the outer part. Then, either the end moraine will melt or degrade and gradually lower the lake, decreasing the GLOF risk, or the moraine will become narrow, reducing its stability and increasing the risk of bursting (Sattar et al., 2021).

4.2.2 Lunana Lakes

Figure 69 displays the PSI displacement rates along the LOS at the four glacier lakes in the Lunana region, and Figure 70 shows two examples of unwrapped interferograms obtained with CDInSAR. Figure 69 reveals that most significant displacement rates can be identified at Lugge Lake's slopes and along the lake boundaries. Higher altitude areas containing all-year-round snow, such as in the north, do not have PS and are incoherent for CDInSAR, just as some slopes that lie in the shadow or cause layover for one of the orbits. The following paragraphs will highlight smaller areas and detail their geomorphology and displacements.

Figure 71a and b displays LOS displacement rates exceeding 30 mm/year at the moraines damming Bechung, Raphstreng, Thorthormi and Lugge Lake. Frame 1 in Figure 71b highlights the area consisting of the end moraines of Bechung and Raphstreng Lake. PSI and CDInSAR reveal the melting of the stagnant ice at Bechung Lake, which will probably rapidly form a larger glacial lake. Some displacement points up to -60 mm/year are identified at the terminal moraine

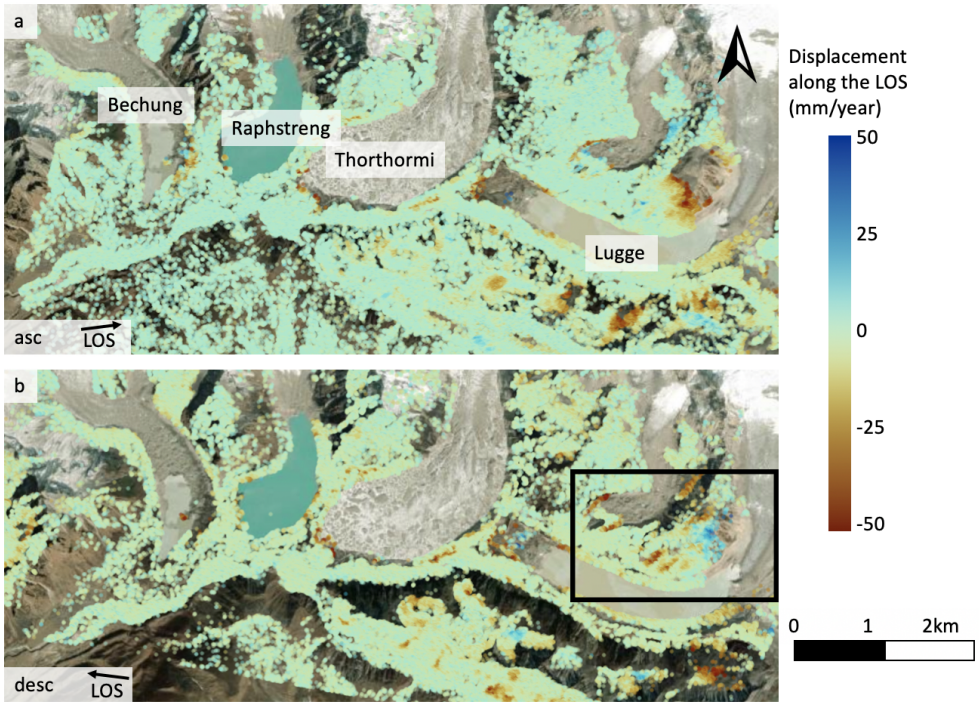

Figure 69: PSI displacement rates along the LOS (temporal coherence > 0.7) at the Lunana Lakes. **(a)** ascending. **(b)** descending.

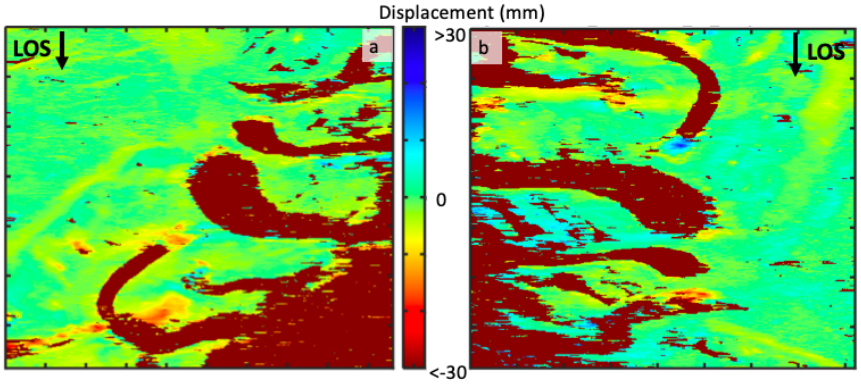

Figure 70: CDInSAR displacements along the LOS at the Lunana Lakes in SAR coordinates. **(a)** ascending, between 2017-12-08 and 2017-12-20. **(b)** descending, between 2015-12-21 and 2016-01-02

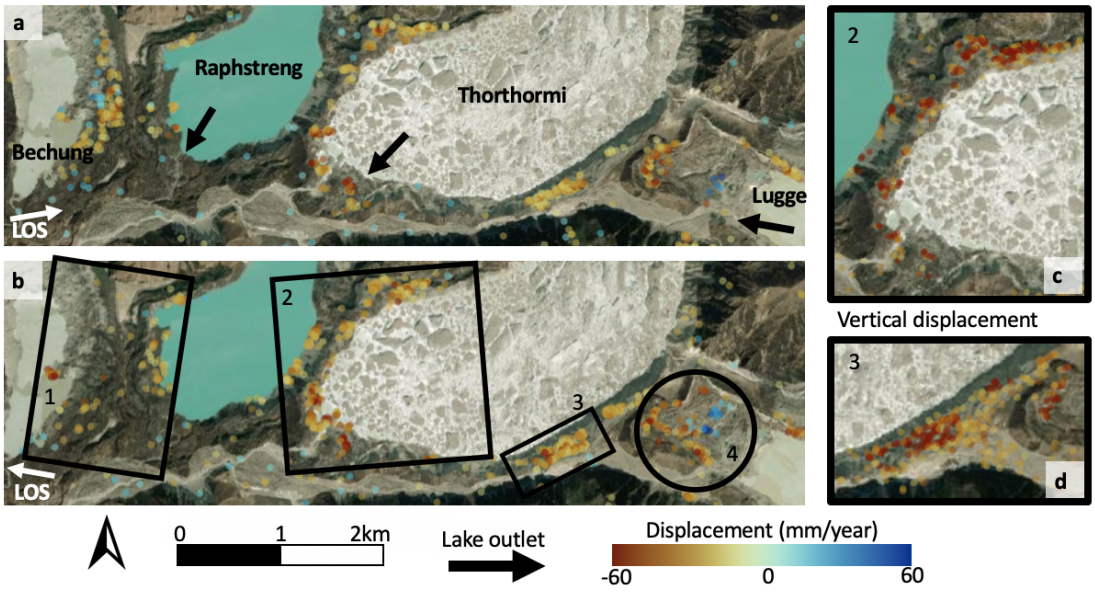

Figure 71: PSI displacement rates along the LOS (temporal coherence > 0.7) exceeding 30 mm/year at Lunana Lakes, with a Sentinel-2 false-colour vegetation image as background. **(a)** ascending. **(b)** descending, the frames (1-4) mark areas that are highlighted in the text and the following figures. **(c)** Vertical displacement rates at Frame 2. **(d)** Vertical displacement rates at Frame 3.

of Raphstreng, presumably due to ice melting, but no significant deformations are observed at the outlet channel.

Frame 2 in Figure 71b and c marks the end moraine of Thorthormi Lake, which also partly dams Raphstreng Lake, and is highlighted in Figure 72. Several PS experience vertical displacement up to -80 mm/year. Figure 72a shows landslide scars on the moraine slope, the degradation of these slopes has also been witnessed during site visits, (NCHM, 2020; Singh, 2009) and geophysical surveys have revealed ice inside the moraine (Nayar, 2009). This ongoing destabilisation is worrisome since the dam is narrow. Figure 72b depicts the elevation profile of the moraine damming the lakes. Since Thorthormi lake lies 90 m higher than Raphstreng Lake, the lake exerts significant hydrostatic pressure on the top part of the dam without counterforce. The elevation profile also shows that Thorthormi lake lies only about 10 m lower than the dam's highest point. With ongoing internal ice melting and lake expansion, water might overflow the dam, inducing erosion and possibly developing a breach. Thorthormi Lake could then burst into Raphstreng Lake at dam failure, causing a combined GLOF. Besides the moraine damming both lakes, the rest of Thorthormi Lake's end moraine has also been experiencing subsidence. LOS displacement rates of -90 mm/year are observed at the outlet channel. A minor breach occurred in June 2019 at this location, presumably due to melting, since the terminal moraine consists of debris-covered stagnant ice (NCHM, 2019). However, no specific changes in the time series were observed before or after the breach. Frame 3 in Figure 71b and d marks a part of Thorthormi Lake's lateral moraine. The vertical displacement points show the area is experiencing subsidence on the crest with rates up to -80 mm/year. The hummocky pattern visible in Figure 73 indicates thermokarst features, providing evidence of subsurface ice melting, explaining the subsidence. The observed subsidence in this area corresponds with the PSI study of Wangchuk et al. (2022).

Frame 4 in Figure 71b depicts the end moraine of Lugge Lake, which differs from the other Lunana lakes. The moraine consists of a more stable outer part and an unstable inner region of substantial dead ice, similar to Imja Lake in section 4.2.1. The unwrapped ascending interferogram in Figure 70a shows displacement away from the satellite. For the descending

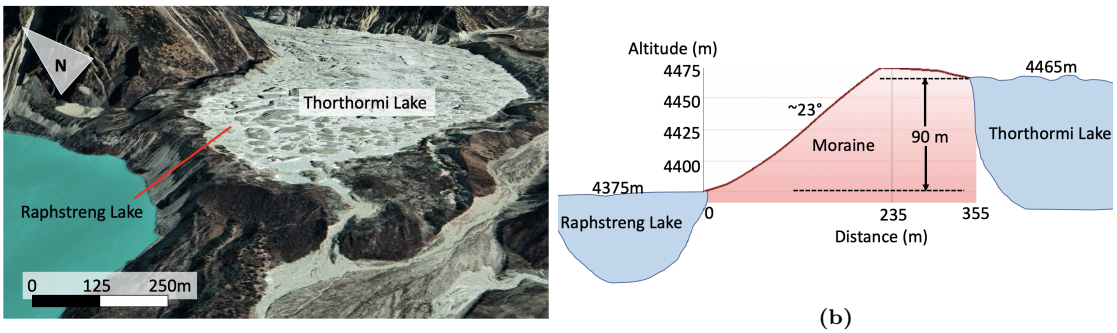

(a) (b)

Figure 72: The narrow moraine between Raphstreng and Thorthormi Lake, corresponding to Frame 2 in Figure 71. (a) Google Earth Image (January 2021), the red line depicts the elevation profile path. (b) Height profile along the red line. Elevation profile was constructed in Google Earth.

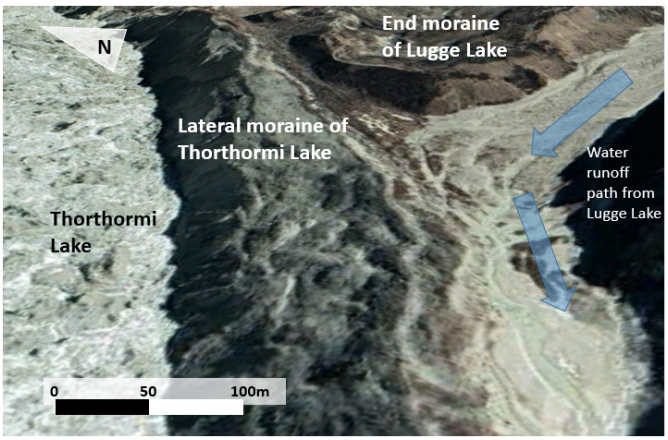

Figure 73: Lateral moraine of Thorthormi Lake (Frame 3 in Figure 71) with visible thermokarst features. Image from Google Earth (January 2021)

orbit in Figure 70b the moraine seems to experience displacements towards the satellite in the moraine centre and movements away from the satellite near the outer moraine. The PSI results in Figure 71b display similar behaviour for the descending orbit. However, the ascending PSI results in Figure 71a show almost no points at the centre moraine, apart from a few points that move strongly towards the satellite. Since CDInSAR (Figure 70a) shows displacements primarily away from the satellite, the inner moraine part would move eastward, lake-inward, a similar observation as for Imja Lake in section 4.2.1. However, in this case, Figure 71a shows that the outlet of Lugge Lake lies before the moraine. So as water might be flowing towards the outlet channel, water from beneath the dead ice might also move towards the outlet. This could cause the dead ice and loose soil to be moving lake inwards. However, more detailed research should be carried out at this location to pinpoint the exact mechanism. Nevertheless, the PSI and CDInSAR results show that the region that lies more towards the outer moraine is experiencing negative LOS displacement rates for ascending and descending orbits up to -100 mm/year. The subsidence is likely because of ice melting since the moraine consists of ice (Iwata et al., 2002). The PSI study of Wangchuk et al. (2022) also obtained nearly no displacement points on the inner moraine, but by differencing DEMs, significant elevation change up to -1.5 m/year was observed which explains that the deformation is probably too fast for PSI to measure.

Figure 74 shows the PSI downslope displacement rates exceeding 40 mm/year at Lugge Lake's north slope (the frame in Figure 69b). The ascending orbit covers a larger area than the descending orbit, but the eastern part does not contain PS for both orbits. The slope angle is between 30 and 50 degrees, and the aspect map in Figure 75b shows that the slope faces south-east. Therefore, the displacement rates might be too high in the LOS direction for the ascending set as the magnitude increases going east, losing temporal coherence. The displacements should then be less significant along the LOS for the descending data set. However, the range index maps in Figure 76 reveal that this area is severely foreshortened and even causing layover, which might be why the site contains no PS. The displacement rates in Figure 74 reach up to -180 mm/year along the slope, consisting of rock glaciers. Figure 75a shows the direction of the downslope movement, using the direction of the flow lobes and the aspect map in Figure 75b. The obtained displacement of the rock glaciers towards the lake corresponds with the PSI results of Wangchuk et al. (2022). Lugge's lateral moraine provides protection at the left arrow, as shown in Figure 75a and b, but eastwards no protection exists between the lake and the slope, raising the hazard of dynamic failure at this location.

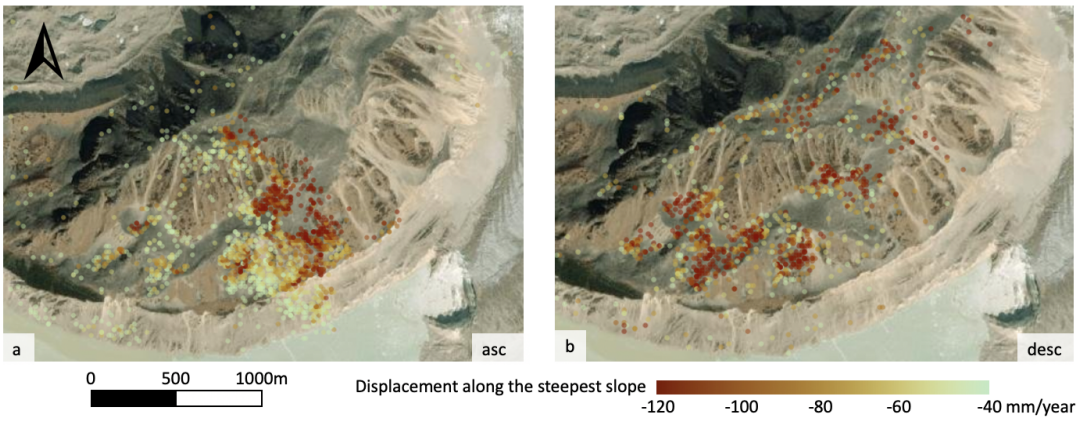

Figure 74: PSI displacement rates (temporal coherence > 0.7) along the steepest slope at the north slope of Lugge Lake (the frame in Figure 69b). (a) ascending. (b) descending.

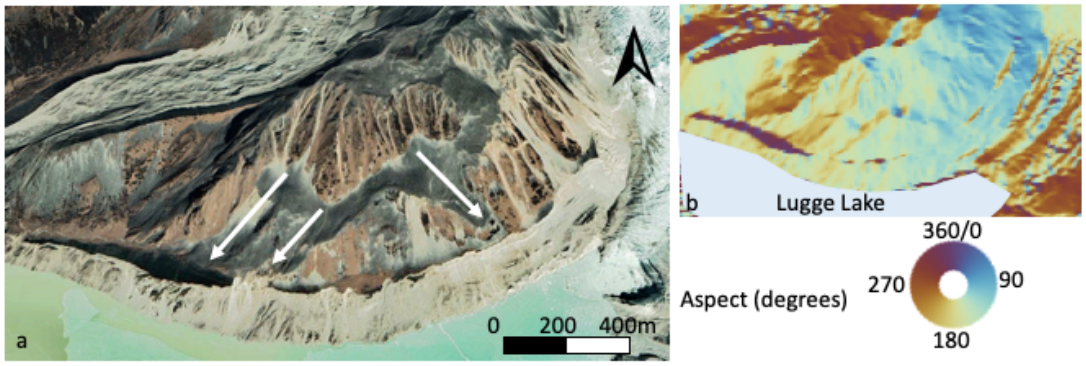

Figure 75: Lugge Lake's north slope. (a) The arrows depict rock glaciers and overall displacement direction. Background image from Google Earth (January 2021). (b) Slope aspect map.

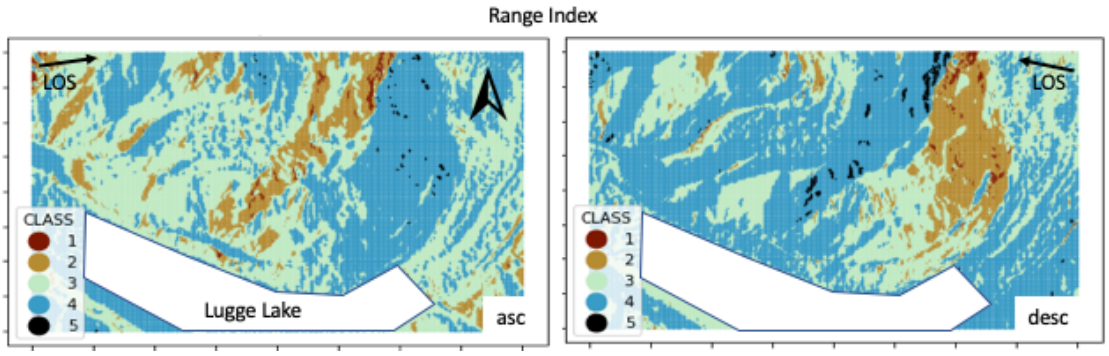

Figure 76: Range index at the north slope of Lugge Lake. Ascending image shows that the slope lies in a convenient orientation (class 3 and 4), whereas the descending image shows that a large region experiences foreshortening or layover (class 1 and 2

.

4.2.3 Barun Lakes

Figure 77 shows two unwrapped interferograms for the whole area. For the integrated analysis, the Barun Lakes are divided into the three lake areas; Lower Barun, Upper Barun and Barun-3. Upper Barun and Barun-3 Lakes are significantly smaller than Lower-Barun, but as they lie upstream of Lower Barun Lake, they could trigger a collective GLOF with Lower Barun if they burst, making them essential to analyse.

Lower Barun Lake

Figure 78 shows the ascending and descending PSI LOS displacement rates at Lower Barun Lake. The terminal moraine shows negative velocities up to -150 mm/year for both ascending and descending orbits. CDInSAR additionally reveals negative LOS displacement rates for both ascending and descending orbits in Figure 77. Consequently, Lower Barun's end moraine is experiencing deformation mainly in the subsiding direction. Haritashya et al. (2018) found subsidence of the moraine between 2010-2015 of maximum -1.5 m/year and on average less than -0.5 m/year by differencing DEMs, which is significantly higher than the InSAR results in this study show. Reasons could be aliasing preventing coherent and correct displacements for PSI or the different time frame used. The north part of the moraine, which is highlighted by the frame in Figure 78b and c, is also experiencing negative displacement rates for both ascending and descending orbits. The subsurface ice melting forms one explanation for the subsidence, another factor might involve river deepening as the river coming from the upstream lakes could be undercutting the slope. Lower Barun's end moraine is not as high and steep as Rolpa's moraine (Figure 4b in section 2.1), for example, which decreases the probability of breaching. However, Lower Barun's volume is the highest of all glacial lakes in this research, so an outburst could cause a significant flood (Haritashya et al., 2018).

Upper Barun Lake

Upper Barun Lake lies 300 m upstream of Lower Barun. The lake is considerably smaller than Lower Barun lake, but steep slopes surround the lake, increasing the risk of dynamic failure. The east slope causes severe foreshortening and layover for the ascending orbit, shown by the RI map in Figure 79a and the reflectivity map in Figure 79c where the high-intensity bands correspond with layover. Consequently, only the descending results can be used to observe deformation on this slope, which does experience some shadowing (Figure 79b), but for a smaller area.

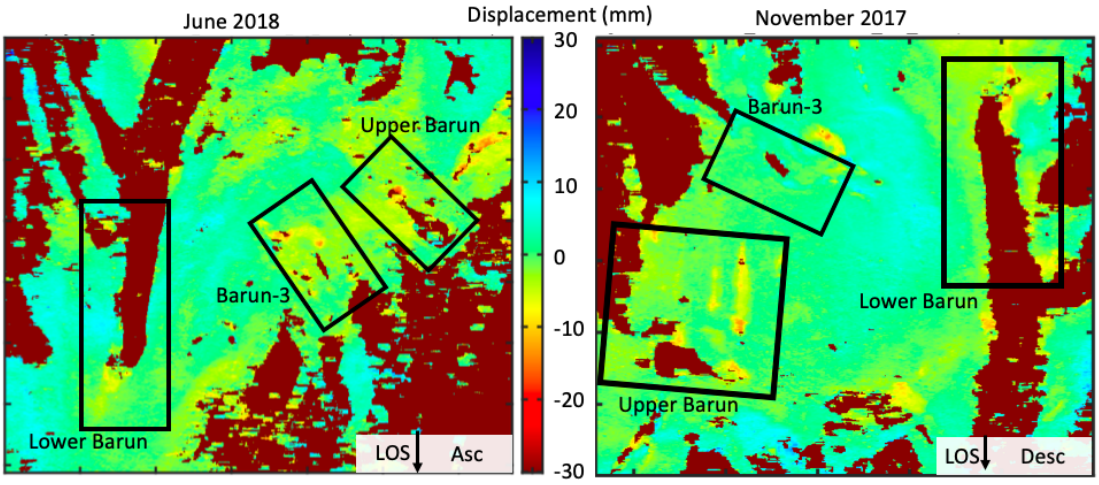

Figure 77: Ascending and Descending CDInSAR LOS displacements over 12 days at the Barun Lakes in SAR coordinates

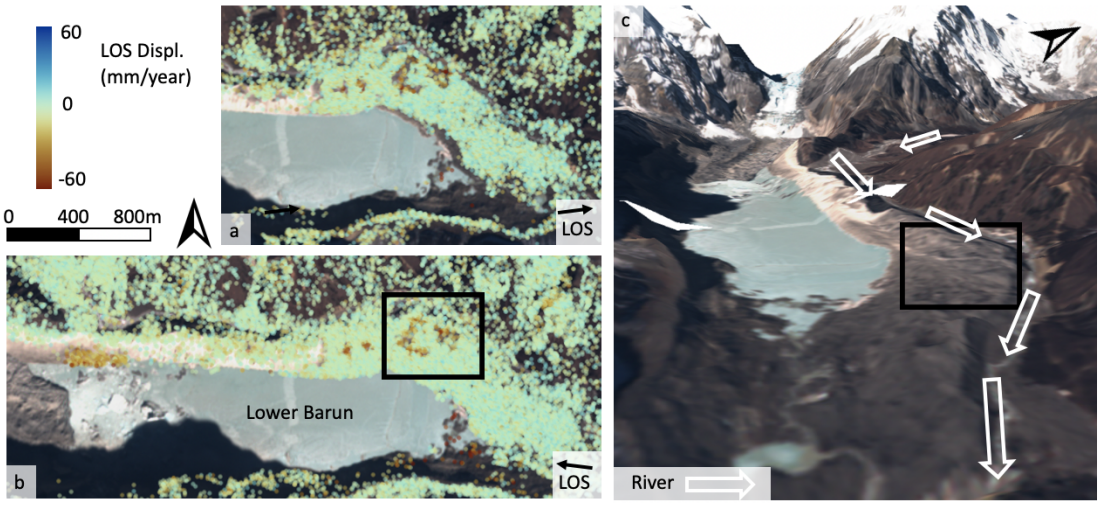

Figure 78: PSI displacement rates along the LOS (temporal coherence > 0.6) at Lower Barun Lake. (a) ascending. (b) descending. (c) 3D image showing the river path

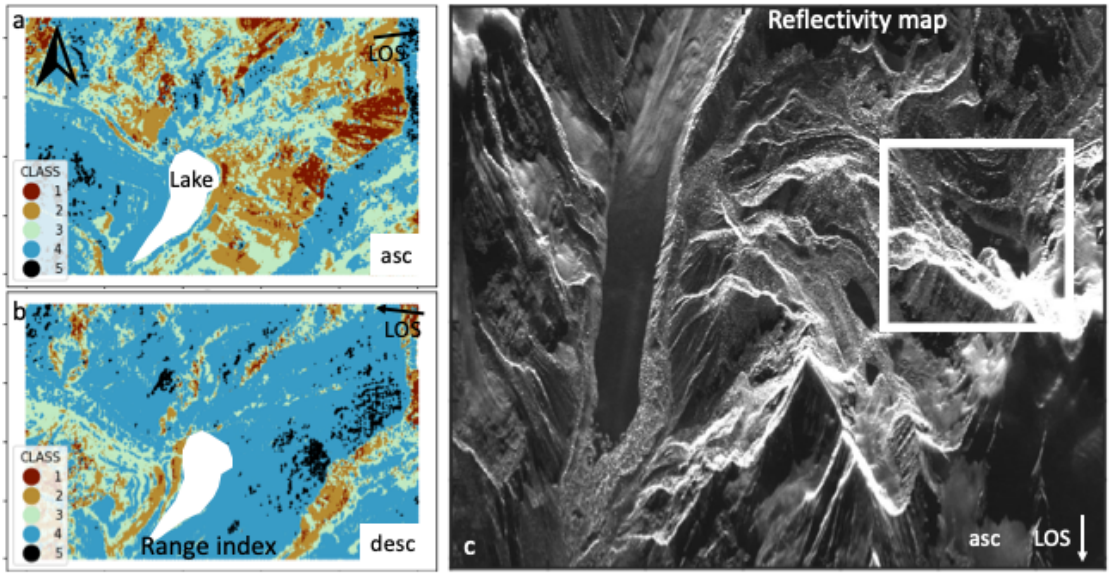

Figure 79: Layover for the ascending orbit at Upper Barun Lake's east slope. (a) Range index for the ascending orbit with class 1 indicating layover, class 2 severe foreshortening, class 3 less significant foreshortening, class 4 ideal orientation and class 5 shadowing (b) Range index for the descending orbit. (c) Reflectivity map for the ascending orbit, with the white frame depicting Upper Barun Lake with high-intensity bands that indicate layover.

Figure 80 shows the descending PSI results at the eastern slope of Upper Barun Lake. Figure 80a displays displacement rates along the steepest slope. Distinct slope areas show seasonal movements up to -150 mm/year. The vertical arrows in Figure 80d point towards landslide scars, which is also where the significant displacements lie, with the two right arrows ending in flow lobes. The lobes and the seasonal displacement pattern in Figure 80b correspond with the behaviour of rock glaciers. The scar at the left arrow in Figure 80d shows no PS in Figure 80a and no coherent CDInSAR result, possibly due to the absence of stable scattering rocks or excessive deformation. Since satellite imagery from 2003 already shows this landslide scar, the decoherence is more likely attributed to the first reason. The horizontal arrow points towards an area that looks like the deposit of the rock glacier, still actively moving down to -120 mm/year. Images from 2003 already show the presence of this structure. Here most points also exhibit a seasonal behaviour with increased movement in the summer. Since no protection exists between the slope and the lake, mass movements could directly fall into the lake at the failure of a rock glacier. In addition, the end moraine of upper Barun lake shows few displacement points with rates of -90 mm/year. Besides the location of base camp Makalu on the end moraine of Upper Barun Lake, an outburst would flow into Lower Barun Lake with the risk of inducing a second and even larger GLOF. Furthermore, many stable points show an apparent seasonal behaviour (Figure 80c) related to intra-annual frost heave and melt, pointing out PSI's sensitivity.

Barun-3 Lake

Barun-3 Lake lies almost 700 m upstream of Lower Barun Lake. Just as for Upper Barun Lake, an outburst of Barun-3 would end up in Lower Barun, possibly also triggering a GLOF at Lower Barun. Figure 81 shows the ascending and descending PSI results along the LOS and the steepest slope. The figures reveal that roughly all displacements are moving downslope with magnitudes up to -150 mm/year. The movement direction is visualised in Figure 82. The downslope displacements on the lateral moraines adjacent to Barun-3 Lake are presumably triggered by glacial debuttressing due to glacial retreat. The larger arrow points to a subsiding

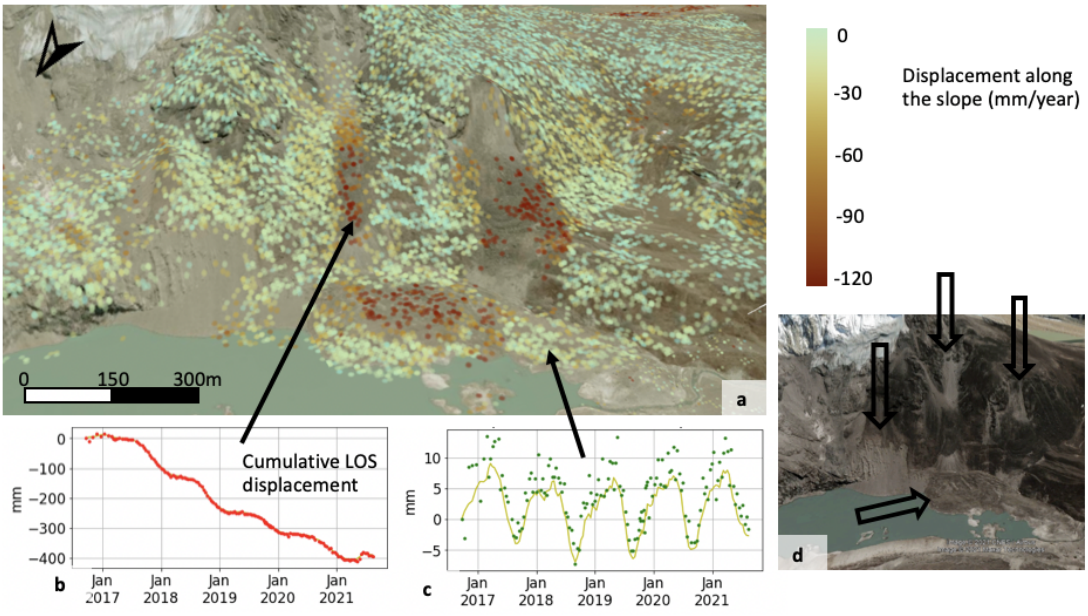

Figure 80: Upper Barun Lake. (a) Descending PSI displacement rates along the steepest slope. (b) Cumulative LOS displacement time series of a red point moving away from the satellite (temporal coherence = 0.86). (c) Cumulative LOS displacement time-series of a green point exhibiting seasonal movement but no cumulative displacement (temporal coherence = 0.89). (d) Arrows point to visible landslide scars.

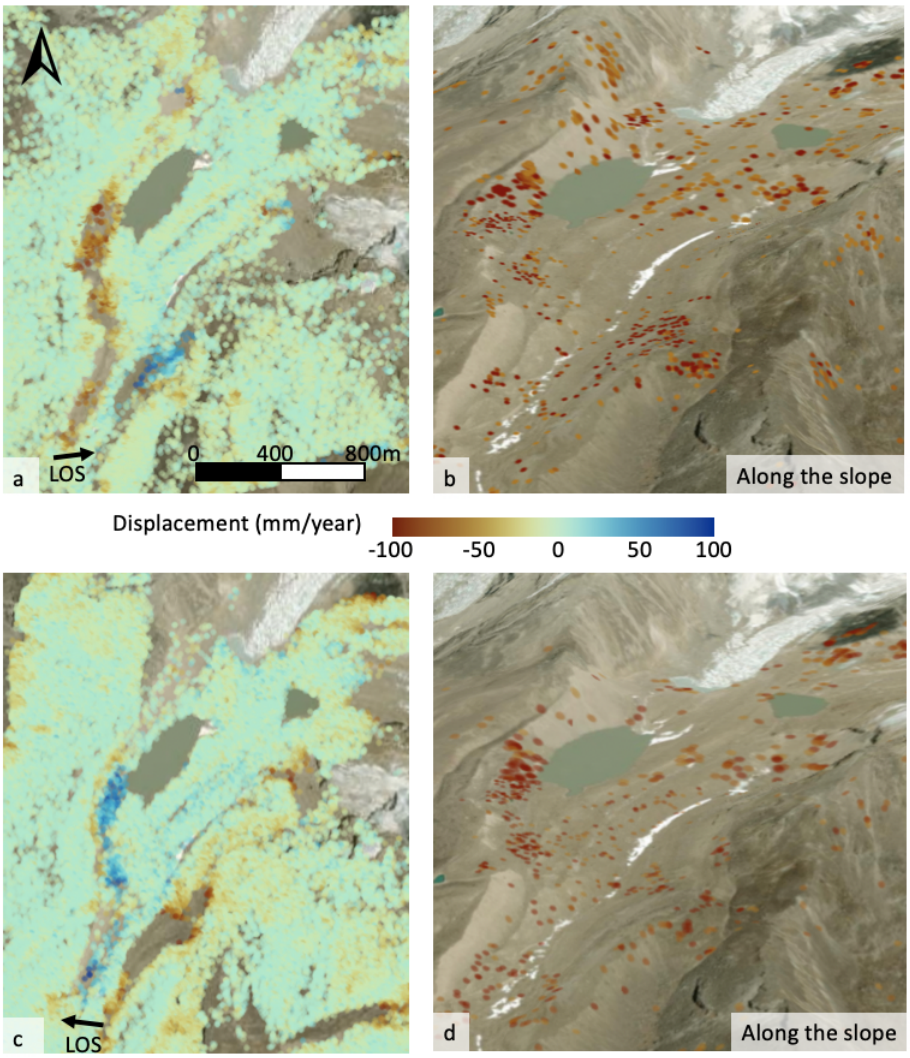

Figure 81: PSI displacement rates at Barun-3 Lake (temporal coherence > 0.7). (a) Along the LOS, ascending. (b) Along the steepest slope, ascending. (c) Along the LOS, descending. (d) Along the steepest slope, descending

area, showing a crest that reveals settling features, suggesting subsurface ice melting. Besides these features, the circles highlighting surface water also indicate subsurface ice. Consequently, these small lakes, and Barun-3, could technically be supraglacial. As melting continues, the lakes might grow, more supraglacial lakes might form, and Barun-3 Lake might expand. Due to the melting of the upstream glaciers, Barun-3 will keep receiving meltwater. This might not directly increase the GLOF risk if water can flow out. However, if subsurface ice continues to melt, the lake could deepen, and Barun-3 might evolve into a larger lake, increasing the risk of dynamic and self-destructive failure. Eventually, that would pose an even more significant risk of flooding Lower Barun lake.

4.2.4 Rolpa Lake

Rolpa Lake provides a clear example of geometric limitations related to steep mountain slopes. Figure 83a displays the slope map of Rolpa Lake's surroundings. Especially the slope facing in the southwest direction is considerably steep, with a significant region steeper than 40°. Figure 83b shows the range index map for the descending orbit, showing shadow areas on this slope

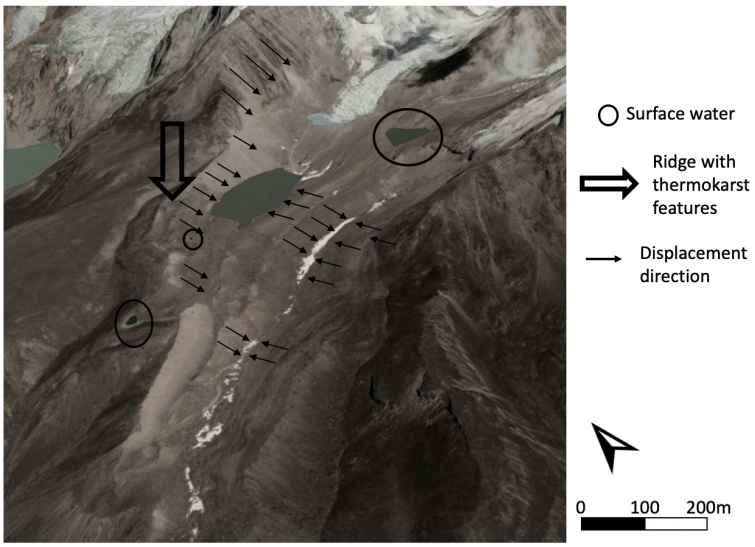

Figure 82: Barun-3 Lake. The red circles denote surface water, and the white arrows represent the primary displacement direction. The orange arrow points towards the crest that is showing settling signs. Background image from Google Earth (April 2016).

caused by the high slope angles. Rolpa Lake falls into two ascending satellite paths, and Figure 84 shows the corresponding reflectivity maps. Figure 84b shows that for the smaller incidence angle, no lake and moraine can be distinguished. As explained in section 3.1.1, the slope's steepness causes the top to be reflected before the lower-lying part, overlaying the signals surrounding the lake. Figure 84a uses a larger incidence angle that slightly overcomes this issue. However, the slope is still experiencing foreshortening and layover, as depicted by the arrow pointing towards enhanced reflectivity. Consequently, parts of the slope will not return results due to layover for the ascending and shadow for the descending orbit. Figures 83 and 84 show that the southwest slope will also experience some geometric limitations, but to a significantly less extent.

For the other slope, the range index shows that some areas will also not be analysable, corresponding with steep slope areas exceeding 45°.

The steep and irregular mountain slopes containing few spatially homogeneous areas probably prevented the correct unwrapping of interferograms. Sharp terrain changes can lead to many phase discontinuities, preventing accurate unwrapping (Gao et al., 2019; Werner et al., 2002). Figure 85 shows the spatial coherence for the ascending and descending data sets. Even though some areas display high spatial coherence, the figures reveal primarily loose patches. This defends the fact that the area is irregular, consisting of many spatially discontinuous areas.

Figure 86 displays the PSI displacements rates along the LOS surrounding Rolpa Lake. The ascending results in Figure 86a show that the northeast slope contains only few PS due to layover as explained above, and Figure 86b for the descending orbit shows the effect of shadowing resulting in no PS in some regions. The figures show significant displacements on the lateral moraine near the glacier terminus and at hanging rock glaciers on the southwest slope.

Figures 86b and 87a reveal that the lateral moraine at the glacier terminus shows significant downslope movement up to -200 mm/year. Slope deformation on lateral moraines is primarily caused by glacial retreat combined with permafrost melting, causing slope relief and subsequent instability (Deline et al., 2021; Klimeš et al., 2016). The lake has already reached the unstable lateral moraines. As the glacier melting continues, the lake will deepen and extend in the glacier direction, reaching more unstable lateral moraines, increasing the risk of dynamic failure.

The north-east slope contains fewer rock glaciers than the southwest slope, but the arrow in

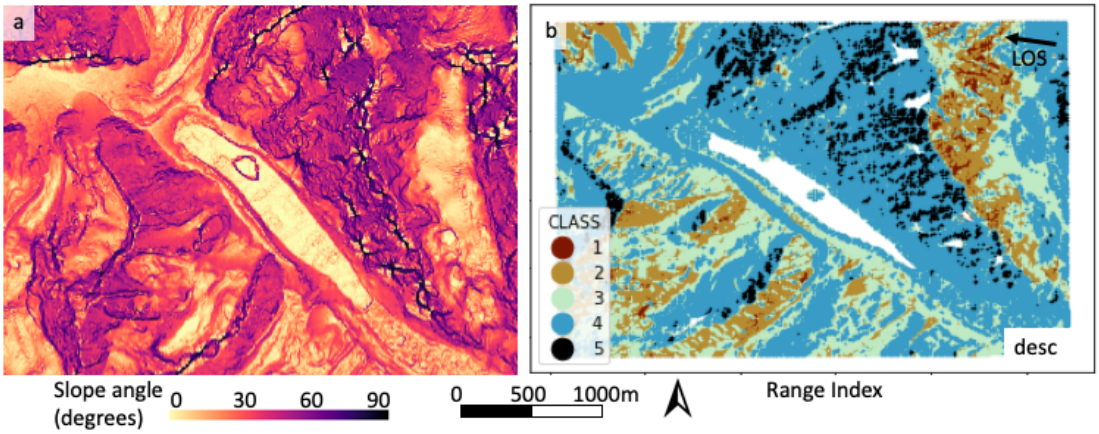

Figure 83: Rolpa Lake. (a) Slope angle map. (b) Range index for the descending orbit, where Class 1 indicates layover, class 2 severe foreshortening, class 3 significant less foreshortening, class 4 ideal orientation and class 5 shadowing.

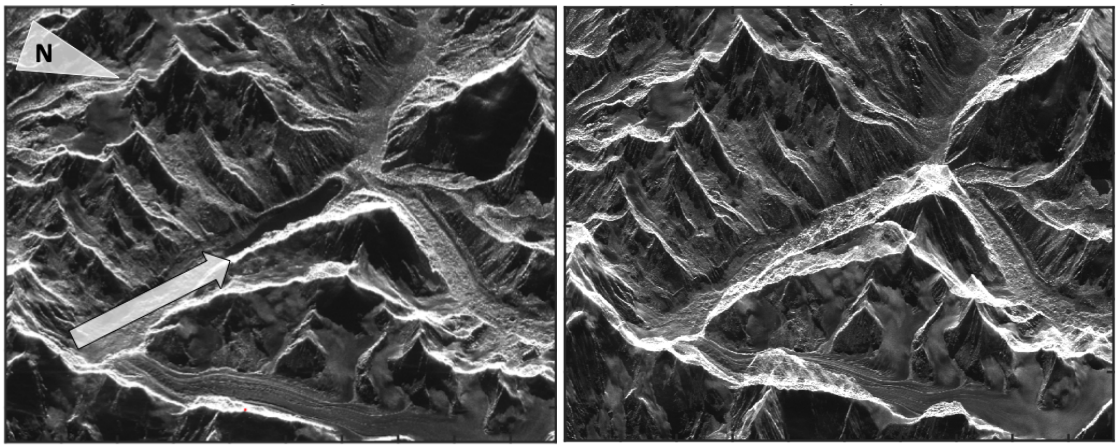

(a) Path 85 - inc. angle of 45 degrees **(b)** Path 12 - inc. angle of 33 deg

Figure 84: Reflectivity maps at Rolpa Lake (ascending). The arrow points towards the northeast slope compressed into a white high-intensity band.

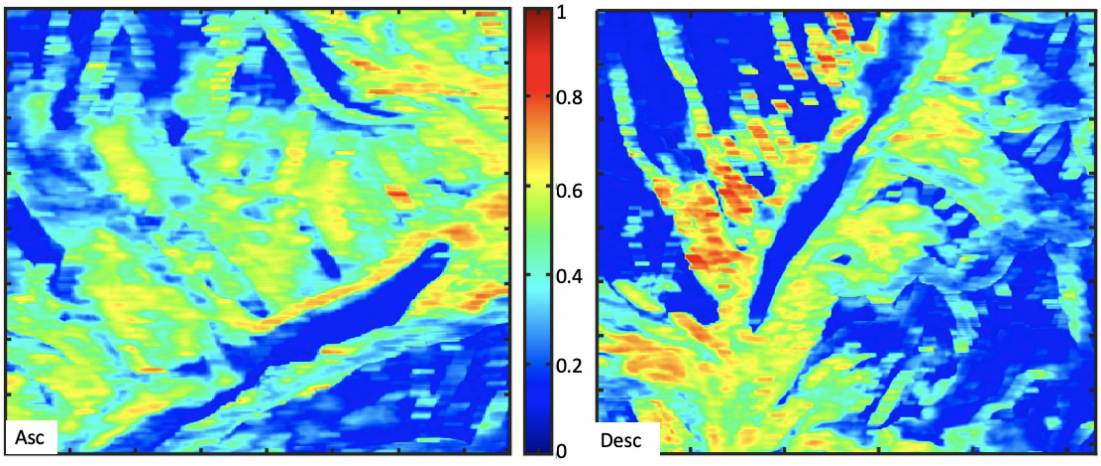

Figure 85: Spatial coherence at Rolpa Lake

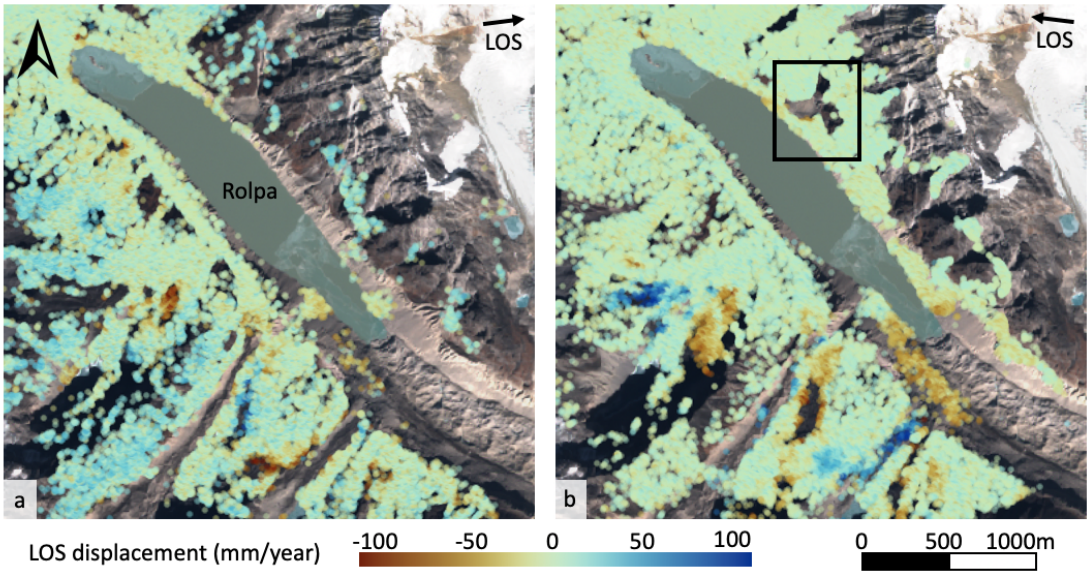

Figure 86: PSI displacement rates along the LOS (temporal coherence > 0.6) at Rolpa Lake. (a) Ascending. (b) Descending. The frame highlights a rock glacier lobe

Figure 87b points to a snow/ice mass hanging above the lake, which could directly plunge into the lake. The circle in Figure 87b highlights a flow lobe that was discovered from the PSI analysis; the black frame in Figure 86b was easily filtered out from the image since the lobe contains no PS. The reasons for no PS might be that the lobe consists of no rocks at the surface, so nothing reflects with stable amplitude, or that the lobe is moving too fast. Figures 86 and 87a also show that the southeast slopes are experiencing significant displacement points. Hanging (rock) glaciers move towards the lake with -200 mm/year rates. This slope is less steep, and not all the hanging glaciers reach the lake yet, but eventually, they could pose a dynamic failure hazard.

Figure 88 displays the ascending and descending PSI LOS displacement rates on the terminal moraine. One area adjacent to the lake is highlighted with a frame in Figure 88b that contains points experiencing LOS displacement rates up to -60 mm/year. The points show movement away from the satellite for ascending and descending orbit, indicating subsidence. The deformation region corresponds precisely with the studies of Rana et al. (2000) and Richardson and Reynolds (2000) two decades ago. Their research found exposed ice and numerous tension cracks, slumps and depressions at this location. The combination of ice melting and hydrostatic pressure is presumably causing the instability of the narrow moraine. The outlet channel constructed in 2000 stabilised the lake's area (Khadka et al., 2019), but apparently, the deformation is still proceeding. Because of its narrow geometry, the entire moraine is susceptible to self-destructive and dynamic failure (Sattar et al., 2021). However, the deforming area is of particular concern since the breach might quickly initiate in this region.

4.2.5 Thulagi Lake

Figure 89 displays the temporal coherence at Thulagi Lake. The PS for both ascending and descending orbits show low coherence values; most are around 0.5. This means that the points do not follow the deformation model well, implying they behave randomly. Therefore, the points cannot be considered accurate, and PSI is not applicable. The figure shows that the descending image consists of less PS than the ascending image. The reason is that the time frame is longer, with some larger temporal baselines in between, for the descending stack than for the ascending stack. For areas with significant temporally varying features, this can result in lower amplitude stability and less PS. In addition, most interferograms are characterised by a high amount of

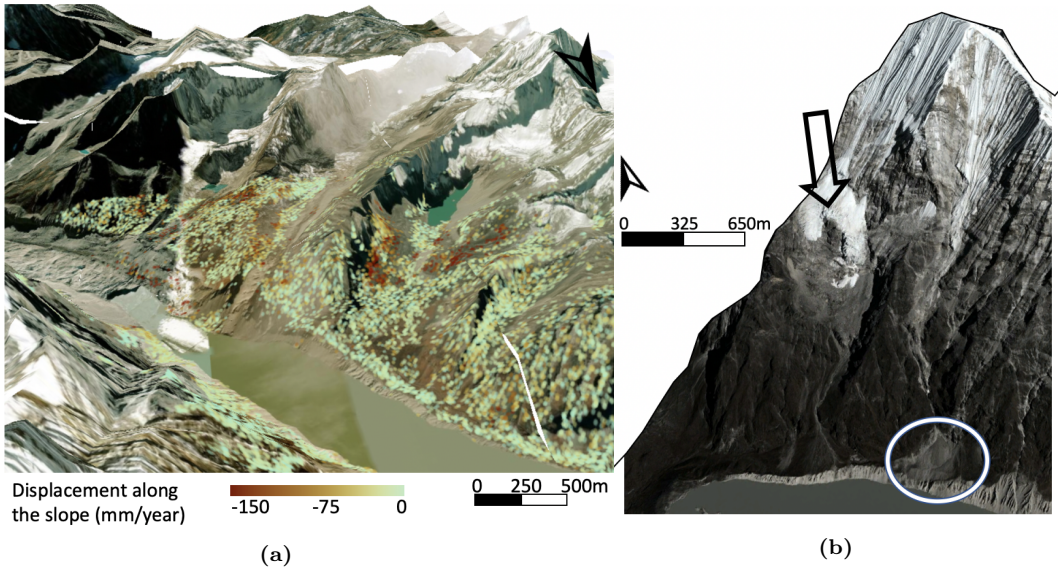

Figure 87: (a) PSI displacement rates along the steepest slope exceeding 55 mm/year (temporal coherence > 0.7) at the lateral moraines and hanging glaciers near the glacier terminus of Rolpa Lake. (b) Northeast slope of Rolpa Lake near the terminal moraine. The orange arrow points towards an ice and snow mass, and the white circle shows a flow lobe, corresponding with the black frame in Figure 86.

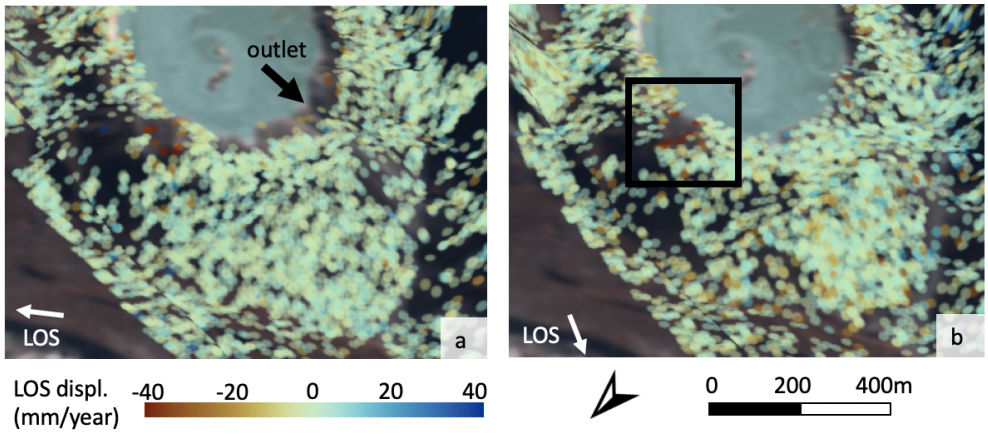

Figure 88: PSI displacement rates along the LOS (temporal coherence > 0.6) at the terminal moraine of Rolpa Lake. **(a)** Ascending. **(b)** Descending. The frame highlights an area of higher deformation rate.

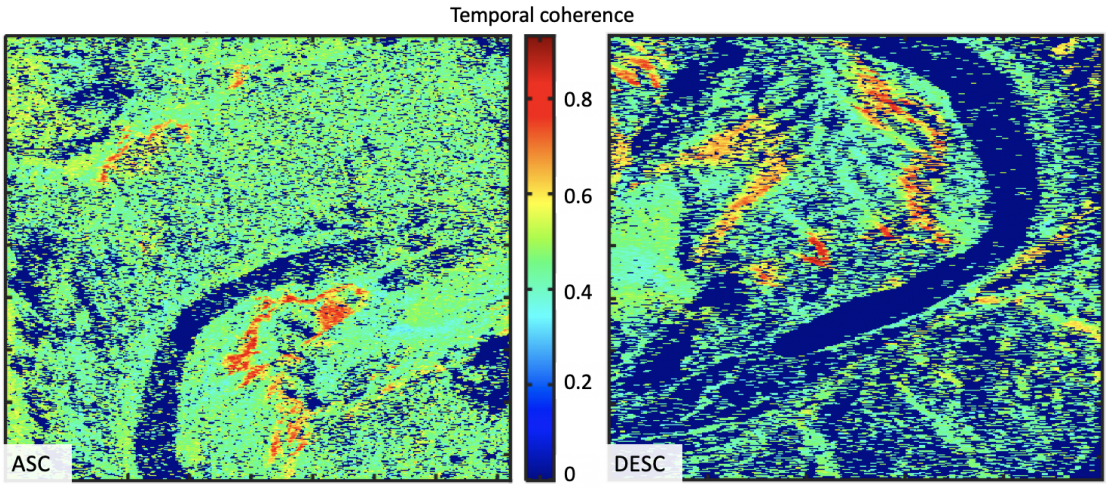

Figure 89: Ascending and descending temporal coherence maps at Thulagi Lake

noise, and the spatial coherence is low. The extant vegetation cover could explain the incoherent PSI results and interferograms. The few high temporally coherent PS primarily lie in no or light vegetation regions. As explained in Chapter 3, vegetation is often temporally incoherent as the vegetated surface conditions continuously change backscattering due to wind, snow and rainfall. Compared to the other lakes, relatively dense vegetation consisting of bushes and trees cover the lake's surroundings. The lower altitude of Thulagi Lake explains the difference in vegetation and local climate (ICIMOD, 2011). The vegetation is absent or less dense on the higher altitude slopes, but since these slopes are steep, causing geometric limitations, and experience significant winter snowfall, also here no coherent results are obtained.

Figure 90 shows two Sentinel-2 images taken during the summer. Figure 90a shows the Sentinel-2 SWIR combination, with bright green corresponding to dense vegetation, cyan to snow or clean ice and white to clouds. This image reveals that extant vegetation covers large parts of the moraine, outlet channel and slopes. Figure 90b displays the Sentinel-2 moisture index. Dark blue indicates high moisture content, yellow medium and red low. Besides the lake and snow showing high moisture, the vegetated surface also corresponds to high moisture content. Figure 91a shows what the vegetation looks like on ground level, showing the moraine area covered in bushes and shrubs. Additionally, Figure 91b reveals that this region experiences relatively high rainfall during the monsoons compared to most other lakes. For example, Imja Lake receives 1100-1500 mm per year, whereas Thulagi Lake receives 2600-3600 mm per year. As explained in Chapter 3, the high monsoonal rains can significantly change the vegetated surface conditions, causing temporal decorrelation. The snow in the winter, and the vegetation in the summer receiving high rainfall, leave a relatively short period for suitable circumstances. Therefore, the temporal and spatial coherence is low, and InSAR is less applicable.

Despite the challenging conditions, four interferograms from December 2016, November 2017, December 2018 and December 2020 showed coherent results at the terminal moraine area. In this period, the region is not yet covered by snow, the monsoon has ended, and vegetation seems less extant on optical images due to the lower temperature. These conditions make the unwrapping less challenging since the surface varies less between satellite acquisitions. Figure 92 shows Sentinel-2 moisture index images during November and December. All the coherently unwrapped images are during dry surface conditions, revealing the impact of surface moisture. However, dry conditions do not necessarily mean that the images are coherent, as then more images should have been unwrapped correctly during these periods. For example, dry vegetation could still cause temporal decorrelation of the results, especially if other conditions are sub-optimal. Like the other case studies, such influences could be the geometric baseline, atmo-

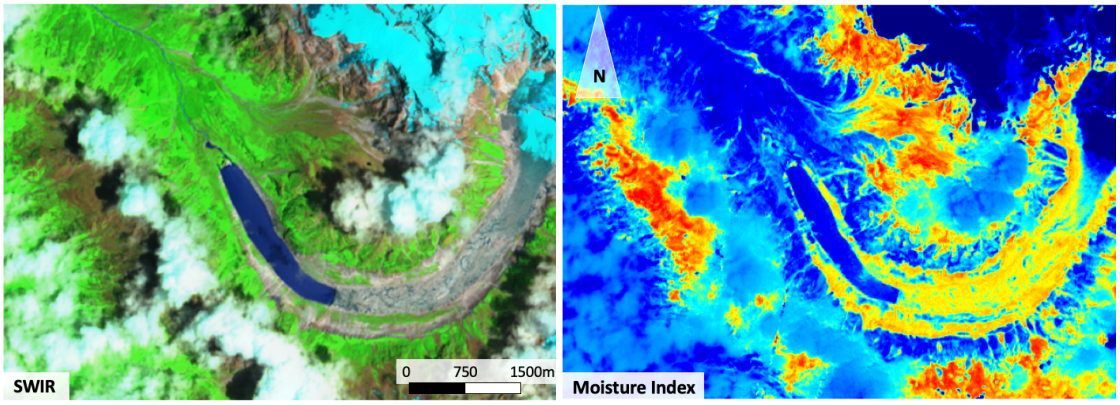

(a) (b)

Figure 90: Sentinel-2 images of Thulagi Lake in August 2020. (a) SWIR combination. (b) Moisture index.

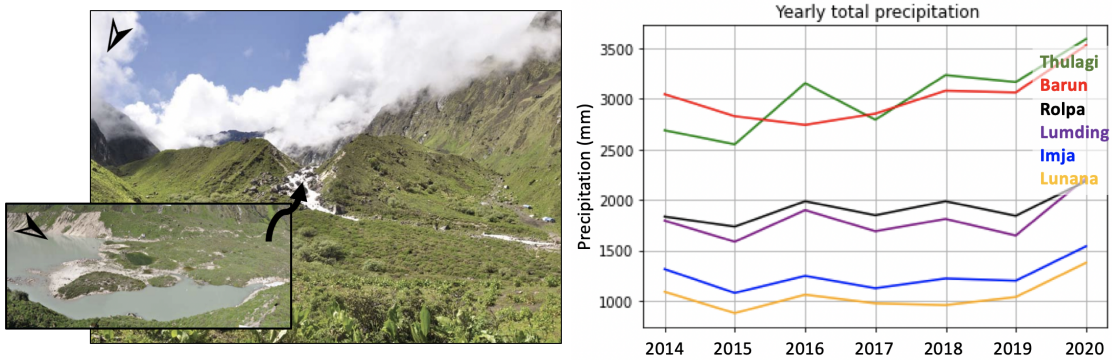

(a) (b)

Figure 91: (a) Thulagi Lake's vegetated surroundings. The primary image shows the moraine downstream of the lake, and the inset displays the terminal moraine adjacent to the lake. Photo's retrieved from (ICIMOD, 2011). (b) Comparison of yearly precipitation amounts per lake.

spheric contributions or geometric limitations resulting in spatial discontinuities causing errors that propagate throughout the image.

Figure 93 shows an ascending and descending unwrapped interferogram, revealing negative LOS displacements at the end moraine. The other coherent images show similar results, indicating that the moraine is experiencing subsidence. This subsidence is likely due to ice melting, as geophysical surveys revealed ice in the moraine (ICIMOD, 2011; Rounce et al., 2016). Haritashya et al. (2018) found a maximum elevation change at the end moraine of -1.2 m/year, with an average change of less than -0.5 m/year between 2000 and 2014 by differencing DEMs. According to CDInSAR in Figure 93, the negative LOS displacement at the end moraine is approximate -10mm/6 days, with a maximum of -15 mm/6 days, translating into -600 mm/year or even -900 mm/year. However, since only two images were unwrapped correctly, this cannot be concluded from InSAR alone.

4.2.6 Lumding Lake

Apart from Thulagi Lake, Lumding Lake proved to be more challenging than the other lakes. PSI and the descending stack for CDInSAR returned coherent results, but for the ascending stack, the unwrapping was too challenging to obtain coherent results. This could be attributed to various reasons. Since the descending stack contains several coherently unwrapped images

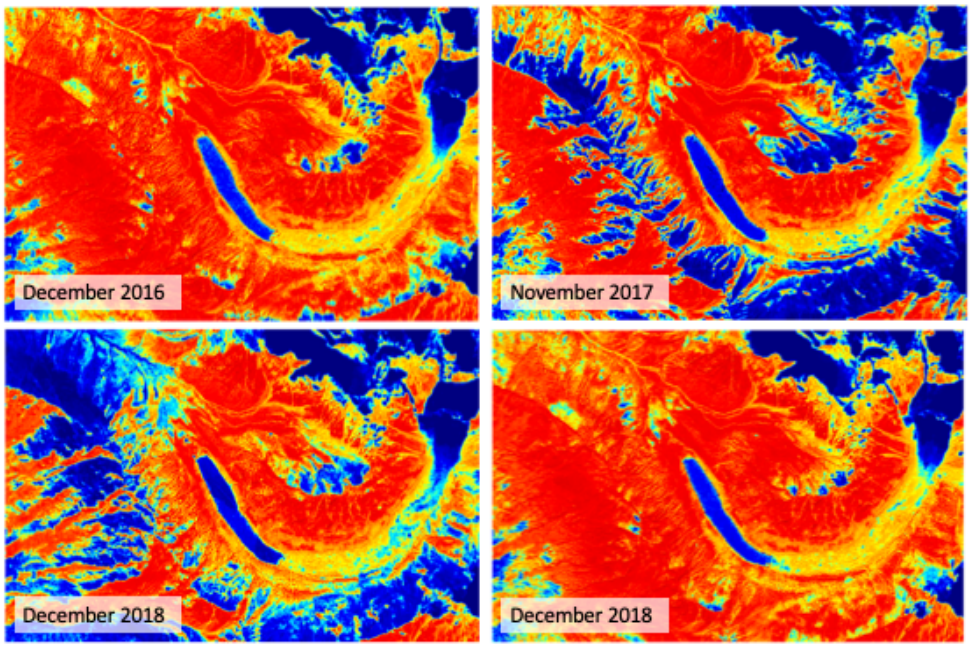

Figure 92: Sentinel-2 Moisture index images during periods of correctly unwrapped interferograms

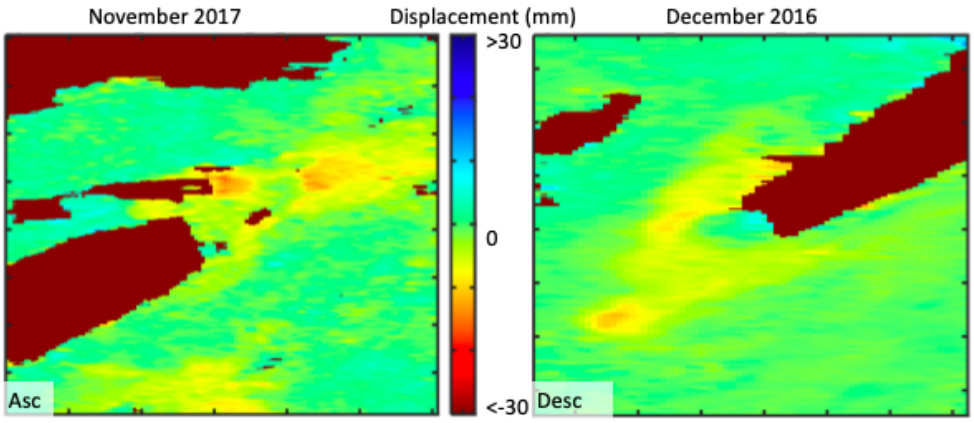

Figure 93: CDInSAR displacement over a 12-day interval at Thulagi Lake's terminal moraine

and the ascending does not, the difference in orbits could have influenced the processing. As explained in section 3.1.1, geometric issues can arise, which can be more significant for a particular orbit. Figure 94 displays the spatial coherence map for the ascending and descending data set. The figure reveals that the spatial coherence is higher in several areas for the descending stack than for the ascending data set. This possibly leads to the difference in results between the two stacks since areas with low coherence are more challenging to unwrap. As explained in section 3.2.1, less spatially homogeneous areas have more spatial discontinuities that can cause unwrapping errors. The variation in spatial coherence between the two orbits is likely attributed to the difference in geometric limitations. Figure 95 displays the ascending and descending range index maps, showing the impact of geometric limitations. From these images, it is not immediately apparent that the descending orbit has a more favourable orientation, only that the ascending orbit experiences more layover (9.3%) than the descending orbit (4.4%). If the difference in spatial coherence is indeed attributed to geometric limitations, it would mean that layover causes a significant amount of spatial discontinuities producing errors that propagate throughout the image. Especially in combination with snow cover, unwrapping can become challenging. A significant area surrounding Lumding Lake contains snow all year round. Figure 96c shows a Sentinel-2 image using the false colour geology combination in the summer of 2019, where cyan corresponds with snow and ice. The image reveals the extent of summer snow, decreasing the area applicable for InSAR. As explained in Chapter 3, snow influences the dielectric properties of the surface, resulting in temporal decoherence (Barboux et al., 2014; Malinverni et al., 2014; Tsai et al., 2019). The southern slope seems more favourable for the ascending orbit from the range index in Figure 95, but since this slope is primarily covered in all-year-round snow, the spatial coherence in Figure 94 is low for both orbits.

Figure 97 shows the timeline of correctly unwrapped descending interferograms. A clear pattern in coherent results emerges; January to July corresponds to decorrelated InSAR results. The interferograms during this period are characterised by noise, and Sentinel-2 images reveal that the area is covered in thick snow during these months, with no bare soil or rocks visible. This timeline shows how significantly the snow influences InSAR's results. The PSI results in Figure 98 also show a sharp boundary of PS at the snow border during the summer visible in Figure 96c. The whole area is covered in snow during the winter, but the snow retreats to approximately this boundary during the summer. This boundary shows snow's significant influence on measuring displacements with PSI.

Figure 98 shows the PSI results and Figures 96a and b provide examples of unwrapped interferograms with CDInSAR. The figures reveal that the terminal moraine is not experiencing significant displacements. No geophysical research has been conducted yet, but optical imagery reveals no thermokarst ponds on the moraine, suggesting the moraine is not ice-cored, agreeing

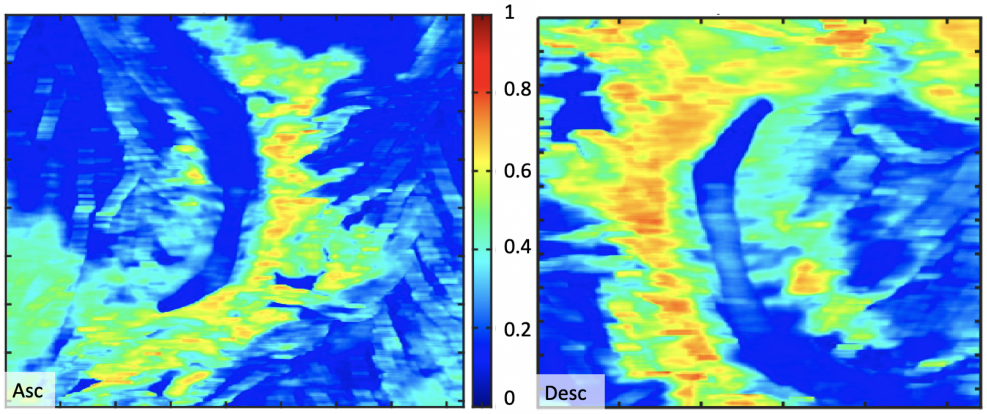

Figure 94: Spatial coherence maps of Lumding Lake

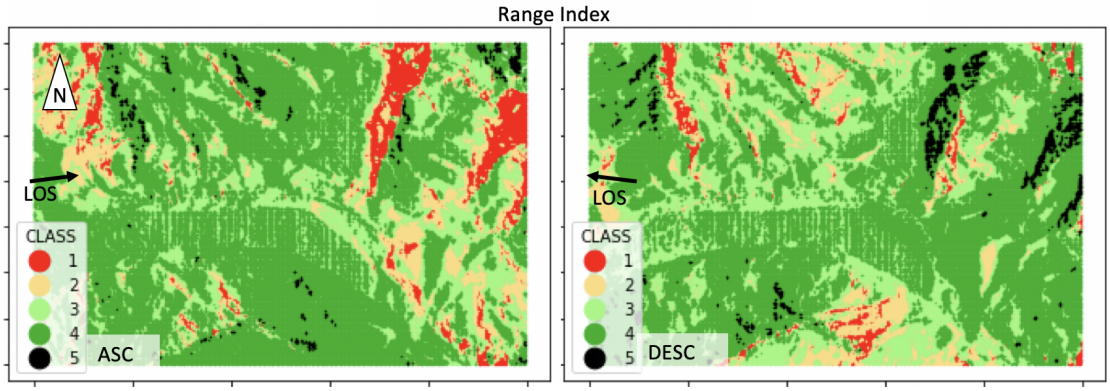

Figure 95: Range index maps of Lumding Lake (asc θ = 33.81, desc θ = 38.31). Class 1 = layover (asc: 9.3%, desc: 4.4%), Class 2 = severe foreshortening (asc: 14.8%, desc: 12.5%), Class 3 = less foreshortening (asc: 29.1%, desc: 34.5%), Class 4 = ideal conditions (asc: 46.3%, desc: 47.1%) and Class 5 = shadow (asc: 0.52%, desc: 1.50%).

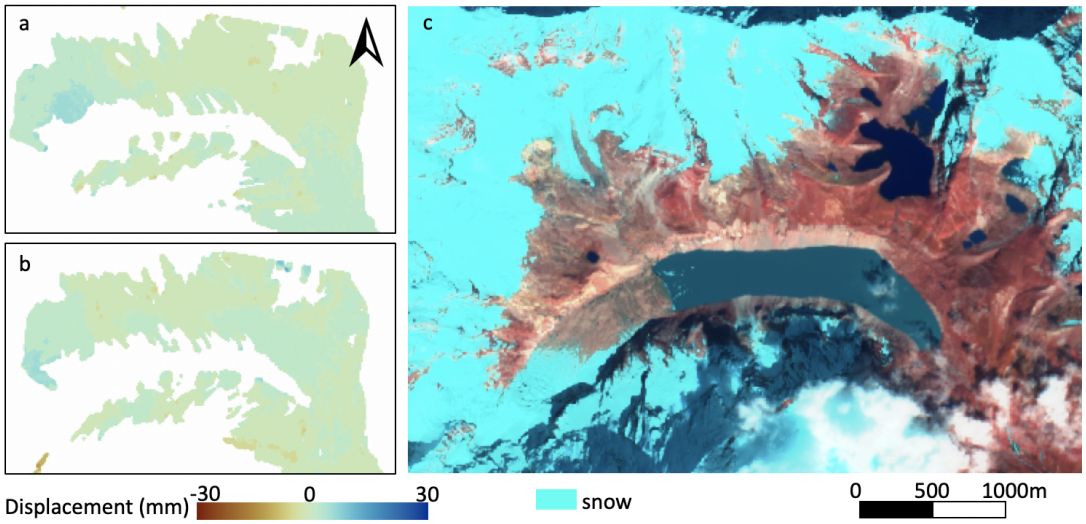

Figure 96: Lumding Lake. (a) CDInSAR (descending) displacement between 2016-11-08 and 2016-11-20. (b) CDInSAR (descending) displacement between 2017-11-15 and 2017-11-27. (c) Sentinel-2 false colour geology image (August 2019).

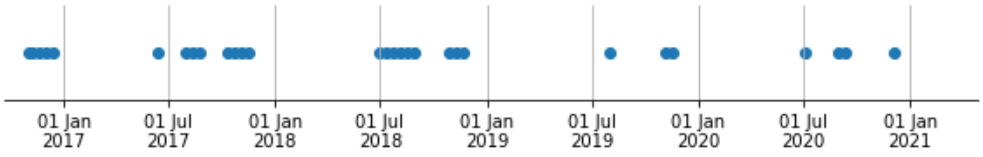

Figure 97: Timeline of coherent interferograms at Lumding Lake (descending)

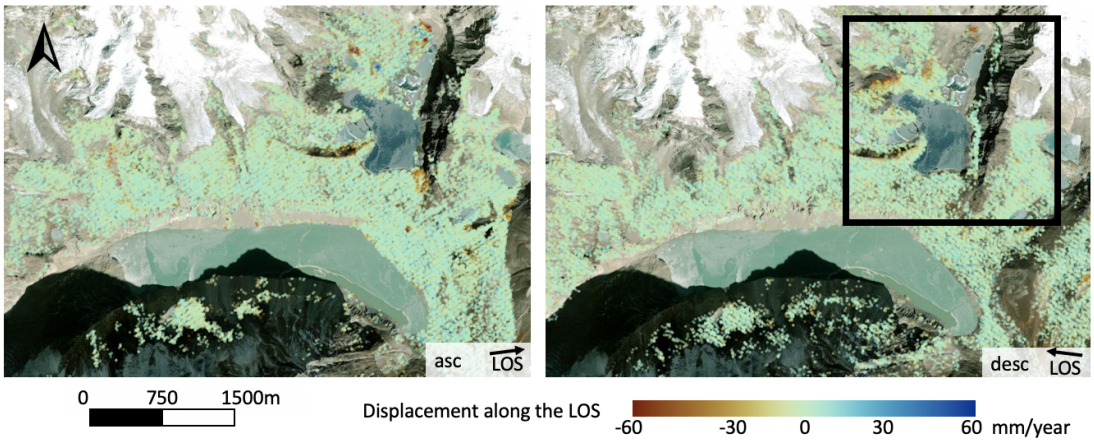

Figure 98: PSI displacement rates along the LOS at Lumding Lake (temporal coherence > 0.65). The area in the frame is displayed in Figure 99.

with Rounce et al. (2016). Nonetheless, since the moraine is steep, the lake is still susceptible to self-destructive failure. The PSI results show that the lakes above Lumding Lake do show some displacement areas. The largest lake lies 300 m higher than Lumding Lake, and if mass falls into one of these lakes, water might burst into the lower-lying Lumding Lake.

Figure 99 displays movements projected along the slope at these upstream lakes. A disadvantage of this method becomes apparent at Lumding Lake. As mentioned in section 4.1.2, errors of PS that lie on slopes will be amplified. For LOS movements, these errors can be minor, but by projecting those points along the slope, they can be multiplied with a factor up to 3.33. Figure 98 shows that most points are relatively stable, with less than 10 mm/year deformations along the LOS. However, when projecting these points along the slope in Figure 99, larger movements with varying displacement rates are witnessed scattered randomly throughout the area. Since they are randomly distributed and are surrounded by stable points, these movements might be inaccurate and attributed to noise. By projecting the displacements along the slope, these errors have been amplified. The probable reason for the noise is that many points have low amplitude stability (around 0.5) due to the high amount of winter snow that completely covers the area for several months. Optical imagery reveals that the amount of snow is significantly higher than at the other lakes, which also have more high amplitude stability points (except for Thulagi Lake in section 4.2.5) than Lumding Lake. Still, if these randomly distributed displacements, which move downslope with rates primarily between -10 and -50 mm/year, are ignored, a few areas stand out near the west lake with along slope displacement rates up to -80 mm/year. This mass moving towards the lake might initiate flood waves that reach Lumding Lake, raising the risk of dynamic failure. Furthermore, Lumding Lake's south slope is steep and lies close to the lake. Therefore, rockfall and ice avalanches could directly fall into the lake, increasing the chance of dynamic failure. However, as mentioned above, optical imagery reveals that this slope is covered in snow year-round, making InSAR not applicable for this region.

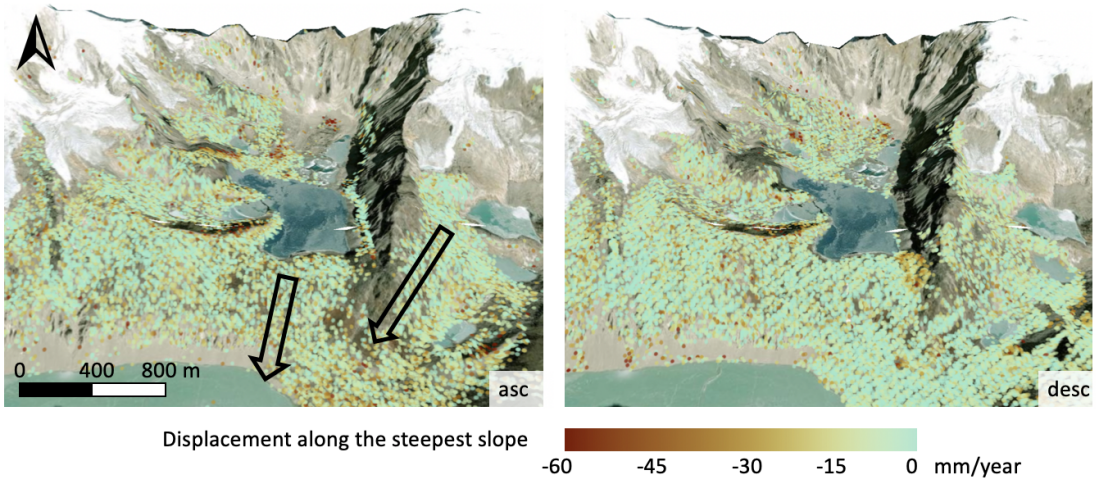

Figure 99: PSI displacement rates along the steepest slope at the smaller lake north of Lumding Lake (temporal coherence > 0.65). The arrows depict the (potential) water flow towards Lumding Lake.

5 Discussion

This chapter will summarise the findings and critically discuss the method and limitations of an InSAR-based analysis by answering the research subquestions of Chapter 1. Together, these answers will explain how satellite InSAR contributes to monitoring and analysing potentially dangerous glacial lakes.

- How should the InSAR observations at glacial lakes be interpreted?

The answer to this question will briefly explain applying an InSAR-based analysis to glacial lakes using the observations from this thesis. Figure 100 summarises how additional data sources can be used to interpret the InSAR observations. Beforehand, the applicability of InSAR can be estimated using the range index and optical imagery. The range index uses the satellite's incidence and azimuth angle and the local slope angle and aspect to calculate geometric distortions (Notti et al., 2014). As a result, this index indicates whether a specific satellite can be used or a slope is analysable using an InSAR-based method. Optical imagery can reveal vegetation and snow covers and continuous optical images should be used to determine whether areas are only affected by snow and vegetation in certain months or specific years, as that will determine the applicability of InSAR. With meteorological data, the snow and monsoon months can be determined, which is convenient for the main image choice for PSI and indicates which images are less challenging to unwrap for CDInSAR.

The dominant direction of InSAR displacements can be determined in various ways. In this research, the movements have been analysed along the LOS, decomposed into vertical and east-west components and projected along the steepest slope (Milillo et al., 2016; Notti et al., 2014). The most convenient method depends on the coverage and type of movement. Decomposing the displacements is only possible for areas covered by both ascending and descending orbits and is useful when the interest lies in the sole east-west or vertical movement. For example, obtaining the vertical component might be desired to measure moraine subsidence. However, this is not always possible due to the variation in ascending and descending coverage, which depends on temporal baselines and geometric limitations. Another limitation is that north-south directions are entirely neglected. The vertical or east-west component might be less interesting for slope movements, regardless that geometric limitations often prevent the decomposition. Instead, projecting down the steepest slope will accommodate low sensitivity relating to the slope's orientation, so north and south displacements can also be plotted. Limitations are that the projection will amplify error contributions and is incorrect for movements that do not behave

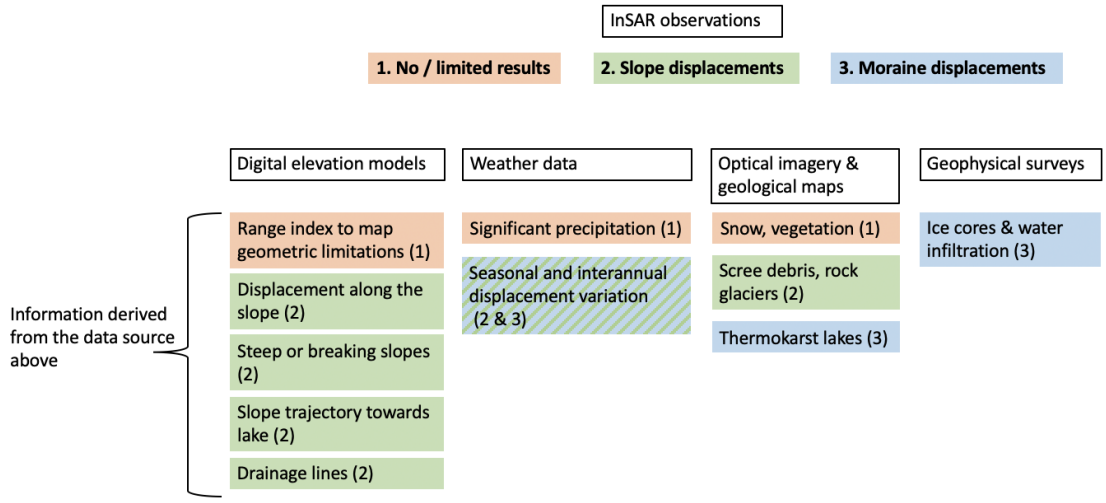

Figure 100: Summary of how additional data sources support the interpretation of InSAR observations

along the steepest slope. Using LOS displacements might be the best option for those regions and flat areas only covered by one orbit. The InSAR data is then presented in its original way; no displacement directions are neglected, and no displacements are incorrectly amplified. It does require careful analysis using both orbits, slope angle, aspect and geomorphological analysis to correctly indicate the dominant direction while considering that the movement is less sensitive in the north-south direction.

The reason and mechanism for deformations observed with InSAR can be explained with geomorphological, topographical, meteorological and optical data. By combining these sources, slope displacements can be linked to rock glaciers, scree deposits and debuttressing lateral moraines and moraine subsidence to melting ice cores. Seasonal displacements can be linked to intra-annual temperature and precipitation variation, but a research time frame of five years is too short to conclude on inter-annual observations. Analysing the impact of climate change or the effect of years with higher precipitation or temperature requires a longer research time frame. Accelerating displacements might be observed near failure for large scale instabilities exhibiting a more ductile or time-dependent behaviour. When analysing over more extended periods, observed activity changes in, for example, rock glaciers could indicate climatic changes in the area, providing a warning for other areas such as the glacier, moraine and slopes susceptible to avalanches or rockfall (Klimeš et al., 2016). In particular, an InSAR-based analysis should be applied to identify displacements developing in beforehand stable (outer) moraine areas or slopes. This method can raise attention to specific regions and aid in applying mitigation measures, performing hazard assessments and modelling outburst scenarios.

- What can be concluded about the GLOF hazards and stability at the six glacial lakes?

Imja Lake's inner moraine is deforming rapidly, presumably caused by ice melting, corresponding with the studies of Dahal et al. (2018) Hambrey et al. (2008) that found dead ice beneath the moraine and with Haritashya et al. (2018) who detected significant subsidence. As a result, the inner moraine will eventually disappear, and the lake will reach the outer part. Then, as highlighted by Sattar et al. (2021), the end moraine could melt and gradually lower the lake, decreasing the GLOF risk, or the moraine could become narrow, reducing its stability and increasing the risk. An unexpected finding was the inner moraine experiencing displacement lake inwards, which might be explained by a decrease of hydrostatic pressure on the moraine because of the lake lowering. This phenomenon calls for further investigation to conclude the mechanism. Rock glaciers and scree deposits dominate the slope movements outside the lateral moraines. The high lateral moraines will protect the lake from these mass movements for now (Khatiwada and Dahal, 2020; Kroczek and Vilimek, 2020; Rounce et al., 2016). The lateral moraines themselves, however, are steep and contain loose and unconsolidated material, which can directly fall into the lake, causing flood waves. Furthermore, the melting glacier south of Imja Lake can raise dynamic failure hazards if it forms a glacial lake behind the lateral moraine of Imja Lake.

Several lateral and terminal moraines are experiencing subsidence and downslope movement at the **Lunana Lakes**, presumably due to the melting of internal ice. The degradation of the moraines and internal ice melting corresponds with previous on-site studies (Nayar, 2009; NCHM, 2020; Singh, 2009). Wangchuk et al. (2022) found similar displacements with InSAR in the area, except for the narrow moraine between Thorthormi and Raphstreng Lake. Where Wangchuk et al. (2022) found no significant displacements, this study did find considerable downslope or subsiding points. This difference could be caused by the different time frames, applied displacement models or amplitude stability threshold. With ongoing glacier melting, the hydrostatic pressure and internal dam melting will increase the probability of bursting. The risk is significant with the lakes containing a significant amount of water and lying in each other's direct vicinity. Especially for the narrow moraine between Thorthormi and Rapshtreng, which is only a few metres higher than Thorthormi's lake level. In addition, Wangchuk et al. (2022) found significant seasonal variation in surface scattering related to ice and melting processes,

corresponding with the displacement seasonality observed in this thesis. Moreover, Lugge Lake's north slope reveals active rock glaciers that can directly plunge into the lake at failure. A moraine or slope failure can trigger a domino effect in the worst-case scenario (NCHM, 2019; Singh, 2009; Wangchuk et al., 2022).

Upper **Barun Lake** shows landslide scars and rock glaciers experiencing significant displacements that, at failure, can directly slide into the lake and cause flood waves. The surroundings of Barun-3 Lake show many downslope and subsiding movements, indicating loose soil and ice underneath. Barun-3 and other supraglacial lakes might expand at further subsurface ice melting. The larger Lower Barun Lake lies downstream of Upper Barun and Barun-3 Lake. Therefore, an outbreak of one of the upstream lakes could induce a second outbreak of Lower Barun. The end moraine of Lower Barun Lake showed some subsidence near the outlet, but not as significant as the study of Haritashya et al. (2018) suggests. The difference in results could be caused by the decorrelation of the PSI analysis or the different time frame. The dam is not as high and steep as Rolpa's moraine, for example, but the volume of water is the highest of all glacial lakes in this research, increasing its risk (Sattar et al., 2021).

Rolpa Lake's high and narrow terminal moraine showed a small area of significant displacement. The subsidence corresponds with the studies of Rana et al. (2000), revealing the length of this instability. In addition, it shows that the outlet channel constructed in 2000 to lower the hydrostatic pressure did not influence the unstable area. Since the moraine is high and narrow, the hydrostatic pressure is high, and the moraine is susceptible to a self-destructive failure or breaching by a dynamic event. Therefore, the moraine and especially the deforming area should be investigated and monitored to prevent breaching at this location. The lateral moraines near the glacier terminus reveal significant downslope movements, increasing their hazard at increasing glacier retreat. Furthermore, the lake slopes contain rock glaciers actively moving towards the lake, posing the threat of ice and rockfalls. A large part of the north slope was too steep to analyse with interferometric synthetic-aperture radar (InSAR). The combination of hanging glaciers, steep slopes, lateral moraines displacements, moraine geometry and the subsidence area of the end moraine highlight the chance of dynamic and self-destructive failure of Rolpa Lake. More studies also highlighted the GLOF danger due to the dam's geometry, its degradation signs and the surrounding steep slopes (Bajracharya et al., 2020; Byers et al., 2017; Fujita et al., 2013; Khadka et al., 2018; Rounce et al., 2017a; Shrestha et al., 2012).

persistent scatterer interferometry (PSI) was not applicable at **Thulagi Lake**, presumably because of the extant vegetation, combined with high rainfall in the summer and snow in the winter, causing temporal decorrelation. However, conventional differential interferometric synthetic-aperture radar (CDInSAR) did return a few coherent results, revealing subsidence at the moraine, probably due to ice melting (Haritashya et al., 2018; ICIMOD, 2011; Rounce et al., 2016). In addition, Thulagi Lake's steep and narrow moraine is less able to withstand significant hydrostatic pressure, increasing the risk of self-destructive failure with a degrading dam.

No displacement was found at the end moraine of **Lumding Lake**, explained by the probable absence of ice (Rounce et al., 2016). However, the smaller lakes upstream of Lumding Lake did show unstable surroundings. If mass fell into one of these lakes, the lake could burst into Lumding Lake. Moreover, Lumding could be susceptible to avalanches and rockfalls from the southern slope, but this slope was hardly analysable because of its snow cover.

Furthermore, seasonal displacement variations could be observed at all glacial lakes ranging from millimetres to decimetres. Stable areas experiencing no significant displacements still showed millimetre seasonal changes, probably attributed to frost heave and melting, whereas downslope displacements showed larger differences, with significantly increased movement after the summer and less activity in the winter. This corresponds with meteorological data and optical imagery that reveal the stark differences in temperature, precipitation and snow cover throughout the year. The increased slope displacements and moraine subsidence in the summer

correspond with the seasonal variation in previous GLOF events, as most events have occurred in the summer (Falátková, 2016; Veh et al., 2019).

- What is the applicability to glacial lakes of the specific InSAR methods used in this study?

This study demonstrates the capability of applying PSI and CDInSAR to glacial lakes. PSI was well capable of monitoring displacements surrounding glacial lakes, probably since the area consists of many bare rocks. However, some situations and regions proved to be more challenging. Overall, the ASI threshold could not be too high since most areas are covered by snow in the winter, significantly decreasing amplitude stability over the research time frame. Areas covered in snow all year round, such as mountain tops, were not analysable with InSAR as expected due to previous research (Barboux et al., 2014; Malinverni et al., 2014; Tsai et al., 2019). The amplitude stability of points at each lake depended significantly on the snow and vegetation coverage. Areas with less winter snow and no vegetation consisted of many points with a threshold between 0.6 and 0.7. Conversely, areas with lots of snow or extant vegetation mostly contained points with an ASI of 0.5-0.6. Terminal moraines that deform fast and have many thermokarst lakes showed either no PS due to too rapid displacements or only showed PS when lowering the ASI to 0.5. Due to the low amplitude stability threshold, assessing single points might be less accurate. Consequently, only areas containing multiple similar displacement points and points that exceed a certain temporal coherence threshold have been used to conclude geomorphological phenomena to increase the likelihood of investigating actual behaviour. Still, a lower amplitude stability index comes at the expense of accuracy. Thulagi Lake returned no coherent PS, presumably because of the extant vegetation. Lumding Lake was significantly affected by the high amount of snow, resulting in less stable PS as they were more affected by noise. This became especially apparent after projecting displacements along the slope, which amplified such errors (Notti et al., 2014).

CDInSAR proved challenging for some lakes since the areas consist of many incoherent and autonomously moving regions. Such discontinuities can cause errors that propagate throughout the image (Zebker and Lu, 1998). However, it proved valuable for some occasions where PSI was incoherent and for validating displacements. For example, CDInSAR measured subsidence at Thulagi Lake's moraine, whereas PSI was incoherent, and CDInSAR confirmed both the subsidence and inward movement at Imja and Lugge Lake's end moraine. This proves that combining PSI and CDInSAR validates observations and increases spatial and temporal coverage. A disadvantage of CDInSAR is the difficulty of assessing the quality of phase unwrapping since every unwrapped image contains correctly and incorrectly unwrapped areas. These areas consist of temporally or spatially heterogeneous areas such as snow, steep mountains and glaciers. Consequently, each image is assessed visually and manually to whether it seems reliable enough in the area of interest. This makes it challenging to judge whether the precise displacement values are accurate. CDInSAR worked best in conditions without snow or monsoons, generally between October and December. In areas significantly covered in vegetation or snow, the phase unwrapping was only possible during those months as wet vegetation and snow distort the SAR signal (Barboux et al., 2014). This implies that a main image acquired during these months should be selected for PSI, as they are probably the least affected by noise.

- What are the limitations and inaccuracies of applying InSAR to glacial lakes?

The steepness and orientation of mountain slopes, vegetation, snow and too fast deformations limited analysable areas for all glacial lakes. These issues would also arise at other glacial lakes when applying InSAR. Geometric limitations might be overcome by combining (future) SAR systems with different orbits, incidence angles and revisit times operating over the area. Decreasing the radar sensitivity by using higher radar wavelengths, such as L-band (e.g. 23 cm for ALOS PALSAR), can achieve deeper penetration of vegetation and snow. However, they will also be less sensitive to smaller displacements and surface roughness, and still be affected by moisture content (Tsai et al., 2019; Zhou et al., 2019). Rapid developing mechanisms, including

brittle rock instabilities or too fast moraine subsidence, will often not be measured by InSAR (Carlá et al., 2019; Klimeš et al., 2016; Scapozza et al., 2019; Wangchuk et al., 2022). This is partly due to the dependence on data availability. For five out of six study areas, the temporal baseline was too large (up to four months) between 2014 and 2016. This prevents obtaining correct measurements at rapidly deforming regions since the displacement between two images can only be as large as 14 mm for C-band data (Ferretti et al., 2005). For example, the deformation at parts of Imja Lake's moraine dam was too large to measure with PSI, and CDInSAR does not provide enough coherent images to monitor landforms continuously. Therefore, such areas require other methodologies. For example, larger wavelengths for quick deforming areas can measure larger quantities between acquisition data before encountering aliasing, provided that the revisit time is still short (Yang et al., 2020). DEM differencing has also proven to measure large moraine displacements (Haritashya et al., 2018; Wangchuk et al., 2022), but continuous high-resolution DEMs should be available to use this as an accurate monitoring strategy.

Some aspects might have influenced the accuracy of InSAR's displacement results. First, the InSAR displacements have not been compared with in situ measurements or GPS other than previous outcomes obtained from the literature. Even though the displacements have been obtained with two different InSAR methods and correspond with geomorphological phenomena, adding on-site measurements could aid in decomposing movements, data validation and indicating noise attributions (Bayer et al., 2017; Hu et al., 2014; Kalia, 2018). Second, selecting a stable reference point is essential to achieving reliable results (Kampes, 2006; Tofani et al., 2013). This method uses a point of high temporal coherence in a seemingly stable area, but it is not known whether this area is precisely stable. Whether an exactly stable point even exists is questionable since glacial lake environments consist of significant mass-wasting and erosive influences, snow and frost heave. PSI revealed that all stable areas exhibit minor displacements due to seasonal ice melt and frost heave variation. Nevertheless, the data sets have been processed with multiple reference points, showing similar results, implying that the atmospheric contribution is minimal and the overall displacements are likely correct but possibly not millimetre accurate. Third, aliasing at rapid moving areas, such as quick degrading terminal moraines, might have underestimated the final signal, suggesting higher possible displacements at such regions (Ajourlou et al., 2019).

Last, geocoding errors can cause PS to lie a few metres from the actual location (Carlá et al., 2019; Leijen, 2014). By translating points from the SAR coordinate system of lines and samples to the geographical system in longitude and latitude, the location of points can shift. A SAR pixel is selected and aligned with the corresponding geographical coordinates, called the ground control point (GCP). Further away from the GCP, the results' location will shift because the SAR coordinates do not linearly correspond with the geographical coordinate system. So the entire SAR image cannot be entirely correctly overlain on a map with geographical coordinates. This error might be insignificant for flatter or smaller areas, but the image can be significantly distorted for regions with high topographic variations. The significance of this error will also depend on the orientation of the satellite versus the slopes and the incidence angle, as those factors influence geometric distortions. For example, for Barun Lakes, three different GCPs had to be selected for each lake, resulting in three different datasets. Otherwise, the results would be shifted and not be correctly translated to the geographical coordinate system. This issue might slightly affect interpreting local movements using underlying geomorphological features and projection along the slope if the displacement does not precisely overlap the corresponding slope or aspect value. In addition, the GCP is selected manually, so this might also affect the accuracy of its location regardless of geometric distortions. Selecting multiple GCPs, using up to date and high-resolution DEMs and carefully selecting a GCP could reduce such errors.

- What does the approach of this study add, and how does it compare to existing methods and research?

As mentioned in section 2.4, analysing GLOF susceptibility includes monitoring lake area,

moraine deformation, slope movements and glacier dynamics (GAPHAZ et al., 2017). Regarding moraine and slope stability, conventional methods such as on-site surveys and optical remote sensing are necessary to obtain subsurface and surface features, but they do not enable continuous monitoring and deformation measurements. As highlighted by many studies that have analysed glacial lake outburst floods, continuous monitoring is essential to understand and predict GLOFs (Emmer et al., 2020; GAPHAZ et al., 2017; Klimeš et al., 2016; Nie et al., 2018; Peppa et al., 2020; Petrakov et al., 2012; Scapozza et al., 2019). This study shows that satellite InSAR adds to these methods in that it can continuously measure millimetre displacements over the entire area of interest. By combining on-site information, optical images and InSAR data, areas can be pinpointed that might represent GLOF hazards.

Some previous studies demonstrated the applicability of InSAR to glacial lakes by supporting geomorphological and hazard analyses at a particular glacial lake with InSAR observations (Klimeš et al., 2016; Scapozza et al., 2019; Wangchuk et al., 2022). Similar to this research, their studies measured displacements on rock glaciers and (lateral) moraines, and they encountered decoherence in regions that experienced too fast deformation. They thoroughly researched a particular glacial lake by adding many detailed data sources to map the geomorphology. As a result, they analysed more detailed geomorphological phenomena in their study areas than this thesis. However, their studies focused less on whether InSAR can be used as the primary tool for analysing glacial lakes in general, and they dive less deeply into the limitations and behaviour of displacements obtained with InSAR. Contrary to these previous studies, this thesis analysed the applicability of InSAR as a general tool for displacement monitoring at glacier lakes by applying it to multiple lakes instead of supporting detailed geomorphological mapping at one lake. This study looked at the best way to interpret displacements, how to map and identify limitations and how to link InSAR-based observations to potential GLOF hazards without having detailed information or visiting the site; demonstrating it as a fast and cost-effective method to analyse GLOF susceptibility while being able to estimate beforehand whether an InSAR-based analysis is possible or feasible. In addition, this thesis differs in that seasonal displacements have been observed by applying a non-linear displacement model, making it easier to link InSAR observations to geomorphological phenomena and seasonal contributions. Since GLOF events have followed a seasonal trend (Falátková, 2016; Veh et al., 2019), it is important to focus on detecting seasonal trends in possible GLOF trigger developments.

As mentioned in section 2.4, the complete GLOF hazard analysis consists of the susceptibility and the impact assessment. This research fulfils a part of the susceptibility assessment, focusing on the moraine and slope stability. More aspects could be considered for a complete susceptibility analysis, such as lake area variation, snow avalanches, and glacier calving. Still, this susceptibility study can indicate where an outburst might initiate, which mechanism might cause it and whether it could directly impact the lake. This then aids in which areas require further or on-site analysis and provides a starting point to model outbursts and execute the impact assessment, forming the overall hazard assessment. With the comprehensive hazard assessment, lakes can be prioritised, and a well-considered decision can be made on the most helpful mitigation measure (GAPHAZ et al., 2017; Scapozza et al., 2019; Wangchuk et al., 2022).

6 Conclusion & Future developments

This study demonstrates InSAR's capability to continuously identify and measure deformations at critical glacial lake areas susceptible to failure that could result in GLOFs. The primary reasons for applying an InSAR-based analysis to glacial lakes are that it overcomes the challenges of continuous and in situ monitoring for assessing potential hazards related to GLOFs. Adding geomorphological, optical, meteorological and topographical data sources is indispensable for interpreting the results, connecting them to GLOF hazards and identifying InSAR's limitations. The applicability of an InSAR-based analysis is limited in areas subjected to significant topographic variations, rapid deformations, vegetation and melting snow. Still, it proved well capable of measuring moraine subsidence, unstable lateral moraines, scree deposits and rock glaciers; identifying areas that could be potential GLOF triggers and indicating lakes with high GLOF susceptibility. With continuous monitoring, InSAR can provide warnings of moraine or slope areas that suddenly become active or experience increased movements, aiding in applying mitigation measures and prioritising interventions.

Future developments should address automating processes, such as downloading and adding new acquisitions to the image stack to speed up the InSAR-based analysis. Still, the interpretation would require manual work to relate them to hazards. Moreover, the study could benefit from adding other InSAR methods or satellite data with larger wavelengths to measure vegetated and rapid deforming moraines, increasing the temporal and spatial coverage of deformation measurements. Finally, besides continuous monitoring to provide warnings of hazard developments, prolonging the analysis to observe climatic influences on displacements would be helpful for understanding and forecasting trigger developments.

References

Agrawala, S., Raksakulthai, V., Larsen, P., Smith, J., and Reynolds, J. (2003). Development and climate change in nepal: focus on water resources and hydropower. Technical report, Organisation for Economic Co-operation and Development, Paris.

Ahmed, R., Wani, G. F., Ahmad, S. T., Sahana, M., Singh, H., and Ahmed, P. (2021). A Review of Glacial Lake Expansion and Associated Glacial Lake Outburst Floods in the Himalayan Region. *Earth Systems and Environment*, 5:695–708.

Ajourlou, P., Samiei Esfahany, S., and Safari, A. (2019). A new strategy for phase unwrapping in insar time series over areas with high deformation rate: Case study on the southern tehran subsidence. In *International Archives of the Photogrammetry, Remote Sensing and Spatial Information Sciences*, volume XLII-4, pages 35–40.

Alatza, S., Papoutsis, I., Paradissis, D., Kontoes, C., and Papadopoulos, G. A. (2020). Multi-Temporal InSAR Analysis for Monitoring Ground Deformation in Amorgos Island, Greece. *Sensors*, 20(338):539–547.

Allen, S. K., Rastner, P., Arora, M., Huggel, C., and Stoffel, M. (2016). Lake outburst and debris flow disaster at Kedarnath, June 2013: hydrometeorological triggering and topographic predisposition. *Landslides*, 13(6):1479–1491.

Aslan, G., Cakir, Z., Lasserre, C., and Renard, F. (2019). Investigating subsidence in the Bursa Plain, Turkey, using ascending and descending sentinel-1 satellite data. *Remote Sensing*, 11(1).

Aslan, G., Foumelis, M., Raucoules, D., De Michele, M., Bernardie, S., and Cakir, Z. (2020). Landslide Mapping and Monitoring Using Persistent Scatterer Interferometry (PSI) Technique in the French Alps. *Remote Sensing*, 12(1305).

Baidya, S. K., Shrestha, M. L., and Sheikh, M. M. (2008). Trends in daily climatic extremes of Temperature and Precipitation in Nepal. *Journal of Hydrology and Meteorology*, 5(1):38–51.

Bajracharya, B., Shrestha, A. B., and Rajbhandari, L. (2007a). Glacial lake outburst floods in the Sagarmatha region: Hazard assessment using GIS and hydrodynamic modelling. *Mountain Research and Development*, 27(4):336–344.

Bajracharya, S., Maharjan, S., Shrestha, F., Sherpa, T. C., Wagle, N., and Shrestha, A. (2020). Inventory of glacial lakes and identification of potentially dangerous glacial lakes in the Koshi, Gandaki, and Karnali river basins of Nepal, the Tibet Autonomous Region of China, and India. Technical report, ICIOMOD and UNDP.

Bajracharya, S. R., Mool, P. K., and Shrestha, B. R. (2007b). Impact of climate change on himalayan glaciers and glacial lakes - Case studies on GLOF and associated hazards in Nepal and Bhutan. Technical report, ICIMOD, Kathmandu, Nepal.

Bamler, R. (1999). The SRTM mission: A world-wide 30m resolution DEM from SAR interferometry in 11 days. In *Photogrammetric Week*, number January, pages 145–154.

Barboux, C., Delaloye, R., and Lambiel, C. (2014). Inventorying slope movements in an Alpine environment using DInSAR. *Earth Surface Processes and Landforms*, 39(15):2087–2099.

Bayer, B., Simoni, A., Schmidt, D., and Bertello, L. (2017). Using advanced InSAR techniques to monitor landslide deformations induced by tunneling in the Northern Apennines, Italy. *Engineering Geology*, 226(March):20–32.

Begam, S. and Sen, D. (2019). Mapping of moraine dammed glacial lakes and assessment of their areal changes in the central and eastern Himalayas using satellite data. *Journal of Mountain Science*, 16(1):77–94.

Benn, D. I., Warren, C. R., and Mottram, R. H. (2007). Calving processes and the dynamics of calving glaciers. *Earth-Science Reviews*, 82(3-4):143–179.

Bennett, G. L. and Evans, D. J. (2012). Glacier retreat and landform production on an overdeepened glacier foreland: The debris-charged glacial landsystem at Kvíárjökull, Iceland. *Earth Surface Processes and Landforms*, 37(15):1584–1602.

Bi, H. X. and Wei, Z. Q. (2016). A new phase unwrapping method based on region recognition and region expansion. *International Journal of Remote Sensing*, 37(22):5287–5303.

Bianchini, S., Herrera, G., Mateos, R. M., Notti, D., Garcia, I., Mora, O., and Moretti, S. (2013). Landslide Activity Maps Generation by Means of Persistent Scatterer Interferometry. *Remote Sensing*, 5:6198–6222.

Bilham, R. (2019). Himalayan earthquakes: A review of historical seismicity and early 21st century slip potential. *Geological Society Special Publication*, 483(1):423–482.

Budillon, A., Crosetto, M., and Monserrat, O. (2019). Urban Deformation Monitoring using Persistent Scatterer Interferometry and SAR tomography. *Remote Sensing*, 11(1306).

Burbank, D. W., Bookhagen, B., Gabet, E. J., Putkonen, J., and June, B. (2012). Modern climate and erosion in the Himalaya. *C. R. Geoscience*, 344:610–626.

Burrough, P. and McDonell, R. (1998). *Principles of Geograhpical Information Systems*. Oxford University Press, New York, 2nd edition.

Byers, A. C., Byers, E. A., McKinney, D. C., and Rounce, D. R. (2017). A field-based study of impacts of the 2015 earthquake on potentially dangerous glacial lakes in Nepal. *Himalaya*, 37(2):26–41.

Byers, A. C., Rounce, D. R., Shugar, D. H., Lala, J. M., Byers, E. A., and Regmi, D. (2019). A rockfall-induced glacial lake outburst flood, Upper Barun Valley, Nepal. *Landslides*, 16:533–549.

Carey, M. (2005). Living and dying with glaciers: People's historical vulnerability to avalanches and outburst floods in Peru. *Global and Planetary Change*, 47:122–134.

Carlá, T., Intrieri, E., Raspini, F., Bardi, F., Farina, P., Ferretti, A., Colombo, D., Novali, F., and Casagli, N. (2019). Perspectives on the prediction of catastrophic slope failures from satellite InSAR. *Nature*, 9(14137).

Carrivick, J. L. and Tweed, F. S. (2016). A global assessment of the societal impacts of glacier outburst floods. *Global and Planetary Change*, 144:1–16.

Ciampalini, A., Raspini, F., Lagomarsino, D., Catani, F., and Casagli, N. (2016). Landslide susceptibility map refinement using PSInSAR data. *Remote Sensing of Environment*, 184:302–315.

Cicoira, A., Beutel, J., Faillettaz, J., and Vieli, A. (2019). Water controls the seasonal rhythm of rock glacier flow. *Earth and Planetary Science Letters*, 528(115844).

Cigna, F., Bateson, L. B., Jordan, C. J., and Dashwood, C. (2014). Simulating SAR geometric distortions and predicting Persistent Scatterer densities for ERS-1/2 and ENVISAT C-band SAR and InSAR applications: Nationwide feasibility assessment to monitor the landmass of Great Britain with SAR imagery. *Remote Sensing of Environment*, 152:441–466.

Clague, J. and Evans, S. (2000). A review of catastrophic drainage of moraine-dammed lakes in British Columbia. *Quaternary Science Reviews*, 19:1763–1783.

Clague, J. and O'Conner, J. E. (2021). Glacier-related outburst floods. In *Snow and Ice-related Hazards, Risks, and Disasters*, chapter 14, pages 467–490. Elsevier, 2nd edition.

Colesanti, C. and Wasowski, J. (2006). Investigating landslides with space-borne Synthetic Aperture Radar (SAR) interferometry. *Engineering Geology*, 88(3-4):173–199.

Costa, J. E. and Schuster, R. L. (1988). Formation and Failure of Natural Dams. *Bulletin of the Geological Society of America*, 100(7):1054–1068.

Crosetto, M., Monserrat, O., Cuevas-González, M., Devanthéry, N., and Crippa, B. (2016). Persistent Scatterer Interferometry: A review. *ISPRS Journal of Photogrammetry and Remote Sensing*, 115:78–89.

Cuellar, A. D. and McKinney, D. C. (2017). Decision-making methodology for risk management applied to Imja Lake in Nepal. *Water*, 9(591).

Cuenca, M. C., Hooper, A. J., and Hanssen, R. F. (2011). A new method for temporal phase unwrapping of persistent scatterers InSAR time series. *IEEE Transactions on Geoscience and Remote Sensing*, 49(11):4606–4615.

Dahal, P. R., Paudyal, K. R., and Rajaure, S. (2018). Geophysical study on moraine dam of Imja Glacial Lake in Eastern Nepal using Electrical Resistivity Tomography Method. *Journal of Nepal Geological Society*, 55(1):15–22.

Dahal, R. K. (2015). Understanding of Landslide Science in the Nepal Himalaya. In Lollino, G., editor, *Engineering Geology for Society and Territory - Volume 2: Landslide Processes*, volume 2, pages 1299–1303. Springer International Publishing Switzerland.

Deline, P., Gruber, S., Amann, F., Bodin, X., Delaloye, R., Failletaz, J., Fischer, L., Geertsema, M., Giardino, M., Hasler, A., Kirkbride, M., Krautblatter, M., Magnin, F., McColl, S., Ravanel, L., Schoeneich, P., and Weber, S. (2021). Ice loss from glaciers and permafrost and related slope instability in high-mountain regions. In *Snow and Ice-related Hazards, Risks, and Disasters*, chapter 15, pages 501–530. Elsevier, 2nd edition.

Dini, B., Manconi, A., and Loew, S. (2019). Investigation of slope instabilities in NW Bhutan as derived from systematic DInSAR analyses. *Engineering Geology*, 259(105111).

Emmer, A. and Cochachin, A. (2013). The causes and mechanisms of moraine-dammed lake failures in the cordillera blanca, North American Cordillera, and Himalayas. *Acta Universitatis Carolinae, Geographica*, 48(2):5–15.

Emmer, A., Harrison, S., Mergili, M., Allen, S., Frey, H., and Huggel, C. (2020). 70 years of lake evolution and glacial lake outburst floods in the Cordillera Blanca (Peru) and implications for the future. *Geomorphology*, 365.

Emmer, A., Vilímek, V., Klimeš, J., and Cochachin, A. (2014). Glacier Retreat, Lakes Development and Associated Natural Hazards in Cordilera Blanca, Peru. *Environmental Science and Engineering*, pages 231–252.

Eriksen, H. O., Lauknes, T. R., Larsen, Y., Corner, G. D., Bergh, S. G., Dehls, J., and Kierulf, H. P. (2017). Visualizing and interpreting surface displacement patterns on unstable slopes using multi-geometry satellite SAR interferometry (2D InSAR). *Remote Sensing of Environment*, 191:297–312.

ESA (2022). Sentinel-1.

esri (2022). How Hillshade works.

Evans, S., Delaney, K., and Rana, N. (2021). The occurrence and mechanism of catastrophic mass flows in the mountain cryosphere. In *Snow and Ice-related Hazards, Risks, and Disasters*, chapter 16, pages 541–584. Elsevier, 2nd edition.

Falátková, K. (2016). Temporal analysis of GLOFs in high-mountain regions of Asia and assessment of their causes. *Acta Universitatis Carolinae, Geographica*, 51(2):145–154.

Fárová, K., Jelének, J., Kopačková-Strnadová, V., and Kycl, P. (2019). Comparing DInSAR and PSI techniques employed to Sentinel-1 data to monitor highway stability: A case study of a massive Dobkovičky landslide, Czech Republic. *Remote Sensing*, 11(2670).

Ferretti, A., Monti-Guarnieri, A., Prati, C., Rocca, F., and Massonnet, D. (2007). *InSAR Principles: Guidelines for SAR Interferometry Processing and Interpretation*, volume 19. ESA Publications.

Ferretti, A., Prati, C., and Rocca, F. (2000). Nonlinear subsidence rate estimation using permanent scatterers in differential SAR interferometry. *IEEE Transactions on Geoscience and Remote Sensing*, 38(5):2202–2212.

Ferretti, A., Prati, C., and Rocca, F. (2001). Permanent scatterers in SAR interferometry. *IEEE Transactions on Geoscience and Remote Sensing*, 39(1):8–20.

Ferretti, A., Prati, C., Rocca, F., Casagli, N., Farina, P., and Young, B. (2005). Permanent Scatterers technology: a powerful state of the art tool for historic and future monitoring of landslides and other terrain instability phenomena. *International Conference on Landslide Risk Management, 18th Annual Vancouver Geotechnical Society Symposium.*

Fischer, L., Kääb, A., Huggel, C., and Noetzli, J. (2006). Geology, glacier retreat and permafrost degradation as controlling factors of slope instabilities in a high-mountain rock wall: The Monte Rosa east face. *Natural Hazards and Earth System Science*, 6(5):761–772.

Fischer, M., Korup, O., Veh, G., and Walz, A. (2020). Controls of outbursts of moraine-dammed lakes in the greater Himalayan region. *The Cryosphere - Discussions Preprint*, pages 1–32.

Fujita, K., Nishimura, K., Komori, J., Iwata, S., Ukita, J., Tadono, T., and Koike, T. (2012). Outline of research project on glacial lake outburst floods in the Bhutan Himalayas. *Global Environmental Research*, 16(1):3–12.

Fujita, K., Sakai, A., Takenaka, S., Nuimura, T., Surazakov, A. B., Sawagaki, T., and Yamanokuchi, T. (2013). Potential flood volume of Himalayan glacial lakes. *Natural Hazards and Earth System Sciences*, 13(7):1827–1839.

Furst, S. L., Doucet, S., Vernant, P., Champollion, C., and Carme, J. L. (2021). Monitoring surface deformation of deep salt mining in Vauvert (France), combining InSAR and leveling data for multi-source inversion. *Solid Earth*, 12(1):15–34.

Gao, Y. D., Zhang, S. B., Li, T., Chen, Q. F., Zhang, X., and Li, S. J. (2019). Refined two-stage programming approach of phase unwrapping for multi-baseline SAR interferograms using the unscented Kalman filter. *Remote Sensing*, 11(199).

GAPHAZ, Allen, S., Frey, H., and Huggle, C. (2017). Assessment of Glacier and Permafrost Hazards in Mountain Regions: Technical Guidance Document. Technical report, International Association of Cryospheric Sciences (IACS) and International Permafrost Association (IPA), Zurich (Switzerland), Lima (Peru).

Garbrecht, J. and Martz, L. W. (1997). The assignment of drainage direction over flat surfaces in raster digital elevation models. *Journal of Hydrology*, 193:204–213.

GISGeography (2021). Sentinel 2 Bands and Combinations.

Hambrey, M. J., Quincey, D. J., Glasser, N. F., Reynolds, J. M., Richardson, S. J., and Clemmens, S. (2008). Sedimentological, geomorphological and dynamic context of debris-mantled glaciers, Mount Everest (Sagarmatha) region, Nepal. *Quaternary Science Reviews*, 27(25-26):2361–2389.

Hanssen, R. (2001). *Radar interferometry: Data interpretation and error analysis.* PhD thesis, Delft University of Technology.

Haritashya, U. K., Kargel, J. S., Shugar, D. H., Leonard, G. J., Strattman, K., Watson, C. S., Shean, D., Harrison, S., Mandli, K. T., and Regmi, D. (2018). Evolution and controls of large glacial lakes in the Nepal Himalaya. *Remote Sensing*, 10(5):1–31.

Harrison, S., Kargel, J. S., Huggel, C., Reynolds, J., Shugar, D. H., Betts, R. A., Emmer, A., Glasser, N., Haritashya, U. K., Klimeš, J., Reinhardt, L., Schaub, Y., Wiltshire, A., Regmi, D., and Vilímek, V. (2018). Climate change and the global pattern of moraine-dammed glacial lake outburst floods. *Cryosphere*, 12(4):1195–1209.

Herrera, G., Gutiérrez, F., García-Davalillo, J. C., Guerrero, J., Notti, D., Galve, J. P., Fernández-Merodo, J. A., and Cooksley, G. (2013). Multi-sensor advanced DInSAR monitoring of very slow landslides: The Tena Valley case study (Central Spanish Pyrenees). *Remote Sensing of Environment*, 128:31–43.

Highland, L. M. and Bobrowsky, P. (2008). *The landslide Handbook - A guide to understanding landslides*. US Geological Survey Circular 1325, Reston, Virginia.

Hooper, A. J. (2008). A multi-temporal InSAR method incorporating both persistent scatterer and small baseline approaches. *Geophysical Research Letters*, 35.

Hu, J., Li, Z. W., Ding, X. L., Zhu, J. J., Zhang, L., and Sun, Q. (2014). Resolving three-dimensional surface displacements from InSAR measurements: A review. *Earth-Science Reviews*, 133:1–17.

ICIMOD (2011). Glacial lakes and glacial lake outburst floods in the Himalayas. Technical report, ICIMOD.

Iwata, S., Ageta, Y., Naito, N., Sakai, A., Narama, C., and Karma (2002). Glacial Lakes and Their Outburst Flood Assessment in the Bhutan Himalaya. *Global Environmental Research*, 6:3–17.

Janský, B., Engel, Z., Šobr, M., Beneš, V., Špaček, K., and Yerokhin, S. (2009). The evolution of Petrov lake and moraine dam rupture risk (Tien-Shan, Kyrgyzstan). *Natural Hazards*, 50(1):83–96.

Jenson, S. K. and Domingue, J. O. (1988). Extracting topographic structure from digital elevation data for geographic information system analysis. *Photogrammetric Engineering and Remote Sensing*, 54(11):1593–1600.

Kahlon, S., Chandel, V. B. S., and Brar, K. K. (2014). Landslides in Himalayan Mountains: A Study of Himachal Pradesh, India. *International Journal of IT, Engineering and Applied Sciences ResearchExplore International Research Journal Consortium*, 3(9):2319–4413.

Kalia, A. C. (2018). Classification of Landslide Activity on a Regional Scale Using Persistent Scatterer Interferometry at the Moselle Valley (Germany). *Remote Sensing*, 10(1880).

Kampes, B. M. (2006). *Radar Interferometry - Persistent Scatterer Interferometry*. Springer, 12 edition.

Kershaw, J. A., Clague, J. J., and Evans, S. G. (2005). Geomorphic and sedimentological signature of a two-phase outburst flood from moraine-dammed Queen Bess Lake, British Columbia, Canada. *Earth Surface Processes and Landforms*, 30(1):1–25.

Khadka, N., Zhang, G., and Chen, W. (2019). The state of six dangerous glacial lakes in the Nepalese Himalaya. *Terrestrial, Atmospheric and Oceanic Sciences*, 30(1):63–72.

Khadka, N., Zhang, G., and Thakuri, S. (2018). Glacial lakes in the Nepal Himalaya: Inventory and decadal dynamics (1977-2017). *Remote Sensing*, 10(12):1–19.

Khatiwada, D. and Dahal, R. K. (2020). Rockfall hazard in the Imja Glacial Lake, eastern Nepal. *Geoenvironmental Disasters*, 7(1).

King, M. D. (2007). *Our changing planet: the view from space*. Cambridge University Press.

Klimeš, J., Novotný, J., Novotná, I., de Urries, B. J., Vilímek, V., Emmer, A., Strozzi, T., Kusák, M., Rapre, A. C., Hartvich, F., and Frey, H. (2016). Landslides in moraines as triggers of glacial lake outburst floods: example from Palcacocha Lake (Cordillera Blanca, Peru). *Landslides*, 13(6):1461–1477.

Kofler, C., Mair, V., Gruber, S., Todisco, M. C., Nettleton, I., Steger, S., Zebisch, M., Schneiderbauer, S., and Comiti, F. (2021). When do rock glacier fronts fail? Insights from two case studies in South Tyrol (Italian Alps). *Earth Surface Processes and Landforms*, 46:1311–1327.

Kos, A., Amann, F., Strozzi, T., Delaloye, R., von Ruette, J., and Springman, S. (2016). Contemporary glacier retreat triggers a rapid landslide response, Great Aletsch Glacier, Switzerland. *Geophysical Research Letters*, 43:466–12.

Kovács, I. P., Bugya, T., Czigány, S., Defilippi, M., Lóczy, D., Riccardi, P., Ronczyk, L., and Pasquali, P. (2019). How to avoid false interpretations of Sentinel-1A TOPSAR interferometric data in landslide mapping? A case study: recent landslides in Transdanubia, Hungary. *Natural Hazards*, 96(2):693–712.

Kroczek, T. and Vilimek, V. (2020). Rockfall/Rockslide Hazard, Lake Expansion and Dead-Ice Melting Assessment: Lake Imja, Nepal. In *Understanding and Reducing Landslide Disaster Risk*, chapter 10, pages 103–110. Springer, Cham, 5 edition.

Kropatsch, W. G. and Strobl, D. (1990). The Generation of SAR Layover and Shadow Maps From Digital Elevation Models. *IEEE Transactions on Geoscience and Remote Sensing*, 28(1):98–107.

Kumar, S., Kumar, D., Chaudhary, S. K., Singh, N., and Malik, K. K. (2020). Land subsidence mapping and monitoring using modified persistent scatterer interferometric synthetic aperture radar in Jharia Coalfield, India. *Journal of Earth System Science*, 129(146).

Larsen, I. J. and Montgomery, D. R. (2012). Landslide erosion coupled to tectonics and river incision. *Nature Geoscience*, 5(7):468–473.

Leijen, F. v. (2014). *Persistent Scatterer Interferometry based on geodetic estimation theory*. PhD thesis, Delft University of Technology.

Li, Z., Zhu, Q., and Gold, C. (2004). *Digital terrain modeling: Principles and methodology*.

Liu, P., Li, Z., Hoey, T., Kincal, C., Zhang, J., Zeng, Q., and Muller, J. P. (2012). Using advanced inSAR time series techniques to monitor landslide movements in Badong of the Three Gorges region, China. *International Journal of Applied Earth Observation and Geoinformation*, 21(1):253–264.

Liu, W., Carling, P. A., Hu, K., Wang, H., Zhou, Z., Zhou, L., Liu, D., Lai, Z., and Zhang, X. (2019). Outburst floods in China: A review. *Earth-Science Reviews*, 197.

Lugon, R. and Stoffel, M. (2010). Rock-glacier dynamics and magnitude-frequency relations of debris flows in a high-elevation watershed: Ritigraben, Swiss Alps. *Global and Planetary Change*, 73:202–210.

Maharjan, S., Mool, P., Lizong, W., Xiao, G., Shrestha, F., Shrestha, R., Khanal, N., Bajracharya, S., Joshi, S., Shai, S., and Baral, P. (2018). The Status of Glacial Lakes in the Hindu Kush Himalaya. *ICIMOD research report*, page 70.

Majeed, U., Rashid, I., Sattar, A., Allen, S., Stoffel, M., Nüsser, M., and Schmidt, S. (2021). Recession of Gya Glacier and the 2014 glacial lake outburst flood in the Trans-Himalayan region of Ladakh, India. *Science of the Total Environment*, 756:144008.

Malinverni, E. S., Sandwell, D. T., Tassetti, A. N., and Cappelletti, L. (2014). InSAR decorrelation to assess and prevent volcanic risk. *European Journal of Remote Sensing*, 47(1):537–556.

Mallet, C., Baghdadi, N., and Zribi, M. (2018). *QGIS and Generic Tools*. John Wiley & Sons.

Maskey, S., Kayastha, R. B., and Kayastha, R. (2020). Glacial Lakes Outburst Floods (GLOFs) modelling of Thulagi and Lower Barun Glacial Lakes of Nepalese Himalaya. *Progress in Disaster Science*, 7.

Meteomatics (2021). Meteomatics.

Milillo, P., Bürgmann, R., Lundgren, P., Salzer, J., Perissin, D., Fielding, E., Biondi, F., and Milillo, G. (2016). Space geodetic monitoring of engineered structures: The ongoing destabilization of the Mosul dam, Iraq. *Nature*, 6(37408).

NASA (2022). Basics of Space Flight - Electromagnetics.

Nayar, A. (2009). When the ice melts: deep in the Himalayas, the disappearance of glaciers is threatening the kingdom of Bhutan. Anjali Nayar trekked through the mountains to see how the country is adapting to a warming world. *Nature*, 461(7267):1042–1047.

NCHM (2019). Report on the Rapid Assessment of Thorthormi Lake and the Restoration of Automatic Water Level Sensors for the GLOF Early Warning System. Technical report, Royal Government of Bhutan.

NCHM (2020). Detailed Assessment Report on GLOF Hazard From Thorthormi Glacial Lake and Associated Glaciers. Technical report.

Nie, Y., Liu, Q., Wang, J., Zhang, Y., Sheng, Y., and Liu, S. (2018). An inventory of historical glacial lake outburst floods in the Himalayas based on remote sensing observations and geomorphological analysis. *Geomorphology*, 308(February):91–106.

Nie, Y., Liu, W., Liu, Q., Hu, X., and Westoby, M. J. (2020). Reconstructing the Chongbaxia Tsho glacial lake outburst flood in the Eastern Himalaya: Evolution, process and impacts. *Geomorphology*, 370.

Notti, D., Herrera, G., Bianchini, S., Meisina, C., García-Davalillo, J. C., and Zucca, F. (2014). A methodology for improving landslide PSI data analysis. *International Journal of Remote Sensing*, 35(6):2186–2214.

Pasquali, P., Cantone, A., Riccardi, P., Defilippi, M., Ogushi, F., Gagliano, S., and Tamura, M. (2014). Mapping of Ground Deformations with Interferometric Stacking Techniques. In Holecz, F., Pasquali, P., Milisavljevic, N., and Closson, D., editors, *Land Applications of Radar Remote Sensing*, number June, chapter 8.

Peppa, M. V., Maharjan, S. B., Joshi, S. P., Xiao, W., and Mills, J. P. (2020). Glacial lake evolution based on remote sensing time series: A case study of tsho rolpa in Nepal. *ISPRS Annals of the Photogrammetry, Remote Sensing and Spatial Information Sciences*, 5(3):633–639.

Perissin, D. (2016). Interferometric SAR multitemporal processing: Techniques and applications. In Ban, Y., editor, *Remote Sensing and Digital Image Processing*, volume 20, chapter 8, pages 145–176. Springer International Publishing AG 2016.

Perissin, D., Wang, Z., and Wang, T. (2011). The SARPROZ InSAR tool for urban subsidence/manmade structure stability monitoring in China. In *Proc. ISRSE*, number 1015, Sydney (Australia).

Petrakov, D. A., Tutubalina, O. V., Aleinikov, A. A., Chernomorets, S. S., Evans, S. G., Kidyaeva, V. M., Krylenko, I. N., Norin, S. V., Shakhmina, M. S., and Seynova, I. B. (2012). Monitoring of Bashkara Glacier lakes (Central Caucasus, Russia) and modelling of their potential outburst. *Natural Hazards*, 61(3):1293–1316.

Prakash, C. and Nagarajan, R. (2018). Glacial lake changes and outburst flood hazard in Chandra basin, North-Western Indian Himalaya. *Geomatics, Natural Hazards and Risk*, 9(1):337–355.

Prodanović, D., Stanić, M., Milivojević, V., Simić, Z., and Arsić, M. (2009). DEM-based GIS algorithms for automatic creation of hydrological models data. *Journal of Serbian Society for Computational Mechanics*, 3(1):64–85.

Quincey, D. J., Richardson, S. D., Luckman, A., Lucas, R. M., Reynolds, J. M., Hambrey, M. J., and Glasser, N. F. (2007). Early recognition of glacial lake hazards in the Himalaya using remote sensing datasets. *Global and Planetary Change*, 56(1-2):137–152.

Rana, B., Shrestha, A. B., Reynolds, J. M., Aryal, R., Pokhrel, A. P., and Budhathoki, K. P. (2000). Hazard assessment of the Tsho Rolpa Glacier Lake and ongoing remediation measures. *Journal of Nepal Geological Society*, 22:563–570.

Raspini, F., Bianchini, S., Ciampalini, A., Del Soldato, M., Solari, L., Novali, F., Del Conte, S., Rucci, A., Ferretti, A., and Casagli, N. (2018). Continuous, semi-automatic monitoring of ground deformation using Sentinel-1 satellites. *Nature*, 8(1):1–11.

Richardson, S. D. and Reynolds, J. M. (2000). An overview of glacial hazards in the Himalayas. *Quaternary International*, 65-66:31–47.

Rinzin, S., Zhang, G., and Wangchuk, S. (2021). Glacial Lake Area Change and Potential Outburst Flood Hazard Assessment in the Bhutan Himalaya. *Frontiers in Earth Science*, 9(775195).

Ritter, D., Kochel, C., and Miller, J. (1995). *Process Geomorphology*. William C Brown Pub, 3rd edition.

Röhl, K. (2008). Characteristics and evolution of supraglacial ponds on debris-covered Tasman Glacier, New Zealand. *Journal of Glaciology*, 54(188):867–880.

Rosi, A., Tofani, V., Tanteri, L., Tacconi Stefanelli, C., Agostini, A., Catani, F., and Casagli, N. (2018). The new landslide inventory of Tuscany (Italy) updated with PS-InSAR: geomorphological features and landslide distribution. *Landslides*, 15(1):5–19.

Rounce, D. R., Byers, A. C., Byers, E. A., and McKinney, D. C. (2017a). Brief communication: Observations of a glacier outburst flood from Lhotse Glacier, Everest area, Nepal. *Cryosphere*, 11(1):443–449.

Rounce, D. R., McKinney, D. C., Lala, J. M., Byers, A. C., and Watson, C. S. (2016). A new remote hazard and risk assessment framework for glacial lakes in the Nepal Himalaya. *Hydrology and Earth System Sciences*, 20(9):3455–3475.

Rounce, D. R., Watson, C. S., and McKinney, D. C. (2017b). Identification of hazard and risk for glacial lakes in the Nepal Himalaya using satellite imagery from 2000-2015. *Remote Sensing*, 9(7).

Sakai, A. (2012). Glacial Lakes in the Himalayas : A Review on Formation and Expansion Processes. *Global Environmental Research*, 16(2011):23–30.

Sakai, A., Chikita, K., and Yamada, T. (2000). Expansion of a moraine-dammed glacial lake, Tsho Rolpa, in Rolwaling Himal, Nepal Himalaya. *Limnology and Oceanography*, 45(6):1401–1408.

Sattar, A., Haritashya, U. K., Kargel, J. S., Leonard, G. J., Shugar, D. H., and Chase, D. V. (2021). Modeling lake outburst and downstream hazard assessment of the Lower Barun Glacial Lake, Nepal Himalaya. *Journal of Hydrology*, 598:126208.

Sawagaki, T., Lamsal, D., Byers, A. C., and Watanabe, T. (2012). Changes in Surface Morphology and Glacial Lake Development of Chamlang South Glacier in the Eastern Nepal Himalaya since 1964. *Global Environmental Research*, 16:83–94.

Scapozza, C., Ambrosi, C., Cannata, M., and Strozzi, T. (2019). Glacial lake outburst flood hazard assessment by satellite Earth observation in the Himalayas (Chomolhari area, Bhutan). *Geographica Helvetica*, 74(1):125–139.

Schlögel, R., Doubre, C., Malet, J. P., and Masson, F. (2015). Landslide deformation monitoring with ALOS/PALSAR imagery: A D-InSAR geomorphological interpretation method. *Geomorphology*, 231:314–330.

Schmidt, S., Nüsser, M., Baghel, R., and Dame, J. (2020). Cryosphere hazards in Ladakh: the 2014 Gya glacial lake outburst flood and its implications for risk assessment. *Natural Hazards*, 104(3):2071–2095.

Shrestha, A. B., Wake, C. P., Mayewski, P. A., and Dibb, J. E. (1999). Maximum temperature trends in the Himalaya and its vicinity: An analysis based on temperature records from Nepal for the period 1971-94. *Journal of Climate*, 12(9):2775–2786.

Shrestha, B. B., Nakagawa, H., Kawaike, K., Baba, Y., and Zhang, H. (2012). Glacial hazards in the Rolwaling valley of Nepal and numerical approach to predict potential outburst flood from glacial lake. *Landslides*, 10(3):299–313.

Shroder, J. F. (1998). Slope failure and denudation in the western Himalaya. *Geomorphology*, 26:81–105.

Shugar, D. H., Burr, A., Haritashya, U. K., Kargel, J. S., Watson, C. S., Kennedy, M. C., Bevington, A. R., Betts, R. A., Harrison, S., and Strattman, K. (2020). Rapid worldwide growth of glacial lakes since 1990. *Nature Climate Change*, 10(10):939–945.

Sica, F., Bretzke, S., Pulella, A., Bueso-Bello, J. L., Martone, M., Prats-Iraola, P., Gonzalez-Bonilla, M. J., Schmitt, M., and Rizzoli, P. (2021). InSAR Decorrelation at X-Band from the Joint TanDEM-X/PAZ Constellation. *IEEE Geoscience and Remote Sensing Letters*, 18(12):2107–2111.

Singh, S. M. (2009). The Cost of Climate Change: The Story of Thorthormi Glacial Lake in Bhutan. *WWF, World Wide Fund for Nature*.

Somos-Valenzuela, M. A., McKinney, D. C., Rounce, D. R., and Byers, A. C. (2014). Changes in Imja Tsho in the Mount Everest region of Nepal. *Cryosphere*, 8(5):1661–1671.

Sousa, J. J., Liu, G., Fan, J., Perski, Z., Steger, S., Bai, S., Wei, L., Salvi, S., Wang, Q., Tu, J., Tong, L., Mayrhofer, P., Sonnenschein, R., Liu, S., Mao, Y., Tolomei, C., Bignami, C., Atzori, S., Pezzo, G., Wu, L., Yan, S., and Peres, E. (2021). Geohazards Monitoring and Assessment using Multi-Source Earth Observation Techniques. *Remote Sensing*, 13(4269).

Strahler, A. N. (1957). Quantitative analysis of watershed geomorphology. *Transactions American Geophysical Union*, 38(6):913–920.

Strozzi, T., Caduff, R., Jones, N., Barboux, C., Delaloye, R., Bodin, X., Kääb, A., Mätzler, E., and Schrott, L. (2020). Monitoring Rock Glacier Kinematics with Satellite Synthetic Aperture Radar. *Remote Sensing*, 12(559).

Strozzi, T., Luckman, A., Murray, T., Wegmüller, U., and Werner, C. L. (2002). Glacier motion estimation using SAR offset-tracking procedures. *IEEE Transactions on Geoscience and Remote Sensing*, 40(11):2384–2391.

Strozzi, T., Wiesmann, A., Kääb, A., Joshi, S., and Mool, P. (2012). Glacial lake mapping with very high resolution satellite SAR data. *Natural Hazards and Earth System Science*, 12(8):2487–2498.

Szypula, B. (2019). Quality assessment of DEM derived from topographic maps for geomorphometric purposes. *Open Geosciences*, 11(1):843–865.

Tessari, G., Floris, M., and Pasquali, P. (2017). Phase and amplitude analyses of SAR data for landslide detection and monitoring in non-urban areas located in the North-Eastern Italian pre-Alps. *Environmental Earth Sciences*, 76(2):1–11.

Tian, X. p. and Sun, L. (2016). Retrieval of aerosol optical depth over arid areas from MODIS data. *Atmosphere*, 7(134).

Tofani, V., Raspini, F., Catani, F., and Casagli, N. (2013). Persistent scatterer interferometry (psi) technique for landslide characterization and monitoring. *Remote Sensing*, 5(3):1045–1065.

Tsai, Y. L. S., Dietz, A., Oppelt, N., and Kuenzer, C. (2019). Remote sensing of snow cover using spaceborne SAR: A review. *Remote Sensing*, 11(12).

Vecchiotti, F., Peduto, D., and Strozzi, T. (2017). Multi-sensor a Priori PSI Visibility Map for Nationwide Landslide Detection in Austria. In Mikos, M., Tiwari, B., Yin, Y., and Sassa, K., editors, *Advancing Culture of Living with Landslides*, pages 45–52, Cham. Springer International Publishing.

Veh, G., Korup, O., Roessner, S., and Walz, A. (2018). Detecting Himalayan glacial lake outburst floods from Landsat time series. *Remote Sensing of Environment*, 207(July 2017):84–97.

Veh, G., Korup, O., von Specht, S., Roessner, S., and Walz, A. (2019). Unchanged frequency of moraine-dammed glacial lake outburst floods in the Himalaya. *Nature Climate Change*, 9(5):379–383.

Vilímek, V., Zapata, M. L., Klimeš, J., Patzelt, Z., and Santillán, N. (2005). Influence of glacial retreat on natural hazards of the Palcacocha Lake area, Peru. *Landslides*, 2(2):107–115.

Virk, A. S., Singh, A., and Mittal, S. K. (2018). Advanced MT-InSAR Landslide Monitoring: Methods and Trends. *Journal of Remote Sensing & GIS*, 7(225).

Vuichard, D. and Zimmermann, M. (1985). The 1985 Catastrophic Drainage of a Moraine-Dammed Lake , Khumbu Himal , Nepal : Cause and Consequences. *Mountain Research and Development*, 7(2):91–110.

Wang, W., Yao, T., Gao, Y., Yang, X., and Kattel, D. B. (2011). A first-order method to identify potentially dangerous glacial lakes in a region of the southeastern Tibetan Plateau. *Mountain Research and Development*, 31(2):122–130.

Wang, X., Liu, S., Ding, Y., Guo, W., Jiang, Z., Lin, J., and Han, Y. (2012). An approach for estimating the breach probabilities of moraine-dammed lakes in the Chinese Himalayas using remote-sensing data. *Natural Hazards and Earth System Science*, 12(10):3109–3122.

Wangchuk, S. and Bolch, T. (2020). Mapping of glacial lakes using Sentinel-1 and Sentinel-2 data and a random forest classifier: Strengths and challenges. *Science of Remote Sensing*, 2.

Wangchuk, S., Bolch, T., and Robson, B. A. (2022). Monitoring glacial lake outburst flood susceptibility using Sentinel-1 SAR data, Google Earth Engine, and persistent scatterer interferometry. *Remote Sensing of Environment*, 271(112910).

Wangchuk, S., Bolch, T., and Zawadzki, J. (2019). Towards automated mapping and monitoring of potentially dangerous glacial lakes in Bhutan Himalaya using Sentinel-1 Synthetic Aperture Radar data. *International Journal of Remote Sensing*, 40(12):4642–4667.

Wasowski, J. and Bovenga, F. (2014). Investigating landslides and unstable slopes with satellite Multi Temporal Interferometry: Current issues and future perspectives. *Engineering Geology*, 174:103–138.

Watanabe, T., Kameyama, S., and Sato, T. (1995). Imja Glacier Dead-Ice Melt Rates and Changes in a Supra-Glacial Lake , 1989-1994 , Khumbu Himal , Nepal : Danger of Lake Drainage. *Mountain Research and Development*, 15(4):293–300.

Watanabe, T. and Rothacher, D. (1996). The 1994 Lugge Tsho Glacial Lake Outburst Flood, Bhutan Himalaya. *Mountain Research and Development*, 16(1):77–81.

Werner, C. L., Wegmüller, U., and Strozzi, T. (2002). Processing Strategies for Phase Unwrapping for InSAR Applications. *Proc. of EUSAR 2002 - 4th European Conference on Synthetic Aperture Radar*, pages 349–352.

Westoby, M. J., Glasser, N. F., Brasington, J., Hambrey, M. J., Quincey, D. J., and Reynolds, J. M. (2014a). Modelling outburst floods from moraine-dammed glacial lakes. *Earth-Science Reviews*, 134:137–159.

Westoby, M. J., Glasser, N. F., Hambrey, M. J., Brasington, J., Reynolds, J. M., and Hassan, M. A. (2014b). Reconstructing historic glacial lakeoutburst floods through numerical modelling and geomorphological assessment: Extreme events in the himalaya. *Earth Surface Processes and Landforms*, 39(12):1675–1692.

Worni, R., Stoffel, M., Huggel, C., Volz, C., Casteller, A., and Luckman, B. (2012). Analysis and dynamic modeling of a moraine failure and glacier lake outburst flood at Ventisquero Negro, Patagonian Andes (Argentina). *Journal of Hydrology*, 444-445:134–145.

Xie, Z., ShangGuan, D., Zhang, S., Ding, Y., and Liu, S. (2013). Index for hazard of glacier lake outburst flood of lake merzbacher by satellite-based monitoring of lake area and ice cover. *Global and Planetary Change*, 107:229–237.

Yamada, T., Naito, N., Kohshima, S., Fushimi, H., and Nakazawa, F. (2004). Outline of 2002: Research activities on glaciers and glacier lakes in Lunana region, Bhutan Himalayas. *Bull. Glaciol. Res.*, 21:79–90.

Yang, Z., Li, Z., Zhu, J., Wang, Y., and Wu, L. (2020). Use of SAR/InSAR in Mining Deformation Monitoring, Parameter Inversion, and Forward Predictions: A Review. *IEEE Geoscience and Remote Sensing Magazine*, 8(1):71–90.

Yao, X., Liu, S., Han, L., Sun, M., and Zhao, L. (2018). Definition and classification system of glacial lake for inventory and hazards study. *Journal of Geographical Sciences*, 28(2):193–205.

Zebker, H. A. and Lu, Y. (1998). Phase unwrapping algorithms for radar interferometry: residue-cut, least-squares, and synthesis algorithms. *Journal of the Optical Society of America A*, 15(3):586.

Zemp, M., Roer, I., Kääb, A., Hoelzle, M., Paul, F., and Haeberli, W. (2008). Global Glacier Changes: facts and figures. Technical report, Unversity of Zurich, Zurich.

Zhang, X. and Liu, S. (2015). A framework of numerical simulation on moraine-dammed glacial lake outburst floods. *Journal of Arid Land*, 7(6):728–740.

Zhou, Z., Li, Z., Waldron, S., and Tanaka, A. (2019). InSAR time series analysis of L-band data for understanding tropical peatland degradation and restoration. *Remote Sensing*, 11(21):1–15.

A Interferograms

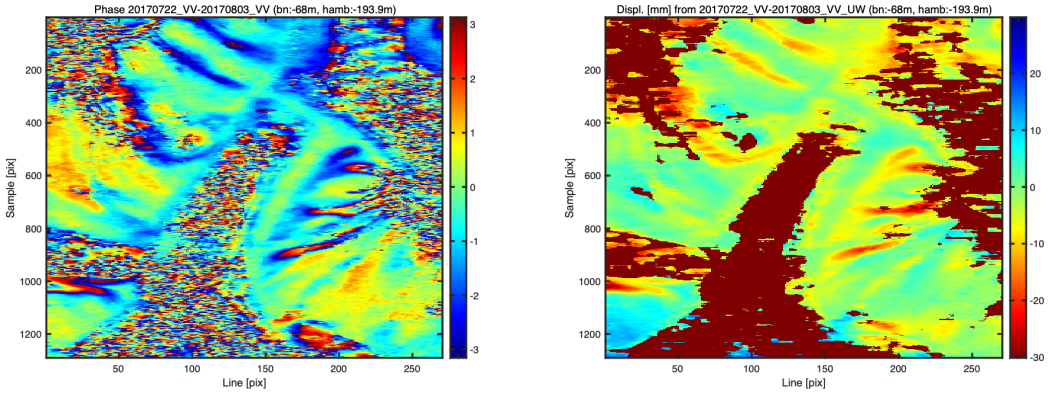

(a) **(b)**

Figure A.1: Ascending interferogram between 22-07-2017 and 03-08-2017 at Imja Lake. (a) wrapped phase. (b) unwrapped into displacements (mm).

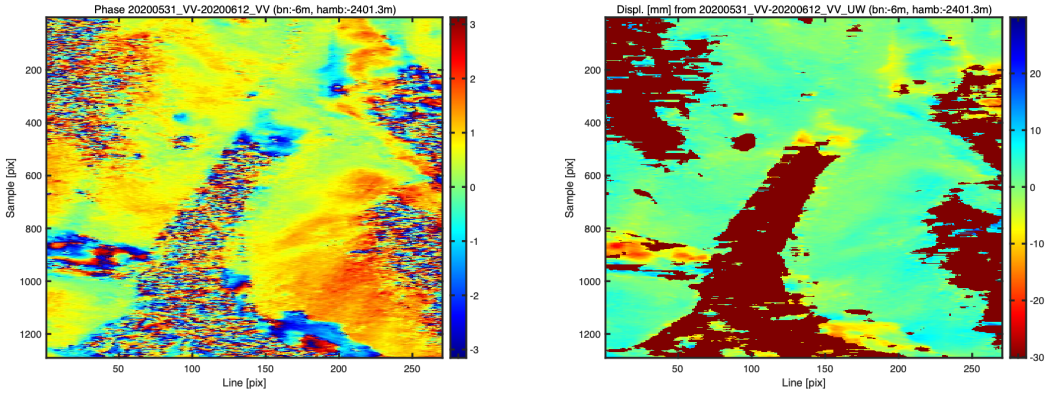

(a) **(b)**

Figure A.2: Ascending interferogram between 31-05-2020 and 12-06-2020. (a) wrapped phase. (b) unwrapped into displacements (mm)

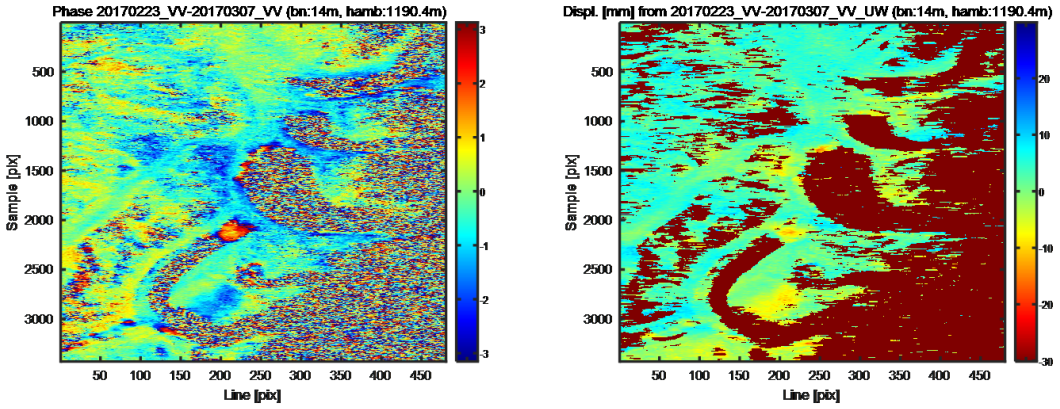

(a) (b)

Figure A.3: Ascending interferogram Lunana Lakes. (a) wrapped phase. (b) unwrapped to displacements (mm).

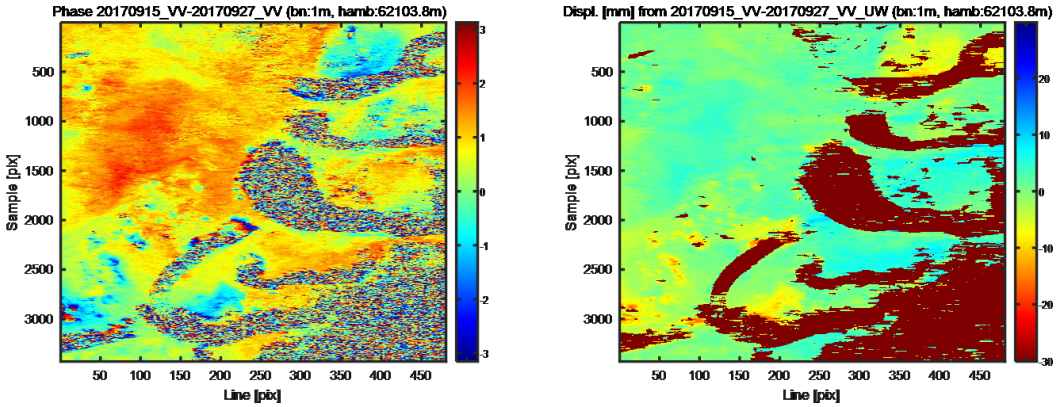

(a) (b)

Figure A.4: Ascending interferogram Lunana Lakes. (a) wrapped phase. (b) unwrapped to displacements (mm).

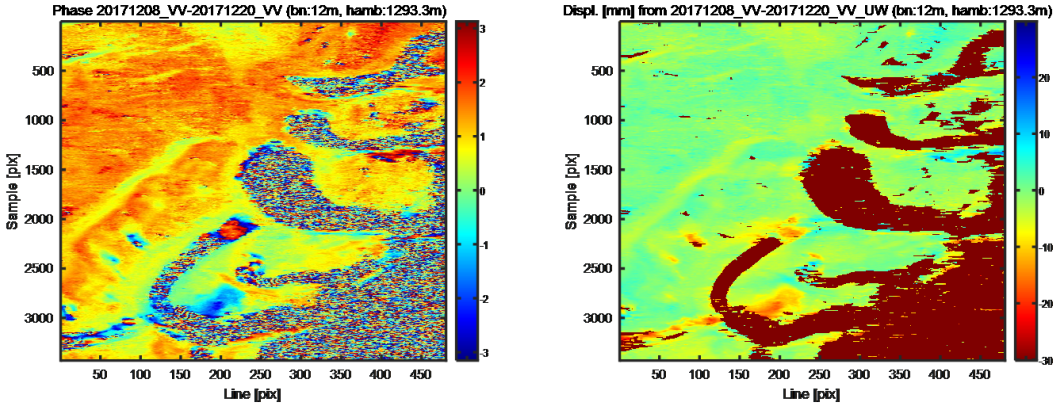

(a) (b)

Figure A.5: Ascending interferogram Lunana Lakes. (a) wrapped phase. (b) unwrapped to displacements (mm).

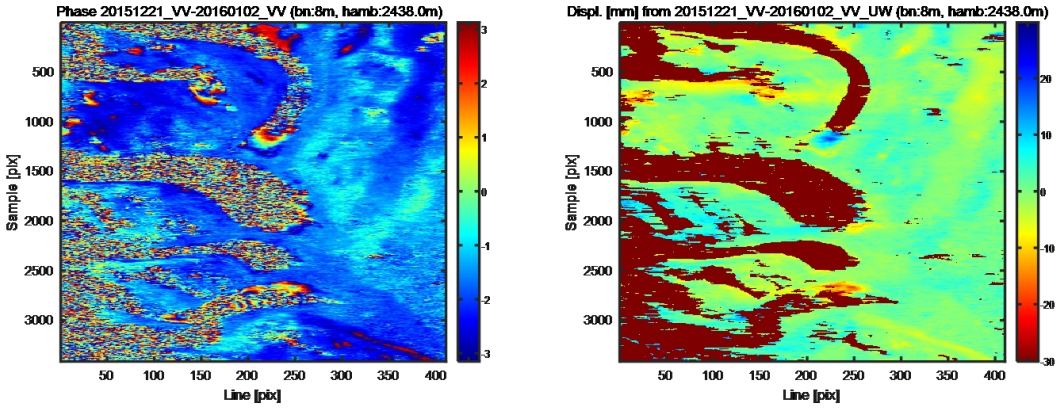

(a) (b)

Figure A.6: Descending interferogram Lunana Lakes. (a) wrapped phase. (b) unwrapped to displacements (mm).

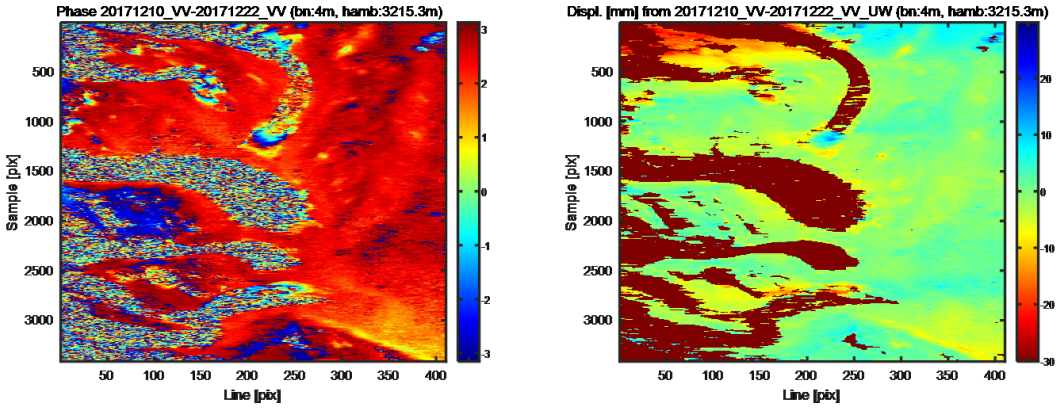

(a) (b)

Figure A.7: Descending interferogram Lunana Lakes. (a) wrapped phase. (b) unwrapped to displacements (mm).

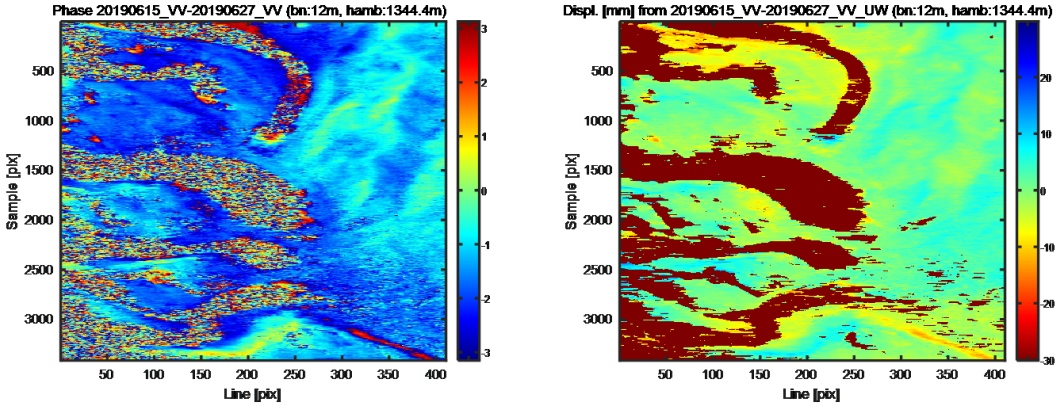

(a) (b)

Figure A.8: Descending interferogram Lunana Lakes. (a) wrapped phase. (b) unwrapped to displacements (mm).

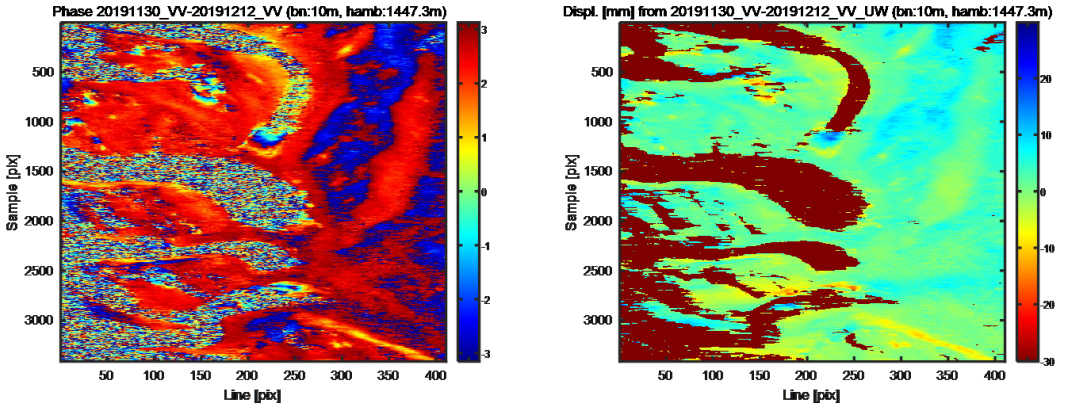

(a) **(b)**

Figure A.9: Descending interferogram Lunana Lakes. (a) wrapped phase. (b) unwrapped to displacements (mm).

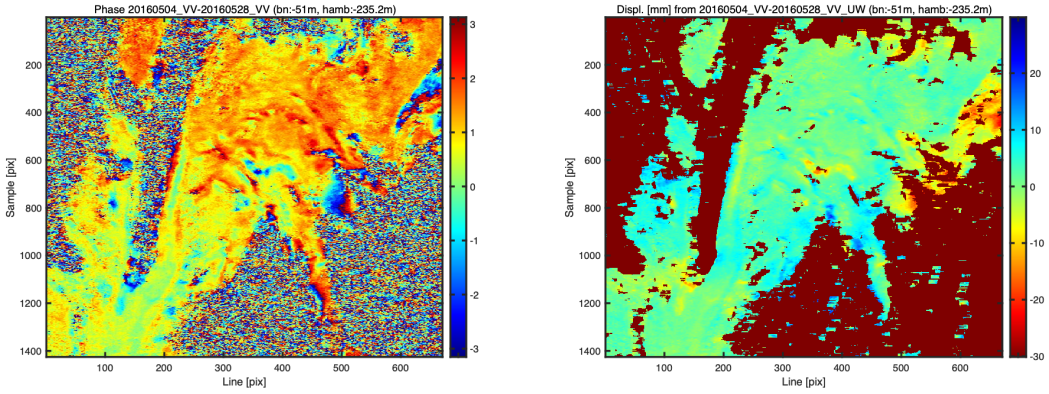

(a) **(b)**

Figure A.10: Interferogram Barun Lakes (ascending). (a) wrapped phase. (b) unwrapped into displacements (mm).

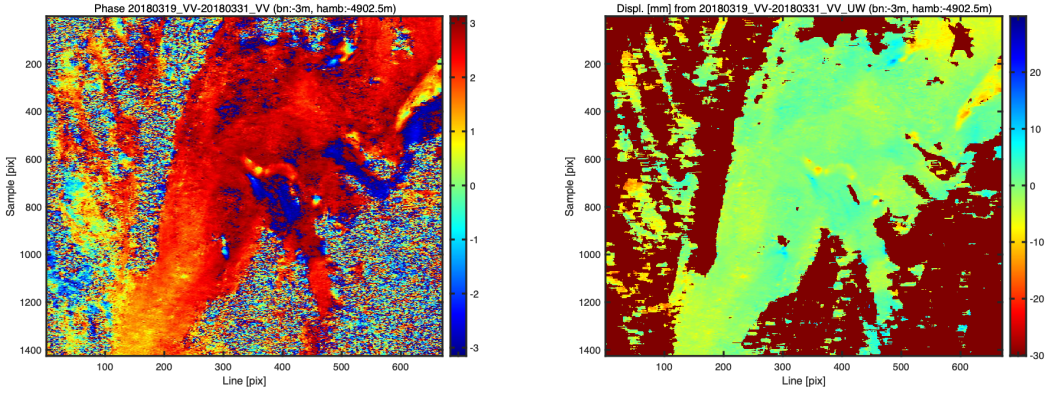

(a) **(b)**

Figure A.11: Interferogram Barun Lakes (ascending). (a) wrapped phase. (b) unwrapped into displacements (mm).

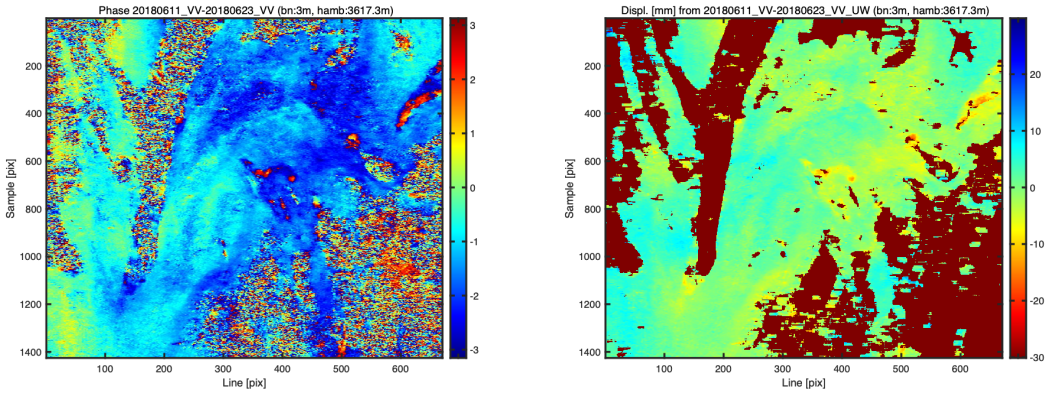

(a) **(b)**

Figure A.12: Interferogram Barun Lakes (ascending). (a) wrapped phase. (b) unwrapped into displacements (mm).

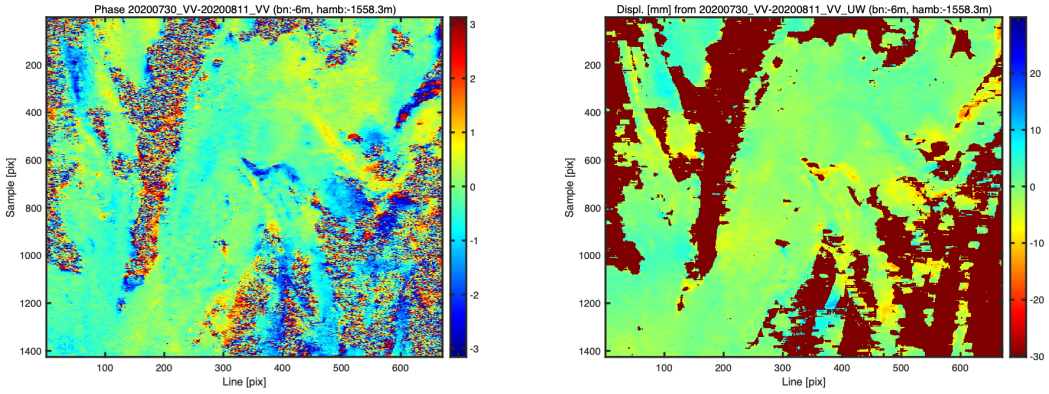

(a) **(b)**

Figure A.13: Interferogram Barun Lakes (ascending). (a) wrapped phase. (b) unwrapped into displacements (mm).

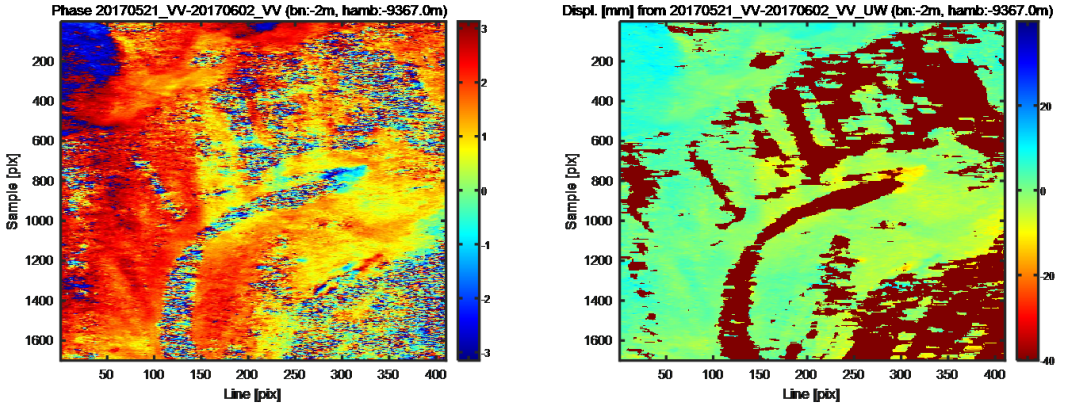

(a) **(b)**

Figure A.14: Ascending interferogram of Thulagi Lake. (a) wrapped phase. (b) unwrapped into displacements (mm).

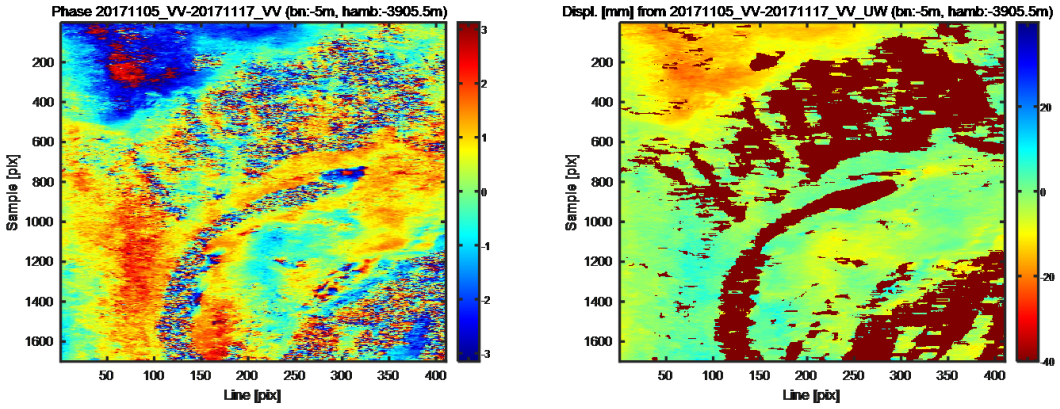

(a) (b)

Figure A.15: Ascending interferogram of Thulagi Lake. (a) wrapped phase. (b) unwrapped into displacements (mm).

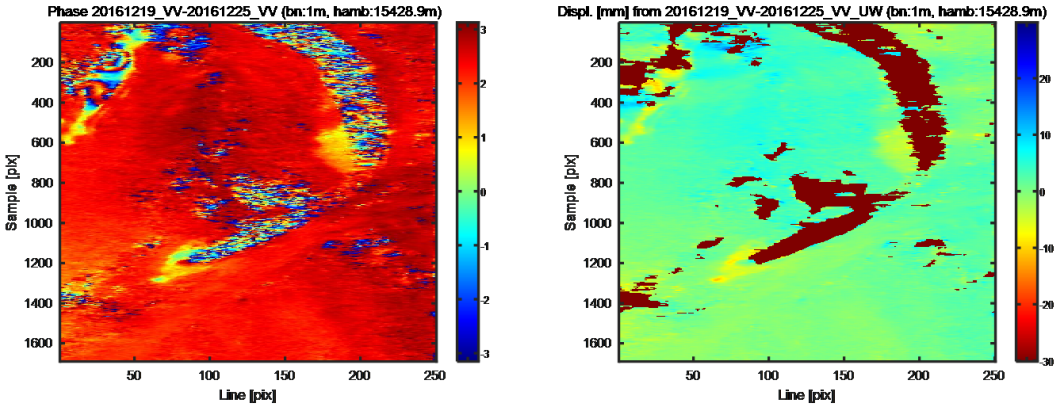

(a) (b)

Figure A.16: Ascending interferogram of Thulagi Lake. (a) wrapped phase. (b) unwrapped into displacements (mm).

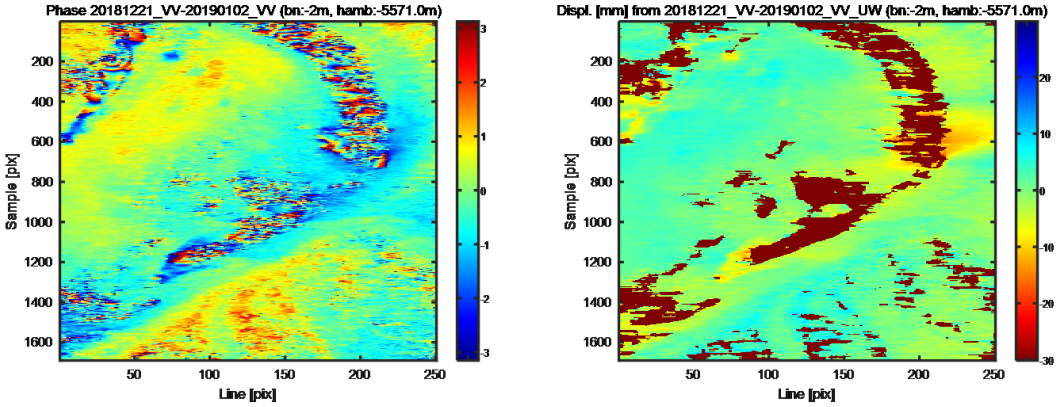

(a) (b)

Figure A.17: Descending interferogram of Thulagi Lake. (a) wrapped phase. (b) unwrapped into displacements (mm).

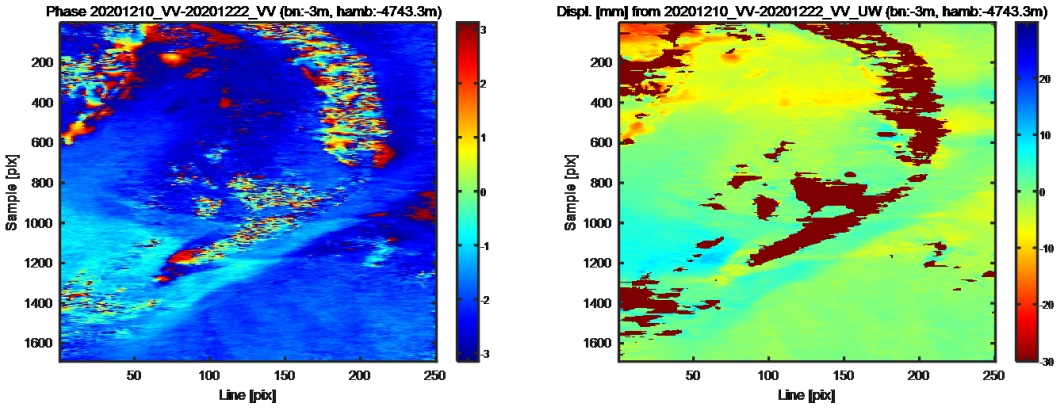

(a) (b)

Figure A.18: Descending interferogram of Thulagi Lake. (a) wrapped phase. (b) unwrapped into displacements (mm).

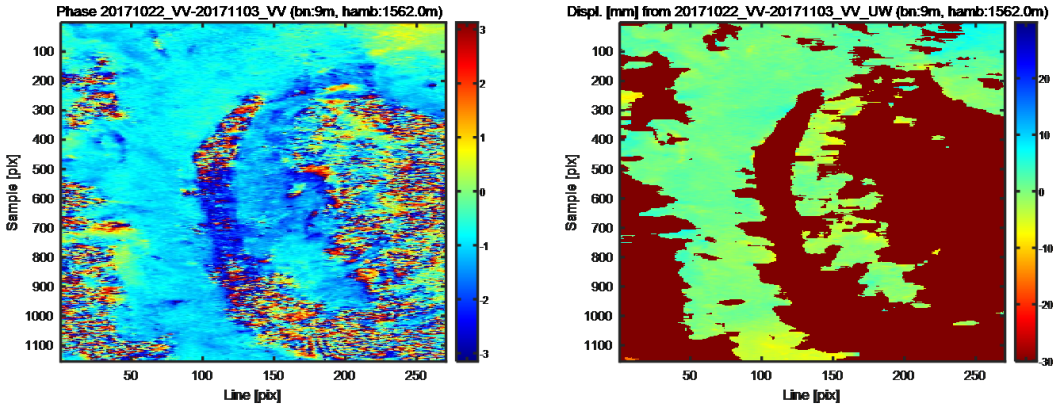

(a) (b)

Figure A.19: Interferogram at Lumding Lake (descending). (a) wrapped phase. (b) unwrapped into displacements (mm).

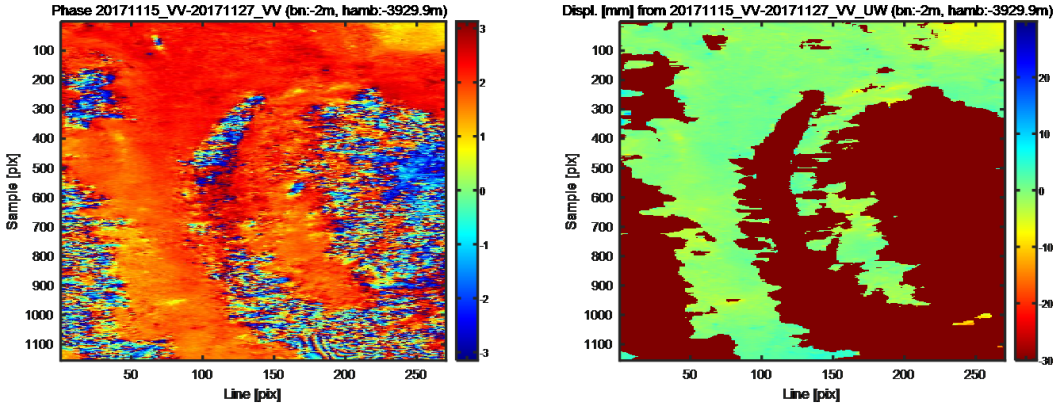

(a) (b)

Figure A.20: Interferogram at Lumding Lake (descending). (a) wrapped phase. (b) unwrapped into displacements (mm).

B PSI displacements

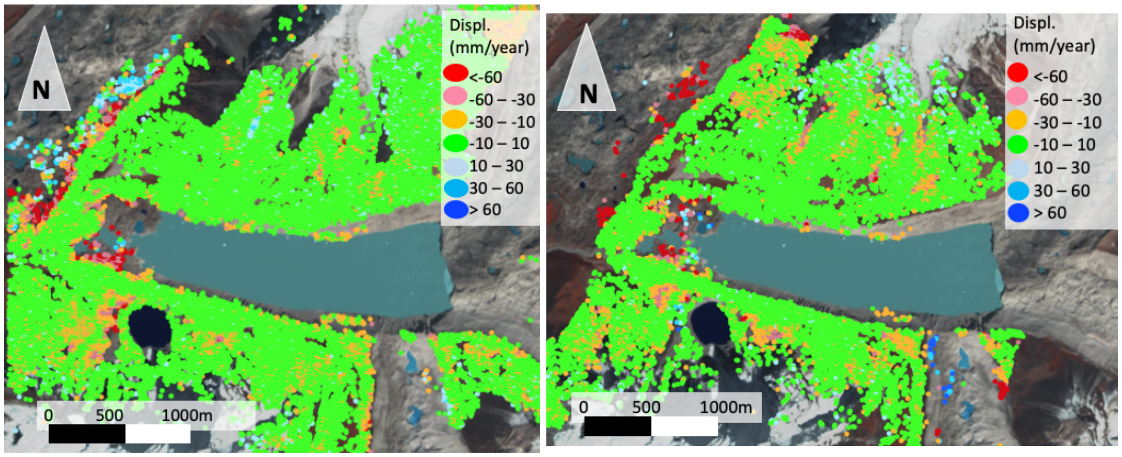

(a) **(b)**

Figure B.1: PSI displacements at Imja Lake. (a) ascending. (b) descending.

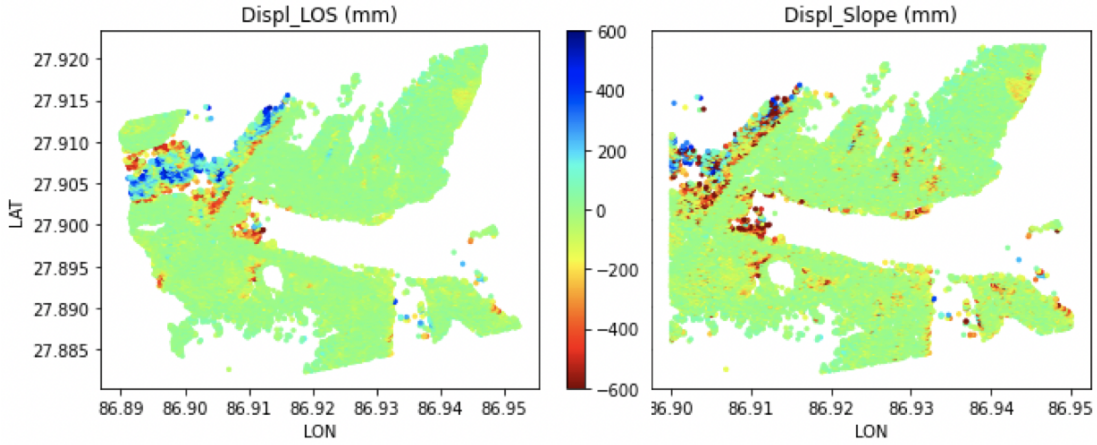

Figure B.2: Cumulative displacement along the LOS and along the steepest slope at Imja Lake (ascending)

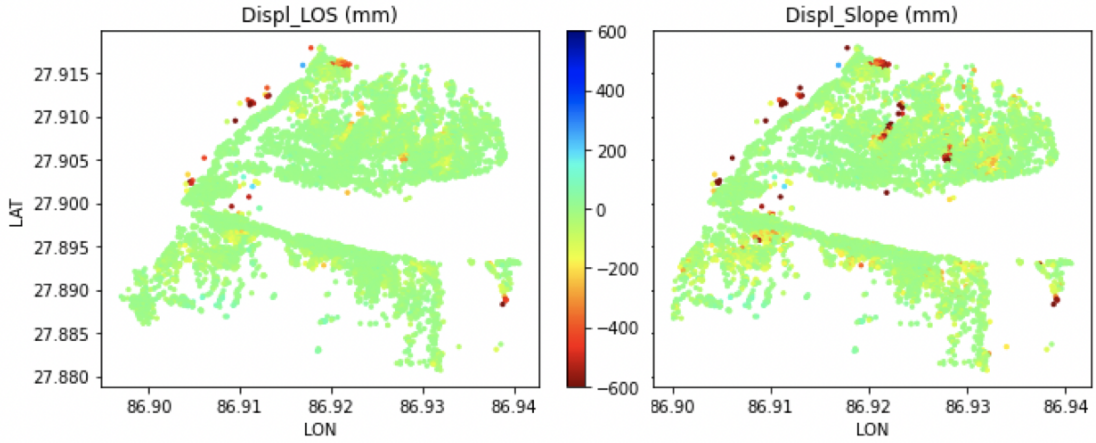

Figure B.3: Cumulative displacement along the LOS and along the steepest slope at Imja Lake (descending)

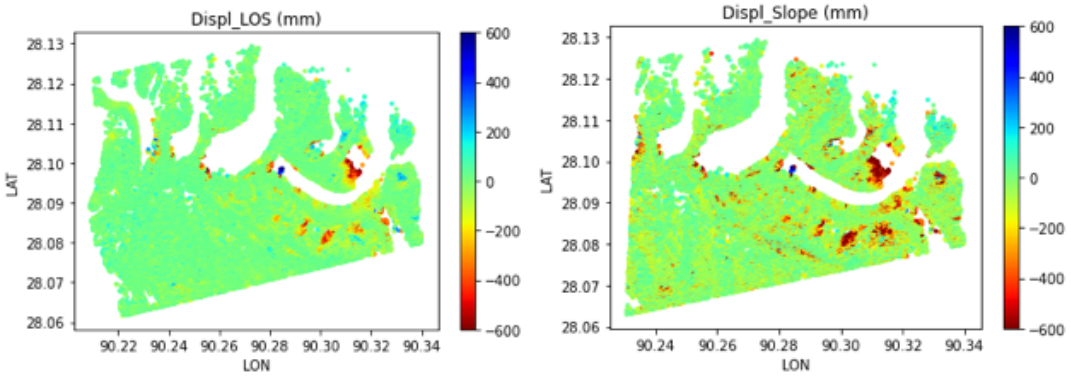

Figure B.4: Cumulative displacement along the LOS and along the steepest slope at Lunana Lakes (ascending)

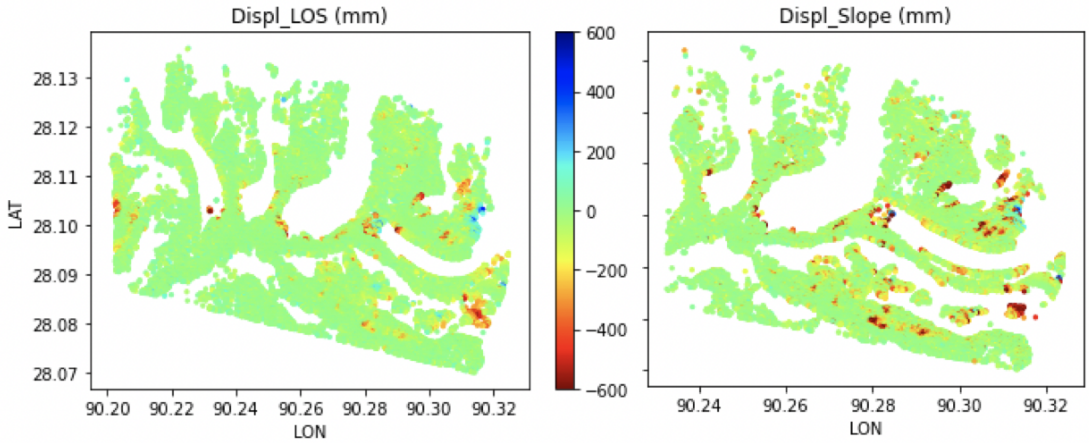

Figure B.5: Cumulative displacement along the LOS and along the steepest slope at Lunana Lakes (descending)

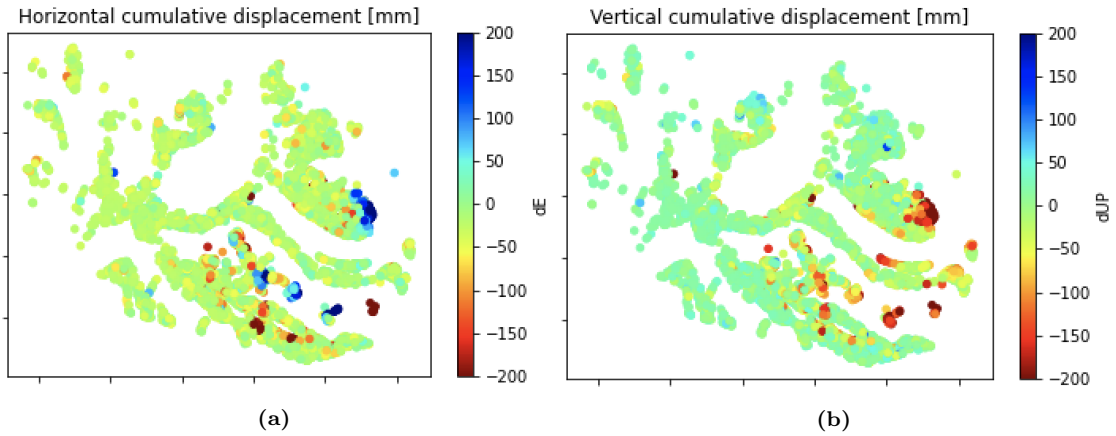

Figure B.6: Decomposed PSI displacements at Lunana Lakes (a) horizontal (east-ward). (b) vertical (upward).

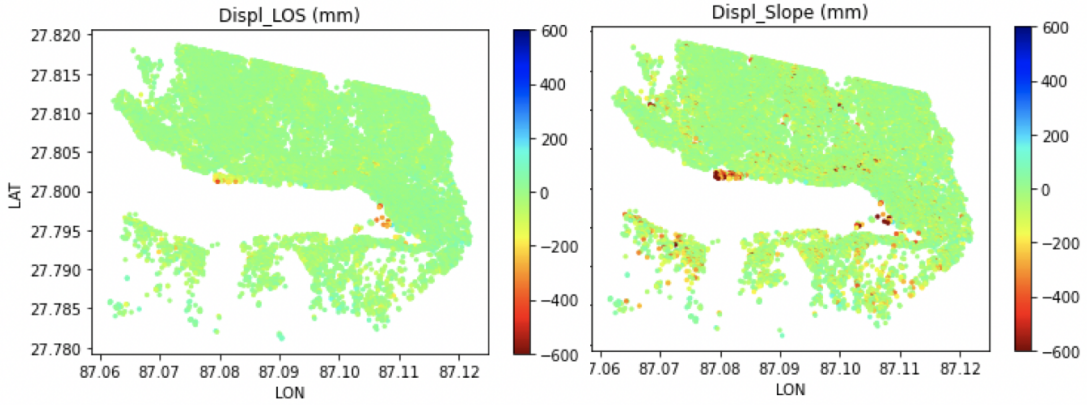

Figure B.7: Cumulative displacement along the LOS and along the steepest slope at Lower Barun Lake (descending)

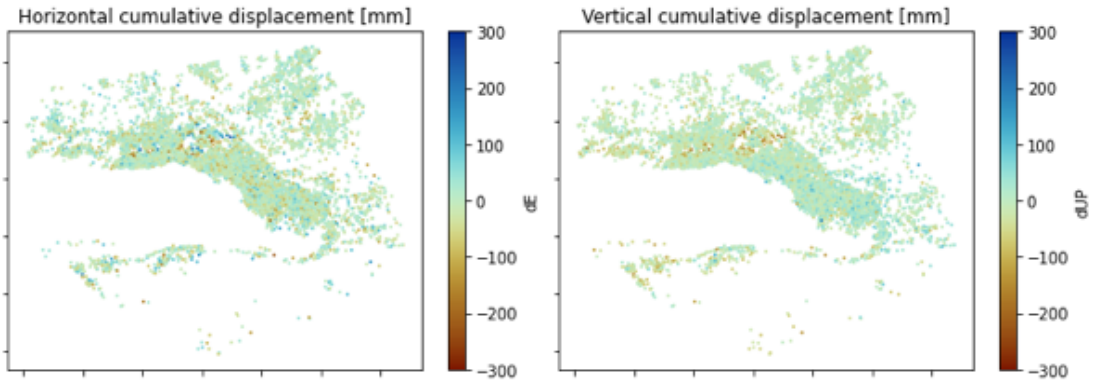

Figure B.8: Horizontal (east-ward) and vertical (upward) decomposed PSI displacements at Lower Barun Lake

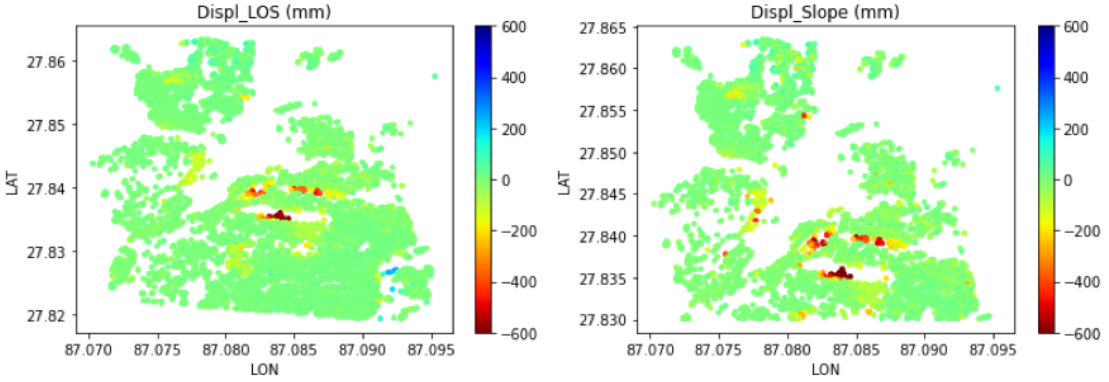

Figure B.9: Cumulative displacement along the LOS and along the steepest slope at Upper Barun Lake (descending)

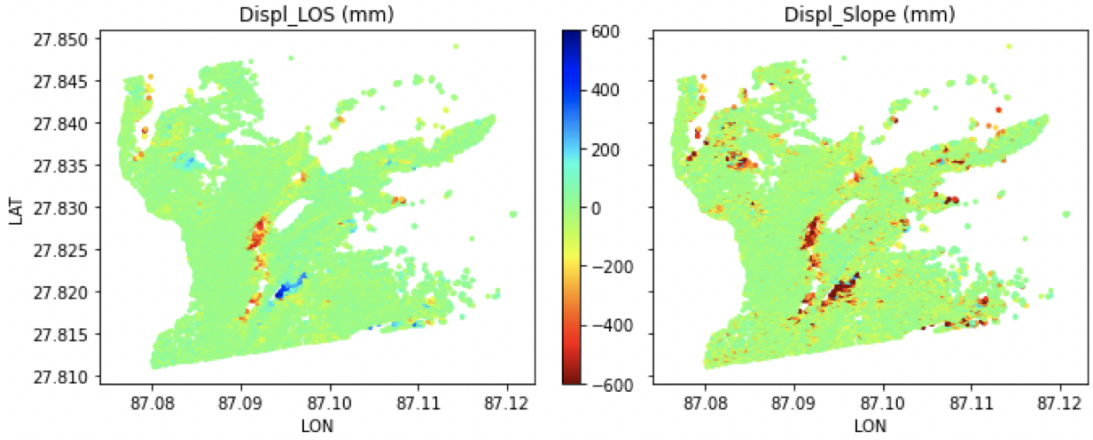

Figure B.10: Cumulative displacement along the LOS and along the steepest slope at Barun-3 Lake (ascending)

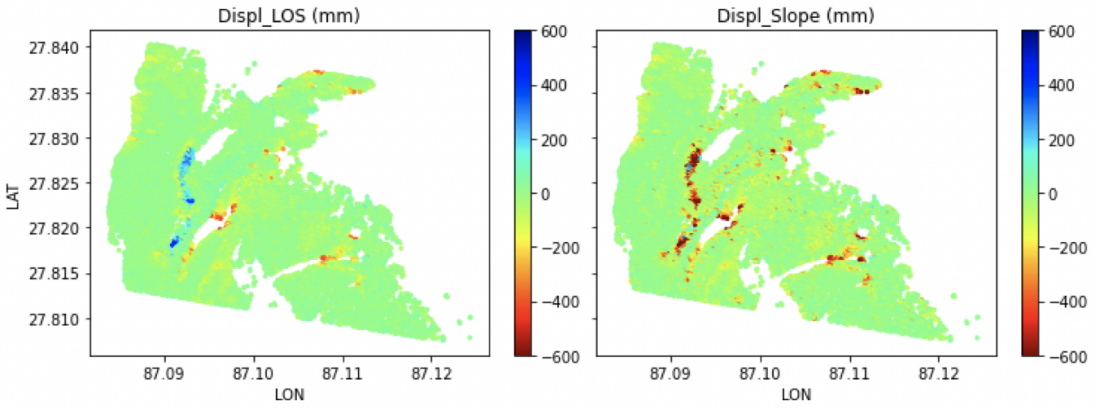

Figure B.11: Cumulative displacement along the LOS and along the steepest slope at Barun-3 Lake (descending)

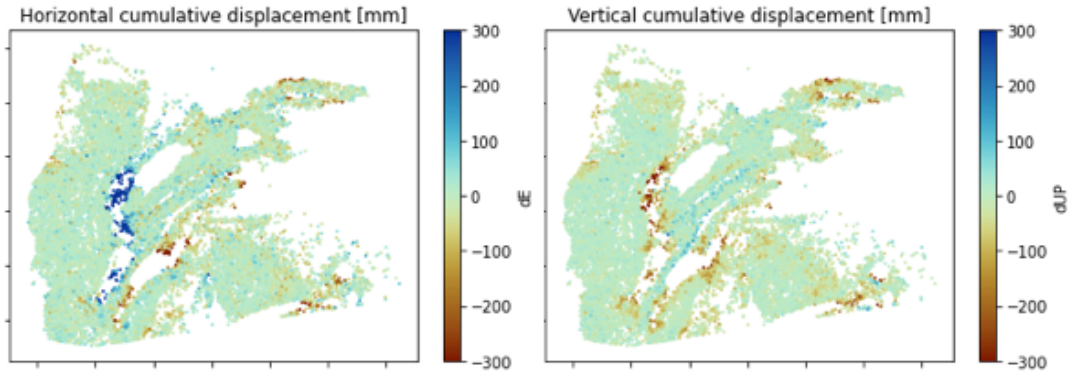

Figure B.12: Horizontal (east-ward) and vertical (upward) decomposed PSI displacements at Barun-3 Lake

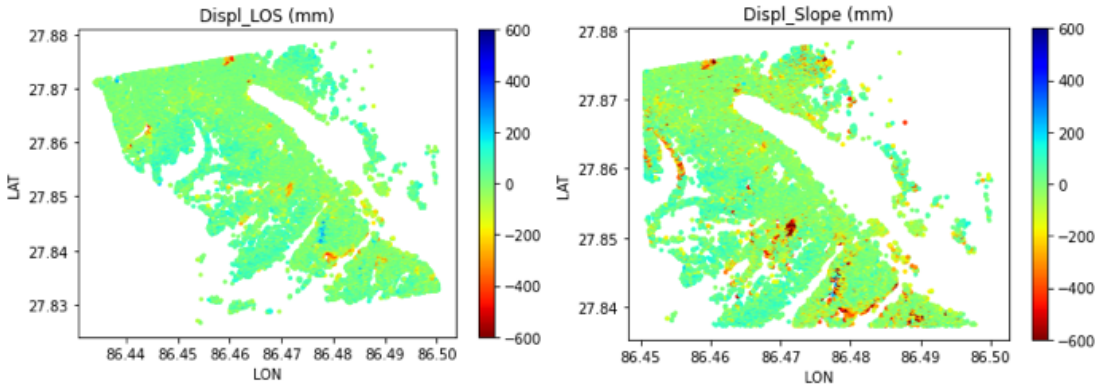

Figure B.13: Cumulative displacement along the LOS and along the steepest slope at Rolpa Lake (ascending)

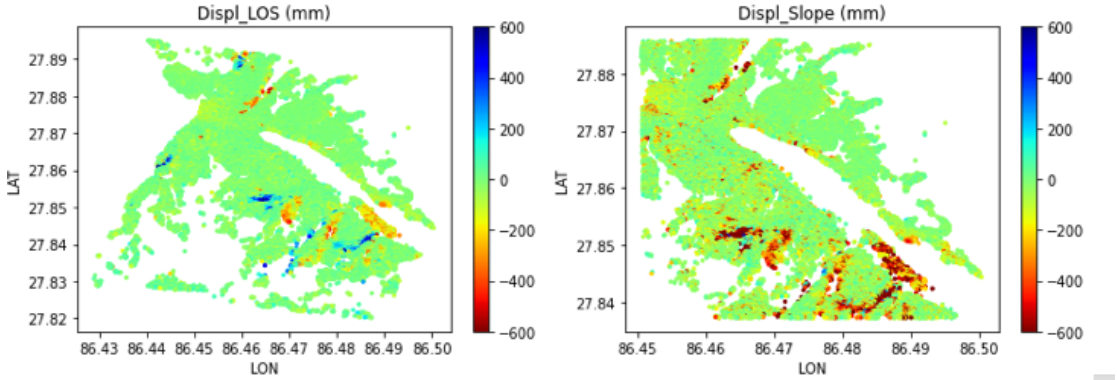

Figure B.14: Cumulative displacement along the LOS and along the steepest slope at Rolpa Lake (descending)

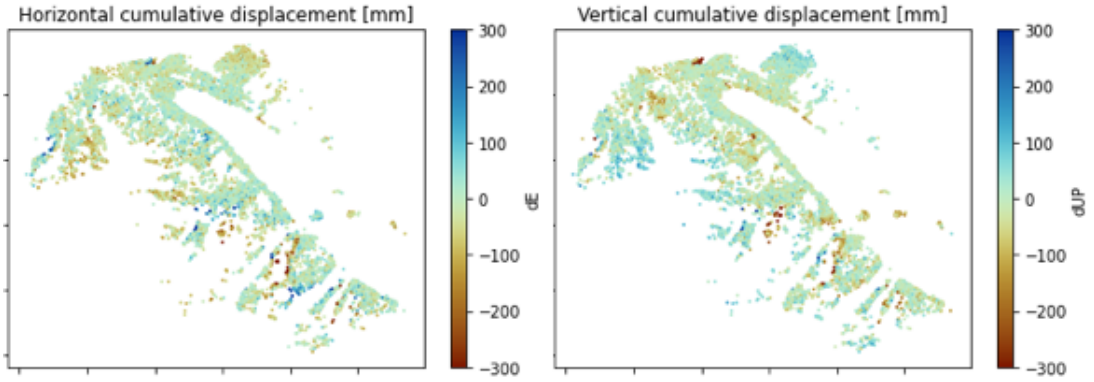

Figure B.15: Horizontal (east-ward) and vertical (upward) decomposed PSI displacements at Rolpa Lake

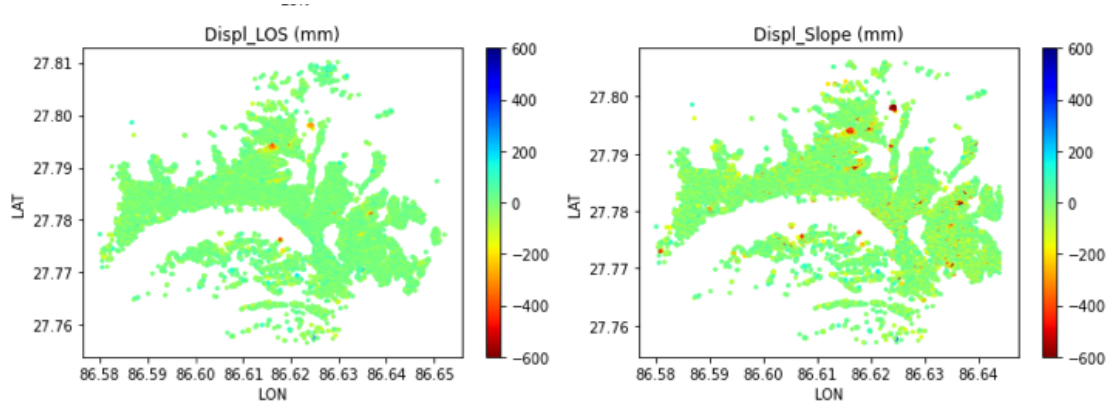

Figure B.16: Cumulative displacement along the LOS and along the steepest slope at Lumding Lake (ascending)

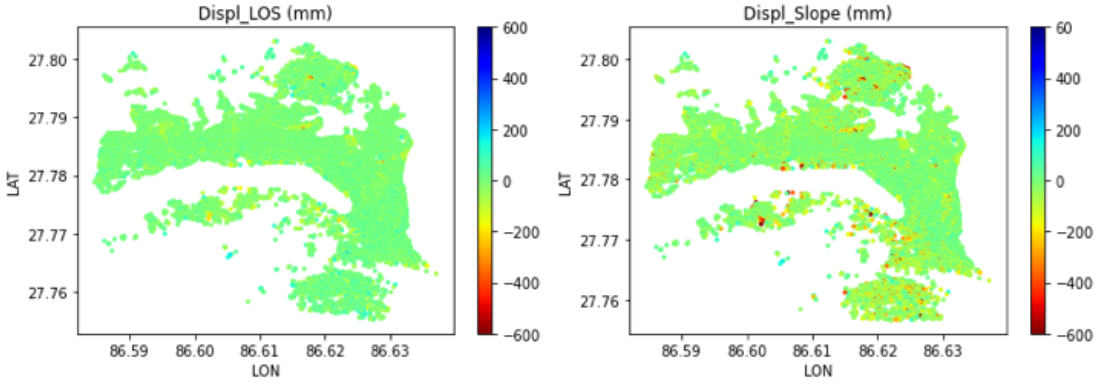

Figure B.17: Cumulative displacement along the LOS and along the steepest slope at Lumding Lake (descending)

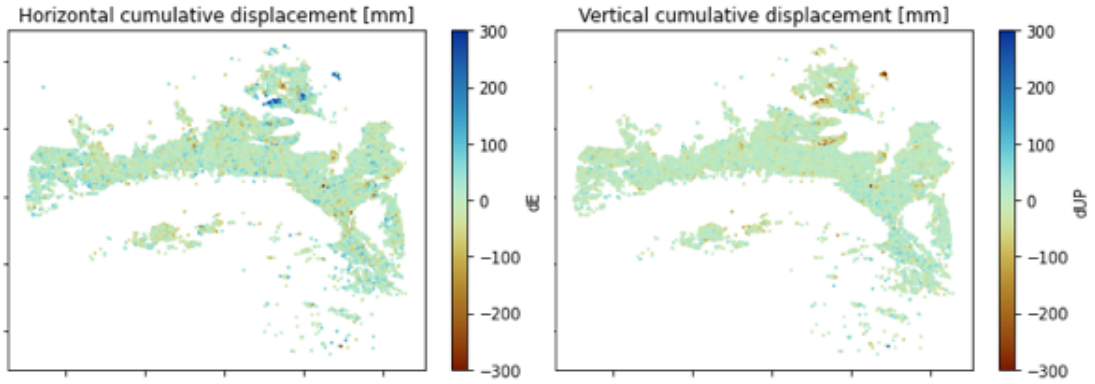

Figure B.18: Horizontal (east-ward) and vertical (upward) decomposed PSI displacements at Lumding Lake

C InSAR processing results

Lunana Lakes

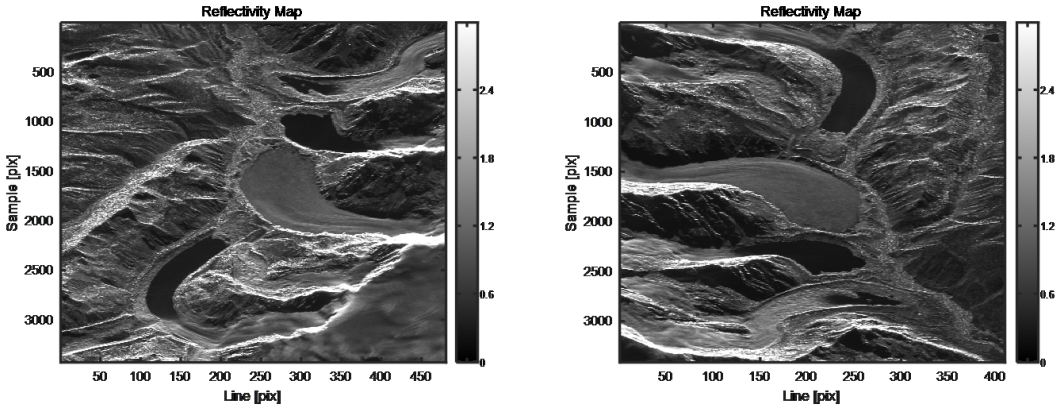

(a) **(b)**

Figure C.19: Reflectivity map Lunana Lakes. (a) ascending. (b) descending.

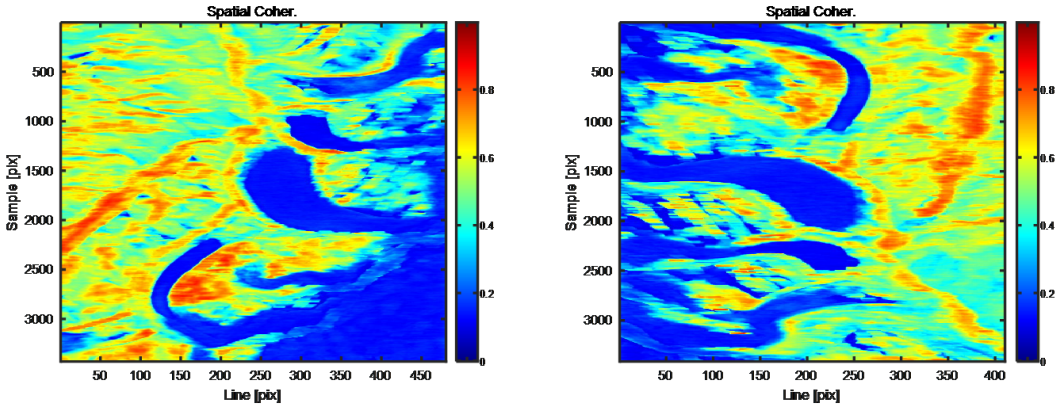

(a) (b)

Figure C.20: Spatial coherence map at Lunana Lakes. (a) ascending. (b) descending.

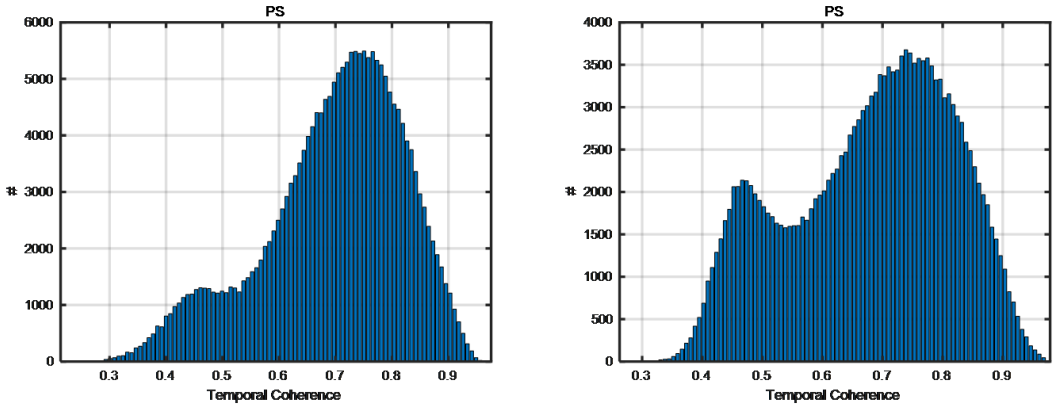

(a) (b)

Figure C.21: Temporal coherence graph of PS at Lunana Lakes. (a) ascending. (b) descending.

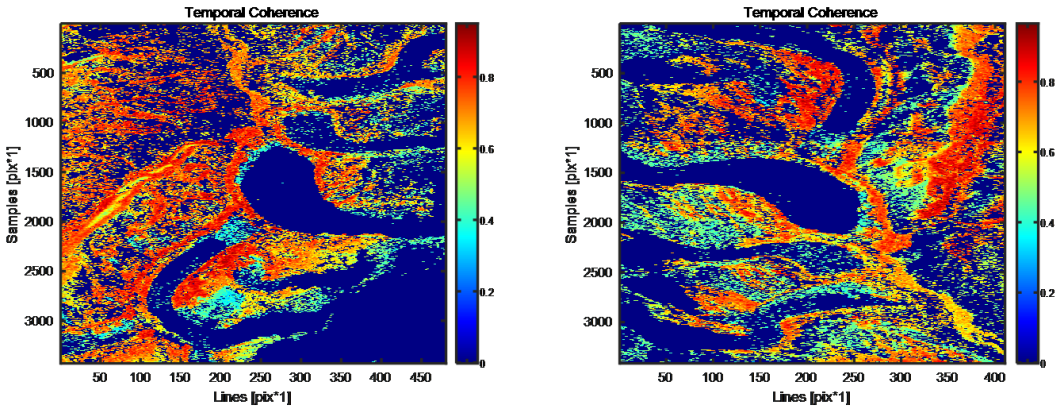

(a) (b)

Figure C.22: Temporal coherence map of PS at Lunana Lakes (a) ascending. (b) descending.

Barun Lakes

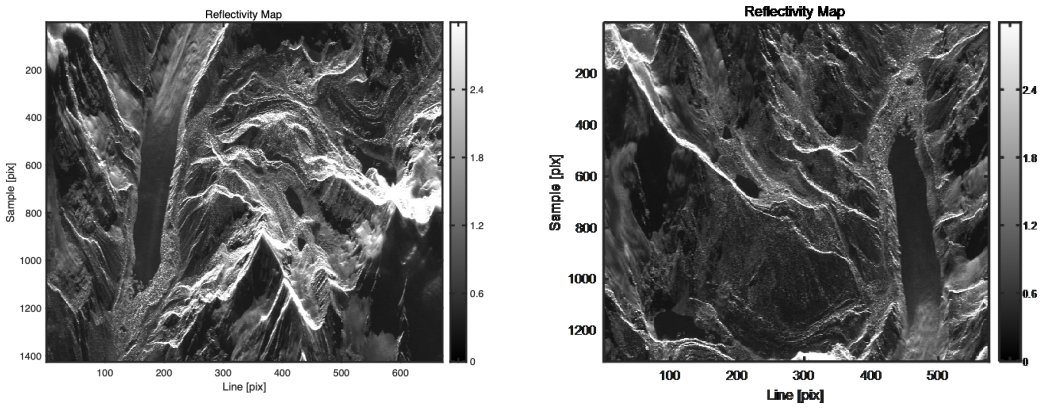

(a) **(b)**

Figure C.23: Reflectivity map of Barun Lakes. (a) ascending. (b) descending

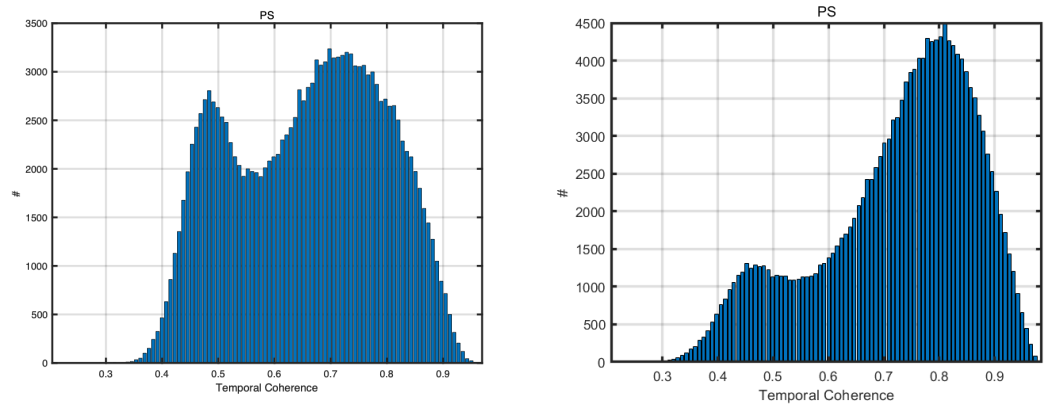

(a) **(b)**

Figure C.24: Temporal coherence graph of PS at Barun Lakes. (a) ascending. (b) descending.

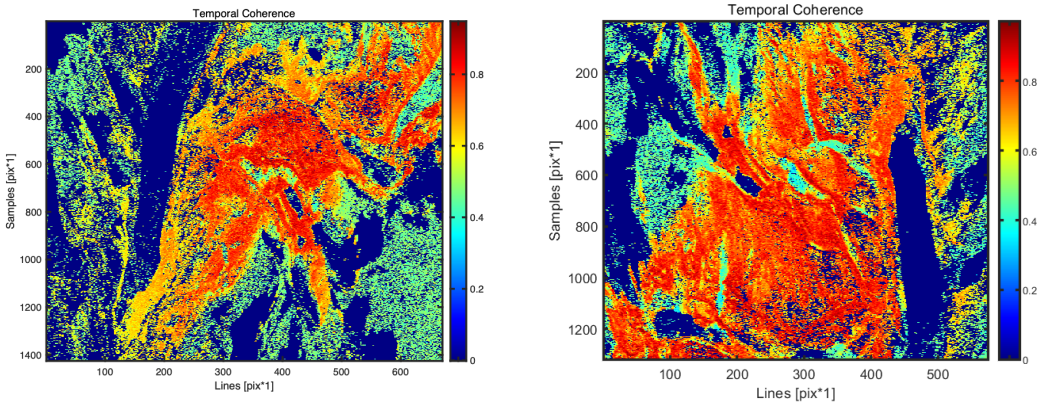

(a) **(b)**

Figure C.25: Temporal coherence map of PS at Barun Lakes. (a) ascending. (b) descending

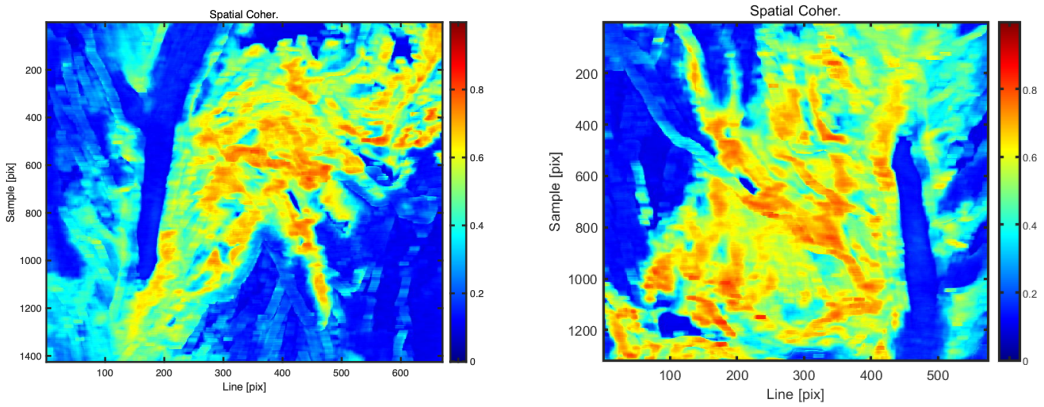

(a) **(b)**

Figure C.26: Spatial coherence map at Barun Lakes. (a) ascending. (b) descending.

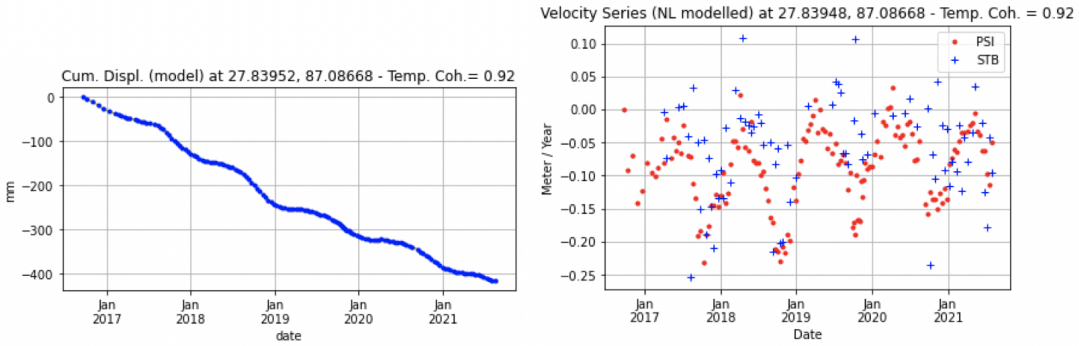

Figure C.27: Velocity series PSI vs CDInSAR - moving point (Barun descending)

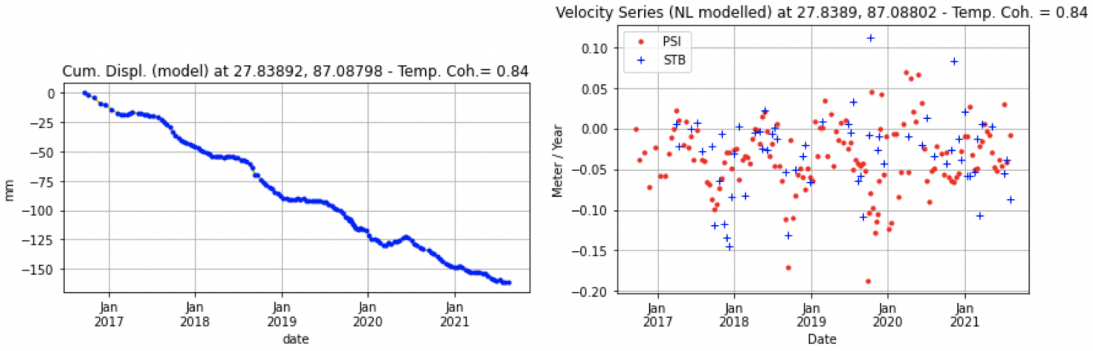

Figure C.28: Velocity series PSI vs CDInSAR - moving point (Barun descending)

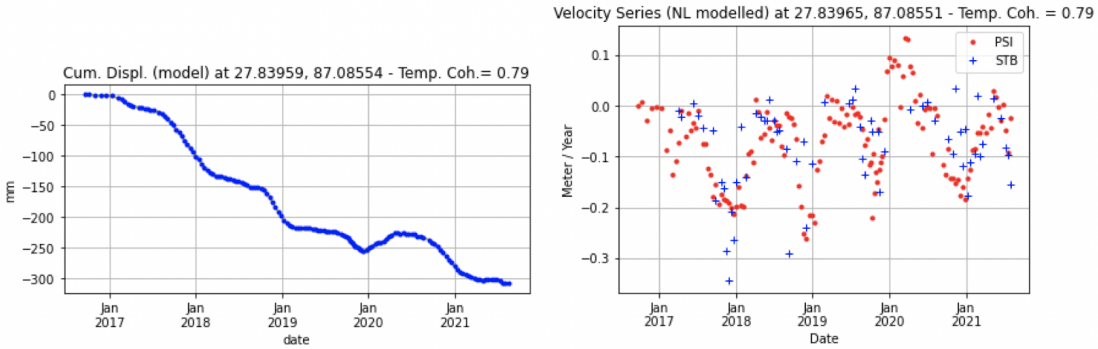

Figure C.29: Velocity series PSI vs CDInSAR - moving point (Barun descending)

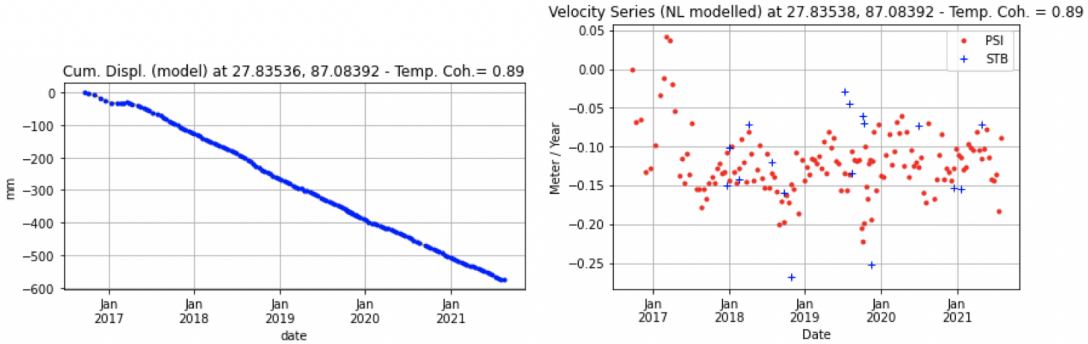

Figure C.30: Velocity series PSI vs CDInSAR - moving point (Barun descending)

Rolpa Lake

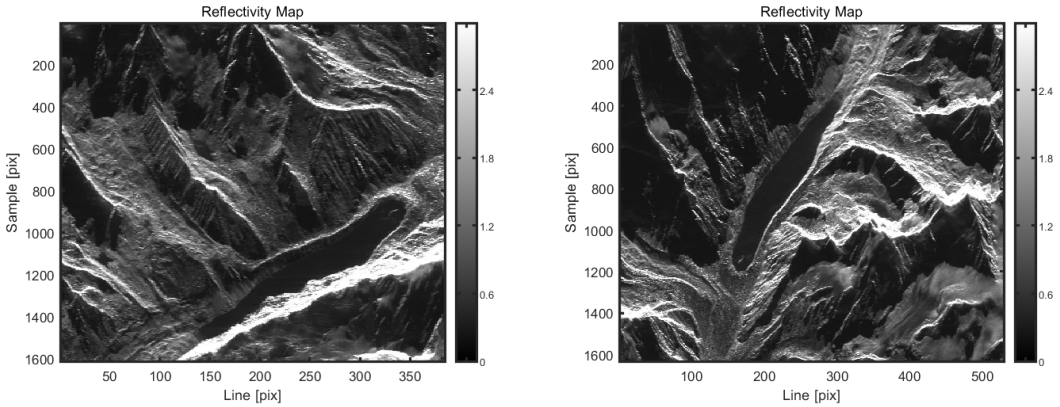

(a) **(b)**

Figure C.31: Reflectivity map of Rolpa Lake. (a) ascending. (b) descending.

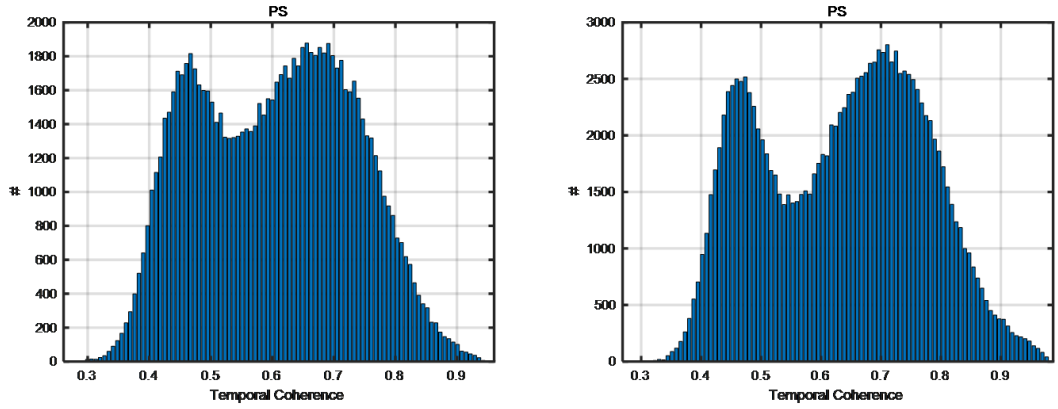

(a) (b)

Figure C.32: Temporal coherence graph of PS at Rolpa Lake. (a) ascending. (b) descending.

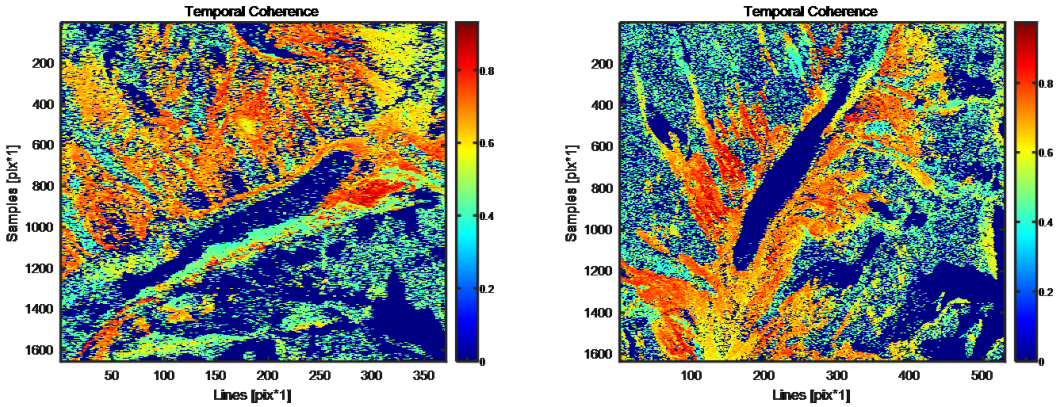

(a) (b)

Figure C.33: Temporal coherence map of PS at Rolpa Lake. (a) ascending. (b) descending.

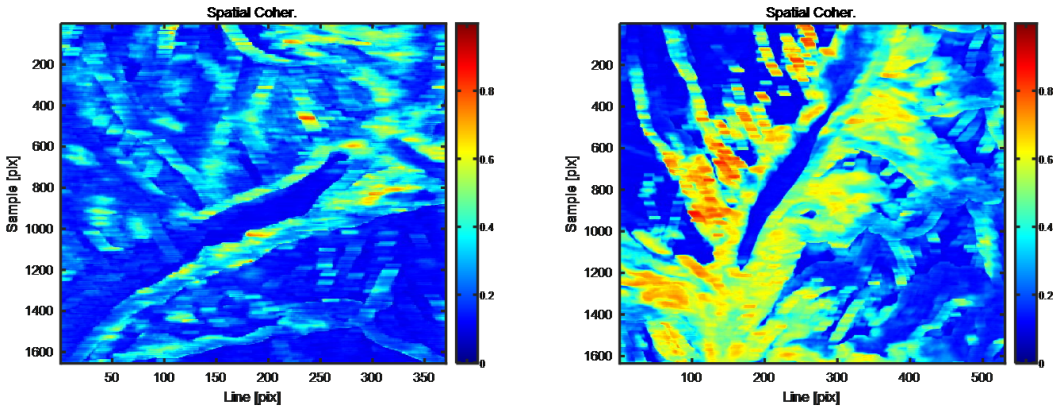

(a) (b)

Figure C.34: Spatial coherence map at Rolpa Lake. (a) ascending. (b) descending.

Thulagi Lake

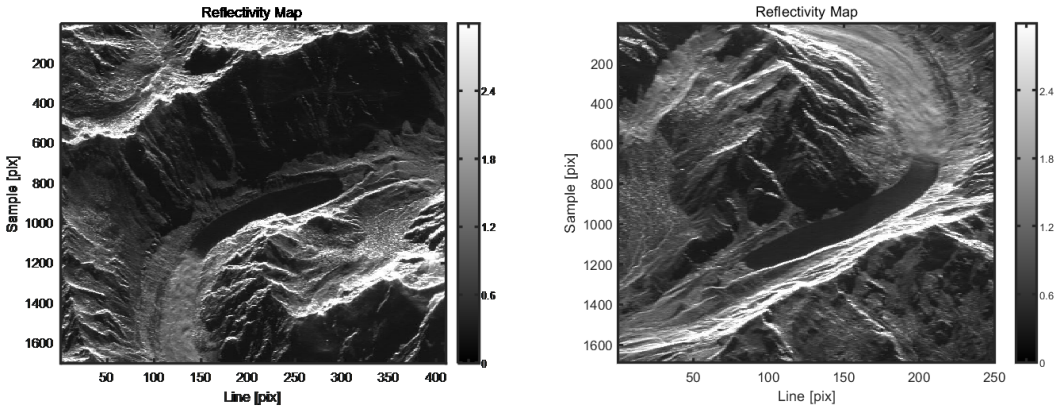

(a) (b)

Figure C.35: Reflectivity map of Thulagi Lake. (a) ascending. (b) descending.

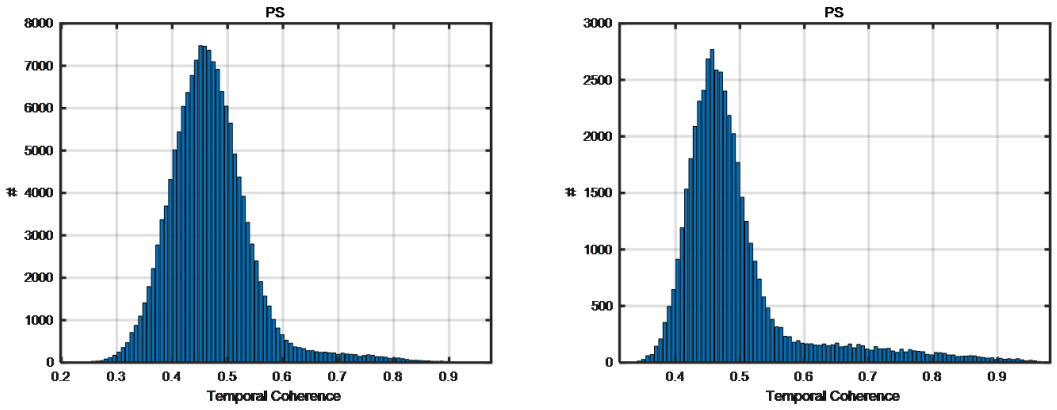

(a) (b)

Figure C.36: Temporal coherence graph of PS at Thulagi Lake. (a) ascending. (b) descending.

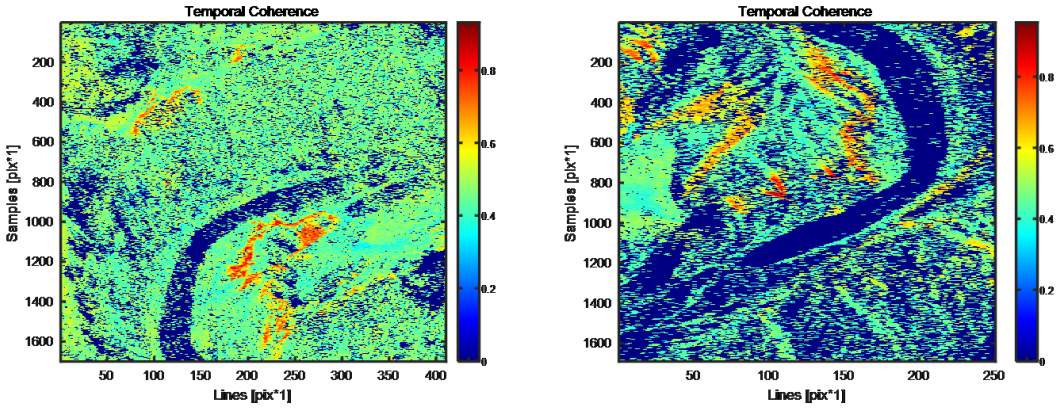

(a) (b)

Figure C.37: Temporal coherence map of PS at Thulagi Lake. (a) ascending. (b) descending.

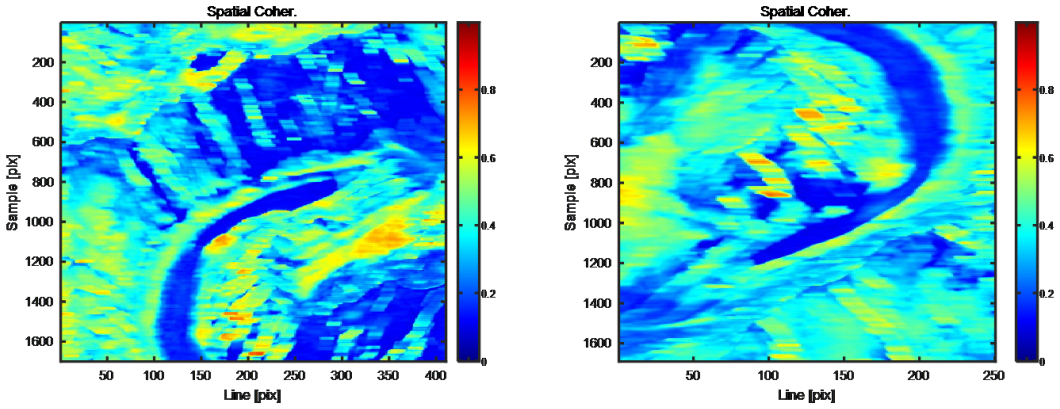

(a) (b)

Figure C.38: Spatial coherence map of Thulagi Lake. (a) ascending. (b) descending

Lumding Lake

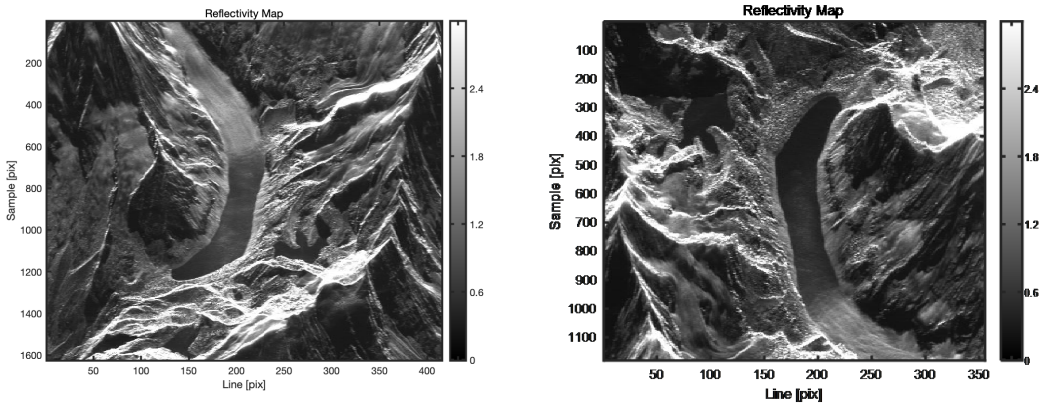

(a) (b)

Figure C.39: Reflectivity map of Lumding Lake. (a) ascending. (b) descending.

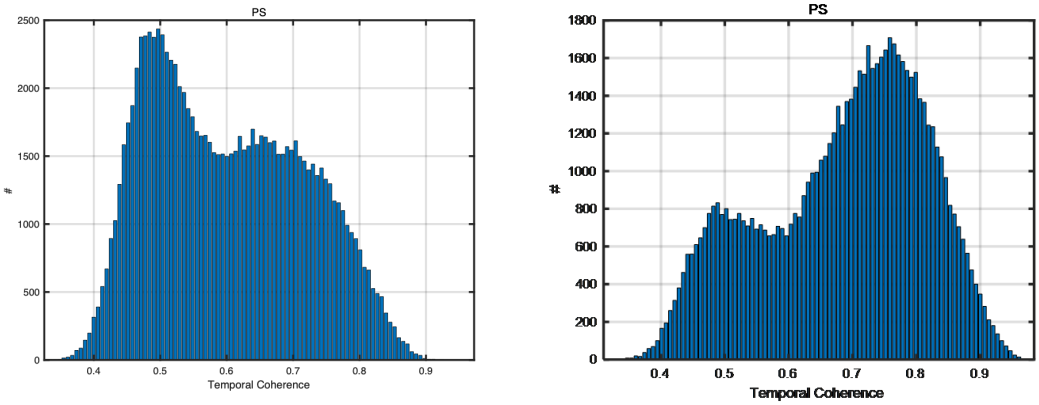

(a) (b)

Figure C.40: Temporal coherence graph of PS at Lumding Lake. (a) ascending. (b) descending.

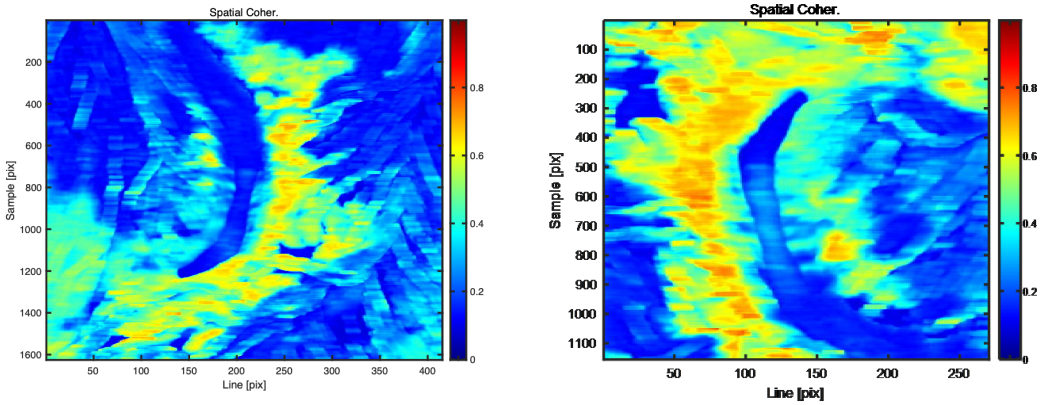

(a) **(b)**

Figure C.42: Spatial coherence map of Lumding Lake. (a) ascending. (b) descending.

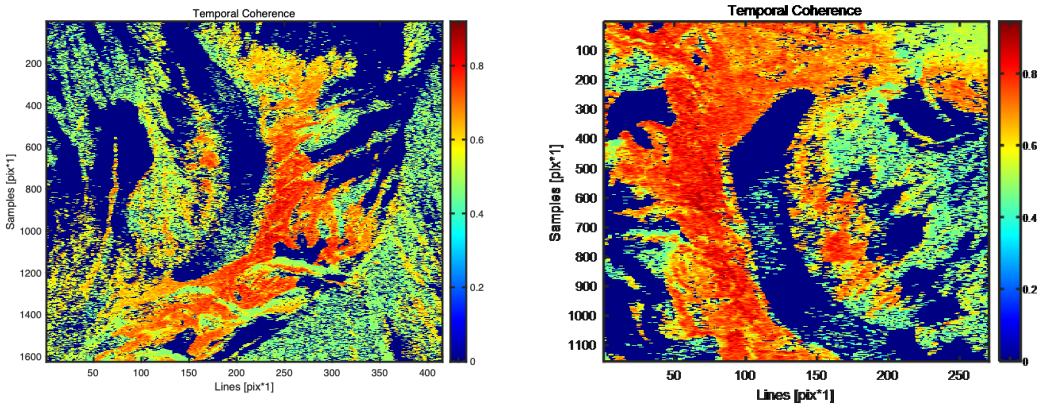

(a) **(b)**

Figure C.41: Temporal coherence map of PS at Lumding Lake. (a) ascending. (b) descending.

D Meteorological data

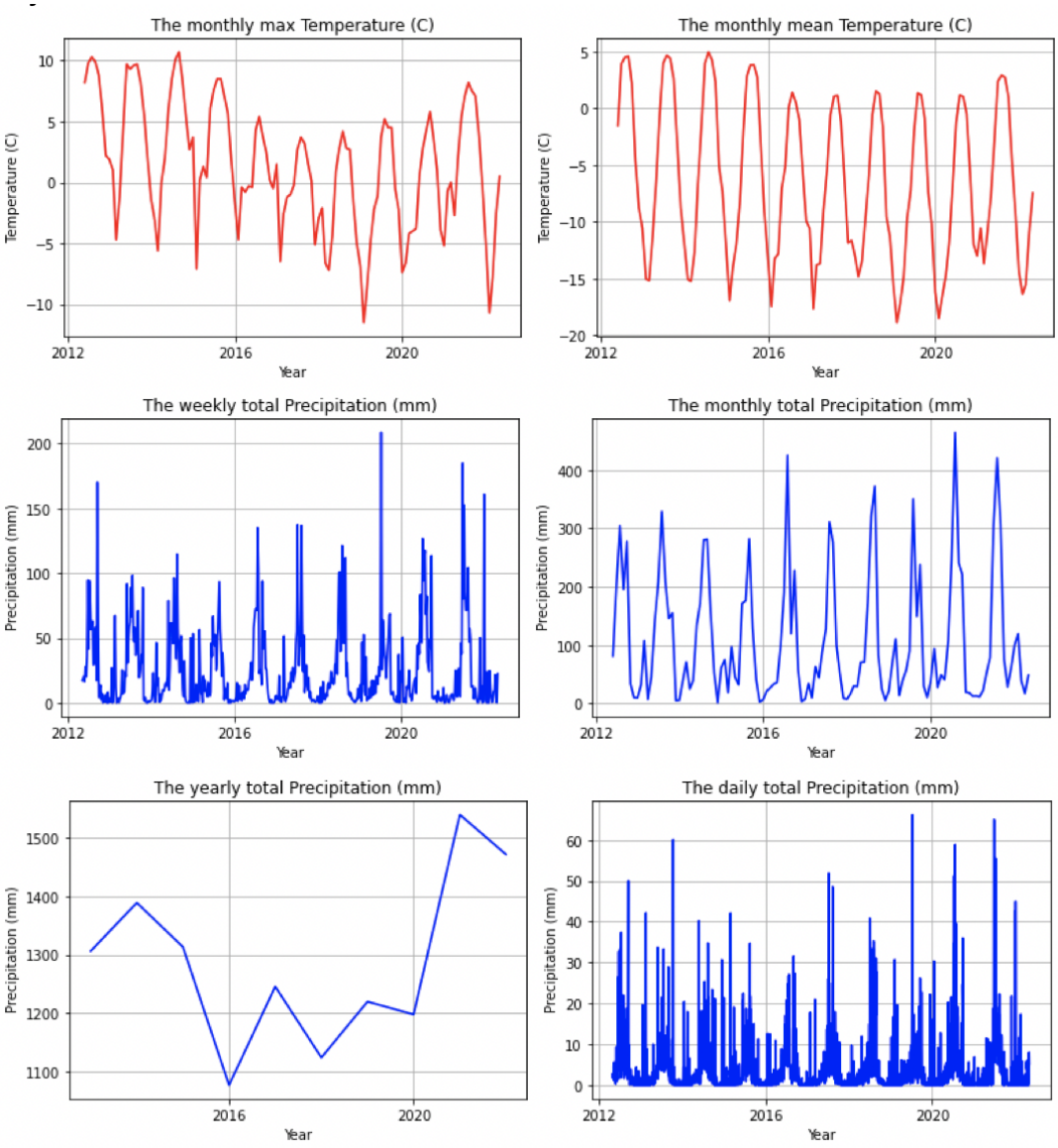

Figure D.1: Weather data at Imja Lake

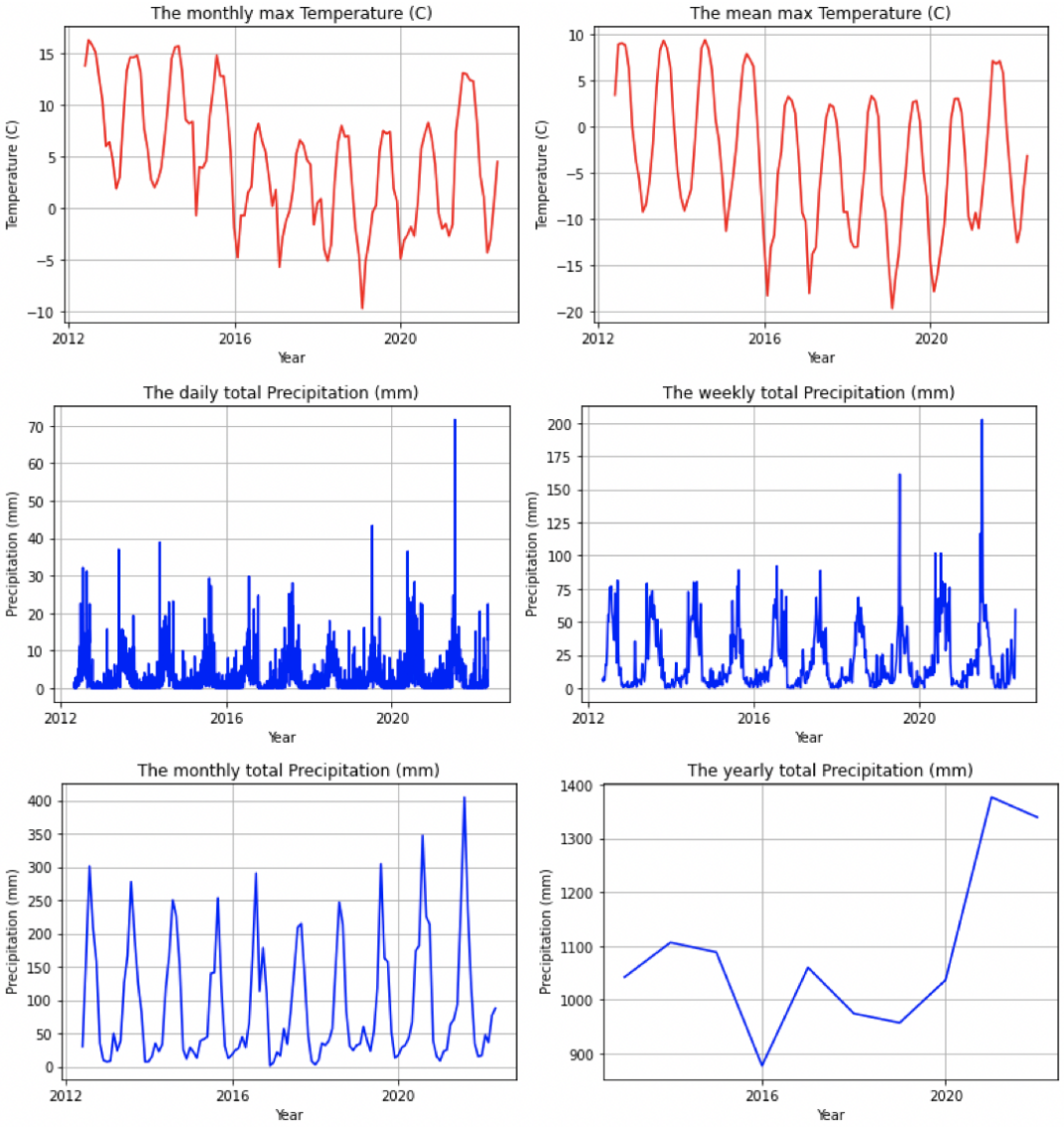

Figure D.2: Weather data at Lunana Lakes

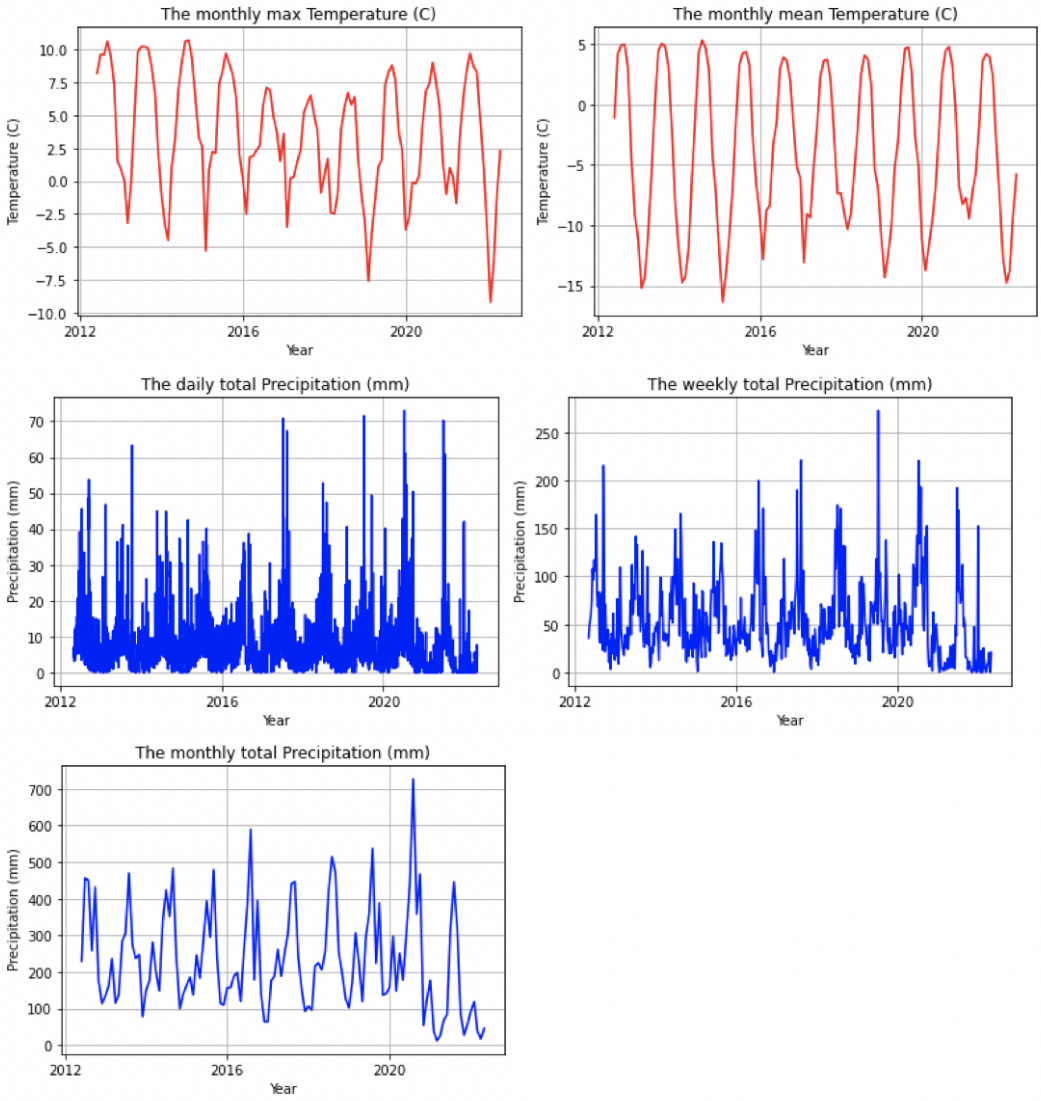

Figure D.3: Weather data at Barun Lakes

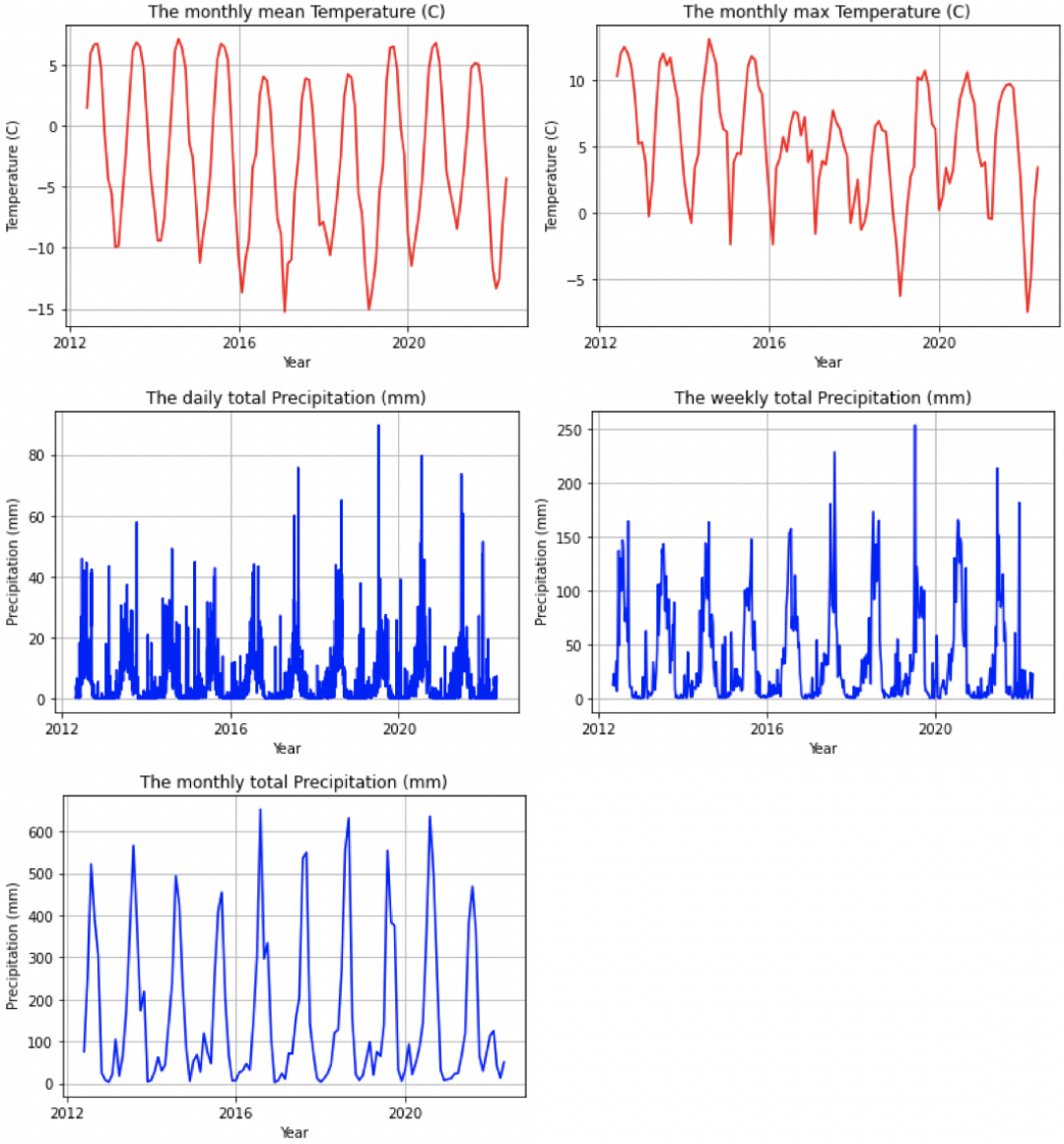

Figure D.4: Weather data at Rolpa Lake

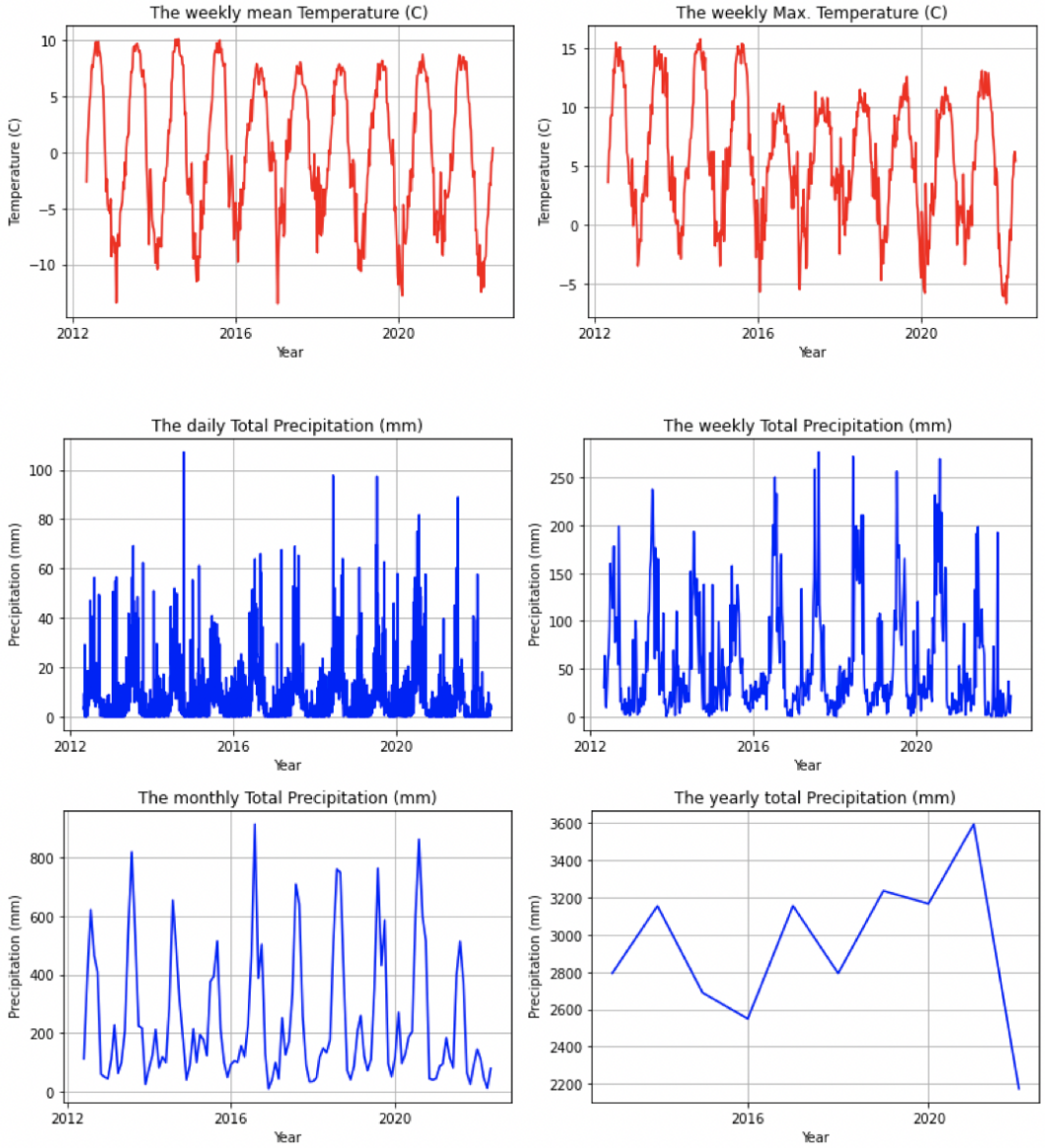

Figure D.5: Weather data at Thulagi Lake

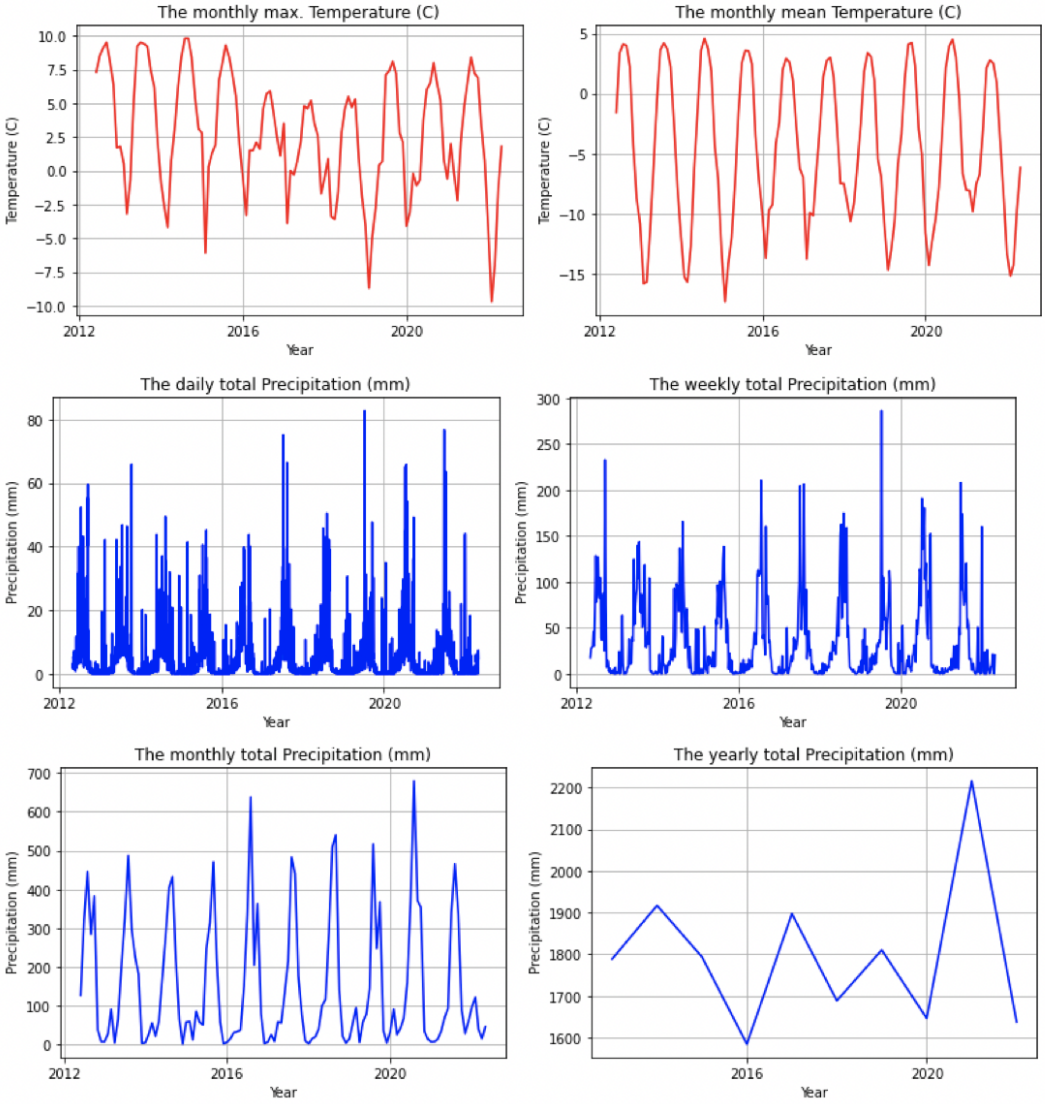

Figure D.6: Weather data at Lumding Lake

E Optical imagery

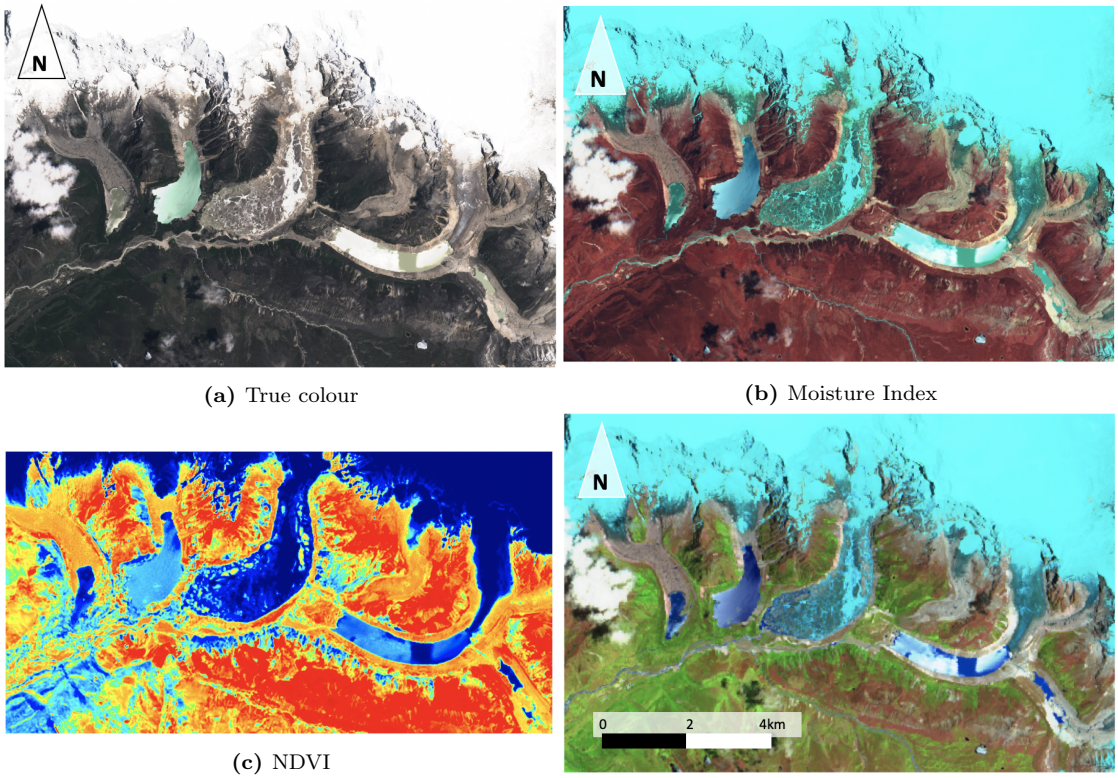

(a) True colour

(b) Moisture Index

(c) NDVI

(d) False colour vegetation

Figure E.1: Sentinel-2 imagery at Lumding Lake in July 2019

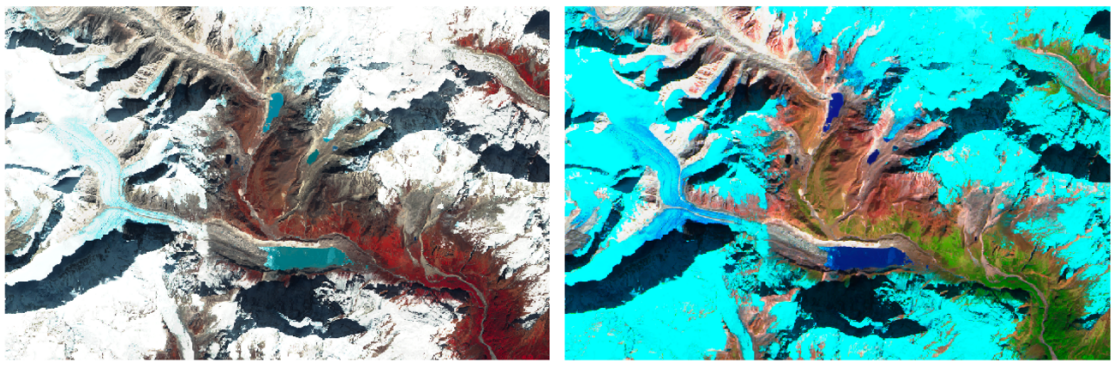

(a) False colour vegetation

(b) SWIR

Figure E.2: Sentinel-2 imagery at Barun Lake in July 2018

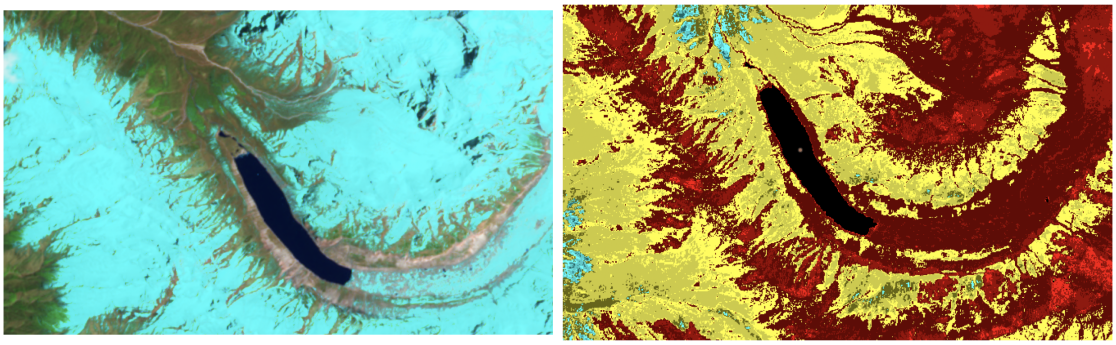

(a) NDVI

(b) False colour vegetation

Figure E.3: Sentinel-2 imagery at Thulagi Lake in March 2019

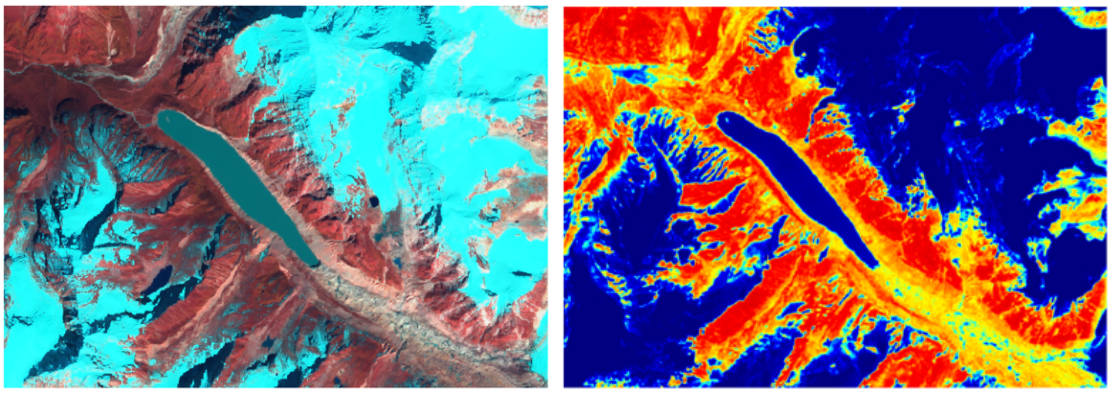

(a) False colour geology

(b) Moisture Index

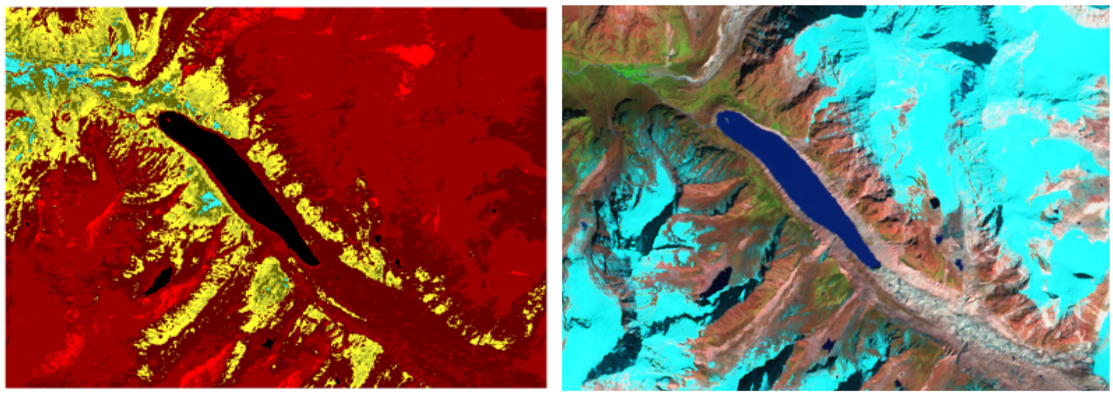

(c) NDVI

(d) SWIR

Figure E.4: Sentinel-2 imagery at Rolpa Lake in July 2019

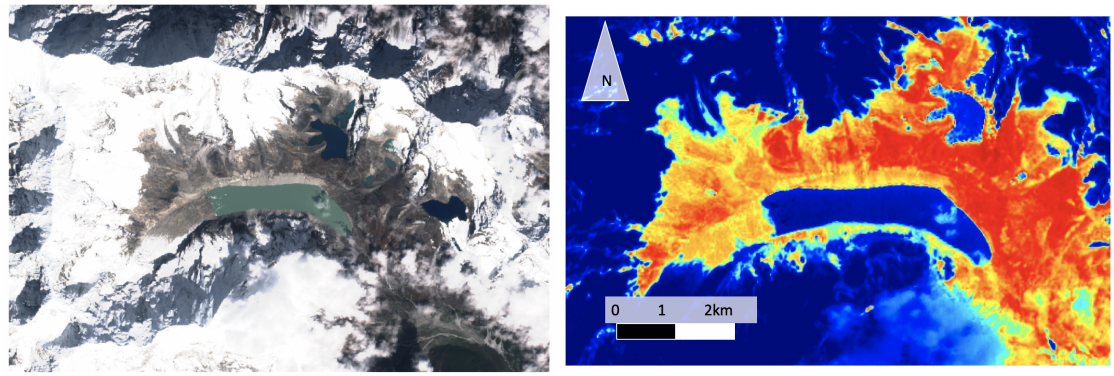

(a) True colour

(b) Moisture Index

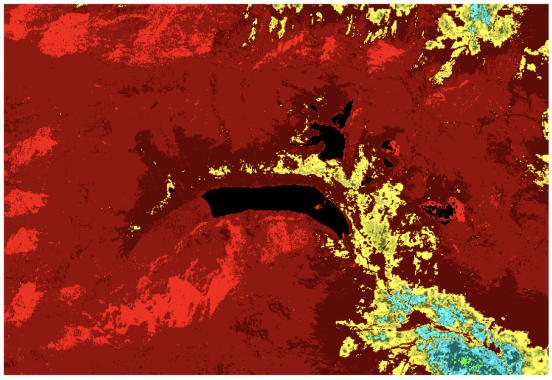

(c) NDVI

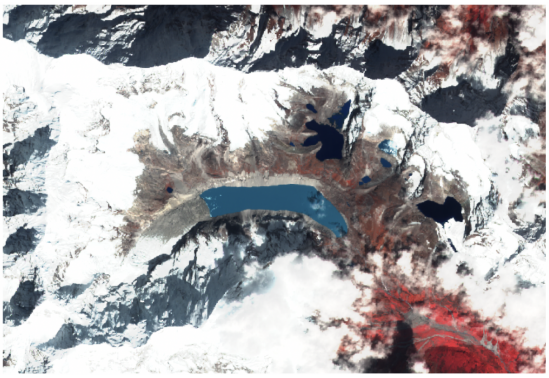

(d) False colour vegetation

Figure E.5: Sentinel-2 imagery at Lumding Lake in July 2019

F Topographical analysis

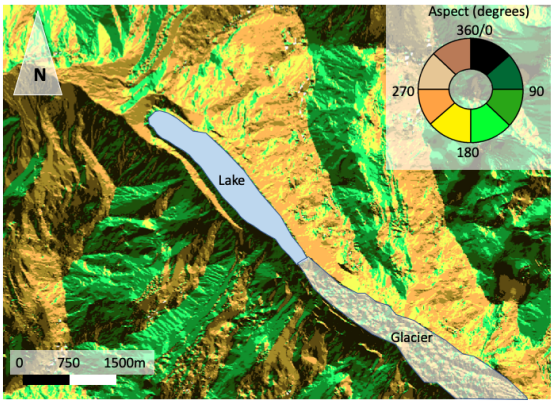

(a) Rolpa Lake

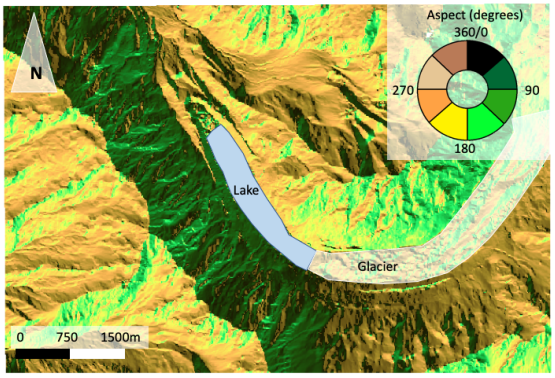

(b) Thulagi Lake

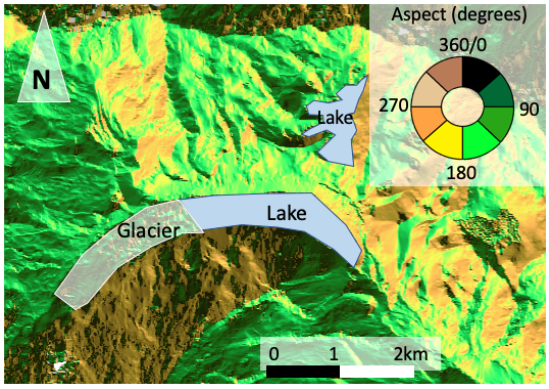

(c) Lumding Lake

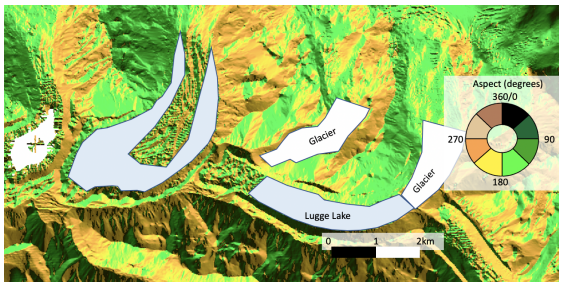

(d) Lunana Lakes

Figure F.1: Aspect maps

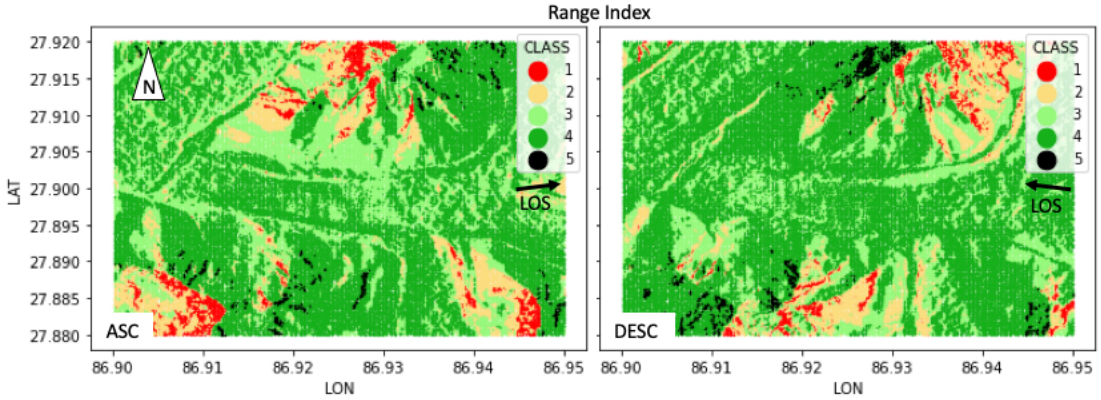

Figure F.2: Range index maps at Imja Lake

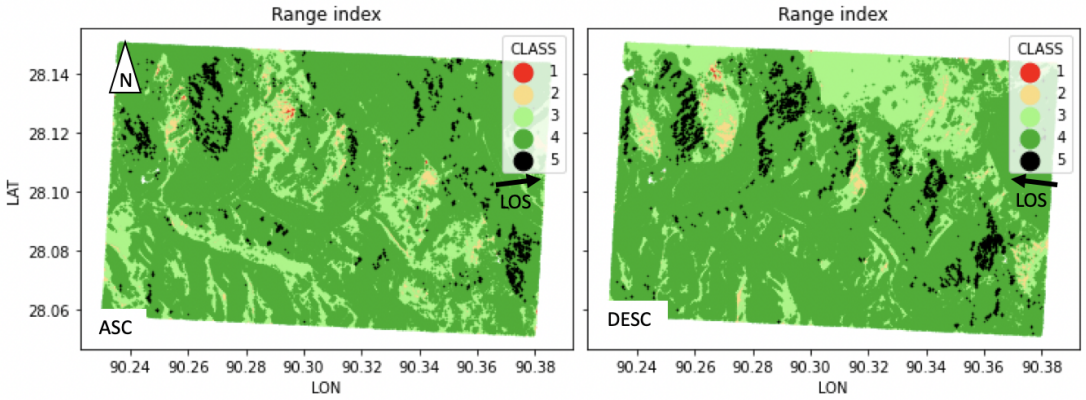

Figure F.3: Range index maps at Lunana Lakes

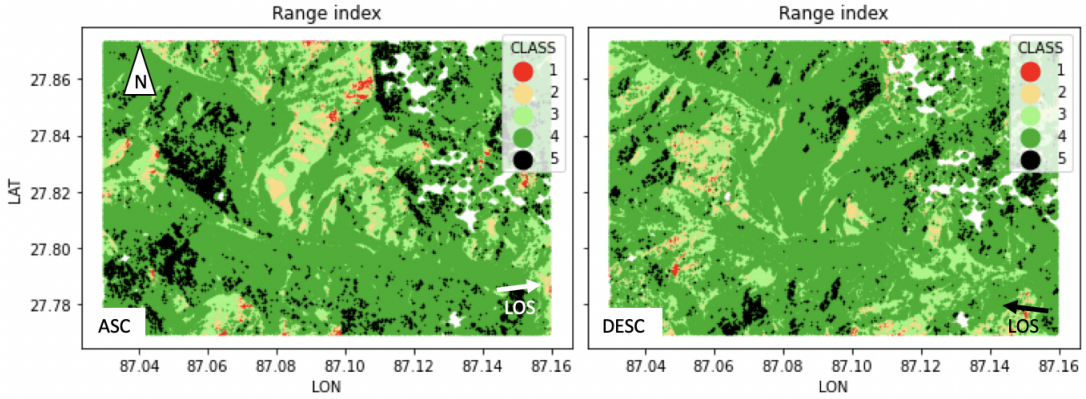

Figure F.4: Range index maps at Barun Lakes

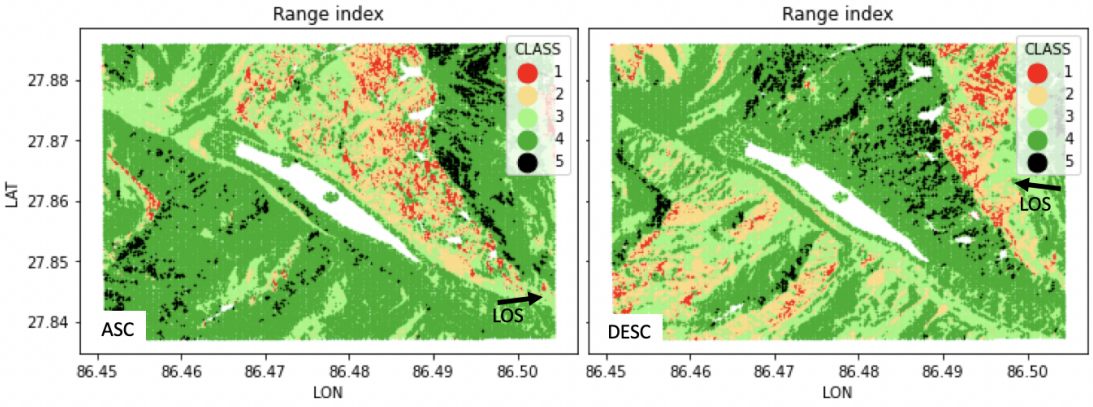

Figure F.5: Range index maps at Rolpa Lake

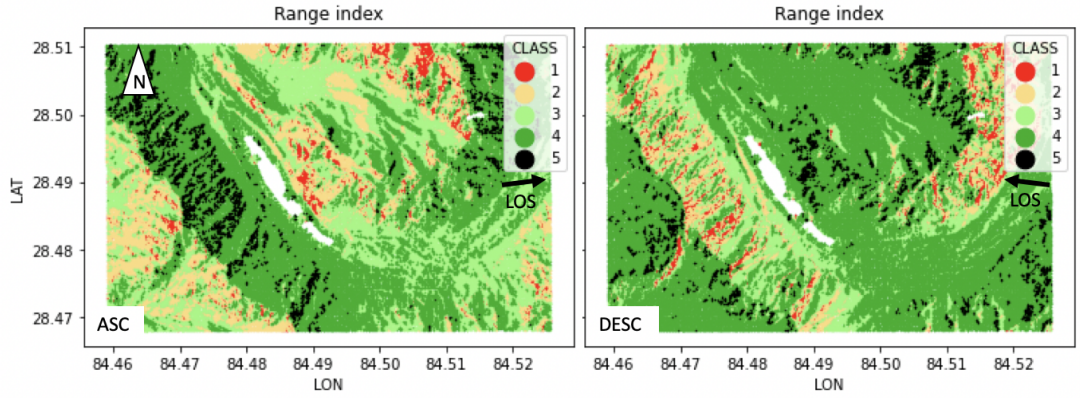

Figure F.6: Range index maps at Thulagi Lake

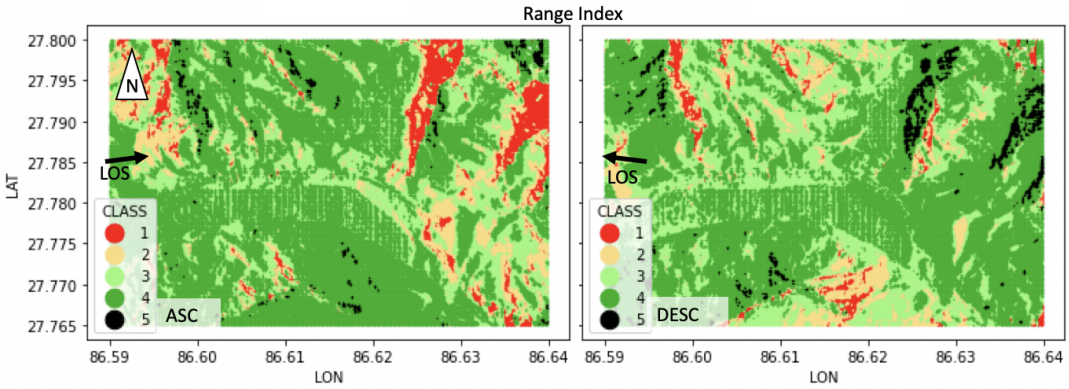

Figure F.7: Range index maps at Lumding Lake